Electrical Structure of Future Off-shore Wind Power Plant with a High Voltage Direct Current Power Transmission

Sharma, Ranjan; Andersen, Michael A. E.; Akhmatov, Vladislav; Jensen, Kim Høj; Rasmussen, Tonny Wederberg

Publication date:
2012

Document Version
Publisher's PDF, also known as Version of record

Citation (APA):
Sharma, R., Andersen, M. A. E., Akhmatov, V., Jensen, K. H., & Rasmussen, T. W. (2012). Electrical Structure of Future Off-shore Wind Power Plant with a High Voltage Direct Current Power Transmission. Kgs. Lyngby: Technical University of Denmark (DTU).

Technical University of Denmark

Ranjan Sharma

Electrical Structure of Future Off-shore Wind Power Plant with a High Voltage Direct Current Power Transmission

PhD Thesis

DTU Electrical Engineering
Department of Electrical Engineering

Ranjan Sharma

Electrical Structure of Future Off-shore Wind Power Plant with a High Voltage Direct Current Power Transmission

PhD Thesis

Electrical Structure of Future Off-shore Wind Power Plant with a High Voltage Direct Current Power Transmission

This report was prepared by
Ranjan Sharma[1,2]

Supervisors
T. W. Rasmussen(PhD)[1] - Assoc. Professor
K. H. Jensen(PhD)[2] - Power System Design Engineer
A. Vladislav(PhD)[3] - Professor, Senior Power System Engineer
Michael A. E. Andersen(PhD)[4] - Professor

Department of Electrical Engineering[1]
Centre for Electric Technology (CET)
Technical University of Denmark
Elektrovej building 325
DK-2800 Kgs. Lyngby
Denmark

www.elektro.dtu.dk/cet
Tel: (+45) 45 25 35 00
Fax: (+45) 45 88 61 11
E-mail: cet@elektro.dtu.dk

E R WP EN 341[2]
Siemens Wind Power A/S
Borupvej 16
DK-7330 Brande
Denmark

www.siemens.com/wind
Fax: (+45) 99 99 22 22
E-mail: info@siemens.com

Energinet.dk[3]
Tonne Kjærsvej 65
DK-7000 Fredericia
Denmark

www.energinet.dk
Fax: (+45) 76 24 51 80
E-mail: info@energinet.dk

Department of Electrical Engineering [4]
Technical University of Denmark
Oersteds Plads 349
DK-2800 Kgs. Lyngby
Denmark

www.elektro.dtu.dk
Tel: (+45) 45 25 38 00
E-mail: elektro@elektro.dtu.dk

Release date: December, 2011
Category: 1(public)
Edition: First
Comments: This report is a part of the requirements to achieve the PhD degree in Electrical Engineering at the Technical University of Denmark.

ISBN: 978-87-92465-87-0

Abstract

The increasing demand of electric power and the growing consciousness towards the changing climate has led to a rapid development of renewable energy in the recent years. Among all, wind energy has been the fastest growing energy source in the last decade. But the growing size of wind power plants, better wind conditions at off-shore and the general demand to put them out of sight have all contributed to the installation of large wind power plants in off-shore condition. However, moving wind power plants far out in the off-shore comes with many associated problems. One of the main challenges is the transmission of power over long distance. Historically, the power transmission from off-shore wind power plants has been done via HVAC submarine cables. This provides a simple solution, but AC cables cannot be arbitrarily long. It is shown in the report that major issues with HVAC cable transmission system are related to surplus reactive power and added losses. On the other hand, HVDC transmission system can be arbitrarily long and for long distance power transmission requirement it provides much better efficiency compared to a corresponding HVAC system.

HVDC may provide a viable solution for high power transmission over long distances, but some issues related to fulfilling different grid code requirements still need further clarification. A transmission system should foremost provide a stable power transmission and participate in network stabilizing by providing efficient support for AC voltage control and frequency response requirements. These objectives are discussed and verification with simulation results is included in the report. A concept of negative sequence voltage compensation during small voltage unbalances and asymmetrical faults at the grid are also discussed. Secondly, a large WPP is not allowed to trip off during temporary grid side faults, commonly described as low voltage fault-ride-through requirement. There are four different fault-ride-through options discussed in the report. The first option includes controlling of collector network frequency. This provides a very good opportunity to use simple fixed speed wind turbines in the wind power plant. Induction generators attached to a large rotating mass show good response to frequency rise by allowing the rotor to speed up while reducing the active power output. However, it is observed that the post fault recovery process is very difficult to control and as such a high current capacity of the WPP side VSC might be required. Detailed simulation results are included in the report. The other option is to use a DC chopper, the results of which are also presented in

detail in the report. It is observed that a DC chopper can provide a simple solution but the efforts required to remove the total heat during power dissipation is enormous. Alternatively, a telecommunication signal may be used, but the reliability and speed of such a system is in doubt.

Finally, a controlled AC voltage drop at the collector network is derived and discussed in detail. It is illustrated in the report that such an option is advantageous in the sense that a fault at the grid side and at the wind power plant side can be dealt in the same way. More importantly, a similar wind turbine type can be used regardless of HVAC or HVDC connection strategy. A good co-ordination between the full-scale wind turbine and wind power plant side voltage sourced converter is also verified in the laboratory model based on real time digital simulation of wind turbine connected to an external voltage source converter via a power amplifier. The overall results show that the power transmission from long distance off-shore wind power plant is viable via HVDC system and at the same time the strict gird code requirements can also be fulfilled by selecting proper control methods.

Acknowledgment

First of all, I would like to express my profound gratitude to my main supervisors, Tonny W. Rasmussen and Kim H. Jensen for their generous support throughout the project. A work of this nature requires support and motivation which I constantly received from them. I would also like to thank my co-supervisor Vladislav Akhmatov for all the detailed discussions and all his invaluable comments and suggestions. The help provided by Michael A. E. Andersen during the start-up phase of the project is also acknowledged.

This work has been performed within Siemens Wind Power A/S and co-funded by Danish Agency for Science, Technology and Innovation. I would like to express my sincere thanks to them for providing me with the opportunity and funding the project.

I would also like to extend my sincere thanks to the entire Grid Connection Group in Siemens Wind Power and all the people at Center for Electric Technology (CET), DTU. I have had many fruitful discussions with my colleagues at Siemens Wind Power and DTU, I like to thank them all for the wonderful time I had during the last three years.

Finally, I like to thank my family for their ever lasting support, love and blessings. At last but not the least, I would like to thank my wife, Riti, for her endless support, good advices and being with me during all the difficult phases.

To H. H. Shree Mataji

Preface

This dissertation has been submitted to the Center for Electric Technology, Technical University of Denmark in partial fulfillment of the requirements for acquiring the PhD degree in electrical engineering and Danish Industrial PhD degree. The project has been conducted from Sept. 2008 to Sept. 2011. The project was carried out as an industrial PhD project. The industrial partner being Siemens Wind Power A/S and is also co-funded by Danish Agency for Science, Technology and Innovation.

The project has been carried out between Technical University of Denmark and Siemens Wind Power A/S. The report deals with electrical structures and power transmission options for future off-shore wind power plants with high voltage DC transmission option.

Ranjan Sharma

October 2011, Kgs. Lyngby, Denmark

Contents

Abbrebiations

ASVC	Advanced static VAR compensator
CHIL	Control-hardware-in-the-loop
DSP	Digital signal processor
HIL	Hardware-in-the-loop
HVAC	High voltage AC
HVDC	High voltage DC
IGBT	Insulated gate bi-polar transistor
LCC	Line-commuted converter
LV	Low voltage
LV-FRT	Low voltage fault-ride-through
MF	Medium frequency
MMC	Modular multi-level converter
MV	Medium voltage
NPC	Neutral point clamped
PCC	Point of common coupling
PHIL	Power-hardware-in-the-loop
PI	Proportional integral
PLL	Phase locked loop
PMSG	Permanent magnet synchronous generator
PWM	Pulse width modulation
RMS	Root mean square

RTDS	Real time digital simulation
SCR	Short circuit ratio
SVC	Static VAR compensator
TSO	Transmission system operator
TSR	Tip speed ratio
UK	United Kingdom
VSC	Voltage sourced converter
WPP	Wind power plant
WTG	Wind turbine generator
XLPE	Cross linked polyethylene insulated power cable

One

Introduction

1.1 Background

Many future WPPs (wind power plants) are commissioned or planned for off-shore installations. The main reasons being that the wind turbines are ever growing bigger by size and the wind conditions are much better at off-shore. To some extend the decision is also driven by various environmental factors and also to keep the WPP out of sight. As the wind conditions off-shore are generally better, the capacity factor[1] of an individual wind turbine or that of an entire WPP will also significantly increase compared to on-shore installations. At the time of writing this report, around 3 000 [MVA] is the total off-shore installed capacity, around 4 000 [MVA] is the total capacity under construction and more than 10 000 [MVA] have been approved for future construction [1]. UK is the current world leader in off-shore wind power installations with over 1.3 [GW]. The trend of future off-shore WPP world-wide is presented in Fig. 1.1 (data source: [2]) and based on the data it can be expected that both the installed capacity and the distance to the shore will increase in the future. It is also estimated in [3] that the total operating off-shore wind energy capacity in the whole of Europe will be between 20 [GW] to 40 [GW] by 2020. Therefore, there exists a clear need to analyze and investigate different power transmission options or possible electrical structures to connect a high power and long distance off-shore WPP to a nearby on-land transmission system.

1.2 Present Scenario

A conventional technique of transmitting power from an off-shore WPP is via HVAC (high voltage AC) sub-marine cables. Most of the present large off-shore wind farms including ‘Thanet off-shore wind farm’, the largest off-shore wind farm to date with total installed capacity of 300 [MVA] [4], and ‘Horns Rev II’ with total installed capacity of 209 [MVA] [5] are based on HVAC transmission system. In case of HVAC transmission, the WPP collector network is usually at a medium voltage (≈ 33 [kV]) level. The total power is collected at an off-shore platform where the medium

---

[1] Capacity factor is usually defined as a ratio of the total energy output from a given WPP over a period of time to the total maximum energy output from the WPP had it been possible to operate the WPP at rated output over the same period of time

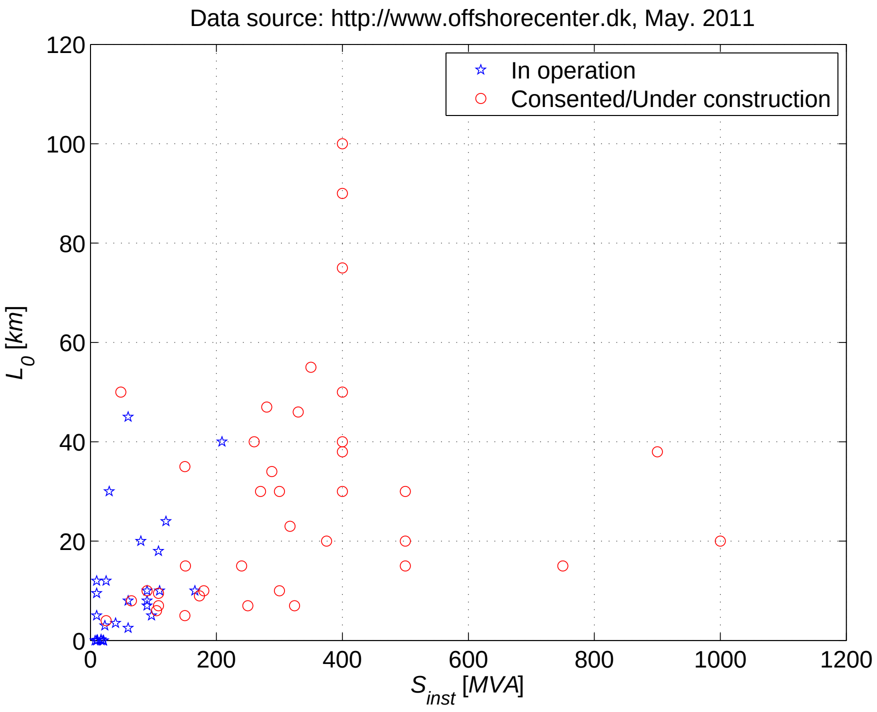

Figure 1.1: The trend of future off-shore WPP - installed power capacity vs distance from the shore

voltage level is transformed into a transmission level voltage (> 100 [kV]). The power transmission distance to the near-by power system is relatively small (< 50 [km]) and, therefore, a HVAC transmission option is justified. The first large off-shore WPP utilizing a HVDC transmission system is ‘BARD off-shore 1’ with total installed capacity of 400 [MW] and located approximately 200 [km] from the AC grid connection at the coast of north sea [6]. The WPP is planned to be in operation by 2012. The main reason for HVDC transmission is to allow high power transmission over the long distance.

1.3 Problem Statement

The bigger the electrical size of a WPP, the higher the number of total wind turbines required. Considering the distance that has to be maintained between the wind turbines in a WPP, the area of the farm could well be several tens of $sq.km$. The distance of the WPP from the coast will also increase accordingly. Current WPPs with relatively shorter distance (< 20 [km]) from the shore acquire HVAC transmission technology. For large distances (> 100 [km]) and high installed capacity (> 100 [MVA]), the suitability of HVAC transmission is questionable. Charging current in long AC cables are too high and the capability of the AC cables to transmit active power diminishes with transmission length. Reactive power compensation can be provided, but only at the two ends of the transmission cables. Building off-shore compensation units are not cost friendly. An alternative solution, therefore, is to use a HVDC transmission system.

A conventional or classical HVDC system is realized with thyristor-based converters. The functionality required to initialize the off-shore WPP collector grid, however, cannot be fulfilled by a classical HVDC system. Alternatively, modern HVDC systems are based on VSC (voltage sourced converter) technology utilizing IGBT (insulated gate bi-polar transistor) type switching devices. As such, AC voltage magnitude and phase at both ends can be controlled rapidly and independently within the system limits. However, the total installed capacity of renewable energy, specifically wind energy, is experiencing a rapid growth; grid code requirements are also becoming more stricter.

Most TSOs (transmission system operators) have set grid code requirement on LV-FRT (low voltage fault-ride-through). This implies that the WPP is obliged to stay connected or enter stand-by mode when the voltage level at the PCC (point of common coupling) to the host power system is temporarily very low or even unavailable as shown in Fig. 1.2. In case of a HVDC transmission system connecting two point-to-point power systems, the issues related to voltage dips are relatively easy to handle. If a voltage dip is experienced at the receiving end AC voltage, the other end VSC control will immediately reduce the transfer of active power. If a similar approach is applied to the HVDC system connecting an off-shore WPP, the AC voltage magnitude at the WPP collector network will increase rapidly causing the WPP to eventually trip off. On the other hand, if no action is taken, the WPP may continue to deliver the same amount of active power as in the pre-fault situation and the excess of energy will rapidly charge the HVDC side capacitors. Again the system will eventually trip off if the DC voltage level exceeds a pre-assigned limit.

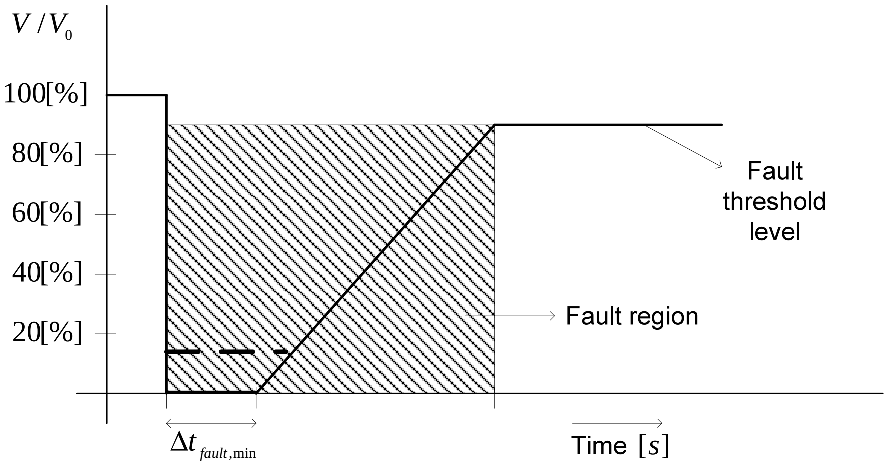

Figure 1.2: Limit curve for voltage at the PCC for WPPs in the event of fault in the grid

Apart from the FRT requirements, it is also expected form a large WPP to provide voltage and frequency support at the PCC, meaning that the output reactive and active power must increase in response to the decrease in grid AC voltage magnitude and frequency respectively or vice-versa. Therefore, even though a HVDC transmission solution may provide economical and technical benefit over long transmission distances, practical fault-ride-through solutions and other requirements of such a system still need clarification.

1.4 Main subjects of study

The major subject of study of this project is to investigate control solutions with HVDC power transmission from an off-shore WPP to the near-by power system. This report is designed to contribute the following areas or subjects:

1. Which parameters (e.g. transmission distance, installed power capacity) are determining the shift from AC to DC transmission technology in connection with an off-shore WPP? It is a known fact that AC cables cannot be arbitrarily long. How long they can be may depend on the power level, cable type, frequency, voltage level, price, reactive power compensation etc. Therefore, it will be investigated in this report for which distances, power levels, etc, a technology shift should be made.

2. Later on, when advantages and disadvantages of the two power transmission technologies (AC and DC) are clarified, a total investigation will also be made on the collector network and connection to the transmission network. Should AC or DC technology be used in the collector network in the wind farm? When the conditions call for the use of DC transmission, this opens up alternative possibilities for design of the collector network. An AC collector network or a DC collector network can be used, as modern converter technology based on IGBTs makes this possible. Another possibility would be a mixed AC-DC network. It will be investigated which is the optimal solution based on current situation and future developments.

3. Which types of wind turbine should or could be used? From the manufacturers prospective, it is a major benefit if a similar wind turbine structure can be used regardless of AC or DC transmission solution. Wind turbine structures based on fixed speed operation (induction generators) and variable speed operation (full-scale with induction or permanent magnet generators) will be investigated.

4. Which control properties will the system have? Modern WPPs must not only be able to deliver maximum power to the network, they must also be controllable like conventional power plants and deliver the demanded power. The WPPs must also participate in controlling the voltage and frequency in the network (network stabilizing) and other grid requirements. Furthermore, the

WPP must be able to enter stand-by during short fall outs of the network. Thus, the proposed system(s) will be examined with regard to the above mentioned properties.

1.4.1 Major Contributions

The major contributions of this report are listed below.

- A very detailed computational method is established in order to compare between different transmission solutions for future off-shore WPPs.
- Comparison between three different transmission solutions (HVAC, HVDC with AC collector network and HVDC with DC collector network) is presented. From the losses point of view and available components development, it is illustrated that a HVDC transmission system with AC collector network is best suited for the near future. However, it cannot be ruled out that a DC collector network solution might me the ultimate solution in the further future.
- A dynamic simulation model is developed with fairly detailed representation of all major components. The total system model is developed so that it could be used to study the synergy between wind turbines and future HVDC transmission system.
- Comparisons between and evaluations of various FRT strategies have been made. It has been suggested in many cases that fixed-speed wind turbines can be employed when the transmission of power is via HVDC system. A very detailed investigation of the FRT capability of such a system is presented and different unforeseen challenges concerning centralized control of fixed-speed wind turbines are outlined.
- A DC chopper solution for handling FRT issues is investigated and compared against controlled AC voltage solution at the WPP. A concept of DC voltage control switch-over between the grid side VSC and the WPP side VSC is investigated and a control system is derived to allow AC voltage control at the WPP collector network during grid side fault. It is verified for all fault conditions (including multiple dips, and unbalanced faults) that the proposed control method is fully applicable.
- The ability of the system to withstand and ride-through WPP side faults (if necessary) is also demonstrated.
- Control strategies to compensate for different levels of network voltage unbalances are presented. The ability of a VSC based HVDC system is evaluated in terms of negative sequence reactive current control during unbalanced faults. It is recommended after due consideration of the findings that such a controlability of a HVDC system can provide added value and efficient support to the grid voltage during unbalanced faults.

- Finally, a partial experimental validation of controlled AC voltage solution at the WPP equipped with full-scale permanent magnet type wind turbine is presented in the report.

1.4.2 Method

The three methods primarily used in the project are theoretical calculations, simulations, and building of a laboratory model. Theoretical calculations are natural for a number of isolated issues such as for e.g., identification of parameters calling for the shift from AC to DC transmission technology. Most of the calculations are performed or coded in ‘Python programming language’. When a larger and more complex system is examined, simulation models are designed and developed such that they can be used for various dynamic simulations, capable of handling various components included in the investigated system. For this purpose ‘Matlab, Simulink’ is used. The most interesting solution or partial solution is tested in a laboratory scale model to secure that missing details in the simulation model does not have significant influence on the results. Laboratory model includes real time digital simulation of a wind turbine in RTDS (real time digital simulation), a power amplifier, and a VSC controlled by a designated DSP (digital signal processor).

1.4.3 Limitations

Based on the methodologies applied during different types of investigation, there are some limitations that needs to be taken into consideration. Some of the limitations are listed below.

1. All the results and comparisons presented in this work are based on technical analysis. The report does not include economical analysis.

2. All the theoretical calculations are based on the data provided in the manufacturer’s data-sheet. Therefore, no experimental verifications are available.

3. This report does not deal with WPPs based on doubly-fed induction generators.

4. The limitations of the simulation tools used during the work are also the limitations of the results presented in the report.

5. Based on the complexity of the simulation, some of the components are represented by reduced order model. Although a valid reason and appropriate verifications are included when such simplifications are made, they can provide some limitations on the final results.

Two

HVAC Transmission System

This chapter introduces to a standard HVAC transmission system for an off-shore WPP. Different technical problems associated with long distance sub-marine AC cables are outlined. Finally, losses evaluation technique is described and results are presented for different components of a HVAC transmission system including collector network, transformers, compensators and cables.

Generation units or power plants are often built far from the load centers. The bulk power, thus, needs to be transported over long distances. HVAC transmission system has been the most common option in transporting bulk electrical power over long distances. Power transmission is often done at a high voltage level (> 100 $[kV]$) to reduce current dependent losses in the transmission line [7]. The choice of transmission voltage level and the frequency (50 $[Hz]$ or 60 $[Hz]$) varies among different countries and power systems. When the HVAC transmission system is on-land, the most common technique is to use over-head lines. Depending upon different variables like environmental impact, visual pollution, government policies, technical requirements etc., there are also cases where under-ground cable transmission is preferred. If the power plant is located in an off-shore location, it is not an option to transport power via over-head lines. In such a situation, power transmission is usually done via single-core or three-core sub-marine HVAC cables. Many off-shore WPPs also use similar technique to transport power to the near-by on-land transmission system. In this chapter, the HVAC power transmission from off-shore WPP is discussed.

2.1 Off-shore Wind Power Plant

An electrical structure of a standard off-shore WPP with HVAC power transmission system is illustrated in Fig. 2.1. Individual wind turbines in such a WPP are connected to a local grid normally referred to as collector network via wind turbine transformers. The collector network, often at medium voltage (≈ 33 $[kV]$) level, connects the WPP to a high voltage transmission system through a park transformer. In case of a small WPP with short distance from the coast, the power transmission can be done at the medium voltage level. This implies that the park transformer is not necessary. However, for a large WPP, the park transformer is necessary and so is the off-shore platform for the installation of a sub-station. The power transmission in all cases is done by sub-marine cables to the coast or the near-by on-land power system.

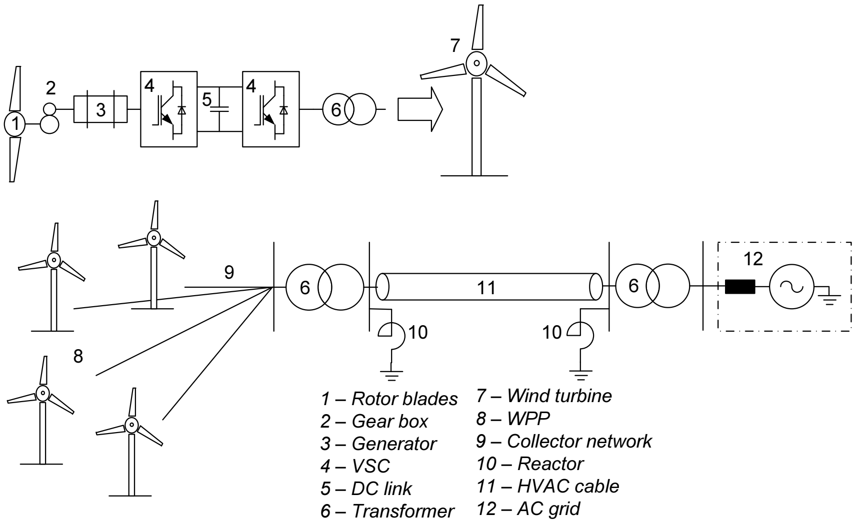

Figure 2.1: HVAC power transmission from an off-shore WPP to the near-by on-land transmission system

2.2 HVAC Cable Transmission

The basic parameters of HVAC over-head lines and HVAC cables are similar, but some characteristic differences exist due to the difference in the values of these parameters. HVAC cables have higher shunt capacitance per unit length compared to the corresponding over-head lines. For long HVAC cables, the surplus of reactive power due to the HVAC cable charging imposes a major drawback on such transmission systems. Though the HVAC cable transmission systems got improved and advanced, the main constraints of such systems still remain in cases of long transmission as presented in [8] & [9]. Specifically, the ability of active power transmission reduces (as illustrated in Fig. 2.2) and reactive power generation and compensation efforts increase as the cable length increases. A simple conclusion drawn for a HVAC cable transmission is that either high power can be transmitted over short distances or low power can be transmitted over long distances.

In Table2.1, the parameters of all the cables used to compute the plots in Fig. 2.2 are presented. The three voltage levels in consideration are 132 $[kV]$, 220 $[kV]$ and 400 $[kV]$, which are also the standard voltage levels used in HVAC cable transmission system. Cables are available in many different cross-section areas (a $[mm^2]$), but only the examples of 800 $[mm^2]$ cables are shown. The selected cables are single-core, copper conductor and XLPE (Cross linked polyethylene insulated power cable) type

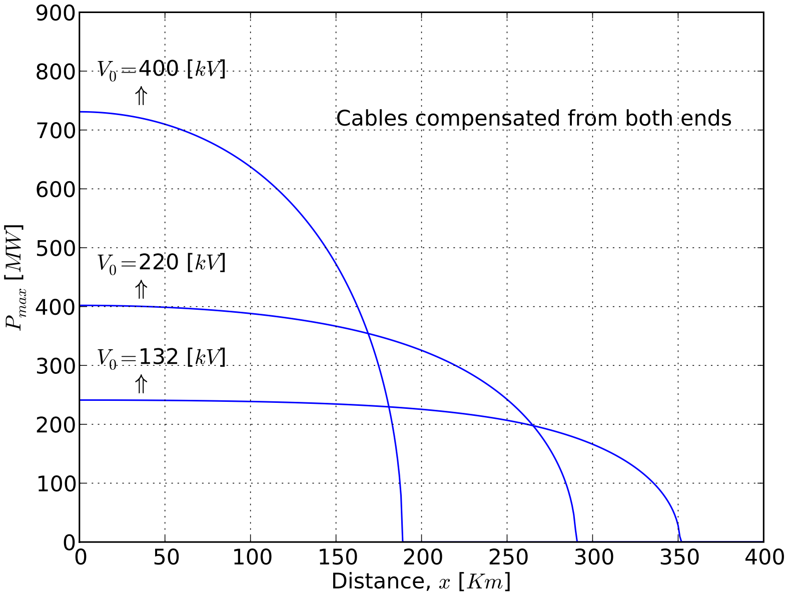

Figure 2.2: Active power capacity reduced due to the HVAC cable charging

and the nominal current is based on the assumption that the cables are laid with wide spacing flat installation.

Table 2.1: Cable parameters

	Parameters		
V	132 [kV]	220 [kV]	400 [kV]
a	800 [mm^2]	800 [mm^2]	800 [mm^2]
R/m	32.6 [$\mu\Omega$]	32.6 [$\mu\Omega$]	32.6 [$\mu\Omega$]
L/m	0.54 [μH]	0.56 [μH]	0.58 [μH]
C/m	0.22 [nF]	0.17 [nF]	0.15 [nF]
I_{nom}	1055 [A]	1055 [A]	1055 [A]

2.2.1 Characteristics of a HVAC Cable Lines

The characteristics and performance of a HVAC cable line can be described using the well known transmission line equations. The general equations for a transmission line can be achieved if it is assumed that the receiving end ($x = 0$) voltage and current are known. The equations for the voltage and current along the line while moving towards the sending end can be written as [7];

$$\vec{V}(x) = \frac{\vec{V_R} + Z_w \cdot \vec{I_R}}{2} \cdot e^{\gamma \cdot x} + \frac{\vec{V_R} - Z_w \cdot \vec{I_R}}{2} \cdot e^{-\gamma \cdot x} \tag{2.1}$$

$$\vec{I}(x) = \frac{\vec{V_R}/Z_w + \vec{I_R}}{2} \cdot e^{\gamma \cdot x} - \frac{\vec{V_R}/Z_w - \vec{I_R}}{2} \cdot e^{-\gamma \cdot x} \tag{2.2}$$

Where,
x: distance from the receiving end along the cable
$\vec{V_R}$: receiving end voltage
$\vec{V_S}$: sending end voltage
$\vec{I_R}$: receiving end current
$\vec{I_S}$: sending end voltage
γ: propagation constant
Z_w: characteristic impedance

The characteristic impedance and the propagation constant of a cable line are defined as,

$$\gamma = \sqrt{y \cdot z} = \alpha + j\beta \tag{2.3}$$

$$Z_w = \sqrt{z/y} \tag{2.4}$$

Where,
$y = R + j(\omega \cdot L)$ (series impedance per unit length)
$z = G + j(\omega \cdot C)$ (shunt admittance per unit length)

The parameters R and G, per unit length, are relatively small and are, therefore, neglected in many cases except for the evaluation of line losses.

The total charging current of a cable line at the terminals can be calculated by the help of an equivalent π circuit. An equivalent π circuit of a transmission line is derived from (2.1) and (2.2), by letting $x = L_0$; where L_0 is the total length of the line. The shunt and series parameters of the equivalent π circuit can be expressed as,

$$\frac{B_c}{2} = \frac{1}{Z_w} \cdot tanh(\frac{\gamma \cdot L_0}{2}) \tag{2.5}$$

$$Z_l = Z_w \cdot sinh(\gamma \cdot L_0) \tag{2.6}$$

As discussed earlier, the limitations outlined by the charging current of the HVAC cables become significant because of surplus reactive power when the transmission distance gets longer. Charging current in a cable is,

$$I_{chg} = B_c \cdot |V_a| \tag{2.7}$$

Where, B_c, derived from the equivalent π circuit of a transmission line [7], is the total capacitive susceptance of the cable and $|V_a|$ is the rated line to neutral voltage.

Besides the shunt capacitance, HVAC cables also have series impedance per unit length. The effect of such series impedance in the HVAC cable line is such that the reactive power demand of the line increases with the increase in active power transfer.

If the transferred power is much below the surge impedance load (P_{SIL}) of the cable line, the demand of reactive power is small compared to what is surplus due to the shunt capacitance as illustrated in Fig. 2.3. The negative sign is used to represent the surplus reactive power while the positive sign represents the total demand.

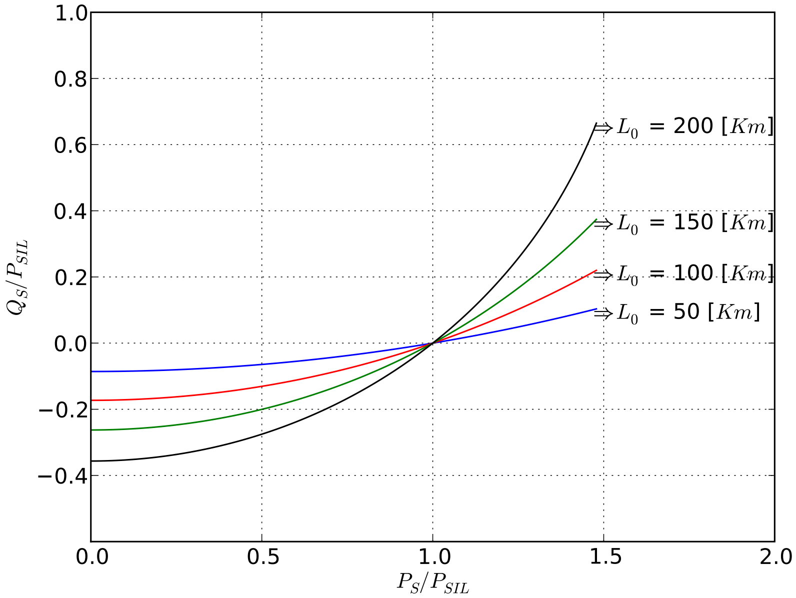

Figure 2.3: Reactive power demand of a cable line as a function of transmitted active power; $V_0 = 132\ [kV]$

Surge impedance load is defined as,

$$P_{SIL} \quad = \quad \frac{|V_0|^2}{Z_w} \tag{2.8}$$

When the transmitted power is less than P_{SIL}, it is required to consume the surplus reactive power at one or both ends of the cable. If the voltage magnitudes at the two cable ends are to be kept constant, the surplus reactive power has to be equally consumed at both cable ends. This can be achieved within tolerable limits by utilizing compensators for e.g. inductors or SVCs (Static VAR compensators). The length of the cable for which the nominal current of the cable equals the charging current is termed as the 'critical length' of the cable. If the cable is equally compensated from two ends, the critical length approximately doubles up compared to one end compensation [10]. The plot showing the critical cable length of a 132 $[kV]$ single core cable when compensated from two ends is presented in Fig. 2.4. The figure also shows the difference in total active power transfer capacity at different distances calculated by taking the line inductance in account and neglecting it. It can be observed that the total critical cable distance remains the same (as there is no more available room for active power) while there exists considerable differences at other distances.

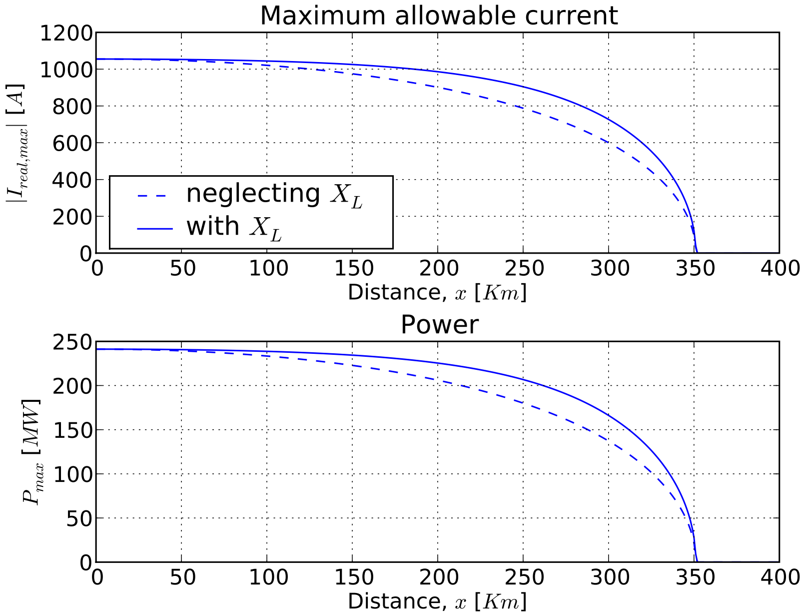

Figure 2.4: Transmission distance vs. current and active power for a sub-marine cable when compensated from both ends; $V_0 = 132$ $[kV]$

The parameters of the cable are presented in Table 2.1. It can be observed that the critical length of the cable in consideration is close to 350 $[km]$. It has to be, however, kept in mind that the critical cable length calculated here is the theoretical limit and is based on the nominal current. However, in practice the allowable limit of maximum current of the cable will be lower than the nominal current due to thermal constraints and thus the critical length and the maximum power will be lower as well.

Due to the charging current, the distribution of the voltage and especially current along the cable length is not uniform. For a fully compensated line from both ends, the magnitude of the voltage at the cable ends remain constant and the surplus reactive current flows equally towards the cable ends. At the middle of the cable, the reactive current is zero and at each cable ends, the value is $I_{chg}/2$. As a consequence, the voltage magnitude at the middle of the cable is maximum. If the losses along the line are neglected during the evaluation of the voltage and current profile, the resulting profile is as shown in Fig. 2.5a. Alternatively, the compensation units can be placed in between the cable sections as for the Horns Rev HVAC cable connection [11]. But for large distances, it is not feasible both technically and economically to locate those units in the sea.

The PV curve of the given transmission system proved that the maximum no load voltage at the midpoint is 133.96 $[kV]$ for a transmission distance of 100 $[km]$, as illustrated in Fig. 2.5b. The different PV curves for different distances are only shown upto the surge impedance load point ($P_{SIL} = 351.7$ $[MW]$). To summarize the results, for a medium sized power transmission level (≤ 400 $[MVA]$), it could be verified that the transmission distance is only limited by the current capacity of the cable and not the voltage rise or the voltage angle.

2.3 Energy Losses Evaluation

The increase in charging current and cable losses with increasing distance, thus, limits the ability of a HVAC cable transmission system to transmit bulk power over long distances. Apart from the cable losses, the other major components contributing energy losses are the losses in the collector network, off-shore and on-shore transformers and compensating reactors. In this section, distribution of losses in all major components of a HVAC cable transmission system from a WPP will be evaluated. Power from a WPP is not constant due to the variation of wind velocity over time. Therefore, it is more reasonable to evaluate energy losses rather than power losses.

The entire WPP is modeled as a single re-scaled wind turbine computed with a multi-turbine power curve approach. Acknowledging good wind conditions offshore, the energy losses are evaluated for the average wind speed 10 $[m/s]$, as compared to 9.7 $[m/s]$ average wind speed for Horns Rev off-shore location [11]. To evaluate the energy losses, the power curve from the WPP is applied to the first component (collector network in this case). The losses at each element (wind speed) of the power curve are calculated to produce the total energy losses. The new power curve adjusted with the losses is then applied to the proceeding component.

2.3.1 Wind Power Plant

In general, the entire WPP power curve can be derived as a product of the single wind turbine power curve and the total number of wind turbines. However, this assumption does not account for uneven wind distribution over the WPP area. In a WPP, wind variation can occur both in space and time. To compensate for this, a multi-turbine power curve is applied according to the description below. The investigated system consists of a WPP comprising 3.6 $[MVA]$ wind turbines (being a standard product of Siemens Wind Power A/S for off-shore applications).

Fig 2.6 is derived for a WPP rated at 180 $[MVA]$ with $N = 50$ number of wind turbines. It can be noticed from Fig. 2.6 that the difference between a multi-turbine power curve and a single turbine representation for a relatively small WPP does not seem so big. However, when annual energy is computed, the difference is still significant, justifying the use of a multi-turbine power curve approach suggested in [12]. Therefore, all the calculations made in this work are based on that methodology. A 10 [%] turbulent intensity is considered within the WPP area. Finally, the multi-turbine power curve is calculated as below,

$$P_{m,i} = \sum_j P_{s_{i+j}} \times p_{s_j} \tag{2.9}$$

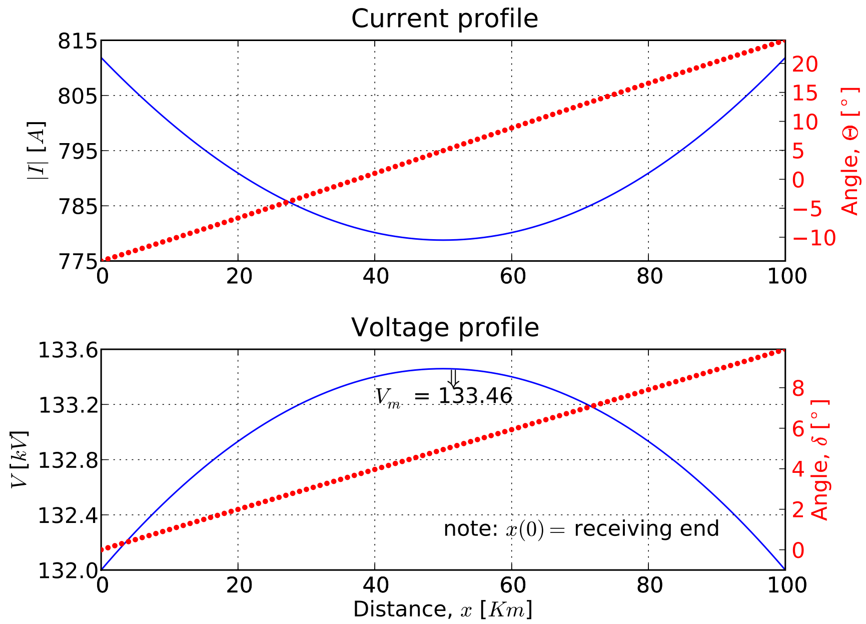

(a) Voltage and current profile; $P_R = 180$ $[MW]$, $V_0 = 132$ $[kV]$

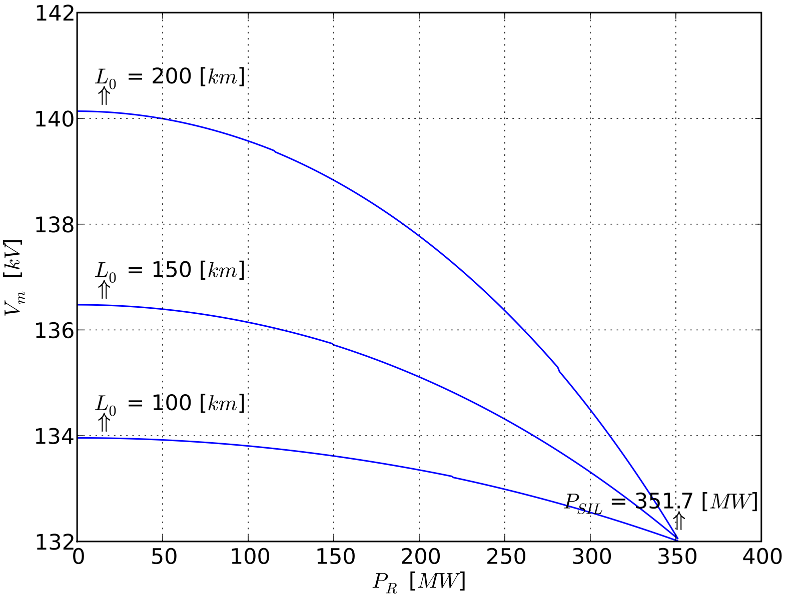

(b) PV curve; $V_0 = 132$ $[kV]$

Figure 2.5: Voltage, current and power relation with transmission distance.

Where P_{s_i} is the i^{th} element of the single turbine power curve, p_{s_j} is the probability of the spatial distribution.

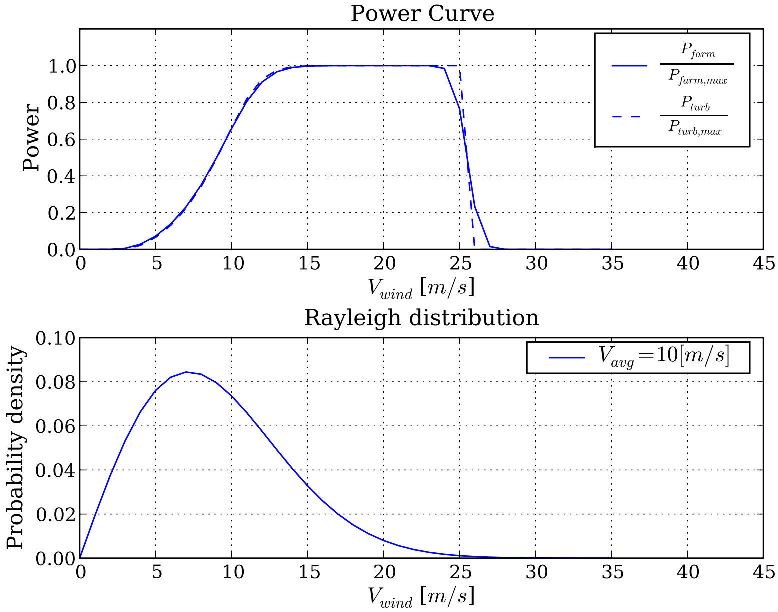

Figure 2.6: Multi-turbine power curve (above) and the wind distribution (below)

When the multi-turbine power curve and the wind distribution over the particular site area are known, the total annual energy production can be calculated as in (2.11). The wind in a site can be represented by different probability distribution functions. The distribution function considered here is a Rayleigh distribution with $k = 2$ as in (2.10);

$$f(v) = \frac{k}{\lambda} \cdot \left(\frac{v}{\lambda}\right)^{k-1} e^{-(v/\lambda)^k} \tag{2.10}$$

$$E_{farm} = \sum_{v} f(v) \cdot P_m(v) \cdot 8760 \tag{2.11}$$

Where v is the range of wind velocity, $\lambda = 2 \cdot V_{avg}/\sqrt{\pi}$ and V_{avg} is the average wind velocity. The total operation utilization of the WPP is taken to be 1. In a real WPP, wind turbines are taken out of service for maintenance, environmental factors like icing shut-down etc. and, hence, the utilization is below 1. These situations with lower utilization factors or different average wind velocitys are not included in this report, however, such evaluations can be easily accomplished by simply adjusting the inputs to the code prepared during the project.

2.3.2 Collector Network

Individual wind turbine in a WPP is connected to the collector network via a wind turbine transformer, $0.690/33$ $[kV]$. Wind turbines in a WPP are arranged in rows. The layout of the WPP that has been considered in this work is shown in Fig 2.7.

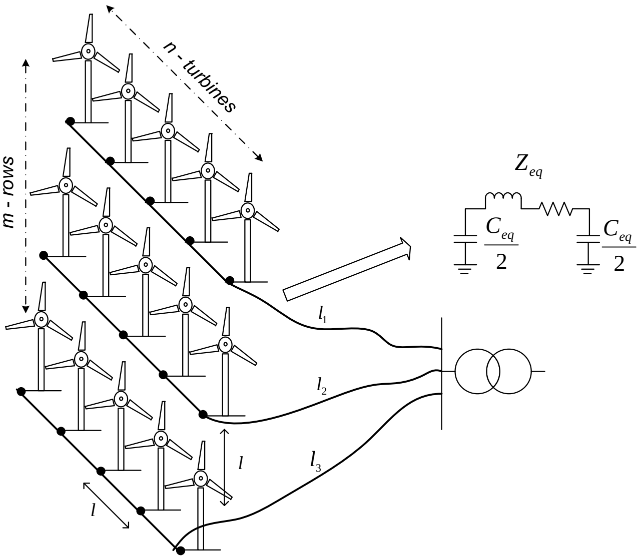

Figure 2.7: Layout of a WPP

The losses in the collector network depend upon the way the wind turbines are positioned in the WPP. To evaluate the losses in the collector network in detail requires a significant number of computations. The total cable length of the collector network is relatively small. Therefore, it is reasonable to model it using a π equivalent network. To formulate the π equivalent model, the cables inter-connecting the wind turbines in the WPP and the cables connecting the wind turbine rows to the off-shore platform are all included in the same π equivalent. The distance between wind turbines in a row and the distance between two rows is selected $l = 0.750$ $[km]$. For comparison, the distance between wind turbines in Horns Rev wind farm [11] is given to be 0.560 $[km]$; while in case of Nysted wind farm [13] the distance between wind turbines is given to be 0.480 $[km]$ and the distance between two rows is 0.850 $[km]$. After defining appropriate distances between each rows and the off-shore platform, the final π equivalent model is prepared.

For example in a 180 $[MVA]$ WPP, wind turbines are arranged in $m = 10$ rows and $n = 5$ turbines in each rows. A pair of rows is connected together to the off-shore platform; as a result $m/2$ cables are required to connect the rows to the off-shore platform. In each row the maximum current is 315 $[A]$, hence a 33 $[kV]$, 150 $[mm^2]$ cable is selected for wind turbines inter-connection. For connecting rows to the off-shore platform, 33 $[kV]$, 500 $[mm^2]$ cables are selected. The electrical parameters of the cables are presented in Table 2.2. From the cable parameters and known distances, the resulting parameters of the π equivalent model of Fig. 2.7 are listed below,

$Z_{eq} = (0.025 + 0.057j)$ $[\Omega]$
$\frac{C_{eq}}{2} = 5.025$ $[\mu F]$

Table 2.2: Collector network cable parameters

	Parameters	
V	33 $[kV]$	33 $[kV]$
a	150 $[mm^2]$	500 $[mm^2]$
R/m	124 $[\mu\Omega]$	36.6 $[\mu\Omega]$
L/m	0.41 $[\mu H]$	0.35 $[\mu H]$
C/m	0.20 $[nF]$	0.30 $[nF]$
I_{nom}	405 $[A]$	770 $[A]$

2.3.3 Cable Losses

As described earlier, current along the cable line is not uniform. This implies that the power losses along the cable line are not uniform either. To take into account the non-uniform power losses along the cable line, the methodology presented in [14] has been implemented for the losses evaluation of the cables. For any small section dx along the line, the power losses is calculated as,

$$P(dx) = P_{max}(dx) \cdot \left[\frac{I(dx)}{I_{nom}}\right]^2 v_\theta + P_d(dx) \tag{2.12}$$

$$v_\theta = \frac{c_\alpha}{c_\alpha - \alpha_T \cdot \Delta\theta_{max}\left[1 - \left[\frac{I(dx)}{I_{nom}}\right]^2\right]} \tag{2.13}$$

The total power losses is obtained by integrating (2.12) over the total cable length. Where

$$P_{max}(dx) = 3 \cdot I_{nom}^2 \cdot R_{ac}(dx) \tag{2.14}$$

Where $R_{ac}(dx)$ is the resistance per length of the cable. $c_\alpha = 1 - \alpha_T \cdot (20°C - \theta_{amb})$, α_T is the temperature coefficient of copper, θ_{amb} is the ambient temperature and $\Delta\theta_{max}$ is the maximum permissible temperature rise of the cable. Ambient temperature in this work is assumed to be 20 $[°C]$ at the sea bed and maximum cable temperature to be 90 $[°C]$.

The di-electric losses of the cable line is calculated as below [15],

$$P_d(dx) = V_0^2 \cdot \omega \cdot C(dx) \cdot tan\delta \tag{2.15}$$

$$tan\delta = \frac{1}{R_d \cdot \omega \cdot C(dx)} \tag{2.16}$$

Where $C(dx)$ is the capacitance per unit length of the cable, R_d is the dielectric resistance and V_0 is the nominal per phase voltage.

In Fig. 2.8, the total cable losses for different transmission distances are presented. The increase in power losses with increasing transmission distance can be observed. For 132 [kV], 200 [MVA] power transmission level, the percentage losses of the total power in the cables is ≈ 4 [%] at 100 [km] distance.

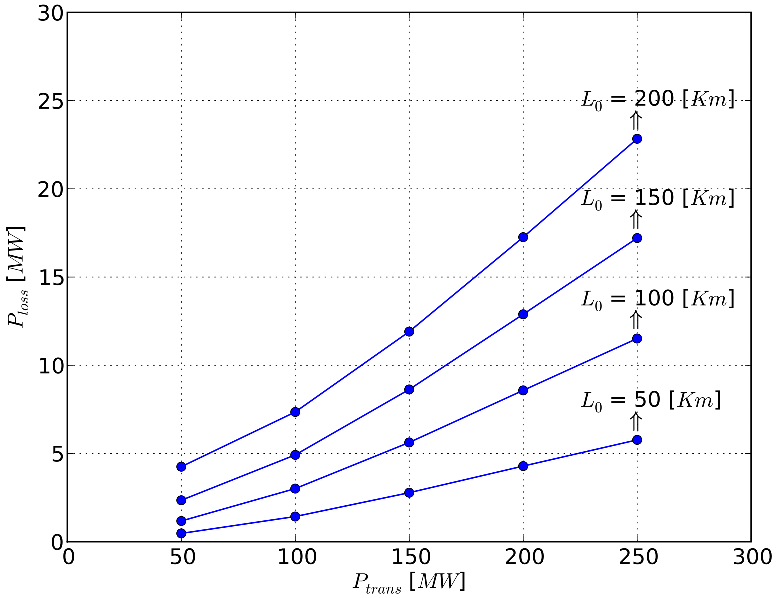

Figure 2.8: Cable losses against the total transmitted power; $V_0 = 132$ [kV]

2.3.4 Transformers and Reactors

The losses in the transformers are calculated using standard procedures from the known values of no-load losses and the winding resistances. The copper resistance is applied $R_c = 0.002$ [pu] and the magnetizing current at no-load is $I_{m,nl} = 0.04$ [%] of the nominal current. The extra components that are required during a HVAC transmission are the compensating reactors placed at the two ends of the transmitting cables. The losses in the reactors are calculated similarly to that of the transformer, but the difference is that a reactor has only one winding. At the off-shore platform the transformer voltage ratio is $33/132$ [kV] while at the on-shore location is $132/400$ [kV].

2.3.5 Losses Distribution

Energy losses at each component is calculated as in (2.17),

$$E_{loss,comp} = \sum_{v} f(v) \cdot P_{loss}(v) \tag{2.17}$$

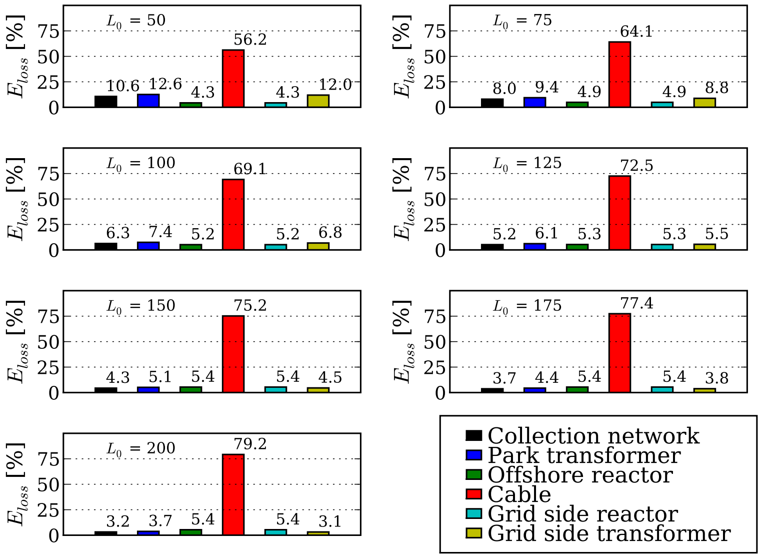

Figure 2.9: Distribution of energy losses as percentage of the total energy losses in the system. $P_{trans} = 180MW$, $V_0 = 132kV$

The majority of the losses is contributed by transmission cables; the selected cable is with $a = 800$ $[mm^2]$. Losses in other components do not change with transmission distance, but the losses in the cables do increase with distance as seen in Fig. 2.8 and Fig. 2.9. For a very long transmission line, the percentage of losses in HVAC cables is so high that the losses in other components become negligible. The cables share 56.2 [%] at $L_0 = 50$ $[km]$ as compared to 79.2 [%] at $L_0 = 200$ $[km]$ of the total energy losses.

In the next step, a WPP of 360 $[MVA]$ is considered; which is twice the size of the one considered previously. The total number of wind turbines is increased to $N = 100$, but the layout of the WPP is assumed to be similar with collector network voltage at 33 $[kV]$. The collector network π equivalent parameters are re-calculated in a similar way as explained earlier.

$Z_{eq} = (0.010 + 0.031j)$ $[\Omega]$

$\frac{C_{eq}}{2} = 13.98$ $[\mu F]$

The transmission voltage is selected to be 220 [kV] and the host power system voltage level to be at 400 [kV]. HVAC cables with $a = 1200$ [mm^2] are selected to allow room for higher current. Distribution of energy losses in different components of the transmission system is shown in Fig. 2.10.

The selection of transmission voltage is generally based on the size of the wind power plant, and eventually the current. Thicker cables are difficult to handle while laying them over the sea-bed. On the other hand, the total charging current requirement of the cables increase with increasing voltage level and the available active power capacity diminishes with increasing distance. As discussed earlier, higher charging current will also increase the cable losses. This is also demonstrated in Fig. 2.10, where the percentage losses in the cables have increased rapidly with increasing distance. The cables share 39.5 [%] at $L_0 = 50$ [km] as compared to 66.3 [%] at $L_0 = 200$ [km] of the total energy losses.

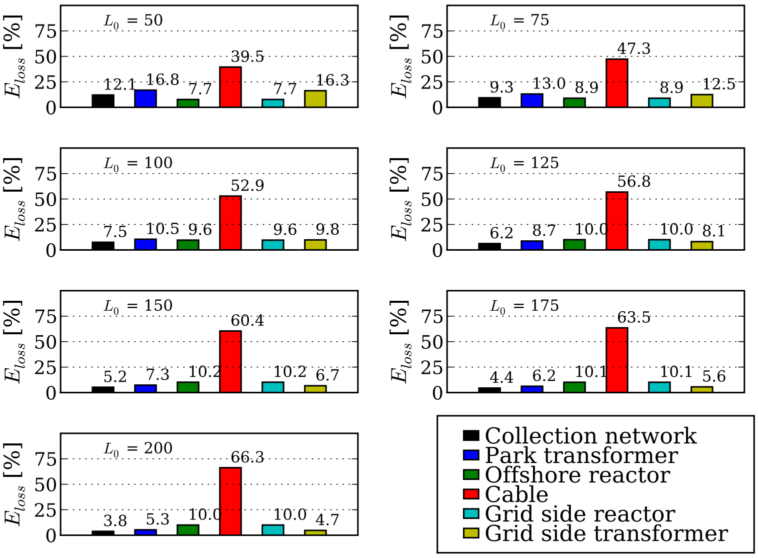

Figure 2.10: Distribution of energy losses as percentage of the total energy losses in the system. $P_{trans} = 360MW$, $V_0 = 220kV$

Three

HVDC Transmission System

In this chapter, two different HVDC transmission systems for an off-shore WPP are discussed - including AC collector network and DC collector network. Losses evaluation method and comparison between the two systems are presented. An over all comparison with a corresponding HVAC system is also illustrated and finally the advantages and disadvantages of all the three systems are outlined.

The choice between an AC system or a DC system (distribution or transmission level) has been under debate since a long time. Important issues like cost, protection units, and transformers etc., have been the major factors in deciding the use of an AC system. However, an AC system has its own associated problems like reactive power, harmonics and limitations of the cable transmission distance. Some components of a HVDC system have advanced in recent years, specifically the VSCs. As a result, the transmission of power from an off-shore power plant is being considered to be done via a HVDC transmission line. Point-to-point power transmission over long distances or connection between two non-synchronous networks is already done via a HVDC line in some cases [16, 17]. At off-shore conditions, the prospect of DC transmission system is considered very attractive due to the limitations of AC cable systems.

HVDC transmission system does not have any theoretical limitations on the transmission distance and as such many research projects are being performed to investigate the use of HVDC transmission system in the future. HVDC transmission system is commonly classified into two categories based on the two end converter topologies [18, 19] - line-commuted converter (LCC) or self-commuted converter (VSC) . A classical HVDC system consists of a thyristor based line-commuted converter system which is well established for high power transmission over many years. Investigation of classical converter type HVDC transmission system is not included in this work. Modern HVDC transmission systems are equipped with IGBT based forced-commuted VSCs [20, 21]. For example, Siemens and ABB have HVDC system under the name ‘HVDC PLUS’ and ‘HVDC Light’. The fundamental difference between the two systems is the topology of the VSC.

Modern HVDC transmission system offers further advantages over HVAC transmission system in terms of grid connection. HVDC transmission system provides better grid connection solution for weak grids. Specifically, the grid side VSC of the HVDC system can operate in all four quadrants with active and reactive power flow in both directions, so it provides efficient voltage and frequency control and support to a weak grid. The strength of the grid (or the host power system) is a measure of SCR (short circuit ratio) [7] such that higher SCR denotes a stronger grid.

$$SCR = \frac{\text{PCC short circuit power}}{\text{max. apparant power of the WPP}} \tag{3.1}$$

Moreover, a HVDC system provides following advantages; [22, 23]

1. AC/AC decoupling between the WPP and the host power system,
2. Transports the same amount of power with a less number of high voltage cables compared to HVAC system,
3. Provides better power flow control-ability and
4. Does not require the reactive current flow (demanded by the grid at PCC) along the entire length of the transmission cables, hereby, reducing the transmission losses. Reactive current can be locally exchanged between the grid side VSC and the host power system irrespective to the WPP .

However, the capital cost of a HVDC system and the losses that occur in the converter system at the two ends of the transmission line are of prime concern. A typical HVDC transmission system from an off-shore WPP to the near-by on-land transmission system is shown in Fig. 3.1. The main components of a HVDC transmission system are the two VSCs at the two ends of the transmission line; while the WPP collection grid may remain the same as in case of a HVAC transmission. The choice of the wind turbine type can be influenced by the choice of control system selected for the HVDC system (the details will follow in the coming chapters).

3.1 Voltage Sourced Converter

For high power HVDC transmission system application, the three main topologies of VSC utilized so far are; (i) two-level VSC, (ii) three-level VSC and, (iii) the MMC (modular multi-level converter) VSC. The building blocks of these VSCs are the forced commutated switching devices (specifically IGBTs), the diodes, and the DC capacitors (to store the required energy so that the power flow can be controlled). Each phase leg of the converter is connected via an inductor and additional filters to the grid.

Two-level VSC offers the most basic and simple topology, however, has the highest harmonics content of all VSCs. A two-level converter consists of six active switches, each with an anti-parallel diode. The voltage and current handling capacity of the presently available IGBTs are limited and hence they cannot individually handle the entire high voltage and power requirements. Many of these IGBTs

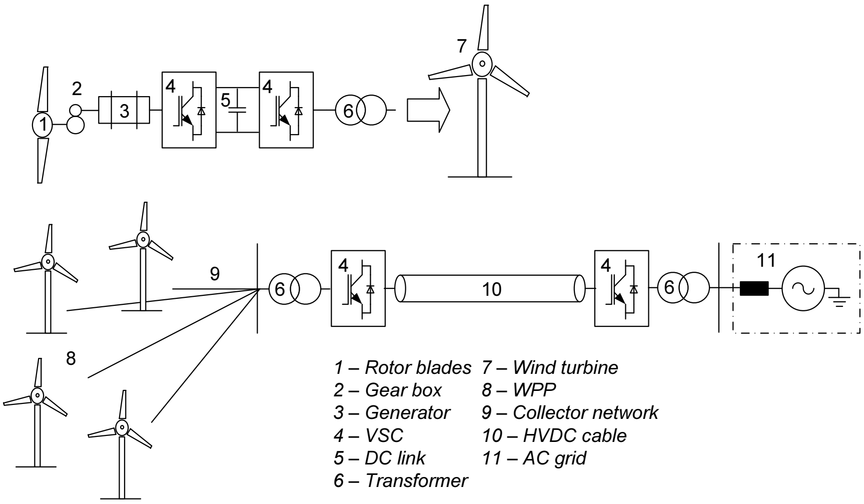

Figure 3.1: HVDC power transmission from an off-shore WPP to the near-by on-land transmission system

are connected in series to meet the voltage requirements. A filter at the AC side is required to eliminate the unwanted higher harmonics from the voltage and current waveform.

A three-level converter topology for e.g., a NPC (neutral point clamped) mainly differs from the two-level converter topology in the addition of a clamping diode. As a result, three different combination of AC voltage output is possible at each phase leg - positive DC voltage, zero voltage and negative DC voltage. The resulting AC voltage is more closer to the desired sinusoidal AC voltage compared to a two-level converter. Therefore, the efforts in filtering higher harmonics are relatively reduced.

3.1.1 Modular Multi-level Converter

A recent development in VSC has provided a scalable modular type system suitable for high power applications [24]. The detailed study of dynamic behavior of such a converter type for use with VSC-HVDC system is presented in many literatures including [25–27]. The structure of a MMC system is shown in Fig. 3.2. Each phase leg consists of two arms and each arm consists of n sub-modules. A sub-module is a two terminal structure with two IGBTs, two diodes and a capacitor as shown in Fig. 3.2. Unlike other topologies discussed earlier, the dc link of the MMC do not require any common DC capacitor and filter, also the total system losses are lower compared to an equivalent two-level converter system [28].

Each sub-module can have three states depending upon the state of the two switches. When T_1 is on and T_2 is off, the capacitor voltage is applied to the terminals of the sub-module (the sub-module can be said to be turned on). In this state, current can either flow through D_1 and charge the capacitor or through T_1 and dis-

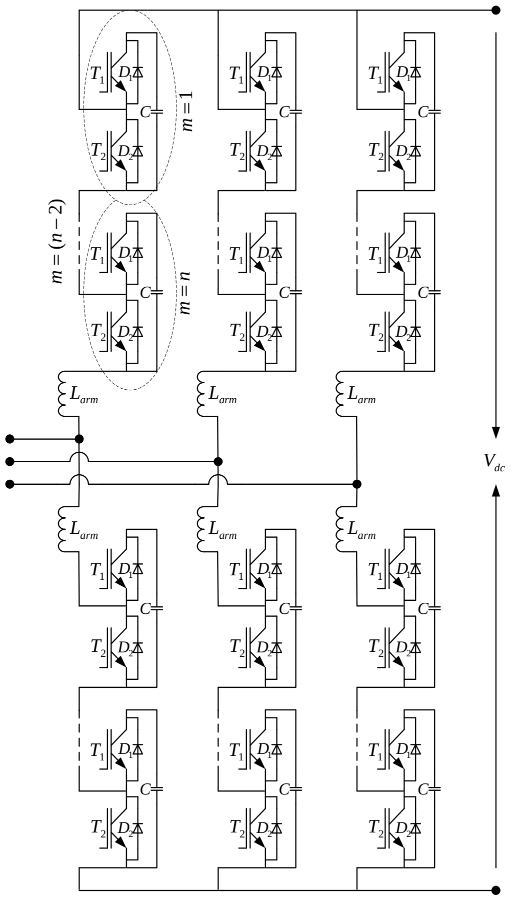

Figure 3.2: Topology of a MMC

charge the capacitor depending upon the direction of the current flow. When T_1 is off and T_2 is on, the capacitor voltage is not applied to the terminals of the sub-module, or zero voltage is applied and the capacitor voltage thus remains unchanged (the sub-module can be said to be turned off). When both the switches are turned off, the converter will be in a blocked state. All the sub-modules will identically follow the state; therefore, this state is not possible during normal operation. The per phase AC voltage of the converter can be adjusted by turning on a number of sub-modules in the upper and the lower arm of the same phase and the DC voltage can be adjusted independently.

The main parameters defining the voltage and the current ratios of the MMC are listed below.

$$k_v = 2 \cdot \frac{\hat{v}_a}{V_{dc}} \tag{3.2}$$

$$k_i = \frac{3 \cdot \hat{i}_a}{2 \cdot I_{dc}} \tag{3.3}$$

Where $\hat{v}_a$ and $\hat{i}_a$ are the peak value of the per phase AC voltage and current. The control system in a modular converter is such that all three phases are equally loaded with the active power to balance the voltage. As a result, each arm of an inverter leg shares a DC current of $\frac{1}{3}I_{dc}$ and a AC current of $\frac{1}{2}i_a(t)$, where $i_a(t)$ is the per phase current of the converter. Assuming sinusoidal phase current, the current through each arm can be written as,

$$i_{arm,1}(t) = \frac{1}{3} \cdot I_{dc} + \frac{1}{2} \cdot i_a(t) \tag{3.4}$$

$$i_{arm,1}(t) = \frac{1}{3} \cdot I_{dc} \cdot (1 + k_i \cdot sin(\omega t + \phi)) \tag{3.5}$$

The voltage expression for each arm becomes,

$$v_{arm,1}(t) = \frac{1}{2} \cdot (V_{dc} - v_a(t)) \tag{3.6}$$

$$v_{arm,1}(t) = \frac{1}{2} \cdot V_{dc} \cdot (1 - k_v \cdot sin(\omega t)) \tag{3.7}$$

If it is assumed that the voltage and the current on the DC side are without ripple,

$$\bar{P}_{dc} = \frac{1}{2\pi} \int_0^{2\pi} v_{dc}(\omega t) \cdot i_{dc}(\omega t) \cdot d(\omega t) \tag{3.8}$$

$$\bar{P}_{dc} = V_{dc} \cdot I_{dc} \tag{3.9}$$

The AC side power is expressed as,

$$\bar{P}_{ac} = 3 \cdot V_a \cdot I_a \cdot cos(\phi) \tag{3.10}$$

To keep the balance between the AC and the DC side, power should equal to each other, $P_{ac} = P_{dc}$.

$$V_{dc} \cdot I_{dc} = 3 \cdot V_a \cdot I_a \cdot cos(\phi) \tag{3.11}$$

$$\frac{\hat{v}_a}{V_{dc}} \cdot cos(\phi) = \frac{2 \cdot I_{dc}}{3 \cdot \hat{i}_a} \tag{3.12}$$

$$k_i = \frac{2}{k_v \cdot cos(\phi)} \tag{3.13}$$

From the arm voltage and current expression it is possible to calculate the power expression in each of the arms.

$$P_{arm,1}(t) = \frac{V_{dc} \cdot I_{dc}}{6} \cdot (1 - k_v \cdot sin(\omega t)) \cdot (1 + k_i \cdot sin(\omega t + \phi)) \tag{3.14}$$

Fig. 3.3 shows the plot of the current, voltage and the power for an arm of a phase leg.

The pulsation of energy in an arm of an inverter leg can be known by calculating the area between the two consecutive zero crossings of the power curve from Fig.

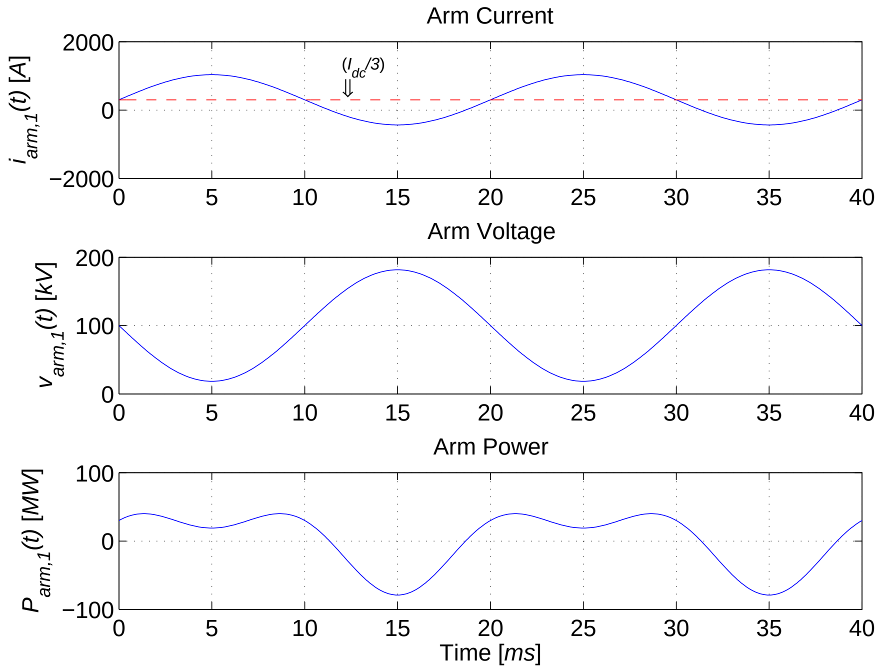

Figure 3.3: Current, voltage and power in each arm of a phase leg of a MMC, $P_{trans} = 180\ [MW]$

3.3. It can be seen that the zero crossing of the power curve is the point at which the current crosses zero. Therefore, the two limits for the integration can be found from the current curve,

$$0 = \frac{1}{3} \cdot I_{dc} \cdot (1 + k_i \cdot sin(\omega t + \phi)) \tag{3.15}$$

The above expression is zero when, $k_i \cdot sin(\omega t + \phi) = -1$.

Solving for ωt,

$$\omega t_1 = -\phi - asin\left(\frac{1}{k_i}\right) \tag{3.16}$$

$$\omega t_2 = \pi - \phi + asin\left(\frac{1}{k_i}\right) \tag{3.17}$$

The pulsation of energy on each arm is thus,

$$\Delta W_{arm,1} = \frac{1}{\omega} \cdot \int_{\omega t_1}^{\omega t_2} P_{arm,1}(\omega t) \cdot d(\omega t) \tag{3.18}$$

$$\Delta W_{arm,1} = \frac{\bar{P}_{dc}}{3 \cdot \omega \cdot k_i^2} \cdot \left(k_i^2 - 1\right)^{3/2} \tag{3.19}$$

If we consider that the energy is distributed equally in all the sub-modules, the pulsation of energy per sub-module can be derived as,

$$\Delta W_{sm} = \frac{\overline{P}_{dc}}{3 \cdot \omega \cdot n \cdot k_i^2} \cdot \left(k_i^2 - 1\right)^{3/2} \tag{3.20}$$

Where subscript *sm* stands for sum-module. The necessary capacitor per sub-module can be determined from the above expression.

$$C_{sm} = \frac{2 \cdot \Delta W_{sm}}{\varepsilon \cdot \overline{V}_c^2} \tag{3.21}$$

$$C_{sm} = \frac{2 \cdot \overline{P}_{dc}}{3 \cdot \varepsilon \cdot \overline{V}_c^2 \cdot \omega \cdot n \cdot k_i^2} \left(k_i^2 - 1\right)^{3/2} \tag{3.22}$$

where $0 < \varepsilon < 1$ is the ripple factor of the voltage in the sub-module.

The ratio of total capacitance per arm of the converter and the capacitance per sub-module in an arm can be defined as,

$$C_{arm} = \frac{C_{sm}}{n} \tag{3.23}$$

Once the current, voltage, capacitance and the parameters of the semiconductor devices of each sub-modules are known, it becomes possible to estimate the losses of the MMC.

3.2 Energy Losses Evaluation

The structure of the WPP is chosen to be exactly the same as in the case of the HVAC transmission system. This applies that the multi-turbine power curve and the parameters of the WPP collector network of the HVDC connected WPP remains the same.

3.2.1 Modular Multi-level Converter Losses

A list of converter parameters used for the losses calculation is presented in Table 3.1.

Table 3.1: Parameters of the converter

		Parameters
P_{dc}	DC side power	$180\ [MW]$
V_{DC}	DC voltage	$200\ [kV]$
V_c	sub module voltage	$1.8\ [kV]$
V_0	AC voltage	$100\ [kV]$
n	no. of modules	$136/arm$

Losses in a MMC can be categorized as semiconductor switching and conduction losses, gate driver losses, losses in the energy storage capacitors, losses in the passive filters and protection inductors and other miscellaneous losses. Power losses in the gate driver of 7.5 $[W]$ is included per IGBT. Approximate power losses associated with the components like passive filter and capacitors are calculated. In case of an inductor, the losses calculation is done when the respective parasitic resistance ($0.001pu$) and core losses are known. The total capacitive losses are approximated to be 0.1% of the total power.

The IGBTs in the MMC are considered to be 'hard switched' (without any snubber circuit). As compared to the switching frequency of a two-level or a three-level VSC, the necessary switching frequency of a MMC is low, around $f_s = 150Hz$ [29]. This reduces the switching losses of the semiconductors significantly [28]. The conduction and the switching losses of the semiconductors are calculated with the assumption that the load current is pure sinusoidal. The parameters of the considered IGBT module are presented in Table 3.2; $V_r = 1800V$ and $I_r = 1500A$. (The subscript r stands for reference).

Table 3.2: Parameters of selected semiconductors for losses calculation

	V_f	r_f	E_{on}	E_{off}	E_{rec}
IGBT(T_1,T_2)	3.1 $[V]$	1.6 $[m\Omega]$	3.3 $[J/P]$	2.7 $[J/P]$	–
Diode(D_1,D_2)	2.3 $[V]$	1.04 $[m\Omega]$	–	–	2 $[J/P]$

The total forward voltage drop and the total on state power losses on a semiconductor is given by [28],

$$P_F = \bar{i}_f \cdot V_F(I_F^*) \tag{3.24}$$

Where, $\bar{i}_f$ is the average forward current in a semiconductor and I_F^* is the equivalent on state current determined from the load current. In the data-sheet of an IGBT device, a plot showing the function of forward voltage (V_F) against the forward current (I_F) is generally provided. A polynomial expression of this function is derived, which makes it possible to calculate the forward voltage at any given current level. The product of this forward voltage times the average switch current gives the conduction losses. The average forward current in the semiconductor of a sub-module are given by [28, 30],

$$\bar{i}_{T1} = \frac{1}{4} \cdot b \cdot x \cdot |\bar{i}_a| \tag{3.25}$$

$$\bar{i}_{T2} = \frac{1}{4} \cdot (1 - b \cdot x) \cdot |\bar{i}_a| + \frac{1}{6} \cdot I_{dc} \cdot \left(1 + \frac{1}{3 \cdot m}\right) \tag{3.26}$$

$$\bar{i}_{D1} = \frac{1}{4} \cdot b \cdot x \cdot |\bar{i}_a| \tag{3.27}$$

$$\bar{i}_{D2} = \frac{1}{4} \cdot (1 - b \cdot x) \cdot |\bar{i}_a| + \frac{1}{6} \cdot I_{dc} \cdot \left(1 - \frac{1}{3 \cdot m}\right) \tag{3.28}$$

where, $b = V_{dc}/(2 \cdot n \cdot V_c)$; $m = k_i \cdot \pi \cdot |\bar{i_a}|/(2 \cdot \hat{i}_a)$ and $x = \left(1 - m^{-2}\right)^{\frac{3}{2}}$.

Similarly, the switching losses in the semiconductor can be evaluated as below,

$$P_{S,IGBT} = f_s \cdot \left(\frac{E_{on} + E_{off}}{V_r \cdot I_r}\right) \cdot V_c \cdot \bar{i}_{arm,1} \tag{3.29}$$

$$P_{S,diode} = f_s \cdot \left(\frac{E}{V_r \cdot I_r}\right) \times V_c \cdot \bar{i}_{arm,1} \tag{3.30}$$

Semiconductor switching losses is due to the product of voltage and current during the switching sequence. Accurate prediction of the switching losses at different power levels is relatively very difficult. A linear approximation based on analytical calculation of eqs. (3.29 and 3.30) and the reference parameters directly taken from the data-sheet can provide a good estimation [31]. For an IGBT or a diode, the total energy dissipation during a switching sequence is provided in the respective data-sheet at a reference voltage and current. In case of an IGBT, dissipation of energy occurs both at the turn on and off sequence, however, in case of a diode, dissipation of energy occurs due to reverse recovery. However, it has to be noted that the arm current, $i_{arm,1}$, is not symmetric (refer Fig. 3.3). During the calculation of the losses, the asymmetry has thus been taken into account; calculating the average arm current using the positive average for one IGBT and the opposite diode and the negative average for the other IGBT and the opposite diode. Fig. 3.4 shows the total semiconductor losses. The upper four plots refer to the losses in an individual IGBT and a diode for a given sub-module. The bottom plot refers to the total losses in all semiconductor parts of the MMC. Conduction losses are the most dominating part of the total semiconductor losses in a MMC. The increment in conduction losses with increasing power shows polynomial increment because the conduction losses are dependent on the square of the current. As the switching losses in a MMC are only a fraction of the total losses, a linear approximation based calculation is justified. The total semi-conductor losses in a MMC contributes approximately 0.833 [%] of the rated power.

3.2.2 HVDC Cables

HVDC cables are generally available in three main types [32].

1. Mass impregnated cables - which are insulated with special papers; available for up to ≈ 600 [kV].

2. Self-contained fluid filled cables - which are also insulated with special papers but are impregnated with low viscosity oil; available for up to ≈ 600 [kV].

3. Extruded cables (XLPE) - which are insulated with polyethylene based compound; available up to ≈ 320 [kV]. XLPE cables are not suitable for rapid polarity reversals. Rapid polarity reversals in XLPE cables create localized high stress and cause fast aging of the cable insulation. However, XLPE cables have become more preferable due to the development of VSC that does

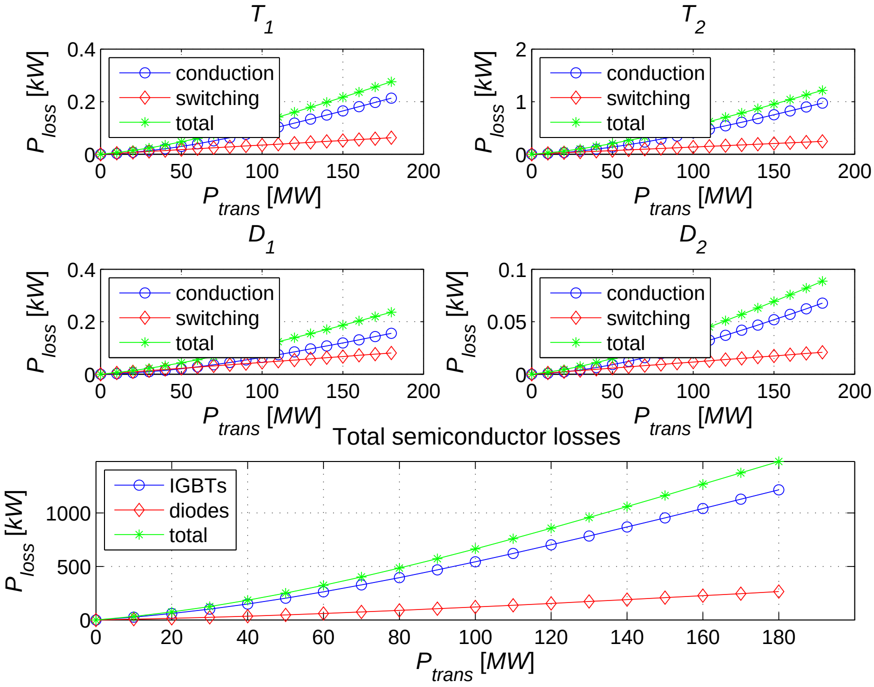

Figure 3.4: Total power losses in the semi-conductor devices of a MMC; $cos\phi = 1.0$

not require polarity reversal for power reversal. All the following analysis in this work is based on XLPE cable types.

Charging current in a HVDC cable transmission system is not present because the DC voltage and the current do not alternate. The voltage distribution is capacitive during the start-up, but the cable acts as a resistor during the static condition. However, a small ripple in the DC voltage can occur. With accurate voltage control strategy and tuning, the ripple can be kept within small tolerable limits [28], and hence the added losses due to this are negligible. The losses along the cable are calculated as suggested in [14].

$$P(dx) = P_{max}(dx) \cdot \left[\frac{I(dx)}{I_{nom}}\right]^2 \nu_\theta \tag{3.31}$$

$$\nu_\theta = \frac{c_\alpha}{c_\alpha - \alpha_T \cdot \Delta\theta_{max}\left[1 - \left[\frac{I(dx)}{I_{nom}}\right]^2\right]} \tag{3.32}$$

The total power losses are obtained by integrating (3.31) over the total cable length. The maximum power per length is given by the expression below.

$$P_{max}(dx) = 2 \cdot I_{nom}^2 \cdot R_{dc}(dx) \tag{3.33}$$

Where $R_{dc}(dx)$ is the resistance per length of the cable. $c_\alpha = 1 - \alpha_T \cdot (20°C - \theta_{amb})$, α_T is the temperature coefficient of copper, θ_{amb} is the ambient temperature and

$\Delta\theta_{max}$ is the maximum permissible temperature rise of the cable. In Fig. 3.5, a comparison of total cable losses for varying transmission distance and transmitted power has been presented. The presented result are for cables with $a = 800$ $[mm^2]$ and $R_{dc}/m = 22$ $[\mu\Omega]$ at $20°C$. At 150 $[km]$ distance with total active power transmission of 200 $[MW]$ the total losses in DC cables is ≈ 4.25 [%] as compared to ≈ 6.45 [%] as compared to an equivalent HVAC cable system.

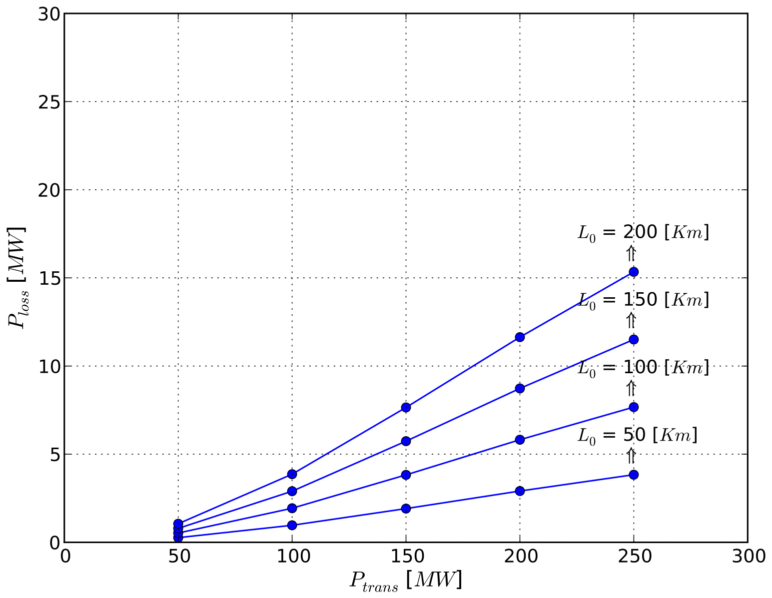

Figure 3.5: Cable losses against the total transmitted power; $V_0 = 200$ $[kV]$

3.2.3 Losses Distribution

Implementing a similar technique as discussed in the earlier Chapter 2, the distribution of losses for a WPP rated at 180 $[MVA]$ with $N = 50$ number of wind turbines is calculated; shown in Fig. 3.6.

It shall be noticed that the majority of the energy losses contribution is from the cables and thereafter from the converters at the two ends of the HVDC transmission line. The efficiency of these MMCs are generally very high due to the low switching losses, smaller converter reactor requirements and the elimination of the filters at both AC and DC side. Furthermore, a transformer at the grid side is not necessarily needed with a MMC HVDC transmission. In the WPP collector network, the AC voltage is relatively low ($\approx 33kV$). A transformer is thus required to step up the voltage and reduce the converter current. In this work, a transformer at both ends of the HVDC transmission system is present to make a comparison to a HVAC solution.

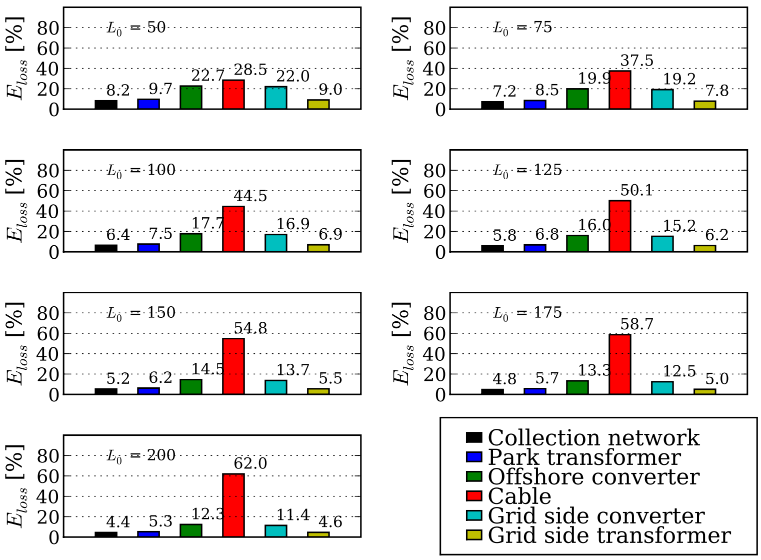

Figure 3.6: Distribution of energy losses as percentage of the total energy losses in the system; $P_{trans} = 180MW, V_0 = 200kV$

The cables share 28.5 [%] at $L_0 = 50$ [km] as compared to 62.0 [%] at $L_0 = 200$ [km] of the total energy losses. The cross-section area of the selected cable is 800 [mm^2].

Likewise with a HVAC transmission system, a WPP of 360 [MVA] is also evaluated; which is twice the size of the one considered above. The total number of wind turbines is increased to $N = 100$, but the layout of the WPP is assumed to be similar with collector network voltage at 33 [kV]. The transmission voltage is selected to be 300 [kV]. HVDC cables with $a = 1400$ [mm^2] are selected to allow room for higher current. Distribution of energy losses in different components of the transmission system is shown in Fig. 3.7. The cables share 18.7 [%] at $L_0 = 50$ [km] as compared to 48.3 [%] at $L_0 = 200$ [km] of the total energy losses. For short transmission distances, the losses in the converter stations dominate but with increasing distance, the losses in the cable start to grow. At $L_0 = 50$ [km], the sum of total losses in the two VSCs is 49.7 [%] as compared to 31.6 [%] at $L_0 = 200$ [km] of the total energy losses.

3.3 HVDC Transmission with DC Collector Network

The scope of a DC system can also be extended to a MV (medium voltage) grid, especially for future off-shore WPP collector network, where the power transmission will be via HVDC sub-marine cables. MVDC grid allows weight saving of components

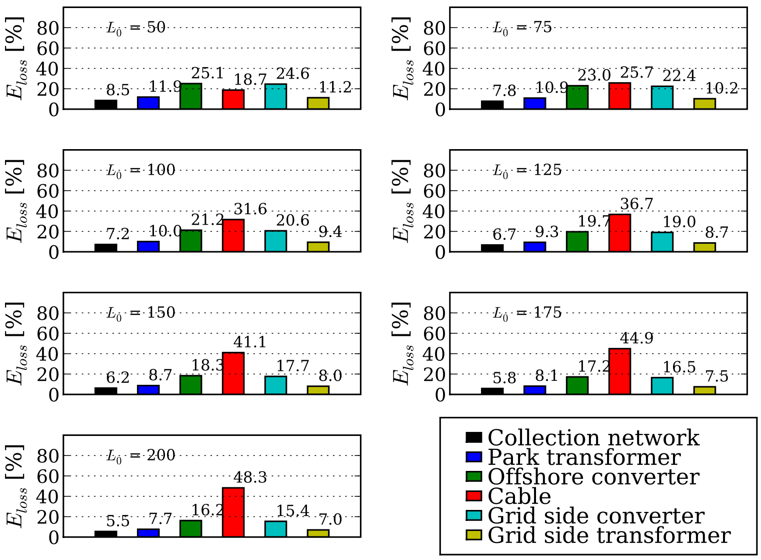

Figure 3.7: Distribution of energy losses as percentage of the total energy losses in the system. $P_{trans} = 360MW$, $V_0 = 300kV$

used in the system [33, 34], specially for voltage transformation. The WPP collector network conventionally is a MVAC system. However, in case the power transmission is done via HVDC transmission system, the use of a DC collector network might provide an advantage. The electrical structure of such a WPP collector network and transmission system is presented in Fig. 3.8.

The use of a MVDC system in the WPP collector grid will require individual wind turbines in a WPP to generate DC output. The AC output of the wind turbine generators should be rectified, and instead of a conventional AC transformer, a DC-DC converter should be used to step-up the voltage level. DC-DC converters are the DC equivalent of the AC transformers, whose primary job is to step-up or step-down the voltage level. The DC-DC converter required for this power and voltage level is, however, not a standardized unit and is under development [33]. A comparison based on power losses of different types of DC-DC converters with MF (medium frequency) AC transformer is also presented in [33]. It has been presented that a full-bridge converter is the most suitable option for WPP applications in terms of energy losses, simple design and control options.

3.3.1 DC-DC Converter

A full-bridge DC-DC converter topology is presented in Fig. 3.9. The low voltage side of a step-up type full-bridge DC-DC converter consists of four active switches

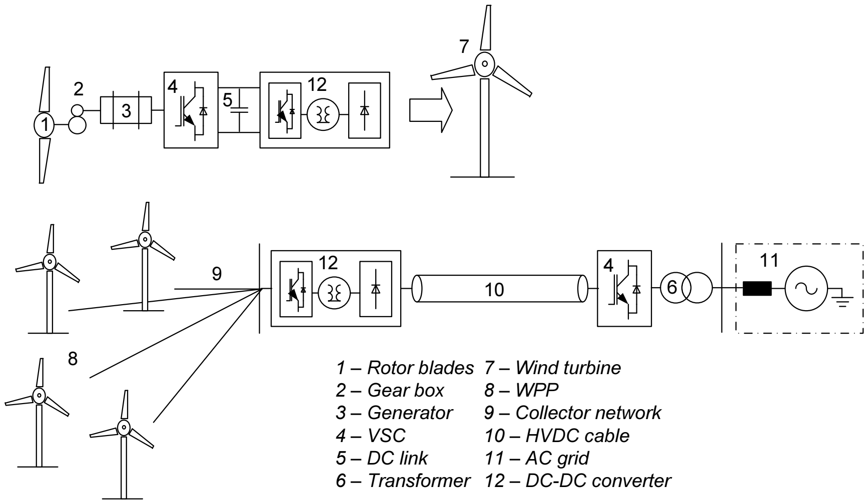

Figure 3.8: HVDC power transmission from an off-shore WPP to the near-by on-land transmission system with DC collector network

and four freewheeling diodes and the high voltage side consists of a passive diode rectifier. The high voltage side and the low voltage side of a full-bridge DC-DC converter is isolated through a MF transformer. As one end of the converter is a passive diode rectifier, the power flow is uni-directional. The diode bridge output on the high voltage side is connected via an output filter so as to minimize the output voltage and current peak ripple. The low voltage side active bridge is controlled via PWM signal by utilizing the duty ratio control. The relationship between the input and the output voltages of a duty cycle controlled full-bridge DC-DC converter can be expressed in terms of duty ratio (D) of the active switches and the turns ratio of the transformer.

$$\frac{V_0}{V_{in}} = \frac{N_s}{N_p} \cdot 2 \cdot D \tag{3.34}$$

Where, V_0 is the output side DC voltage, V_{in} is the input side DC voltage, N_s and N_p are the secondary and primary side number of turns of the MF transformer. Therefore, to optimize the transformer turns ratio, it might be advantageous to operate the DC-DC converter with a highest possible duty ratio. The maximum possible duty ratio for the active switches is 50 [%]. But in practice a slightly lower duty ratio is implemented to account for a small dead time between the two opposite pair of switches (required to avoid complete short circuit), transmission voltage drop and the transformer leakage reactance current reversal time. This needs to be compensated by increasing the transformer turns ratio.

The other technique to control such a full-bridge DC-DC converter is to utilize a phase shift control between the two legs of the low voltage side bridge [35]. This technique utilizes the transformer leakage inductance and the active switches para-

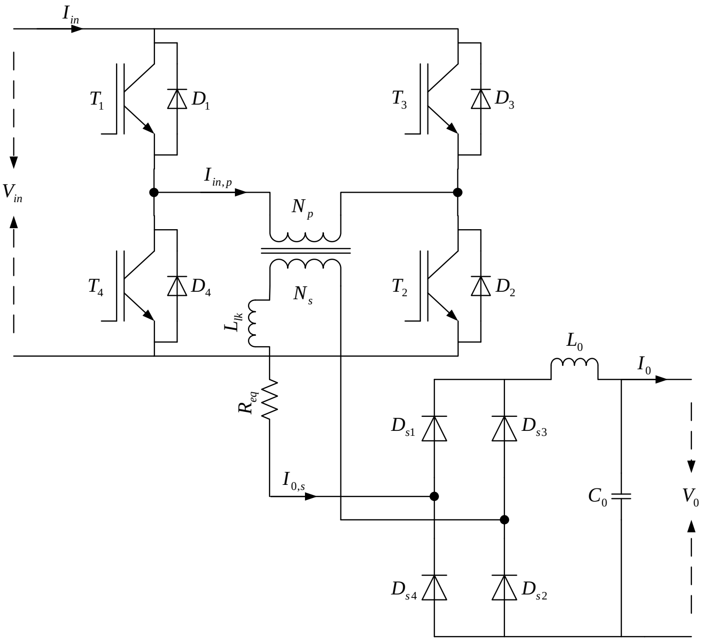

Figure 3.9: Full-bridge DC-DC converter

sitic capacitors to achieve a soft switching, hereby, reducing the switching losses. The range of zero voltage switching is thus limited by the leakage inductance of the transformer and the parasitic capacitors. Zero voltage switching over a wider range of operation demands higher leakage inductance, making the optimized transformer design complicated. An additional inductor might become necessary and also an additional capacitor across each of the switches will be required. Additional inductor and capacitors will, nevertheless, introduce additional losses. Therefore, design and control of such a converter is relatively complicated. The cost and benefit of such a system for a very high power level application is not obvious and will require a detailed comparison. In this work only a hard switched duty ratio controlled full-bridge converter will be analyzed as it offers relative simple control and design options (which for a very high power application is a major advantage).

A MF transformer is composed of a core (magnetic material) and the windings of primary side and the secondary side. The choice of the core material can be influenced by various application requirements and specifications like power level, frequency of operation etc. For example, for low frequency power transformer applications, laminated steel cores are preferred. They offer higher saturation flux density and hence reduce the weight (size) of the transformer. On the other hand they have higher core losses, specifically the eddy current losses are high due to their lower electrical resistance, hence laminated sheets are used to reduce eddy current losses [36]. For relatively small power application with high frequency over 10 [kHz], ferrite cores are generally preferred [36, 37]. Ferrite materials offer lower eddy current losses as they have very high electrical resistance but low saturation flux density. The other material class used in transformers is the alloys of mainly iron and small part of other elements. Amorphous alloys of iron and other transition metals, trade name as METGLAS, is also presented in [37]. These materials offer higher electrical resistance than steel cores and higher saturation flux density compared to the ferrites, thus making it suitable for MF transformers of around 2 [kHz] ranges [37]. With this in consideration, an amorphous alloy core material 2605SA1 [38] is chosen for the design of the MF transformer used in a full bridge DC-DC converter application (also referenced in [39]). The size (volume and weight) of an off-shore transformer is an important parameter, while the losses in the core and the windings are also equally significant. During the design of the transformer, the main focus should, therefore, be put on those parameters. Lower copper losses are achieved by using lowest possible turns in both the primary and the secondary winding. However, lower turns result in higher core loss and higher transformer weight as seen in Fig. 3.10. Although higher turns reduce both the core losses and the core weight, the copper losses are increased and more importantly it also increases the weight of the windings. It is seen in Fig. 3.10 that the lowest losses occur at around $N_p = 12$ while the weight of the core and copper added together does not reduce significantly with additional turns in the primary winding. The plots in Fig. 3.10 are calculated for a 1 [kHz] transformer designed for a 3.6 [MW] wind turbine DC-DC converter. The weight of a MF transformer (approx. 500 [Kg]) is only around $7-10$ [%] of a standard 50 [Hz] transformer (approx. 6000 [Kg]). The transformer design procedure is described in detail in B.1.

3.4 Energy Losses Evaluation

The VSC and the transformer representation at the grid end are the same as in the earlier case of HVDC transmission with MVAC collector grid. The layout of the WPP is again considered to be exactly the same as in the earlier cases; however, the collector network is a MVDC system. This implies that only two cables are required instead of three (or three core) as compared to MVAC system. The equivalent π parameters of the collector network are re-calculated based on the DC cables and the resulting parameters are,

$Z_{eq} = (0.014 + 0.047j)$ [Ω]

$C_{eq} = 6.529$ [μF]

3.4.1 DC-DC Converter Losses

A list of DC-DC converter parameters used for the calculation are presented in Table 3.1.

Losses in a DC-DC converter can be categorized into three main groups, (i) transformer losses, (ii) semiconductor conduction losses and, (iii) semiconductor switching losses. Losses in the transformer are mainly due to the core losses and the copper losses. Core losses are constant irrespective to the power transfer, as they depend

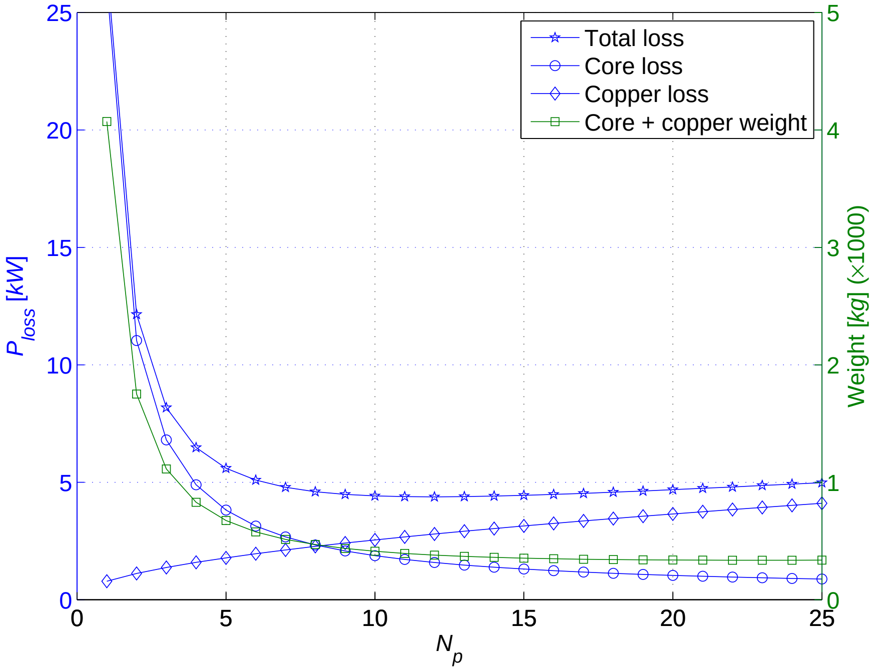

Figure 3.10: Dependence of transformer losses and size on number of turns

Table 3.3: Parameters of the DC-DC converter at the WPP

		Parameters
P_{dc}	DC side power	180 $[MW]$
V_{DC}	DC voltage	200 $[kV]$
V_{cn}	collector network voltage	33 $[kV]$
N_s/N_p	Transformer turns ratio	7
F_{sw}	switching frequency	1 $[kHz]$

upon the voltage level. Copper losses, however, depend upon the current and hence the power level. The total core losses ($P_{loss,c}$) can be estimated when the volume of the core (v_c) is known.

$$P_{loss,c} = k_1.\rho_c.F_s^{k_2}.B_{pk}^{k_3}.v_c \tag{3.35}$$

Where $\rho_c = 7.18$ $[gm/cm^3]$ is the density of the core material, $k_1 = 6.5$, $k_2 = 1.51$, $k_3 = 1.74$ are the constants given in the data-sheet [38] and B_{pk} is the peak flux density in the core. The total copper losses can be calculated when the length of the winding of the primary ($l_{cu,p}$) and the secondary ($l_{cu,s}$), cross-section area of the primary and secondary windings (a_{cu}) and resistivity of a copper wire (ρ_{cu}) are known.

$$P_{loss,cu} = I_{in}^2 \cdot \frac{\rho_{cu} . l_{cu,p}}{a_{cu,p}} + I_0^2 \cdot \frac{\rho_{cu} . l_{cu,s}}{a_{cu,s}} \tag{3.36}$$

The total transformer losses are the sum of the total core losses and the total copper losses.

$$P_{loss,tx} = P_{loss,c} + P_{loss,cu} \tag{3.37}$$

The semiconductor switching and conduction losses can be calculated using similar technique as discussed in case of the MMC.

In Table 3.4, the parameters of the semiconductor components used for the WPP DC-DC converter is presented. In the table, the terms 'S' and 'P' stand for the number of units per switch that are either series or parallel connected to achieve the rated voltage and current requirements. The total calculated losses for the WPP DC-DC converter is shown in Fig. 3.11 and the rated WPP power level, the percentage of the total losses is approximately 1.63 [%] of the rated power. The most dominant losses are the switching losses followed by the conduction losses. The contribution of transformer losses to the total losses is very small.

Table 3.4: Parameters of the selected semiconductors for the WPP DC-DC converter.

	V_{ces}	I_c	E_{on}	E_{off}	E_{rec}	S	P
IGBT	3300 $[V]$	1500 $[A]$	3.3 $[J/P]$	2.7 $[J/P]$	–	20	4
Diode	6000 $[V]$	1100 $[A]$	–	–	5 $[J/P]$	58	1

3.4.2 Losses Distribution

The distribution of losses on different components for WPP with rated capacity of 180 $[MVA]$, $N = 50$ is presented in Fig. 3.12. The sizing of the cables ($a = 800$ $[mm^2]$) and the parameters of the grid side VSC and transformers are also chosen to be identical as in the case of a HVDC transmission with AC collector network. The losses in the DC-DC converter are slightly higher than that of an equivalent MMC. Therefore, the contribution of DC-DC converter losses for short transmission distance is more significant. Losses contribution due to the gate drivers (7 $[W]$) per IGBT and due to the output filter (0.2 [%]) is included during the converter losses evaluation. The cables share 25.2 [%] at $L_0 = 50$ $[km]$ as compared to 57.9 [%] at $L_0 = 200$ $[km]$ of the total energy losses.

3.5 Transmission System Comparison

The wind turbine topology for a HVAC transmission system and a HVDC transmission system with MVAC collector network is selected to be a standard full-converter

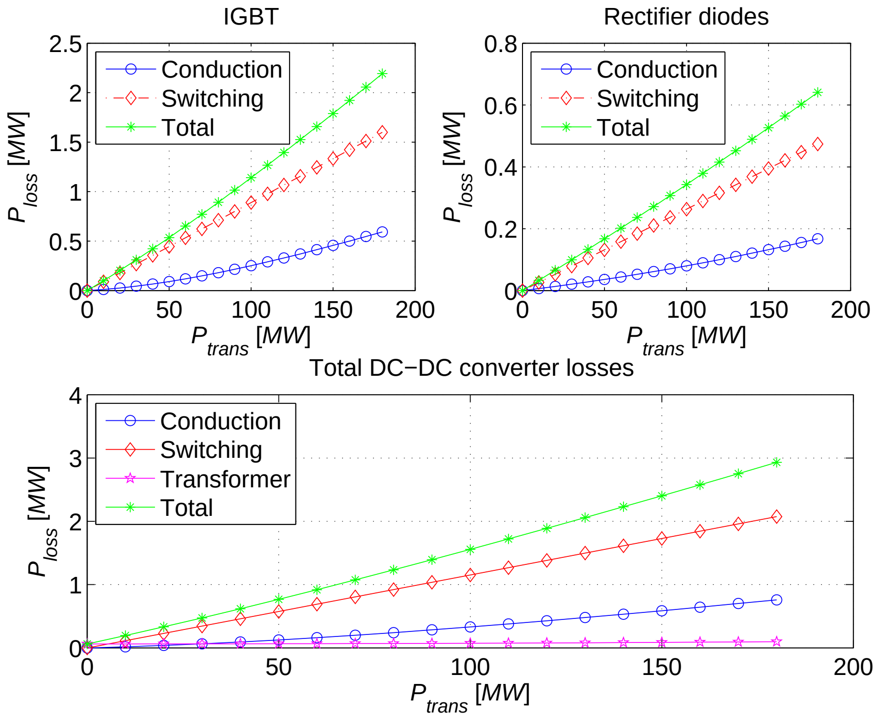

Figure 3.11: Total power losses in the WPP side DC-DC converter

design based on induction generator. However, when the collector grid is replaced with a MVDC transmission system, the topology of the wind turbine converter system should be modified. The AC collector network side VSC and the AC transformer of the wind turbine will be replaced by a DC-DC converter. It is assumed that the generator side VSC and the DC link voltage will, nevertheless, remain the same in both cases. Based on this assumption, losses comparison between a standard two-level VSC (semiconductor losses plus the wind turbine transformer losses) and a DC-DC converter (semiconductor losses plus the MF transformer losses) is performed. At the rated power of the wind turbine, the percentage losses in a DC-DC converter system was calculated to be 1.608 [%] compared to 1.757 [%] in case of a VSC system. The DC-DC converter system seems to offer slightly lower losses which are mainly due to the lower losses in the MF transformer. The contribution of output filter has been neglected in the above comparison. Therefore, assuming that the wind turbine losses would not differ significantly among the two wind turbine systems, they are not considered in the total system comparison.

The total energy losses for a HVAC and the two HVDC transmission solutions are compared in Fig. 3.13. Each transmission solution is first individually optimized in terms of transmission voltage rating and component sizing. The comparison of cost has not been performed as a part of this work (an example can be found in [40]), but the comparison has been performed in terms of total annual energy losses. As

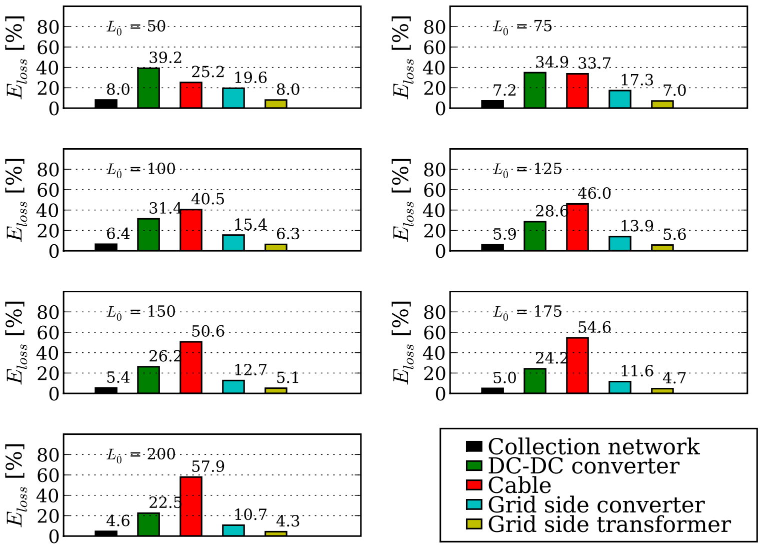

Figure 3.12: Distribution of energy losses as percentage of the total energy losses in the system. $P_{trans} = 180MW, V_0 = 200kV$

seen in the figure, the losses in an HVAC transmission system are lower than those in a HVDC system for shorter transmission distances. However, when the length of the transmission line becomes longer, the HVDC system is more efficient; as the losses in the HVAC cables increase rapidly with length. The results presented are for 180 [MW] and 360 [MW] WPPs; which are medium sized WPPs compared to those presently announced. For a medium sized WPP it can be confirmed that below 90 [km], the HVAC solution provides more efficient solution while above 110 [km] the HVDC solution provides the most efficient transmission solution. In case of large WPPs ($>$ 500 [MVA]), it can be expected that the HVDC system will provide a further efficient solution intersecting the losses curve of the corresponding HVAC system at a shorter distance. Based on Fig. 2.2 a higher amount of surplus reactive current is required to be compensated as the power level (or the voltage level) increases. Although total system losses is only one of the major factors, the process of optimization will also include many other factors. Some of them would be the investment cost, running cost, system services, system control, PCC grid strength etc. These comparisons will have to be made based on individual project requirements and parameters.

On the other hand, the difference between a HVDC system with a MVAC collector network and a HVDC system with DC collector network is not as obvious in terms of efficiency only. Except for the collector network and the WPP side DC-DC converter, the two transmission systems are identical so they do not show much

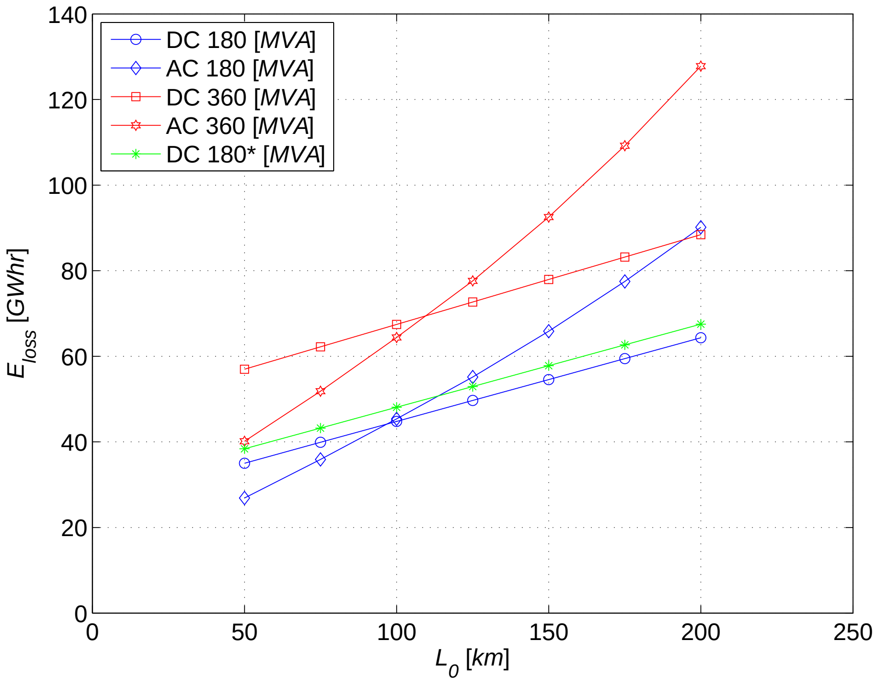

Figure 3.13: Comparison of energy losses among different transmission systems; *MVDC collector network

variation with transmission length. As discussed in earlier sections, it can be seen that all the pre-requisites and system control are available for constructing a MVDC collector grid in a WPP. Much research are being performed in selecting and developing DC-DC converters and their control. But even though there are many DC-DC converter topologies available for small power level, these converters are not tested enough for high power applications.

A brief summary of the three transmission solutions are presented below.

HVAC system

1. Is the most mature transmission solution and most of the components are well known; the past experience is vital for the reliability of the system operation. (+)
2. Provides the lowest losses of the three compared solutions for short transmission distances. (+)
3. Offers the lowest off-shore platform cost, because no power electronics devices are required. (+)
4. Generates considerable amount of reactive current and thus the cable capacity is limited. Reactive power compensation becomes necessary. (-)

5. Requires more number of transmission cables than the equivalent DC transmission solution, and hence the cable cost is higher. (-)
6. Due to the higher capacitance in a HVAC cable line, resonances may occur between the WPP collector network grid and the main grid at the on-shore; causing voltage distortion. Fig. 3.14 shows the network impedance of a cable space-state model calculated as a transfer function from the current input to the voltage output at the receiving end. It can be observed that the frequency of the oscillatory modes of a cable line are decreasing for increasing transmission length. Lower resonance frequency results in higher filtering efforts. A good approximation of the maximum frequency range represented by the cable model is $f_{max} = (N_\pi \cdot v)/(8 \cdot L_0)$, $v = 1/\sqrt{L \cdot C}$, $N_\pi =$ number of π sections, $L_0 =$ cable length [41]. (-)
7. The WPP collector network is AC-AC coupled with the main grid, so the AC side disturbances are directly reflected to each other. (-)
8. Modern WPPs are expected to support the grid with reactive current. In case of a HVAC cable transmission, the required reactive current will need to be delivered over the entire transmission length. This implies that the losses in the cables will increase accordingly and as such the cables need to be considerably over-sized. Alternatively, an extra reactive power compensation unit (e.g. SVC) is required to be installed at the PCC. (-)

HVDC system with MVAC collector network

1. Provides very fast active and reactive power control options, which is ideal for weak grid connection of WPP. (+)
2. The reactive power demanded by the host power system can be locally supported by the grid side VSC. (+)
3. HVDC provides an AC-AC de-coupling between the WPP collector network and the main grid, so the AC disturbances at either ends are not necessarily reflected to the opposite end. (+)
4. There is also no resonance between the transmission cables and other components in the AC grid at the two ends of the transmission system. (+)
5. Requires less number of transmission cables and also the losses in the DC transmission line is lower. (+)
6. There are no theoretical limits on the active power transmission distance. (+)
7. Requires more components (VSCs) and bigger off-shore platform size. (-)
8. The cost of added components and the amount of losses does not make it competive for short distances. (-)

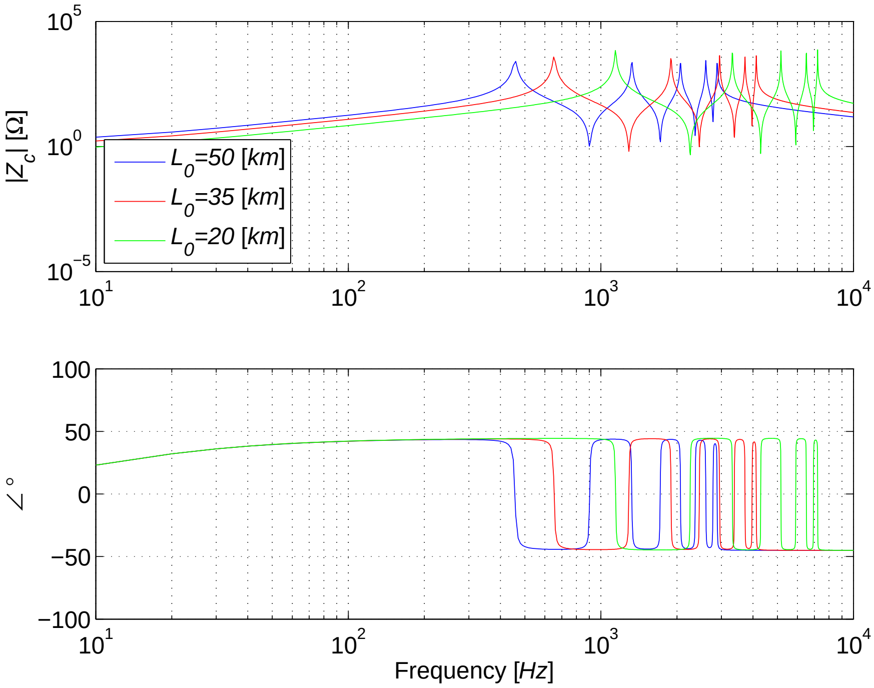

Figure 3.14: Network impedance of a cable space-state model calculated as a transfer function from the current input to the voltage output; $V_0 = 132$ $[kV]$, $N_\pi = 5$

HVDC system with MVDC collector network

The system does not vary so much from the HVDC system with MVAC collector network, but some differences are itemized below.

1. MVDC collector network results in reduced component weight, especially in case of transformer and number of medium voltage cables. (+)
2. MVDC system does not offer any natural zero crossings and, therefore, requires more complicated switch gear and protection units. (-)
3. The DC-DC converters are relatively unproven for high power applications. (-)

Therefore, based on known technology and components development, HVDC with MVAC collector grid might be preferred in the current context, but the use of MVDC collector grid cannot be ruled out for the future.

Four

Dynamic Simulation Model

In this chapter, a dynamic simulation model of a VSC-HVDC connected off-shore WPP will be discussed including wind turbine, VSC, cables, other major components and associated control systems. The model presented here will be further used to investigate the system for satisfactory operation and will also be tested to verify various grid compliance capabilities of the system.

The electrical structure of the system selected for further investigation is as shown in Fig. 4.1. A more generic diagram of the system is the same as in Fig. 3.1 with MVAC collector network. The HVDC transmission system in consideration is based on VSC which enables bi-directional flow of active power between the WPP and the host power system. However, the flow of active power from the power system towards the WPP is limited mainly during the system start-up. The simulation model has been prepared in 'Simulink, Matlab' ®. In Table 4.1, the parameters of the system under consideration are presented. N is the number of turbines in the WPP, subscripts wt stands for wind turbine, cn stands for WPP collection network, dc stands for DC, k stands for a VSC, g stands for grid and L_0 is the HVDC transmission distance. The nomenclature of different parameters presented here will be used to illustrate different electrical behaviors and plots further on in the report.

Table 4.1: System parameters

	Parameters		Parameters
WPP Location	Offshore	N	50
S_{wt}	3.6 $[MVA]$	V_{wt}	690 $[V]$
V_{cn}	33 $[kV]$	S_k	180 $[MVA]$
V_{dc}	200 $[kV]$	V_k	100 $[kV]$
V_g	400 $[kV]$	L_0	100 $[km]$

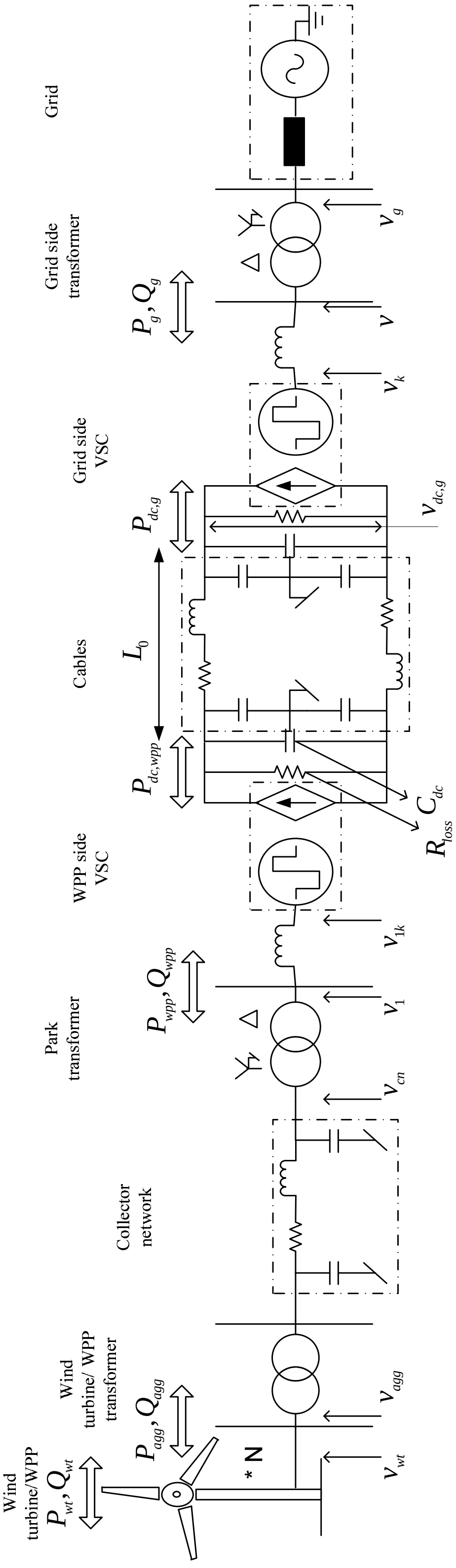

Figure 4.1: General overview of the simulation model

4.1 Grid Side Voltage Sourced Converter

The grid side VSC is referred to the HVDC VSC at the host power system end (Fig. 4.1) which is represented by a generic VSC model - equivalent circuit shown in Fig. 4.2. A detailed vector control structure is then implemented to control the voltage magnitude and angle at the terminals of the VSC.

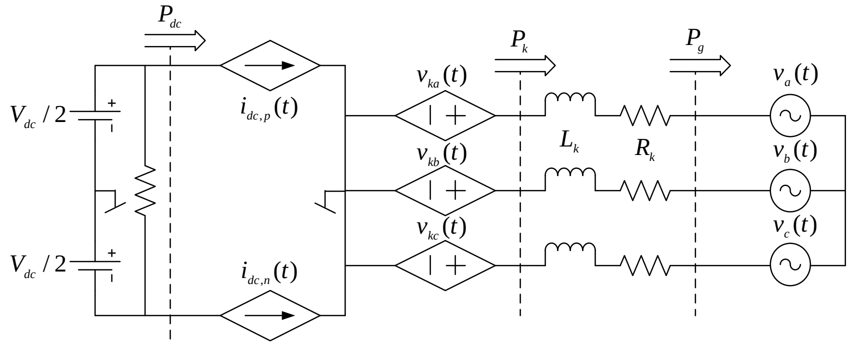

Figure 4.2: Equivalent circuit of the VSC model

The control of a VSC can be divided into two loops. The inner current loop controls the current by sending controlled reference voltages to the VSC modulation unit. The inner current loop operates in a dq rotating reference frame synchronized to the PCC AC voltage by a PLL (phase locked loop). The $d-$ axis current, i_{kd} controls the active power while the $q-$ axis current, i_{kq} controls the reactive power. The $d-$ and $q-$ axis are defined as the components in phase with the AC voltage phase angle reference and in quadrature to the AC voltage phase angle reference respectively. The output voltage references generated by the current loop is also in dq reference frame, which is then transformed to abc stationary reference frame. The active and reactive power exchange of a VSC is, therefore, determined by the VSC terminal voltages with respect to the reference voltages. At the grid side of Fig. 4.1, if v is taken as the terminal voltage (for e.g. the magnitudes in $d-$ and $q-$ axis as $v_d = 81.65$ $[kV]$, $v_q = 0$ $[kV]$), the expression for active and reactive power can be derived as in the following equations.

$$P_g = \frac{v_d \cdot \left[(v_d - v_{kd}) \cdot R_k - v_{kq} \cdot X_L\right]}{X_L^2 + R_k^2} \tag{4.1}$$

$$Q_g = \frac{v_d \cdot \left[(v_d - v_{kd}) \cdot X_L + v_{kq} \cdot R_k\right]}{X_L^2 + R_k^2} \tag{4.2}$$

The plots for P_g and Q_g are presented in Fig. 4.3. It can be observed that the active power can be controlled by adjusting v_{kq} with respect to the terminal voltage while changing v_{kd} has very little effect on active power exchange except for the resistive losses. Similarly, reactive power can be controlled by adjusting v_{kd} with respect to the terminal voltage while changing v_{kq} has very little effect on reactive power.

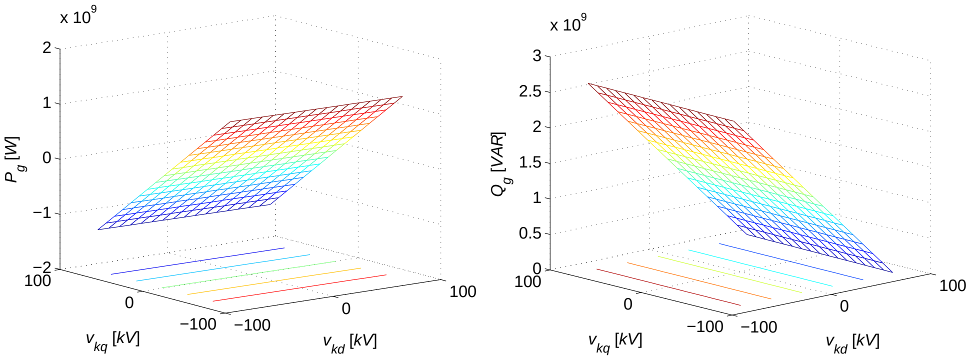

Figure 4.3: Active and reactive power exchange of a grid connected VSC

The active and reactive power exchange between a VSC and the grid can also be explained through standard equations applied between two inter-connected AC systems with impedance in between. The control of active power is done by controlling the voltage angle δ between the fundamental voltage of the VSC and the grid voltage; whereas the reactive power control is achieved by controlling the amplitude of the VSC voltage with respect to the grid voltage [7].

$$P_g = \frac{V \cdot V_k \cdot sin\delta}{X_L} \tag{4.3}$$

$$Q_g = \frac{V \cdot (V - V_k \cdot cos\delta)}{X_L} \tag{4.4}$$

4.1.1 Current Control

The current control of a VSC is, therefore, designed to control the VSC terminal voltages in $d-$ and $q-$ axis and performs the following tasks,

1. Take current command (reference) from external controllers,
2. Apply current limits to the reference values if necessary and,
3. Ensure that the VSC is exchanging the right amount of current as being commanded.

The active and reactive current capability diagram of the VSC system is shown in Fig. 4.4. The figure cannot be generalized to all VSCs but is the representation of the limits applied in this work. The inner dashed circle represents the unit circle of the current and the outer curve is the available current over-rating. The $d-$ axis current is over-rated to 1.1 $[pu]$ while the $q-$ axis current is limited to 1.0 $[pu]$.

The reference values for the active and reactive current control are derived from relatively slower outer control loops. A VSC can operate in all four quadrants; absorbing and releasing both active and reactive power. Therefore, a VSC can actively

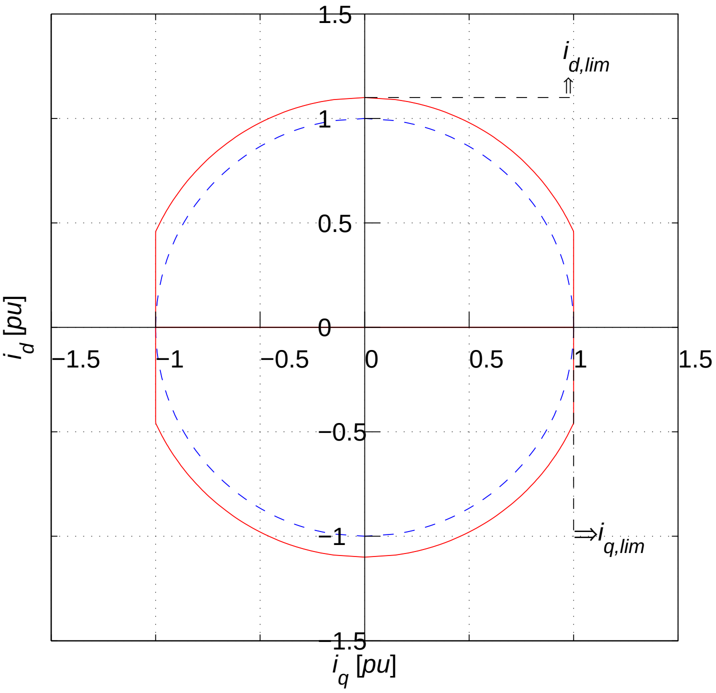

Figure 4.4: Current capability of a VSC converter

control a number of parameters including: (i) AC side frequency (f_m), (ii) active power (P_g), (iii) DC voltage (v_{dc}), (iv) AC voltage (V_0) and, (v) reactive power (Q_g).

Control of either f_m, P_g or the v_{dc} can be used to generate the i_{kd} reference (denoted by i^r_{kd}) and the control of either V_0 or the Q_g can be used to generate i_{kq} reference (denoted by i^r_{kq}). It has to be noted that not all parameters can be controlled at one time. The choice depends upon the situation and the connecting power system.

The inner current control structure of a VSC can be derived from the terminal voltage equation. The grid side VSC is connected to the grid side transformer's LV (low voltage) side through a three phase inductor. The voltage equation of a VSC can is expressed as in eq. (4.5). The system parameters are shown in Fig. 4.5. The synchronization signals, v_{abc} and i_{abc}, are obtained from the LV side of the grid side transformer. Therefore, the transformer and its leakage inductance can be considered as a part of the host power system.

$$v_k(t) - v(t) \quad = \quad L_k \cdot \frac{di_k(t)}{dt} + R_k \cdot i_k(t) \tag{4.5}$$

Where v_k is the converter side phase voltage, v is the transformer LV side phase voltage, i_k is the phase current through the inductor, L_k is the phase inductance and R_k is the resistance associated with the inductor. The numerical values of the VSC parameters are presented in Table 4.2. For all the three phases, eq. (4.5) can be

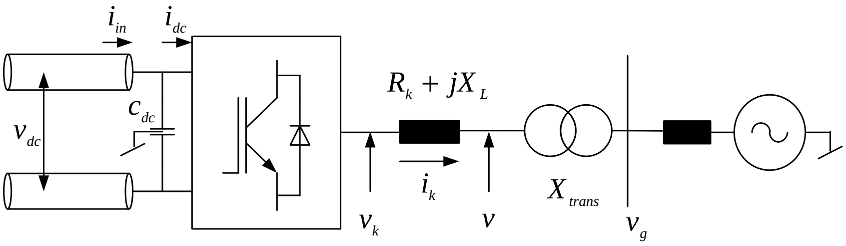

Figure 4.5: Representation of a grid side VSC

re-written as in eq (4.6).

$$\frac{d}{dt}\begin{bmatrix} i_{ka}(t) \\ i_{kb}(t) \\ i_{kc}(t) \end{bmatrix} = -\frac{R_k}{L_k}\cdot\begin{bmatrix} i_{ka}(t) \\ i_{kb}(t) \\ i_{kc}(t) \end{bmatrix} + \frac{1}{L_k}\cdot\begin{bmatrix} v_{ka}(t)-v_a(t) \\ v_{kb}(t)-v_b(t) \\ v_{kc}(t)-v_c(t) \end{bmatrix} \tag{4.6}$$

Table 4.2: Parameters of grid side VSC

		Parameters
L_k	VSC output inductor	15.9 $[mH]$
R_k	Inductor resistance	50 $[m\Omega]$
$C_{dc}/2$	DC side capacitor	250 $[uF]$

It is possible to apply Clarke's transformation between *abc* reference frame and $\alpha\beta$ through a transformation matrix. Ensuring equal peak values in two reference frames, the transformation can be done through eq. (4.7).

$$\begin{bmatrix} x_\alpha(t) \\ x_\beta(t) \end{bmatrix} = \frac{2}{3}\cdot\begin{bmatrix} 1 & -\frac{1}{2} & -\frac{1}{2} \\ 0 & \frac{\sqrt{3}}{2} & -\frac{\sqrt{3}}{2} \end{bmatrix}\cdot\begin{bmatrix} x_a(t) \\ x_b(t) \\ x_c(t) \end{bmatrix} \tag{4.7}$$

Thus in $\alpha\beta$ reference frame, eq. (4.6) can be written as:

$$\frac{d}{dt}\begin{bmatrix} i_{k\alpha(t)} \\ i_{k\beta}(t) \end{bmatrix} = -\frac{R_k}{L_k}\cdot\begin{bmatrix} i_{k\alpha}(t) \\ i_{k\beta}(t) \end{bmatrix} + \frac{1}{L_k}\cdot\begin{bmatrix} v_{k\alpha}(t)-v_\alpha(t) \\ v_{k\beta}(t)-v_\beta(t) \end{bmatrix} \tag{4.8}$$

Eq. (4.8) describes a VSC operating under balanced voltage conditions (symmetrical three phases). An additional negative sequence needs to be taken into consideration when the VSC is operating under unbalanced voltage conditions. The zero sequence components can be assumed zero for the considered three wire system. In the $\alpha\beta$ reference frame, the two network sequences can be decomposed as:

$$x_{\alpha(\beta)}(t) = x_{\alpha(\beta)p}(t) + x_{\alpha(\beta)n}(t) \tag{4.9}$$

Where the subscripts p and n stand for positive and negative sequence components respectively. Different techniques to separate the sequence components from the $\alpha\beta$ reference frame are discussed in [42]. Among different techniques, it is concluded that the delayed signal cancellation method is the best adapted. The sequence separation is achieved by introducing a delay of one fourth ($T_m/4$) of the network fundamental period. The equations implemented for the decomposition is as follows:

$$x_{\alpha n}(t) = \frac{1}{2}\cdot\left[x_\alpha(t) + x_\beta\left(t - \frac{T_m}{4\cdot T_s}\right)\right] \tag{4.10}$$

$$x_{\beta n}(t) = \frac{1}{2}\cdot\left[x_\beta(t) - x_\alpha\left(t - \frac{T_m}{4\cdot T_s}\right)\right] \tag{4.11}$$

$$x_{\alpha p}(t) = x_\alpha(t) - x_{\alpha n}(t) \tag{4.12}$$

$$x_{\beta p}(t) = x_\beta(t) - x_{\beta n}(t) \tag{4.13}$$

Where $T_m = 1/f_m$, f_m is the fundamental frequency of the AC system and T_s is the sampling time.

The separation of sequence components under unbalanced voltage condition is shown in Fig. 4.6. At $t = 0.08$ $[s]$, a negative sequence voltage of -0.2 $[pu]$ is imposed on the three phase voltages. It can be observed that the positive sequences remain unchanged in the $\alpha\beta$ reference frame and similarly in the dq reference frame, but the negative sequences are introduced.

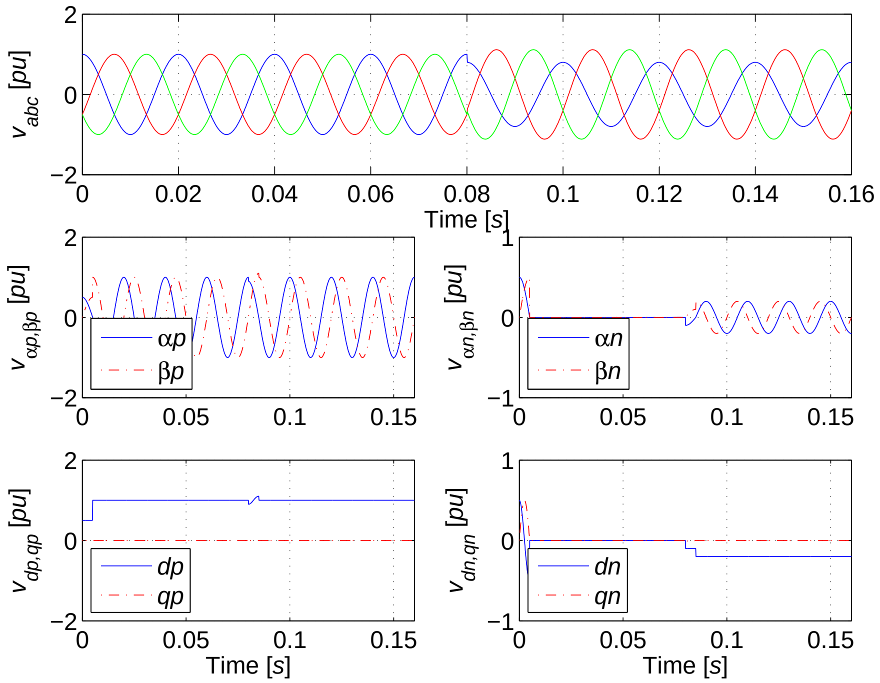

Figure 4.6: Separation of network sequences during unbalanced conditions

Therefore, eq (4.8) can now be split into positive and negative sequence components.

$$\frac{d}{dt}\begin{bmatrix} i_{k\alpha p}(t) \\ i_{k\beta p}(t) \end{bmatrix} = -\frac{R_k}{L_k}\cdot\begin{bmatrix} i_{k\alpha p}(t) \\ i_{k\beta p}(t) \end{bmatrix} + \frac{1}{L_k}\cdot\begin{bmatrix} v_{k\alpha p}(t) - v_{\alpha p}(t) \\ v_{k\beta p}(t) - v_{\beta p}(t) \end{bmatrix} \tag{4.14}$$

$$\frac{d}{dt}\begin{bmatrix} i_{k\alpha n}(t) \\ i_{k\beta n}(t) \end{bmatrix} = -\frac{R_k}{L_k}\cdot\begin{bmatrix} i_{k\alpha n}(t) \\ i_{k\beta n}(t) \end{bmatrix} + \frac{1}{L_k}\cdot\begin{bmatrix} v_{k\alpha n}(t) - v_{\alpha n}(t) \\ v_{k\beta n}(t) - v_{\beta n}(t) \end{bmatrix} \tag{4.15}$$

The $\alpha\beta$ reference frame can be further transformed into dq reference frame which gives a space vector standing still in a new rotating co-ordinate system. If $\omega = 2\cdot\pi\cdot f_m$ is the fundamental angular frequency, the transformation can be obtained through the following Park's transformation:

$$\begin{bmatrix} x_{dp}(t) \\ x_{qp}(t) \end{bmatrix} = \begin{bmatrix} cos(\theta) & sin(\theta) \\ -sin(\theta) & cos(\theta) \end{bmatrix}\cdot\begin{bmatrix} x_{\alpha p}(t) \\ x_{\beta p}(t) \end{bmatrix} \tag{4.16}$$

$$\begin{bmatrix} x_{dn}(t) \\ x_{qn}(t) \end{bmatrix} = \begin{bmatrix} cos(\theta) & -sin(\theta) \\ sin(\theta) & cos(\theta) \end{bmatrix}\cdot\begin{bmatrix} x_{\alpha n}(t) \\ x_{\beta n}(t) \end{bmatrix} \tag{4.17}$$

Where the angular position of the supply voltage can be calculated as in (4.18) or generally derived from a PLL,

$$\theta = tan^{-1}\left(\frac{v_\beta}{v_\alpha}\right) \tag{4.18}$$

A PLL is implemented such that the AC voltage vector is aligned along $d-axis$. Therefore, the $q-axis$ voltage is compared against a zero reference value. The error is applied to a PI controller to derive angular frequency (ω). The required angular position (θ) is further derived by integrating the angular frequency.

The active power and reactive power flow in dq reference frame can be expressed as below with the scaling factor used in the transformation.

$$P_g = \frac{3}{2}\cdot\left((v_{dp}\cdot i_{kdp} + v_{qp}\cdot i_{kqp}) + (v_{dn}\cdot i_{kdn} + v_{qn}\cdot i_{kqn})\right) \tag{4.19}$$

$$Q_g = -\frac{3}{2}\cdot\left((v_{dp}\cdot i_{kqp} + v_{qp}\cdot i_{kdp}) + (v_{dn}\cdot i_{kdn} + v_{qn}\cdot i_{kqn})\right) \tag{4.20}$$

Since $d-axis$ is aligned with the voltage position given by θ, $v_{qp(n)}$ is zero during steady state condition. The active and reactive power will, thus, be proportional to $i_{kdp(n)}$ and $i_{kqp(n)}$ respectively. The rotation for the negative sequence voltage and current ($e^{-j\omega t}$) is in the opposite direction to that of the positive sequence voltage and current ($e^{j\omega t}$). Eqs. (4.14) & (4.15) can after transformation be written as:

$$\frac{d}{dt}\begin{bmatrix} i_{kdp}(t) \\ i_{kqp}(t) \end{bmatrix} = [A]\cdot\begin{bmatrix} i_{kdp}(t) \\ i_{kqp}(t) \end{bmatrix} + \frac{1}{L_k}\cdot\begin{bmatrix} v_{kdp}(t) - v_{dp}(t) \\ v_{kqp}(t) - v_{qp}(t) \end{bmatrix} \tag{4.21}$$

$$\frac{d}{dt}\begin{bmatrix} i_{kdn}(t) \\ i_{kqn}(t) \end{bmatrix} = [B]\cdot\begin{bmatrix} i_{kdn}(t) \\ i_{kqn}(t) \end{bmatrix} + \frac{1}{L_k}\cdot\begin{bmatrix} v_{kdn}(t) - v_{dn}(t) \\ v_{kqn}(t) - v_{qn}(t) \end{bmatrix} \quad (4.22)$$

Where, $[A] = \begin{bmatrix} -\frac{R_k}{L_k} & \omega \\ -\omega & -\frac{R_k}{L_k} \end{bmatrix}$, $[B] = \begin{bmatrix} -\frac{R_k}{L_k} & -\omega \\ \omega & -\frac{R_k}{L_k} \end{bmatrix}$.

By solving eqs. (4.21) & (4.22), the converter side AC voltages can be obtained.

$$v_{kdp}(t) = R_k \cdot i_{kdp}(t) + L_k \cdot \frac{di_{kdp}(t)}{dt} - \omega \cdot L_k \cdot i_{kqp}(t) + v_{dp}(t) \quad (4.23)$$

$$v_{kqp}(t) = R_k \cdot i_{kqp}(t) + L_k \cdot \frac{di_{kqp}(t)}{dt} + \omega \cdot L_k \cdot i_{kdp}(t) + v_{qp}(t) \quad (4.24)$$

$$v_{kdn}(t) = R_k \cdot i_{kdn}(t) + L_k \cdot \frac{di_{kdn}(t)}{dt} + \omega \cdot L_k \cdot i_{kqn}(t) + v_{dn}(t) \quad (4.25)$$

$$v_{kqn}(t) = R_k \cdot i_{kqn}(t) + L_k \cdot \frac{di_{kqn}(t)}{dt} - \omega \cdot L_k \cdot i_{kdn}(t) + v_{qn}(t) \quad (4.26)$$

Integrating eqs. (4.23 - 4.26) over the sampling period $n \cdot T_s$ to $(n+1) \cdot T_s$ (n being an integer);

$$\frac{1}{T_s}\int_{n\cdot T_s}^{(n+1)\cdot T_s} v_{kdp}(t)\cdot dt = \frac{1}{T_s}\int_{n\cdot T_s}^{(n+1)\cdot T_s}\Bigg(R_k \cdot i_{kdp}(t) + L_k \cdot \frac{di_{kdp}(t)}{dt} - \omega \cdot L_k \cdot i_{kqp}(t) + v_{dp}(t)\Bigg)\cdot dt \quad (4.27)$$

$$\frac{1}{T_s}\int_{n\cdot T_s}^{(n+1)\cdot T_s} v_{kqp}(t)\cdot dt = \frac{1}{T_s}\int_{n\cdot T_s}^{(n+1)\cdot T_s}\Bigg(R_k \cdot i_{kqp}(t) + L_k \cdot \frac{di_{kqp}(t)}{dt} + \omega \cdot L_k \cdot i_{kdp}(t) + v_{qp}(t)\Bigg)\cdot dt \quad (4.28)$$

$$\frac{1}{T_s}\int_{n\cdot T_s}^{(n+1)\cdot T_s} v_{kdn}(t)\cdot dt = \frac{1}{T_s}\int_{n\cdot T_s}^{(n+1)\cdot T_s}\Bigg(R_k \cdot i_{kdn}(t) + L_k \cdot \frac{di_{kdn}(t)}{dt} + \omega \cdot L_k \cdot i_{kqn}(t) + v_{dn}(t)\Bigg)\cdot dt \quad (4.29)$$

$$\frac{1}{T_s}\int_{n\cdot T_s}^{(n+1)\cdot T_s} v_{kqn}(t)\cdot dt = \frac{1}{T_s}\int_{n\cdot T_s}^{(n+1)\cdot T_s}\Bigg(R \cdot i_{kqn}(t) + L_k \cdot \frac{di_{kqn}(t)}{dt} - \omega \cdot L_k \cdot i_{kdn}(t) + v_{qn}(t)\Bigg)\cdot dt \quad (4.30)$$

The integration of voltage or current over a sampling period divided by the sampling time will return a mean value of the voltage or current respectively. For further analysis it can be assumed that the current changes linearly and the AC voltage at

PCC is relatively constant during the period of integration [43]. The mean value of VSC side voltages ($\bar{v}_k(n,n+1)$) are the parameters to be controlled.

$$\begin{aligned}
\frac{1}{T_s}\int_{n\cdot T_s}^{(n+1)\cdot T_s} i_k(t)\cdot dt &= \frac{1}{2}\cdot\left(i_k(n+1)+i_k(n)\right) &\quad (4.31)\\
\frac{1}{T_s}\int_{n\cdot T_s}^{(n+1)\cdot T_s} v_k(t)\cdot dt &= \bar{v}_k(n,n+1) &\quad (4.32)\\
\frac{1}{T_s}\int_{n\cdot T_s}^{(n+1)\cdot T_s} v(t)\cdot dt &= v(n) &\quad (4.33)
\end{aligned}$$

Therefore, the above voltage equations can be re-written as,

$$\begin{aligned}
\bar{v}_{kdp}(n,n+1) &= \frac{R_k}{2}\cdot\big(i_{kdp}(n+1)+i_{kdp}(n)\big)+\frac{L_k}{T_s}\cdot\big(i_{kdp}(n+1)-i_{kdp}(n)\big)-\\
&\quad \frac{\omega\cdot L_k}{2}\cdot\big(i_{kqp}(n+1)+i_{kqp}(n)\big)+v_{dp}(n) &\quad (4.34)\\
\bar{v}_{kqp}(n,n+1) &= \frac{R_k}{2}\cdot\big(i_{kqp}(n+1)+i_{kqp}(n)\big)+\frac{L_k}{T_s}\cdot\big(i_{kqp}(n+1)-i_{kqp}(n)\big)+\\
&\quad \frac{\omega\cdot L_k}{2}\cdot\big(i_{kdp}(n+1)+i_{kdp}(n)\big)+v_{qp}(n) &\quad (4.35)
\end{aligned}$$

$$\begin{aligned}
\bar{v}_{kdn}(n,n+1) &= \frac{R_k}{2}\cdot\left(i_{kdn}(n+1)+i_{kdn}(n)\right)+\frac{L_k}{T_s}\cdot\left(i_{kdn}(n+1)-i_{kdn}(n)\right)+\\
&\quad \frac{\omega\cdot L_k}{2}\cdot\big(i_{kqn}(n+1)+i_{kqn}(n)\big)+v_{dn}(n) &\quad (4.36)\\
\bar{v}_{kqn}(n,n+1) &= \frac{R_k}{2}\cdot\big(i_{kqn}(n+1)+i_{kqn}(n)\big)+\frac{L_k}{T_s}\cdot\big(i_{kqn}(n+1)-i_{kqn}(n)\big)-\\
&\quad \frac{\omega\cdot L_k}{2}\cdot\left(i_{kdn}(n+1)+i_{kdn}(n)\right)+v_{qn}(n) &\quad (4.37)
\end{aligned}$$

The values of current at $(n+1)$ are replaced by the current reference values from the outer loops at (n). This is also justified considering the unit sampling time delay in the control system. The mean value of the VSC side voltages are considered as the required reference voltage command to the VSC.

$$\begin{aligned}
v^r_{kdp}(n) &= \frac{R_k}{2}\cdot\big(i^r_{kdp}(n)+i_{kdp}(n)\big)+\frac{L_k}{T_s}\cdot\big(i^r_{kdp}(n)-i_{kdp}(n)\big)-\\
&\quad \frac{\omega\cdot L_k}{2}\cdot\big(i^r_{kqp}(n)+i_{kqp}(n)\big)+v_{dp}(n) &\quad (4.38)\\
v^r_{kqp}(n) &= \frac{R_k}{2}\cdot\big(i^r_{kqp}(n)+i_{kqp}(n)\big)+\frac{L_k}{T_s}\cdot\big(i^r_{kqp}(n)-i_{kqp}(n)\big)+\\
&\quad \frac{\omega\cdot L_k}{2}\cdot\big(i^r_{kdp}(n)+i_{kdp}(n)\big)+v_{qp}(n) &\quad (4.39)
\end{aligned}$$

$$
\begin{aligned}
v^r_{kdn}(n) &= \frac{R_k}{2}\cdot(i^r_{kdn}(n)+i_{kdn}(n))+\frac{L_k}{T_s}\cdot(i^r_{kdn}(n)-i_{kdn}(n))+ \\
&\quad \frac{\omega\cdot L_k}{2}\cdot\left(i^r_{kqn}(n)+i_{kqn}(n)\right)+v_{dn}(n) \qquad (4.40) \\
v^r_{kqn}(n) &= \frac{R_k}{2}\cdot\left(i^r_{kqn}(n)+i_{kqn}(n)\right)+\frac{L_k}{T_s}\cdot\left(i^r_{kqn}(n)-i_{kqn}(n)\right)- \\
&\quad \frac{\omega\cdot L_k}{2}\cdot(i^r_{kdn}(n)+i_{kdn}(n))+v_{qn}(n) \qquad (4.41)
\end{aligned}
$$

Therefore, eqs. (4.38 - 4.41) can be directly used to control the positive and negative sequence currents. Eq. (4.38) can be further simplified; while the same can be done to the remaining three eqs., but are not shown in detail in this report.

$$
\begin{aligned}
v^r_{kdp}(n) &= R_k i_{kdp}(n)+G_c\left(i^r_{kdp}(n)-i_{kdp}(n)\right)- \\
&\quad \frac{\omega\cdot L_k}{2}\cdot\left(i^r_{kqp}(k)+i_{kqp}(k)\right)+v_{dp}(k) \qquad (4.42)
\end{aligned}
$$

Where, G_c is a function of the error signal, $\tilde{e}=\left(i^r_{kdp}(n)-i_{kdp}(n)\right)$ representing a PI (proportional integral) controller. The current control block diagram is shown in Fig. 4.7. The PI controller processes the error signals $(i^r_{kdq(pn)}-i_{kdq(pn)})$ in order to stabilize the current control, and the remaining terms in the above equation are feed-forward terms mainly responsible to de-couple the dynamics of $i_{kd(pn)}$ from $i_{kq(pn)}$ (or vice-versa) and to de-couple the dynamics of $i_{kd(pn)}$ and $i_{kq(pn)}$ from those of the host power system.

To design the current control system, it can be assumed that the current controllers in d and q reference frames act independently, while the cross-coupling term is considered as a disturbance to the system. The plant transfer function is derived to be,

$$
\begin{aligned}
G_p(s) &= \frac{1}{R_k+L_k s} \qquad (4.43) \\
G_p(z) &= \frac{K_s}{z-A} \qquad (4.44)
\end{aligned}
$$

Where, $K_s=(1-A)/R_k$ and $A=e^{-(R_k/L_k)\cdot T_s}$. The sampling time used is $T_s=100$ $[\mu s]$. A unit delay, $1/z$, is included to account for the controller delay. The numerical values of R_k and L_k parameters are presented in Table 4.2. By using the following controller of eq. (4.45), a design for damping ratio of $\zeta=0.7827$ and close-loop natural frequency of $\omega_n=7431$ $[rad/s]$ can be obtained.

$$
G_c(z) = \frac{50\cdot(z-0.9992)}{z-1} \qquad (4.45)
$$

In Fig. 4.8, frequency response of the system from the reference current, i^r_{kdp}, to the converter actual current, i_{kdp}, is shown for different gain values ($K_p=K_{p,s}\cdot K_{p,c}$; where $K_{p,s}=(L_k/T_s)+(R_k/2)$ is the system gain and $K_{p,c}$ is the PI compensator gain). To obtain fast response usually a higher gain is preferred, however, it shall be noted that a very high gain can result in an undesirable or unstable system.

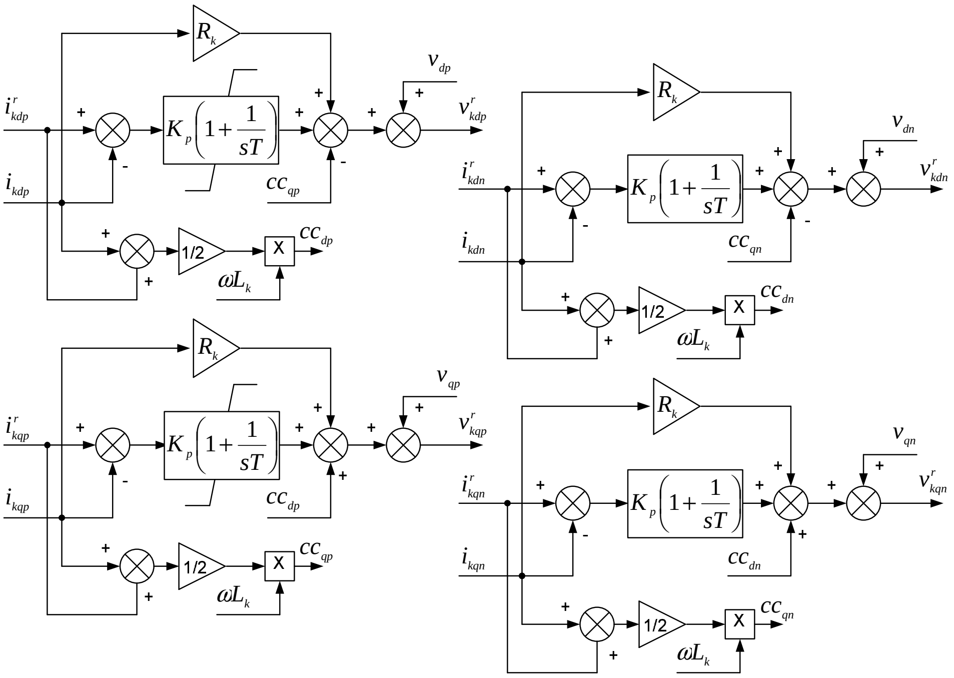

Figure 4.7: Current control block diagram

4.1.2 DC Voltage Control

One of the main functions of the grid end VSC of a HVDC transmission system is to maintain the DC voltage level at a pre-defined value. By controlling the DC voltage, the grid end VSC ensures that the total active power from the WPP is delivered to the host power system and the system balance is maintained.

If it is assumed that the voltage and current at the AC side are balanced, the expression for the AC side active power will consists of only the positive sequence terms. Furthermore, $v_{qp} = 0$, so the active power expression is,

$$P_{ac} = \frac{3}{2} \cdot \left(v_{dp}(t) \cdot i_{dp}(t) + v_{qp}(t) \cdot i_{qp}(t)\right) \tag{4.46}$$

$$P_{ac} = \frac{3}{2} \cdot \left(v_{dp}(t) \cdot i_{dp}(t)\right) \tag{4.47}$$

Similarly, the power in the DC side can be written as,

$$P_{dc} = i_{dc}(t) \cdot v_{dc}(t) \tag{4.48}$$

If the losses in the system are to be neglected, active power in the AC side should equal the power in the DC side to maintain energy balance in the system. If the balance in energy is not maintained in the system, the DC side voltage will be affected.

$$P_{ac} = P_{dc} \tag{4.49}$$

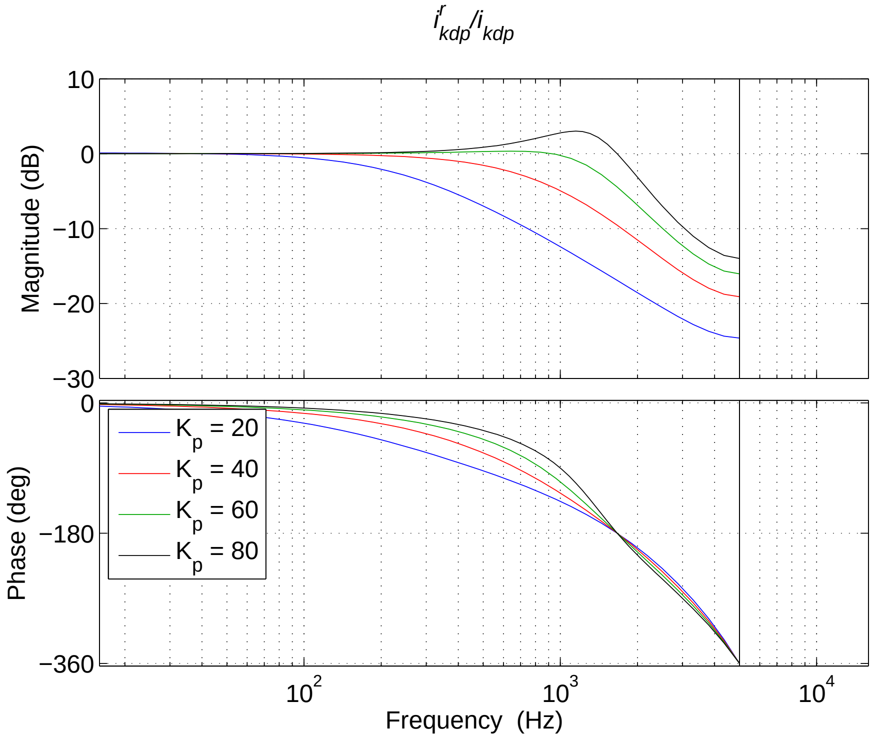

Figure 4.8: Frequency response of the current control

If the active power equality between the AC and DC side is satisfied, the following expression can be derived.

$$i_{dc}(t) = \frac{3\cdot\left(v_{dp}(t)\cdot i^r_{dp}(t)\right)}{2\cdot v_{dc}(t)} \tag{4.50}$$

In the above eq. (4.50), the AC side $d-$ axis current $i_{dp}(t)$ is replaced with the reference current value $i^r_{dp}(t)$. The DC voltage control (outer loop) is relatively slower than the current control loop (inner loop). So for the consideration of DC voltage control, the AC side current in consideration can be considered equal to its equivalent reference value [43].

The main idea behind the DC voltage control is to keep the energy balance over the VSC DC capacitor, given by the following eq. (4.51) - the system parameters are shown in Fig. 6.3. The HVDC transmission is a bi-polar system, with ±100 $[kV]$ voltage level and the value of capacitor per converter per pole is 250 $[\mu F]$.

$$i_{in}(t) - i_{dc}(t) = C_{dc}\cdot\frac{dv_{dc}(t)}{dt} \tag{4.51}$$

Integrating the above equation over the sampling period $n \cdot T_s$ to $(n+1) \cdot T_s$,

$$\int_{n \cdot T_s}^{(n+1) \cdot T_s} (i_{in}(t) - i_{dc}(t)) \cdot dt \quad = \quad C_{dc} \cdot \int_{n \cdot T_s}^{(n+1) \cdot T_s} \frac{dv_{dc}(t)}{dt} \cdot dt \tag{4.52}$$

The DC side currents, i_{in} and i_{dc} can be considered constant during steady state (or the considered time interval), which implies, $\int_{n \cdot T_s}^{(n+1) \cdot T_s} i_{in(dc)}(t) \cdot dt = i_{in(dc)}(n)$.

$$i_{in}(n) - \quad i_{dc}(n) = \quad C_{dc} \cdot \frac{1}{T_s} \cdot (v_{dc}(n+1) - v_{dc}(n)) \tag{4.53}$$

$v_{dc}(n+1)$ is the DC voltage reference, $v^r_{dc}(n)$. Using eq. (4.50), the following expression can be derived.

$$\begin{aligned}
i_{in}(n) - \frac{3 \cdot \left(v_{dp}(n) \cdot i^r_{dp}(n) \right)}{2 \cdot v_{dc}(n)} \quad &= \quad C_{dc} \cdot \frac{1}{T_s} \cdot (v^r_{dc}(n) - v_{dc}(n)) && (4.54) \\
\frac{3 \cdot \left(v_{dp}(n) \cdot i^r_{dp}(n) \right)}{2 \cdot v_{dc}(n)} \quad &= \quad i_{in}(n) - C_{dc} \cdot \frac{1}{T_s} \cdot (v^r_{dc}(n) - v_{dc}(n)) && (4.55) \\
i^r_{dp}(n) \quad &= \quad \frac{2}{3} \cdot \frac{v_{dc}(n)}{v_{dp}(n)} \cdot i_{in}(n) - \\
&\quad\quad \frac{2}{3} \cdot \frac{v_{dc}(n)}{v_{dp}(n)} \cdot \frac{C_{dc}}{T_s} \cdot (v^r_{dc}(n) - v_{dc}(n)) && (4.56)
\end{aligned}$$

Therefore, eq. (4.56) can be directly utilized to control the DC voltage from the grid side converter. While designing the DC voltage controller, the inner current control can be assumed ideal [44]; while the plant transfer function is given as, $C_{dc} \cdot T_s/(z-1)$. The following controller, therefore, gives a design with damping ratio of $\zeta = 0.746$ and close-loop natural frequency of $\omega_n = 174$ $[rad/s]$.

$$G_c(z) \quad = \quad \frac{0.13(z - 0.9885)}{z - 1} \tag{4.57}$$

The response of the inner current control and the outer DC voltage control for a step change in input active power at the DC side is shown in Fig. 4.9. At $t = 0.2$, a step input of DC current from 0.0 $[pu]$-0.9 $[pu]$ is applied at the sending end of the transmission system. The response shown in Fig. 4.9a is when the host power system is set with the strength of $SCR = 5$ and $|Z_g| = 160$ $[\Omega]$, which is a considered to be a relatively weak grid. The response shown in Fig. 4.9b is when the host power system is set with the strength of $SCR = 20$ and $|Z_g| = 40$ $[\Omega]$ and thus it is considered to be a very strong grid. The effect of sudden increase in active power is seen in the voltage at the PCC ($v_{d,q}$) and also in the DC voltage. However, the impact on the grid voltage is less significant as the grid strength increases. Voltage magnitude, v_d, at the PCC is controlled by the implemented AC voltage controller (Section 4.1.3). A rise in DC voltage is observed while the controller finds a new steady state value.

The disturbance in DC voltage is also affected by the implemented current limit, as the current command exceeds the limit, the active power transfer to the grid is momentarily restricted to the maximum limit value. As soon as the output active power (P_g) equals the input DC power, the DC voltage is controlled back to the preset value.

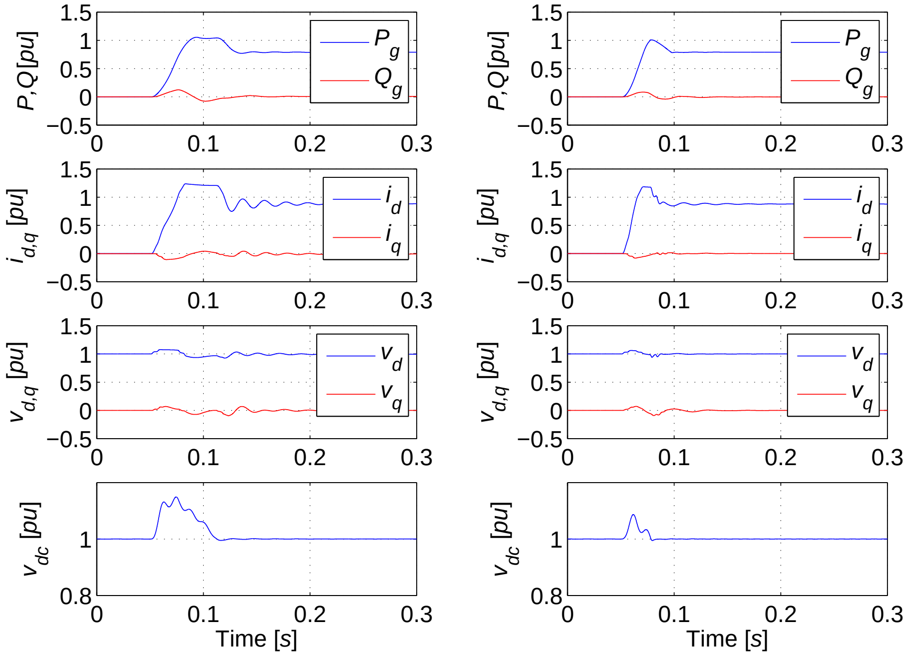

(a) SCR = 5

(b) SCR = 20

Figure 4.9: Power step response of the grid side VSC

4.1.3 AC Voltage Control

To calculate the reference value of reactive current delivered to the grid, an AC voltage control at the PCC is implemented. The implemented control is divided into two parts: (i) control during normal operation, (ii) control during fault operation. A combination of feed-forward and PI controller is implemented during the normal operation; this mode of operation is termed as voltage control mode. To derive the feed-forward term, the measured AC voltage (at the LV side of the grid transformer) is compared against a reference value and a voltage gain $k_{v,gain}$ is applied to the difference.

$$i^r_{kqp}(n) = k_{v,gain} \cdot i_{q,lim} \cdot (v^r_d - v_d(n)) + G_c\,(v^r_d - v_d(n)) \tag{4.58}$$

Where, G_c is a function of error $\tilde{e} = \left(v^r_d - v_d(n)\right)$ representing a PI controller. However, if the voltage at the HV side of the transformer is to be compensated, the above control eq. can be re-written as,

$$i^r_{kqp}(n) = k_{v,gain} \cdot i_{q,lim} \cdot \left(v^r_{gd} - v_{gd,eq}(n)\right) + G_c \left(v^r_{gd} - v_{gd,eq}(n)\right) \tag{4.59}$$

Where, $i_{q,lim}$ is the maximum $q-$ axis current limit, v^r_{gd} is the reference grid voltage, and $v_{gd,eq}(n)$ is the equivalent grid voltage measured from the primary side of the transformer.

$$v_{gd,eq}(n) = v_{dp}(n) - i_{qp}(n) \cdot X_{trans} \tag{4.60}$$

v_{dp} is the voltage magnitude at the LV side of the grid transformer, X_{trans} is the transformer equivalent impedance. However, during a fault sequence or voltage dip in the host power system, the PI controller is by-passed and only the feed-forward part is implemented; this mode of operation is termed as LV-FRT mode. As the feed-forward term only consists of a proportional gain in the form of voltage gain $K_{v,gain}$, the stability of the control can be ensured relatively easily over the entire range of voltage dips. The numerical value of the voltage gain is normally determined by the nature of the grid and usually by the grid code requirements. In this work, $k_{v,gain} = 2$ is implemented as recommended in [45].

4.1.3.1 Voltage Dip Detection

The detection of the voltage dip directly follows from the voltage measurement at the PCC. The $d-$ axis voltage, which corresponds to the amplitude of the three phase AC voltage due to the implemented transformation factor, is monitored and compared against a reference threshold, $v_{d,th} = 0.9$ $[pu]$. The threshold value of the voltage is based on the recommendation in [45]. When the voltage is lower than the threshold value, the dip detected flag is turned on (flag = 1) and the mode of operation is - LV-FRT. The current reference priority in the control system is set such that active current (or i_{kd}) gets the highest priority during normal condition, while at fault or voltage dip, reactive power (or i_{kq}) gets the highest priority. When the voltage recovers or the voltage exceeds the threshold value, the dip detected flag is turned off (flag = 0) and the mode of operation is - voltage control mode. However, at this instance the flag = 0 is latched such that the flag switch-over is restricted for $t_{latch} = 60$ $[ms]$. The main purpose of this latch is to avoid any control instability during the voltage recovery process, specifically for the weak grid inter-connection. When the remote fault is cleared, the active power transfer from the grid side VSC will increase and the voltage recovery process will be influenced by the sudden increase in active power. The level of influence is dependent upon the relative strength of the host power system.

4.1.4 Power Curve

The PQ characteristic of the grid side VSC, outlining the active and reactive power transfer capabilities, is shown in Fig. 4.10. The active power characteristics are only shown in the positive axis as it is not so relevant on the other side when connecting a WPP.

The PQ capability curve of a VSC is generally determined by the current and the voltage limits of the VSC. As explained earlier in section 4.1.1, any VSC has a predefined current limitation predominantly imposed by the current carrying capacity of the switching components. Both active and reactive power contribute to the current that flows through the VSC or the switching device usually IGBT. Besides the current limitation, a VSC PQ characteristic is also determined by the voltage limitation set by the modulation index limit or the total available DC voltage. In Fig. 4.10, the upper flat portion ($+ve$ Q limit) of each curve is due to the voltage limit of the VSC. The $+ve$ P limit and the $-ve$ Q limit of the VSC is due to the current limit of the VSC. In some cases, it is also desired to apply an under voltage limit such that the $-ve$ Q is restricted well above -1.0 [pu] value to allow adequate AC voltage to transmit the active power.

The PQ characteristics of a VSC are further influenced by the level of the grid side AC voltage magnitude. The shift in the PQ curve for different voltage magnitudes is shown Fig. 4.10; where increase in AC voltage magnitude at the PCC means decrease in maximum Q export capability or increase in maximum P export capability. The maximum over voltage limit of the grid end VSC is set at 1.1 [pu].

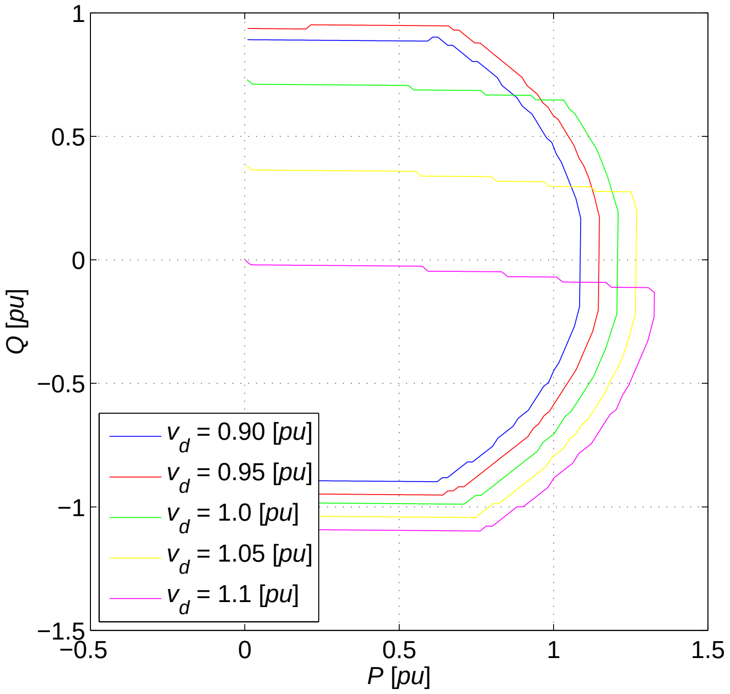

Figure 4.10: PQ characteristics of the grid side VSC; v_d is the peak value of the reference voltage at the LV side of the grid transformer

4.1.5 Negative Sequence Control

As presented earlier, the inner current control of the positive and negative sequence currents can be achieved via eqs. (4.38 - 4.41). The reference values for the positive sequence $d-$ axis and $q-$ axis currents are determined from the dc voltage control and AC voltage control loops. However, the reference current values for negative sequence control cannot be generated through a similar approach.

One approach is to assign zero reference values to the negative sequence currents such that,

$$i^r_{kd(q)n} = 0 \tag{4.61}$$

This implies that all three phase currents from the VSC are commanded to remain balanced regardless of the grid voltage. The other approach is to generate a controlled reference value for the negative sequence currents [46–51]. During unbalanced grid voltage conditions, the apparent power to the grid can be expressed as,

$$\begin{aligned} S(t) &= \left\{e^{j\omega t}\cdot\left(v_{dp}(t)+jv_{qp}(t)\right)+e^{-j\omega t}\cdot\left(v_{dn}(t)+jv_{qn}(t)\right)\right\}\cdot \\ &\quad \left\{e^{j\omega t}\cdot\left(i_{kdp}(t)+ji_{kqp}(t)\right)+e^{-j\omega t}\cdot\left(i_{kdn}(t)+ji_{kqn}(t)\right)\right\}^* \end{aligned} \tag{4.62}$$

Where $e^{j\omega t}\cdot x(t)$ rotating clockwise denotes a positive sequence and $e^{-j\omega t}\cdot x(t)$ rotating counter-clockwise denotes a negative sequence; $x(t)$ represents either voltage or current. The active and reactive power can be thus expressed as,

$$P_g(t) = P_0+P_1\cdot sin(2\cdot\omega t)+P_2\cdot cos(2\cdot\omega t) \tag{4.63}$$

$$Q_g(t) = Q_0+Q_1\cdot sin(2\cdot\omega t)+Q_2\cdot cos(2\cdot\omega t) \tag{4.64}$$

The components, P_1 and P_2, are non-zero when the AC side voltage is unbalanced. A non-zero value of either P_1 or P_2 will introduce an oscillating term on the active power delivered to the grid with frequency of $\omega_{2\omega} = 4\cdot\pi\cdot f_m$. Since the exchange of active power between the AC and the DC side determines the DC voltage, an oscillation or ripple in the DC voltage will be introduced as a result of active power oscillation. The frequency of DC voltage oscillation is also equal to $2\cdot f_m$, 100 $[Hz]$ for a 50 $[Hz]$ AC system. Therefore, during AC voltage unbalance, the negative sequence currents can be controlled such that the DC voltage oscillation is minimum. The *sine* and *cosine* components of the reactive power do not directly affect the DC voltage so they can be taken out of consideration. Using eqs. (4.19-4.20), the following eq. can be derived.

$$\begin{bmatrix} \frac{2}{3}\cdot P_0 \\ \frac{2}{3}\cdot Q_0 \\ \frac{2}{3}\cdot P_1 \\ \frac{2}{3}\cdot P_2 \end{bmatrix} = \begin{bmatrix} v_{dp} & v_{qp} & v_{dn} & v_{qn} \\ v_{qp} & -v_{dp} & v_{qn} & v_{dn} \\ v_{qn} & -v_{dn} & -v_{qp} & v_{dp} \\ v_{dn} & v_{qn} & v_{dp} & v_{qp} \end{bmatrix} \cdot \begin{bmatrix} i_{kdp} \\ i_{kqp} \\ i^r_{kdn} \\ i^r_{kqn} \end{bmatrix} \tag{4.65}$$

Solving the above eq. for VSC currents in positive and negative sequence,

$$\begin{bmatrix} i_{kdp} \\ i_{kqp} \\ i^r_{kdn} \\ i^r_{kqn} \end{bmatrix} = \begin{bmatrix} v_{dp} & v_{qp} & v_{dn} & v_{qn} \\ v_{qp} & -v_{dp} & v_{qn} & v_{dn} \\ v_{qn} & -v_{dn} & -v_{qp} & v_{dp} \\ v_{dn} & v_{qn} & v_{dp} & v_{qp} \end{bmatrix}^{-1} \cdot \begin{bmatrix} \frac{2}{3}\cdot P_0 \\ \frac{2}{3}\cdot Q_0 \\ 0 \\ 0 \end{bmatrix} \tag{4.66}$$

The negative sequence currents derived from the above eq. to achieve $P_1 = 0$ and $P_2 = 0$ are treated as reference values to the negative current controller. Therefore,

$$i_{kdn}^{r} = \left(\frac{-\frac{2}{3} \cdot P_0 \cdot v_{dn}}{A_-} + \frac{\frac{2}{3} \cdot Q_0 \cdot v_{qn}}{A_+} \right) \tag{4.67}$$

$$i_{kqn}^{r} = \left(\frac{-\frac{2}{3} \cdot P_0 \cdot v_{qn}}{A_-} - \frac{\frac{2}{3} \cdot Q_0 \cdot v_{dn}}{A_+} \right) \tag{4.68}$$

Where $A_- = \left((v_{dp}^2 + v_{qp}^2) - (v_{dn}^2 + v_{qn}^2) \right)$ and $A_+ = \left((v_{dp}^2 + v_{qp}^2) + (v_{dn}^2 + v_{qn}^2) \right)$.

In Fig. 4.11, two cases are presented with zero negative sequence current reference and controlled negative sequence current reference. In both the cases, identical grid voltage conditions are maintained, with strength of the host power system $SCR = 7$ and $|Z_g| = 11.43$ $[\Omega]$. A negative sequence voltage of -0.1 $[pu]$ is introduced at 0.05 $[s]$. When zero negative current reference is used, the AC side three phase currents are relatively balanced compared to controlled negative sequence current reference. The imbalance in the current waveform for controlled negative sequence current reference counters the voltage imbalance to exchange non-oscillating active power. On the other hand, a 100 $[Hz]$ oscillation is obvious in the active power and DC voltage waveform for zero negative sequence current reference. The peak-to-peak DC voltage ripple magnitude is dependent upon the amplitude of the negative sequence voltage and the available DC link equivalent capacitance.

4.2 DC Cables

The DC power is transmitted using two cables of a bi-polar system, with each pole rated at $V_0 = 100$ $[kV]$. The DC cables are modeled as series connected π equivalent circuit between the two end VSC capacitors as shown in Fig. 4.1 and 4.12. The total transmission length of the HVDC transmission system is considered to be $L_0 = 100$ $[km]$, so each cable is modeled with $N_\pi = 5$ number of segments connected in series and each segment as a π equivalent. The maximum frequency range approximated by such a cable model is given by,

$$f_{max} = \frac{N_\pi \cdot v}{8 \cdot L_0} \tag{4.69}$$

where $v = 1/(\sqrt{L_{cable} \cdot C_{cable}})$, L_{cable} and C_{cable} are the cable inductance and capacitance respectively per unit km. Adding more cable segments will offer more detailed results for very high frequency transients, but at the same time the required simulation time will be much longer. It was confirmed that by using 5 number of segments would provide sufficient accuracy for the system dynamics in concern.

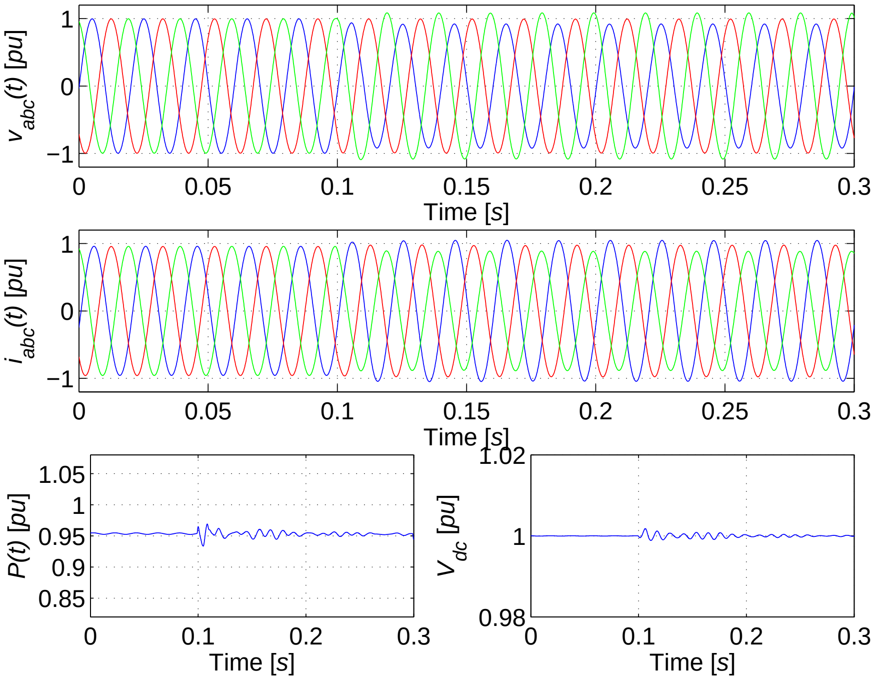

(a) Controlled negative sequence current reference

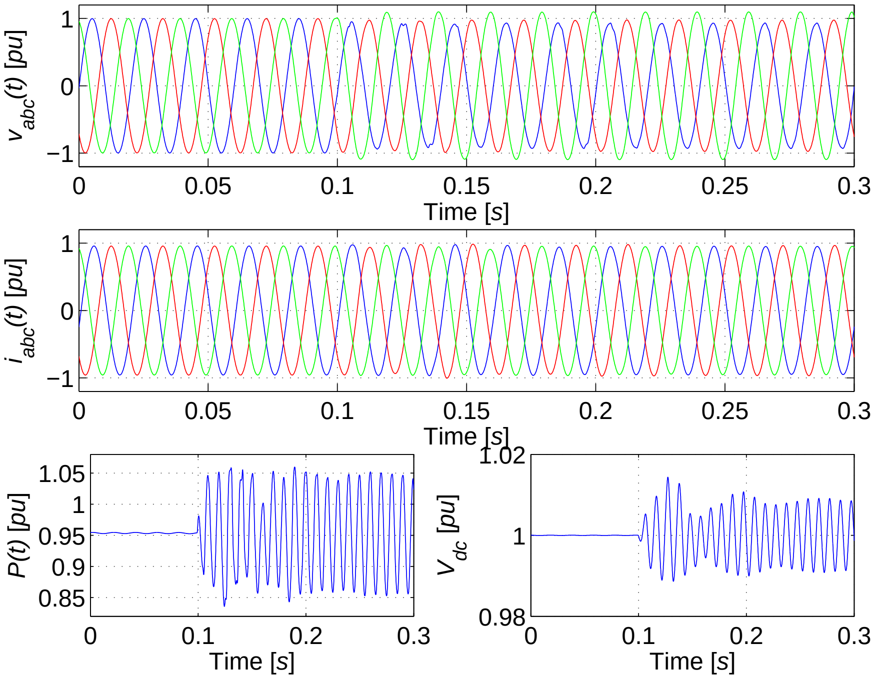

(b) Zero negative sequence current reference

Figure 4.11: Comparison of negative sequence control

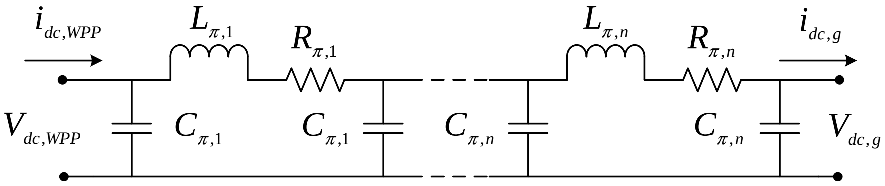

Figure 4.12: HVDC cable model representation

4.3 Wind Power Plant Side Voltage Sourced Converter

An off-shore WPP is often an isolated network system. Individual wind turbines are directly connected to the collector network generally at MV level. The WPP side VSC, referred to the HVDC VSC at the WPP end as represented in Fig. 4.1, is responsible to provide a synchronizing grid to the entire WPP.

A simple control system is implemented based on DC voltage feed-forward loop to provide a constant AC voltage and frequency reference to the WPP collector network via the WPP side VSC. To implement a constant voltage, the voltage references are defined in synchronous reference frame. The dq/abc transformation constant is selected such that the voltage vector in the $d-$ axis equals the peak value of the per phase AC voltage. The three voltage references are, therefore, $v^r_{1kd} = 1.0\ [pu]$, $v^r_{1kq} = 0.0\ [pu]$ and $v^r_{1k0} = 0.0\ [pu]$. It is possible to calculate the modulation index, m, from the measured DC voltage together with the peak AC voltage reference. The three AC voltage references can be further calculated as below,

$$m = \frac{2 \cdot v^r_{1kd}}{v_{dc,wpp}} \tag{4.70}$$

$$v^r_{1ka} = m \cdot sin(\omega \cdot t) \tag{4.71}$$

$$v^r_{1kb} = m \cdot sin\left(\omega \cdot t + \frac{2 \cdot \pi}{3}\right) \tag{4.72}$$

$$v^r_{1kc} = m \cdot sin\left(\omega \cdot t + \frac{4 \cdot \pi}{3}\right) \tag{4.73}$$

A constant frequency ($\omega = 2 \cdot \pi \cdot f_m$) can be generated with the help of a virtual PLL or the frequency measurement signal communicated from the grid end. This ensures that the AC voltage amplitude and frequency at the collector network is constant regardless of the DC voltage fluctuation. The fluctuations in the WPP side DC voltage ($V_{dc,wpp}$) can be due to the variation in active power transfer over the HVDC cables, or AC voltage unbalances in the host power system. The WPP side VSC can, therefore, be compared to an equivalent AC slack bus (infinite bus) which absorbs the power produced by the WPP without altering the voltage amplitude and angle. The theoretical reference value of the MVAC system frequency at the WPP collector network, however, is open to a further optimization process. As the WPP is an isolated system, the choice of AC frequency in the power plant can be set higher than the standard 50 $[Hz]$ or 60 $[Hz]$ value to reduce transformer material costs [52].

The wind turbines selected in this work represent a standard 50 $[Hz]$ product. The collector grid frequency reference is also set at 50 $[Hz]$ to match the wind turbines.

This provides a simple control mechanism to the WPP side VSC and as such there is no direct current control implemented. In a normal steady-state situation the total current in the WPP side electrical system is controlled by the wind turbine converters (provided that the wind turbines in the WPP are based on full converter technology). The WPP side VSC shall, therefore, ensure to have a current capacity slightly higher than the WPP ratings. During disturbances in the collector network, an indirect current control is implemented by using voltage drop technique. As the current through the converter exceeds an upper threshold limit, the terminal voltage of the VSC is reduced sufficiently in a controlled manner to limit the fault current. The upper threshold limit of the current is mainly determined by the sum of total active current from the WPP at maximum rated wind velocity and the total reactive current demand by the collector network at rated active power production.

$$v^r_{1kd,new} = v^r_{1kd} + G_c\,(i^r_{1k} - |i_{1k}|) \tag{4.74}$$

Where G_c represents a PI controller and $|i_{1k}| = \sqrt{i^2_{1kd} + i^2_{1kq}}$.

4.4 Wind Turbine Model

The three major types of generally adopted commercial wind turbines are; (i) fixed-speed, (ii) partial-scale wind turbine, and (iii) full-scale wind turbine [22, 53]. A fixed speed wind turbine utilizes an induction generator connected to a host power system with a reactive power compensation unit (usually capacitors) and a soft-start mechanism. The frequency of the host power system and the number of pole pairs of the generator determines the rated speed of the generator shaft, while the speed of the wind turbine rotor blades is further determined by the gear-box ratio. As the speed of the wind turbine system is constant, it cannot be possible with a fixed-speed system to achieve maximum power point tracking over the entire range of operation (wind speed). The total annual energy production is, therefore, relatively lower. The other main drawback of such a system is its need to stand high stresses on the gear-box and the rotor shaft during fast change in the wind speed (wind turbulence). Nevertheless, a fixed-speed wind turbine is simple and cheaper.

The most common example of a partial-scale wind turbine is a doubly-fed induction generator concept. In such a wind turbine configuration, a partial-scale back-to-back VSC is implemented on the rotor circuit of the generator. The back-to-back VSC on the rotor circuit handles $\approx 20 - 30$ [%] of the rated power and, therefore, the wind turbine can only provide a partial variable speed range.

A full-scale wind turbine configuration consists of a full-scale back-to-back VSC implemented on the stator circuit of the generator. The frequency range of operation of the generator is not restricted by the frequency of the host power system, as the VSC provides a de-coupling between the generator and the host power system. The wind turbine system is designed to obtain maximum power coefficient over a wide range of operation (wind speed). The TSR (tip speed ratio), defined as the ratio between the tip speed of the rotor blades and the wind speed, is maintained at a constant value that results in maximum power output; $\lambda = v_{tip}/v_{wind}$. Also the fast variations in the wind speed (wind turbulence) are absorbed by the inertia of the rotor mass by allowing rotor speed to change. As a result the total annual energy output of a full-scale wind turbine system is relatively higher and the stress on the mechanical system is also reduced.

A full-scale wind turbine can adopt either an asynchronous (induction) generator or a synchronous generator (electrically excited or permanent magnet). Asynchronous generators require magnetizing current or reactive power to produce active power. The use of an active bi-directional AC-DC VSC at the generator end with 6 active switches is very essential in such an application. In case of a synchronous machine, it does not require any reactive power. Hence, it is also presented in [54–56] that a simple three phase diode rectifier can be used together with a DC-DC boost converter. The electrical structure of the wind turbine equipped with a synchronous generator and boost converter is shown in Fig. 4.13. A system as such is generally applied to small or medium wind turbines. The major advantage of using a DC-DC boost converter can be seen in terms of the total number of active switching elements and hence the lower losses in those semiconductor devices. The system redundancy can be increased by simply adding an extra IGBT, in case the other fails to operate; the total IGBT count will still be significantly lower than that of a two level VSC system. However, detailed comparison will be required before it can be claimed that a system with a DC-DC boost converter is suitable for very high power applications.

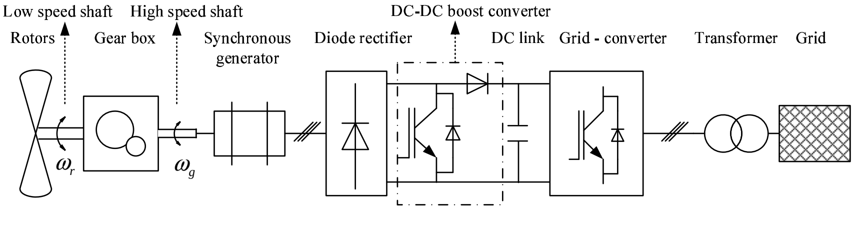

Figure 4.13: Wind turbine with a synchronous generator, passive rectifier, DC-DC boost converter and grid side VSC

A typical configuration of a full-scale wind turbine system is shown in Fig. 4.14. The necessity of a gear-box is mainly determined by the generator type. For example, some permanent magnet wind turbine generators are constructed with multiple-poles, particularly to operate at lower rotational speed and hence eliminate the need of a gear-box. Siemens wind power has adopted a full-scale wind turbine configuration in its entire current product portfolio. A new development in direct-drive (gear-less) permanent magnet wind turbine has also been recently announced. The study of full-scale wind turbines have been presented in different literatures including [57–61].

In this work, a 3.6 [MVA] full-scale geared wind turbine based on an induction

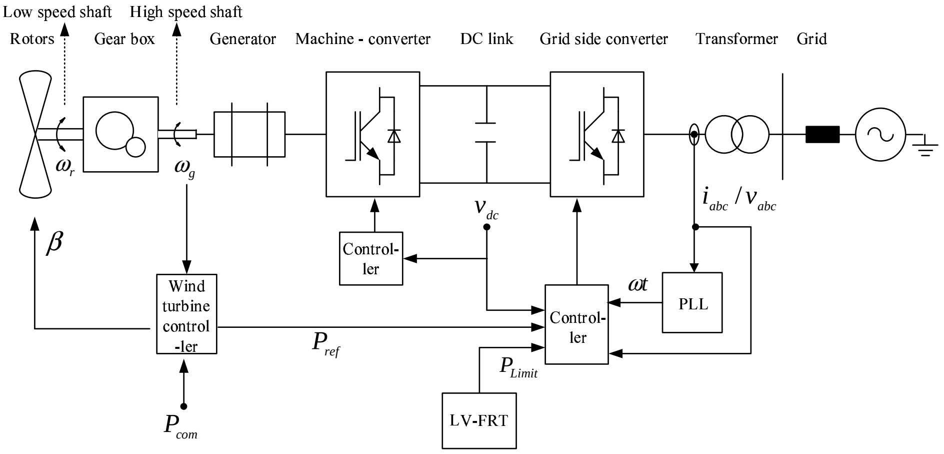

Figure 4.14: A full-scale wind turbine configuration

generator has been selected; being a standard product of Siemens wind power for off-shore applications. The selection of wind turbine topology based on full-converter system for use with off-shore application is also based on the fact that many manufacturers have such turbine types in their product portfolio including Siemens and Enercon. Siemens has also experienced a great amount of success with such wind turbine design in the off-shore conditions [62]. The wind turbine model is described below in detail; while the LV-FRT validation of the wind turbine model against real wind turbine experimental results are presented in [58].

4.4.1 Mechanical System

1. Aerodynamic model - including power coefficient (C_p), TSR (λ) and the pitch angle (β) representation,
2. Shaft model - with inertia and damping of two mass rotor, gear-box and generator,
3. Turbine controller - including three stage speed/pitch control (changing between modes as determined by the generator speed and power reference), and active damping of the drive train.

The aerodynamic model of the wind turbine calculates the aerodynamic torque (τ_{aero}) based on wind speed (v_{wind}), rotor speed (ω_r), pitch angle (β) and power coefficient (C_p). The power coefficient is calculated from the $C_p - \lambda - \beta$ look-up table.

$$\tau_{aero} = \frac{1}{\omega_r} \cdot C_p \cdot \left(\frac{\rho \cdot A_r \cdot v_{wind}^3}{2} \right) \tag{4.75}$$

The aerodynamic torque is then passed on to the shaft model (shown in Fig. 4.15), which is represented by a two mass model. The shaft model includes the inertia of the rotor (J_r) and the generator (J_g), damping (D_s) and stiffness (K_s) of the shaft.

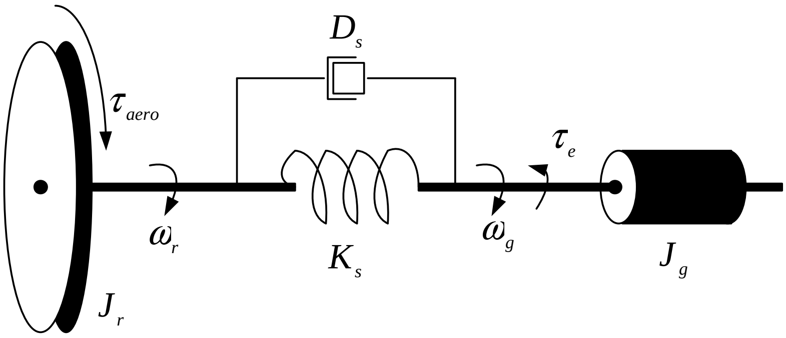

Figure 4.15: Two mass model of the wind turbine drive train

The control of the wind turbine is achieved in three stages - via the wind turbine controller. At low wind speed, the rotor blades pitch angle is maintained at a constant optimum value. The wind turbine is run at a speed that corresponds to an optimum TSR such that the highest power coefficient (C_p) is achieved. The speed/power control of a wind turbine during this low wind speed region is done via the generator side VSC control by applying an equivalent breaking torque through the generator. At medium wind speed, the control is set to maintain the rotor speed constant, $\omega_r = \omega_{r,rated}$. The pitch angle is still kept constant at the optimum value. However, at higher wind speed when the wind turbine active power equals the nominal value, the rotor speed is controlled by adjusting the pitch angle and, hereby, the mechanical torque.

4.4.2 Electrical system

1. Converters - grid side and generator side converters,
2. Control system - to regulate the active and reactive power as well as the DC link voltage,
3. A DC link - including the DC link capacitance,
4. FRT limiter - limiting active current injection to the network upon fault detection,
5. Unbalanced control - including the injection of zero negative sequence current during normal voltage unbalances and unbalanced faults.

The wind turbine induction generator and the generator side VSC are represented by an equivalent zero order/reduced order model. It has been shown in many work, including [61] and the working group report on specifications for generic WTG (wind turbine generator) models [63], that any transients at the generator side and the generator flux dynamics will be removed or eliminated by the DC link and the fast response of the grid end VSC (further confirmed through the experimental results presented in the Chapter 6). The added accuracy of the system response by implementing a fully detailed model is minimal compared to the added complexity. The equivalent zero order model is divided into two sections, (i) power controller to control the DC link voltage and the generator power and, (ii) calculation of generator electrical torque from the generator power and speed.

The active power reference from the wind turbine controller is sent to the grid side VSC as shown in Fig. 4.14, which determines the active power delivery by the wind turbine to the host power system. The control of the grid side converter is mainly divided into two parts with active and reactive power controller. As in most VSC control, the active power control is directly related to the control of active current (i_d) and reactive power control directly related to the control of reactive current (i_q). The controller sets the wind turbine to export the active power as commanded by the wind turbine controller. At the same time the grid side VSC can exchange reactive power as determined by the AC voltage controller. In case a constant reactive current is demanded by the host power system, the reactive power control can be switched to a constant i_q mode. The current control of the grid side VSC in dq rotating reference frame requires that the phase angle of the connecting AC grid be measured; which is done by using a PLL. Furthermore, two different wind turbine current priority modes are set depending upon the AC voltage retain value at the high voltage side of the wind turbine transformer. The current limit of the grid side VSC is shown in Fig. 4.16.

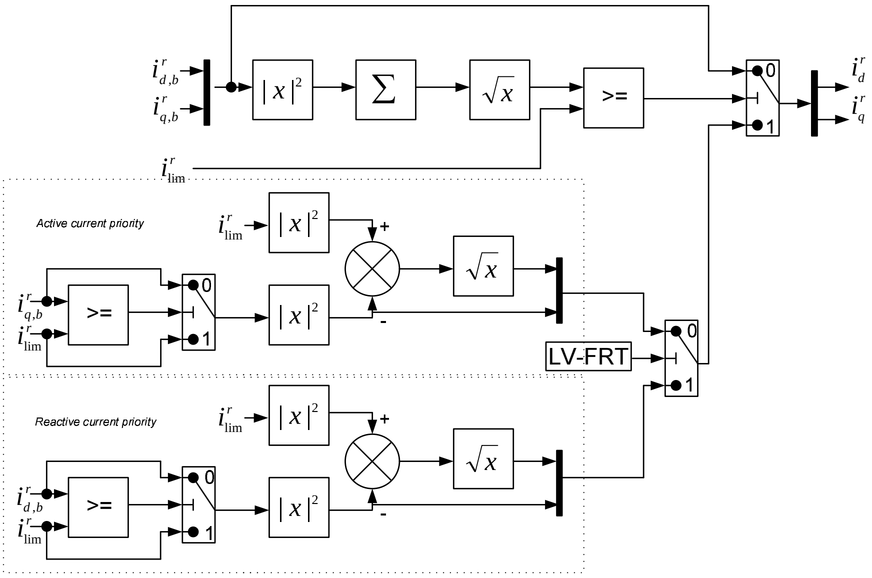

Figure 4.16: Current limits of the wind turbine grid side VSC

The grid side VSC of the wind turbine is also set to control the negative sequence current during asymmetrical voltage condition at the collector network. Zero negative sequence current reference is applied ($i^r_{dn} = i^r_{qn} = 0$), such that the three phase currents from the grid end VSC is symmetrical or balanced regardless of the collector network voltage unbalance. The response of the wind turbine model for different fault voltages (V_{retain}) at the HV side of the wind turbine transformer is presented in Fig. 4.17. At $t = 1.0$ [s], fault voltage of 0.15 [pu], 0.40 [pu] and 0.60 [pu] are applied respectively and the resulting active power (P_{wt}), reactive power (Q_{wt}), and the generator speed (ω_g) response are shown. The export of reactive current by the wind turbine during fault condition is determined by the voltage magnitude of the retain voltage and the applied voltage gain.

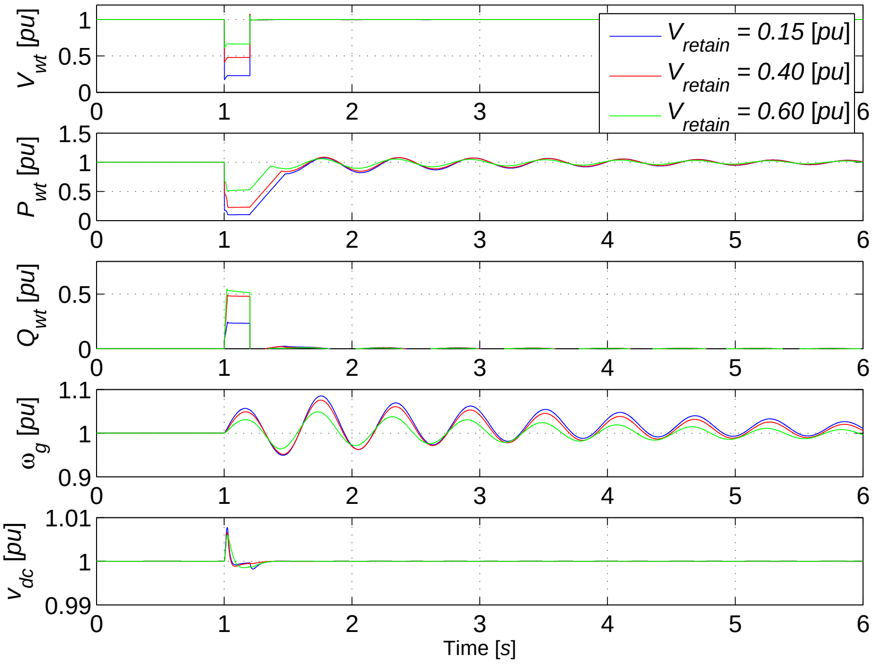

Figure 4.17: Wind turbine performance during voltage dip at the HV side of the wind turbine transformer

4.4.3 Wind Power Plant and Collector Grid

An aggregate model of a WPP can be derived in different ways. An extremely accurate way would be to utilize a detailed wind turbine model and inter-connecting cable representation for each and every wind turbine in a wind farm area. This makes it is possible to model the internal WPP dynamics at the collector grid and also the electrical behavior of the power plant at the PCC (off-shore sub-station in case of a HVDC transmission system). However, in most dynamic studies it is the electrical behavior of the power plant at the PCC which is of major importance.

If it is assumed that the conditions at each wind turbines in a WPP are similar, the total WPP can be represented as a single up-scaled wind turbine. The cables inter-connecting individual wind turbines and cables connecting WPP feeder rows to the off-shore sub-station can be represented as a π equivalent model as explained in section 2.3.2. It has also been presented in [64–66] that if no mutual interaction of the control system between the wind turbines is indicated, a WPP based on variable speed wind turbines can be represented by a single up-scaled wind turbine model for dynamic and transient studies with tolerable electrical behavior accuracy. Among other variables, such an up-scaled wind turbine representation of WPP does not take into account the wake effect and the propagation delay of the wind along the WPP length. Depending upon the direction of the wind in the given WPP area and the layout of the wind turbines, the total amount of active power generated by the entire power plant differs by a factor of c_{wake} as a result of wake effect.

$$c_{wake} = \frac{\text{total active power with wake consideration}}{\text{total active power without wake consideration}} \tag{4.76}$$

In this work, an aggregate model with single up-scaled wind turbine is implemented with $c_{wake} = 1$. As mentioned earlier, it is also assumed that the mutual interaction between individual wind turbines is not present within the operation range of interest of the WPP.

Five

Control of VSC-HVDC Connected to a Wind Power Plant

This chapter introduces and validates via simulation results the different control structures of a HVDC transmission connection from an off-shore WPP. The start-up process, steady state operation, FRT response and the negative sequence voltage compensation of a HVDC system connecting WPP are evaluated. Different FRT options are analyzed and also a FRT scheme for a WPP based on fixed-speed wind turbines is illustrated for comparison.

In Chapter 2 and Chapter 3, different power transmission solutions for off-shore WPPs were discussed. It was illustrated that a VSC-HVDC transmission system with MVAC collector grid at the WPP provides an attractive solution in terms of total energy losses and development of available components. Apart from the system efficiency prospective, it is also necessary to validate the dynamic response of the system in accordance to different requirements. A dynamic simulation model introduced in Chapter 4 will be used to evaluate the electrical performance and behavior of such a transmission system. In this chapter, different control structures for a VSC-HVDC system will be evaluated based on the prepared simulation model.

5.1 System Start-up

Prior to the first grid connection, a HVDC transmission system needs to be energized. The energizing process involves charging of the cable capacitors plus the VSC capacitors to a nominal HVDC value. VSCs are bi-directional; therefore, power can be drawn from the grid during the start-up operation. Initially the WPP end VSC is blocked, while the grid side VSC is grid connected. When the grid side VSC is directly connected to the grid with no control over the active switches, the anti-parallel diode across the switching elements will provide a three phase AC-DC rectification. As the rectifying action is uncontrolled, the HVDC side capacitors will be charged to a level determined by the AC side voltage magnitude.

$$V_{dc} = \sqrt{2} \cdot V_0 \tag{5.1}$$

Where V_{dc} is the HVDC voltage determined by the grid side AC voltage level and V_0 is the AC side rated line-line voltage. However, uncontrolled rectification can result in a very high inrush current. The magnitude of initial inrush current is determined by the total of AC side impedance. It may be preferable to limit the charging current during the start-up by using a three phase series resistance, which is later by-passed upon the charging of the HVDC capacitors. After the HVDC cables are energized, control signals may be applied to the grid side VSC. As the DC voltage dynamics are let to settle down, the WPP side VSC can be un-blocked. The assigned controller will slowly ramp up the AC voltage magnitude at the WPP collector network as shown in Fig. 5.1. The no-load active and reactive power demand of the collector network is provided by the WPP side VSC. Once the collector network is energized, synchronizing voltages are available to the wind turbines. The wind turbine DC link voltage can be set up similarly. All the active power consumed during the start-up sequence including those required changing the wind turbines blade pitch angle and other auxiliary demands are drawn from the host power system.

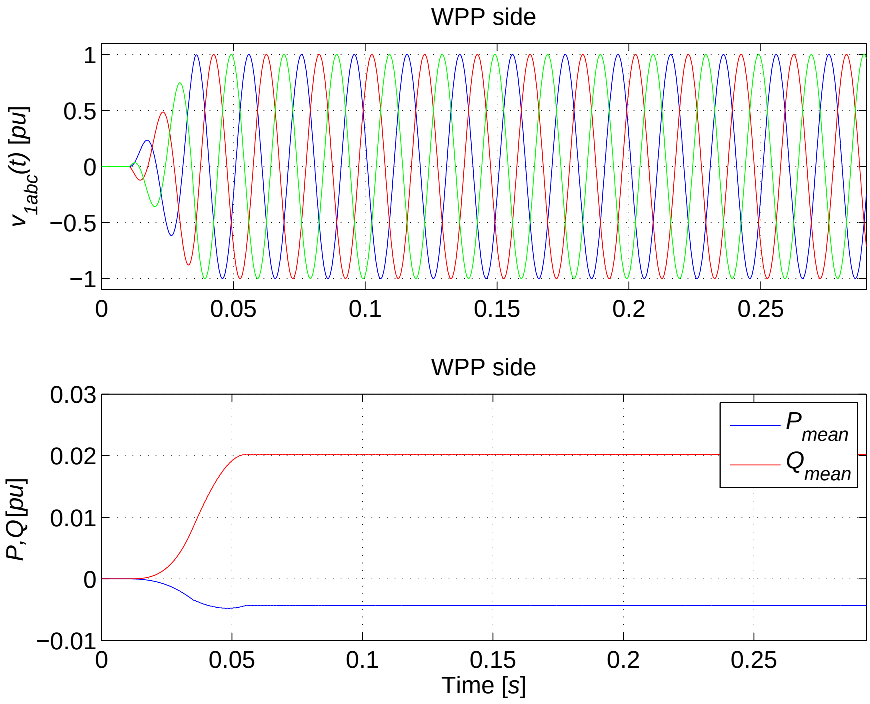

Figure 5.1: Start-up process of the WPP collector network

5.2 Steady state Operation

During normal operating conditions, active power from a WPP is mainly determined by the available wind velocity (v_{wind}) in the WPP area. As discussed earlier, the WPP side VSC of the HVDC transmission line is controlled as an infinite bus ($V\angle\delta^\circ =$ constant). This implies that the voltage magnitude and frequency at the WPP collector network is kept tolerably constant. Wind turbines in the WPP synchronize to the voltage set at the collector grid. As such, the total active power delivered by the WPP is transmitted to the HVDC link by the WPP side VSC.

The reactive power compensation of the WPP collector network can either be provided by individual wind turbines (if set at voltage control mode) or can be distributed between the wind turbines and the WPP side VSC. As the WPP side VSC controls the collector network voltage magnitude, it may not be desirable to control the same voltage from the wind turbine end as well. Therefore, the wind turbines can be set to a constant reactive current (i_q) mode instead. To optimize the sharing of reactive power, an estimation of total requirement can be made for the rated conditions (or at average wind speed in the WPP area) and the known values of cable and transformer parameters. Based on the estimation, optimized reactive current command can be set to each wind turbine control system. As for the WPP side VSC of the HVDC transmission, it is not possible to set the reactive current command directly as no direct current control is defined. However, an indirect control can be achieved by adjusting the reference voltage magnitude of the WPP side VSC, such that the required reactive current flow is achieved.

The distribution of reactive power between the wind turbines and the WPP side VSC is shown in Fig. 5.2. The nomenclature of different parameters follows directly from Fig. 4.1, where Agg side ($_{agg}$) refers to the aggregated wind power plant side and the WPP side ($_{WPP}$) refers to the WPP side VSC. As an example, a constant reactive current reference is applied to the wind turbines $i_q^r = 0.1$ $[pu]$, where as the voltage magnitude reference of the WPP side VSC is assigned $v_{1kd}^r = 1.01$ $[pu]$. During the simulation, the wind velocity is changed from 15 $[m/s]$ to 11 $[m/s]$ and the resulting drop in active power output (P_{agg}) of the aggregated WPP model can be observed. However, the reactive power (Q_{agg}) is relatively constant because of the applied reactive current reference. The dynamic reactive power compensation of the WPP collector network is provided by the WPP side VSC as shown in the Fig. 5.2 (middle plot). The AC voltage magnitude at the collector grid is, therefore, tolerably constant.

The HVDC voltage is maintained by the grid end converter as it transports the available active power from the DC side to the host power system. The grid end VSC independently provides voltage support at the PCC. This way a stable steady state operation of a VSC-HVDC connected WPP is ensured.

The frequency response control demanded by the grid code requirements can be fulfilled using communication signal. The grid side frequency measured by the grid side PLL is transmitted to the WPP side VSC control system. As the WPP is an isolated network, any frequency can be assigned to the collector network via the WPP side VSC. Therefore, the grid side frequency can be imitated at the collector network at all time. Similarly to other modern wind farms, a high level park pilot control can be used to command a new power reference to the individual wind turbines based on the collector network frequency. In special conditions, an absolute production

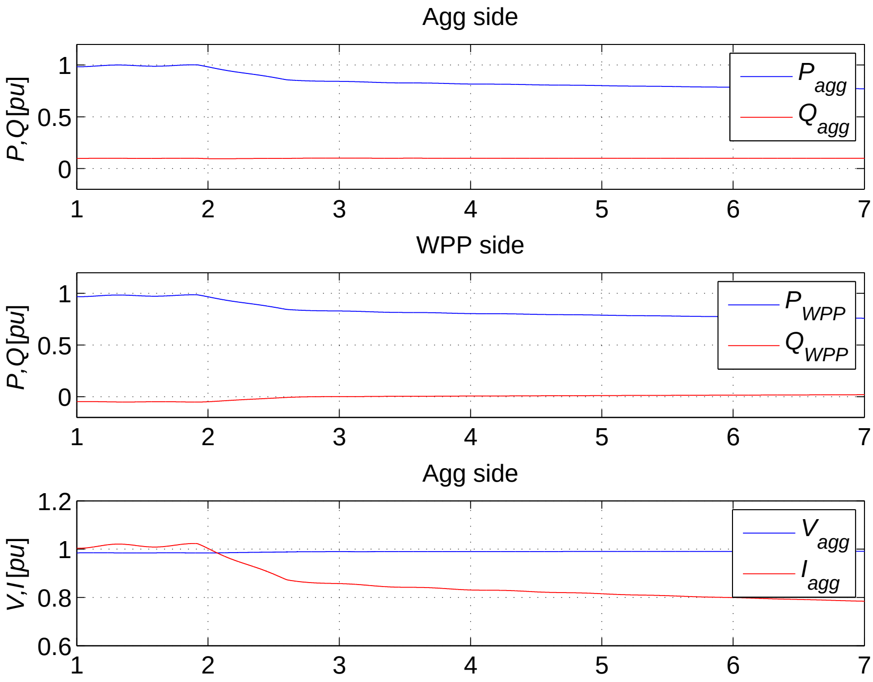

Figure 5.2: Reactive power compensation of the WPP collector network

constraint (limit active power production) may be necessary to avoid overloading of the power grid, in which case a new power command can be directly communicated to the park pilot control by the grid operator.

5.3 Low-voltage Fault-ride-through

Once a stable steady state operation is ensured, a large WPP connected to a grid or a host power system is also required to fulfill different demands from the power system operators. Some of these requirements are very strict and essential for the stability and smooth operation of the power system. One of the major requirements is to stay connected to the grid during a severe voltage dip or fault at least temporarily or during a specified length of time.

When the host power system is subjected to a disturbance or a fault, the grid voltage retain value at the PCC is reduced or in other words, a voltage dip is observed by the grid side VCC. The level of the voltage dip will depend upon the nature of the fault and the electrical distance from the fault to the grid side VSC. The grid side VSC will respond by injecting more active current into the system in order to balance the HVDC voltage (and hence the energy). However, if the grid voltage dip is large enough, the active power capacity of the grid side VSC will be limited because of the applied current limits. Also the reactive current takes the highest priority over the active current as regulated by the grid code requirements, further reducing the active current capability. To calculate the reference value of reactive current delivered to the grid, the measured voltage (at the LV side of the grid transformer) is compared against a reference value and a voltage gain $K_{v,gain} = 2$ is applied to the difference (see section 4.1.3).

As the active power transfer is reduced or limited, consequently the HVDC voltage will start to the rise if the WPP is producing the same amount of active power as in the pre-fault condition. The rate of rise of the DC voltage (dv_{dc}/dt) is mainly determined by the amount of active power generated by the WPP and the equivalent capacitors in the HVDC side. The AC-AC de-coupling between the WPP collector network and the on-land transmission system or the host power system makes it impossible for the wind turbines to directly respond to the changes in the voltage at the main grid without any external influence. If no action is taken, the HVDC system will subsequently trip-off and the LV-FRT requirements are not met. To avoid the subsequent trip-off of the HVDC system, additional control structures are necessary.

There are some litterateurs [67–75] dealing with different control methods to over-come the aforementioned problem related to LV-FRT. The choice of control method is often affected or determined by the choice of generator and/or converters equipped in each wind turbine of the WPP.

5.3.1 DC Chopper

A common solution to achieve the required LV-FRT criterion is by implementing a DC chopper [69, 70]. A DC chopper is a power electronic device which burns the excess of energy in a resistor by means of a controlled electronic switch (usually an IGBT for high power applications). A full-power rated DC chopper is generally connected in the HVDC line close to the grid side VSC as shown in Fig. 5.3. When the system is operating near its full capacity and a voltage dip occurs at the main grid, the power delivered by the grid end VSC will be reduced. Consequently, the DC voltage may rise and exceed a threshold value where the DC chopper is activated. A hysteresis control can be applied to the DC chopper so the frequency of operation during DC over voltage is determined by the size of the resistor and the dissipated active power. Alternatively, a PWM (pulse width modulation) control method can also be applied to control the breaking chopper [76].

$$P_{diss} = I_{ch}^2 R_{ch} \tag{5.2}$$

$$R_{ch} = \frac{V_{dc,uth}^2}{P_{WPP}} \tag{5.3}$$

Where I_{ch} is the chopper current and R_{ch} is the chopper resistor. The upper and the lower voltage threshold value for the DC chopper control are set at $v_{dc,uth} = 1.1\ [pu]$ and $v_{dc,lth} = 1.05\ [pu]$ respectively.

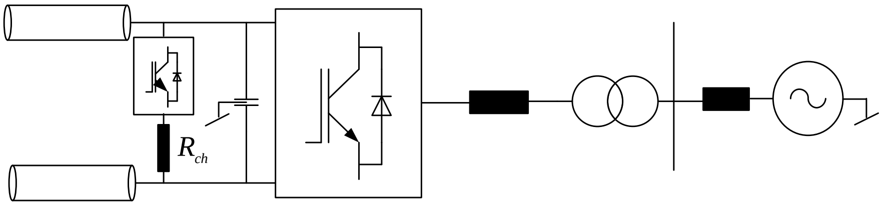

Figure 5.3: Representation of a grid side VSC and the DC chopper

5.3.1.1 Results

The role of a DC chopper to achieve LV-FRT is evaluated in this section. A complete three phase to ground short circuit is applied at the HV side of the grid side transformer at $t = 0.05$ [s] for a duration of $\Delta t_{fault} = 250$ [ms] and the grid strength is set at the $SCR = 5$ and $|Z_g| = 160$ [Ω]. A wind velocity of ≈ 10 [m/s] is applied at the WPP. Simulated voltage response of the system at different locations during a fault event is shown in Fig 5.4. The grid side instantaneous three phase voltages are measured at the LV side of the transformer, therefore, they retain a non-zero value based on the transformer impedance and the amount of reactive current export from the grid end VSC. The grid side transformer has a $X_{trans} = 12$ [%] impedance in the simulation model.

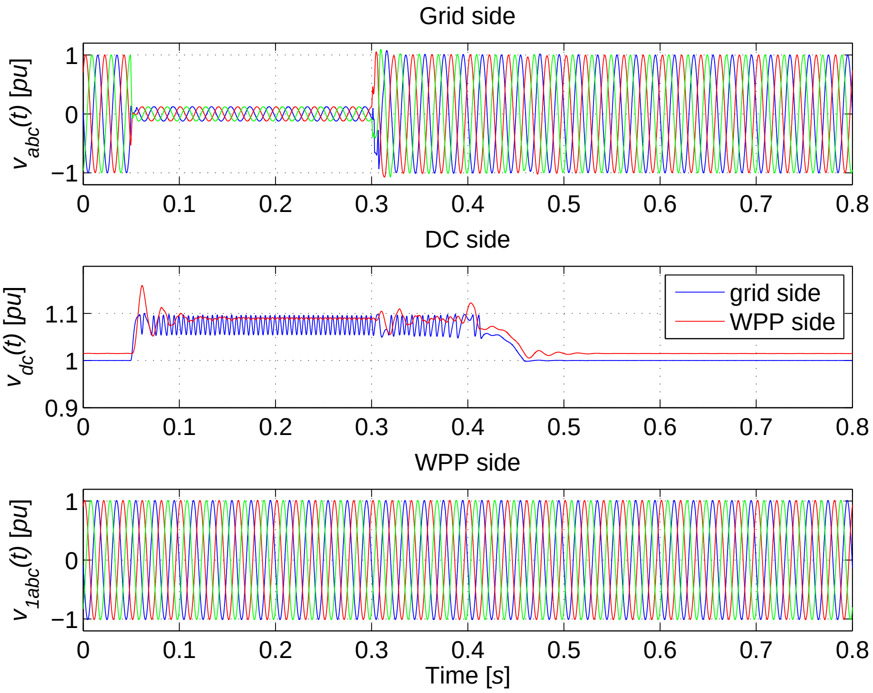

Figure 5.4: Simulated voltage response during three-phase fault using a DC chopper

The simulated power and current response at different locations are illustrated in Fig. 5.5a and 5.5b. The AC side active and reactive power are plotted as a mean value over a period $T_m = 1/f_m$, while the DC side powers are plotted as instantaneous values.

$$P_{mean} = \frac{1}{T_m}\int_0^{T_m} P(t)\,d(t) \tag{5.4}$$

As seen in the plots, the active power and voltages at the WPP end are virtually unaffected. In other words, the dynamics of fault at the grid end are completely de-coupled from the WPP end. This implies that a DC chopper equipped HVDC transmission system can be implemented to any wind turbine type in the WPP, even though the simulation results presented here are based on full-scale wind turbines. The total active power produced by the WPP is totally uninterrupted during any disturbances occurring at the grid end. Therefore, mechanical stresses on the wind turbines are also significantly reduced.

As the fault is cleared, the grid side VSC can restore the active power back to the pre-fault value. It should be noted that the DC voltage recovery is slightly delayed as it does not recover instantaneously. The delay is caused by a combination of the grid side VSC control recovery time and mainly due to the power gradient or the ramp rate (dP/dt) applied during the post fault power recovery process.

The minimum permissible ramp rate during the power recovery process is generally determined by the host power system requirements. However, in a relatively weak grid, a very fast recovery of active power during the post fault recovery process can result in an overshoot in the recovering voltage at the PCC or in worst cases, the voltage may get unstable and a significant voltage back-swing can occur. Examples are shown in Fig. 5.6, where the grid strength is set at, $SCR = 5$ and the WPP producing the maximum rated power at $v_{wind} = 15$ $[m/s]$ in both the cases. In Fig. 5.6a, the post fault active power recovery is relatively fast as no ramp or power gradient is applied. In the top plot, the three phase RMS (root mean square) grid voltages at the PCC are shown and it can be observed that the voltages suffer from higher over-voltage (and considerable back-swing) during the recovery process as compared to the slow active power recovery in Fig. 5.6b. The recovering voltage gets more depressed as the strength of the host power system decreases, which may trigger consecutive FRT. On the other hand, a slower power recovery utilizes the DC chopper for a longer period of time.

In the simulation model, the power gradient is applied by applying a ramp in the active current reference. As the fault is cleared and the AC voltage at the PCC starts to recover, a ramp function or the slope is activated (when the voltage dip flag switch over from 1 to 0). The DC voltage controller sets the active current at the maximum limit in order to recover the DC voltage. The active current reference from the DC voltage controller is then compared against a ramp signal; the slope is given by the selected value of constant A in eq. (5.5). The ramp signal is given an initial condition (x_0) based on the pre-calculated active current during the fault. The smaller value among the two, slope reference or the active current reference from the DC voltage

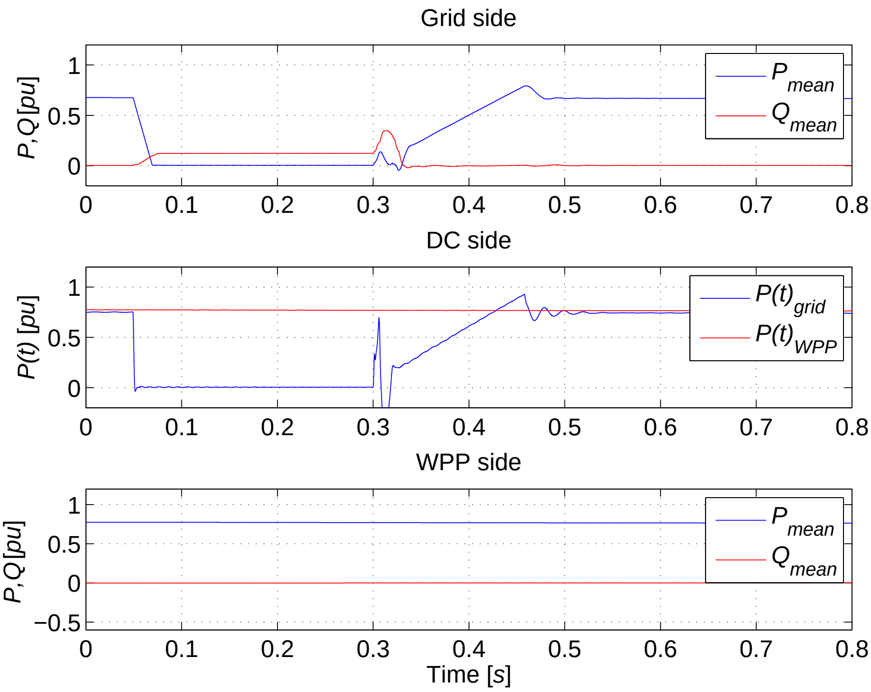

(a) Simulated power response

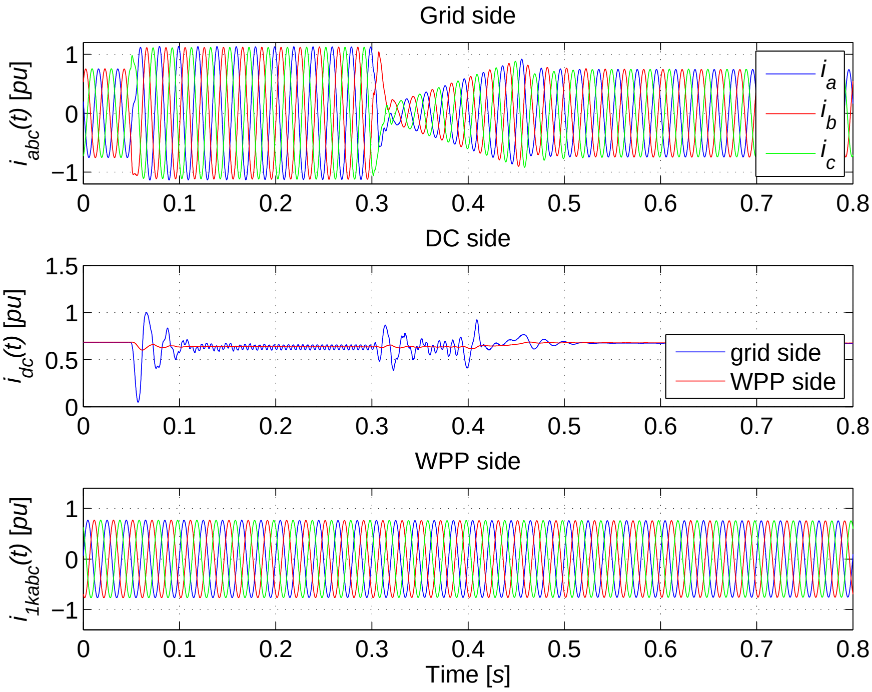

(b) Simulated current response

Figure 5.5: Simulated power and current response during three-phase fault using a DC chopper

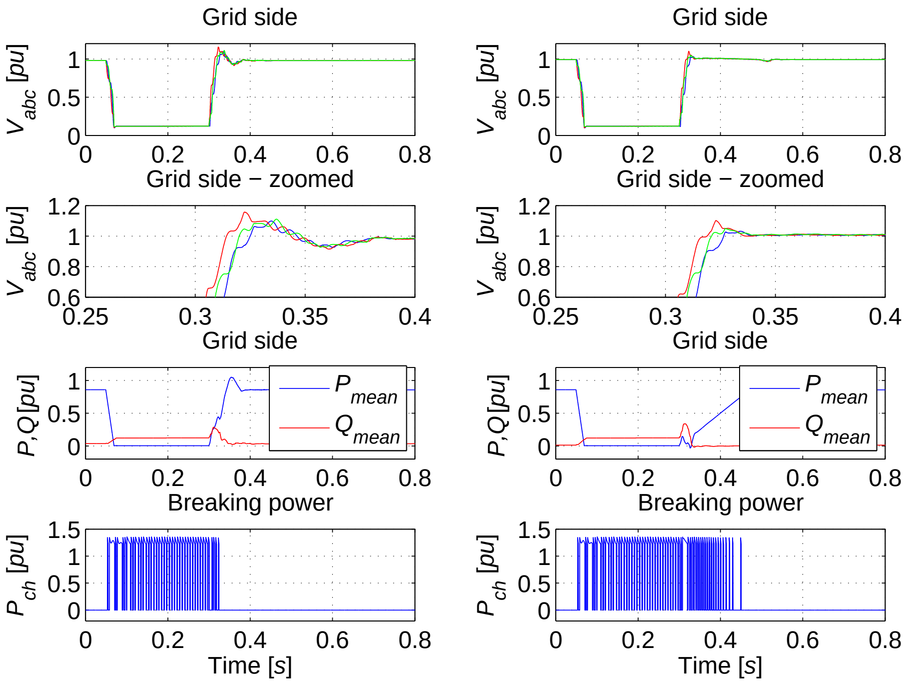

(a) No active power ramp applied

(b) Active power ramp applied

Figure 5.6: Simulated active power recovery process

controller, is used as i^r_{kd} for the current control. When the slope value reaches a maximum limit (lim), it is held constant until the next trigger (dip flag switch over from 1 to 0) is available.

$$slope = \begin{cases} x_0 + \int_0^{inf} Ad(t) & \text{dip flag 1 to 0} \\ lim & \text{else} \end{cases} \tag{5.5}$$

$$i^r_{kd} = \begin{cases} i^r_{d,dc} & slope \geq i^r_{d,dc} \\ slope & slope \leq i^r_{d,dc} \end{cases} \tag{5.6}$$

Besides three phases to ground faults, the other commonly occurring fault types in a power system are unbalanced in nature - line to ground or line to line. Power, voltage and current responses of the system under a single line to ground fault (applied at the HV side of the grid side transformer) are shown in Fig. 5.7 and 5.8. The grid condition is set with $SCR = 7$ and the wind velocity at 15 $[m/s]$. The grid side transformer utilizes a $\Delta - \mathrm{Y}$ configuration, so the three phase voltages at the LV side of the transformer under one phase to ground at the HV side appears as shown in the grid side voltage plot in Fig. 5.8a.

Under unbalanced voltage conditions at the PCC, the power delivered by the grid side VSC is oscillating with twice the grid fundamental frequency ($2 \cdot f_m$). During a fault event, the negative sequence current references are assigned the lowest priority

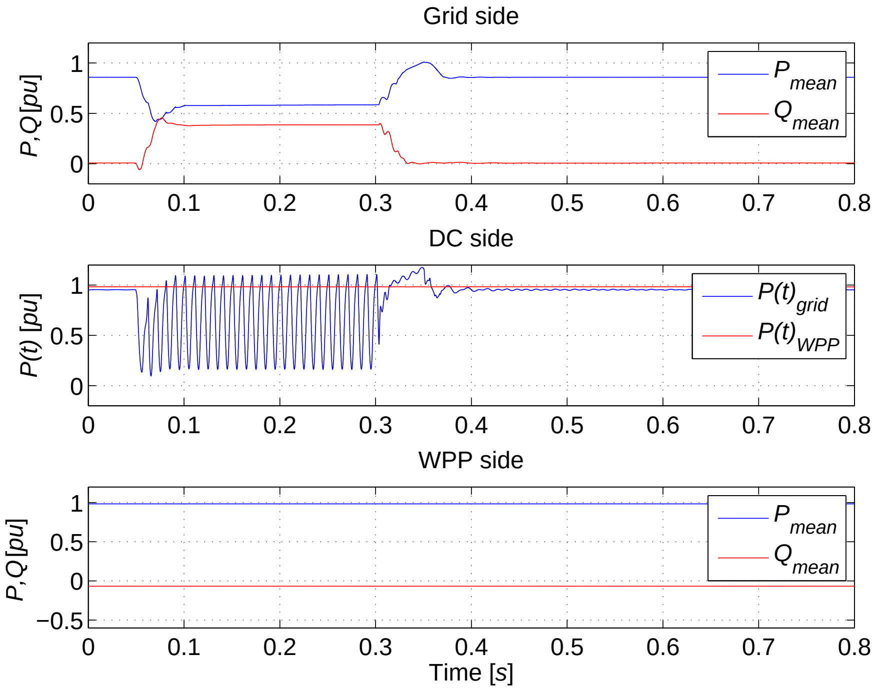

Figure 5.7: Simulated power response during single-phase fault using a DC chopper

to allow room for active and reactive power. In case of rated active power transport, the condition will be equivalent to applying zero negative sequence current reference. However, when the DC chopper is active, controlled negative sequence to eliminate DC voltage oscillation is anyway irrelevant because the DC voltage oscillation is suppressed by the chopper.

The control of reactive power during unbalanced condition require further consideration as three phase voltages are not equal in magnitude. The amount of reactive current support to the grid in the presented results is based on the positive sequence voltage dip as in the case of balanced three phase fault condition. This might in some cases result in the highest phase over voltage. An alternative solution is to provide reactive current support based on the highest of the three phase voltage magnitude.

The major advantage of using a DC chopper is that a reliable LV-FRT can be achieved irrespective to the type of wind turbine used in the WPP. The DC chopper can also be advantageous in other situations such as when a fast grid side power regulation is required. During a short instance, the active power transfer to the grid can be reduced or the direction of the grid side active power flow can be reversed, burning the excess of active power in the chopper resistor. This way a very fast active power damping can be achieved. With all its advantages, the use of DC chopper are being considered for HVDC connected WPPs. However, some major disadvantages of a DC chopper are (i) the added cost of the DC chopper components and, (ii) the amount of heat that needs to be removed during the fault event. It was also

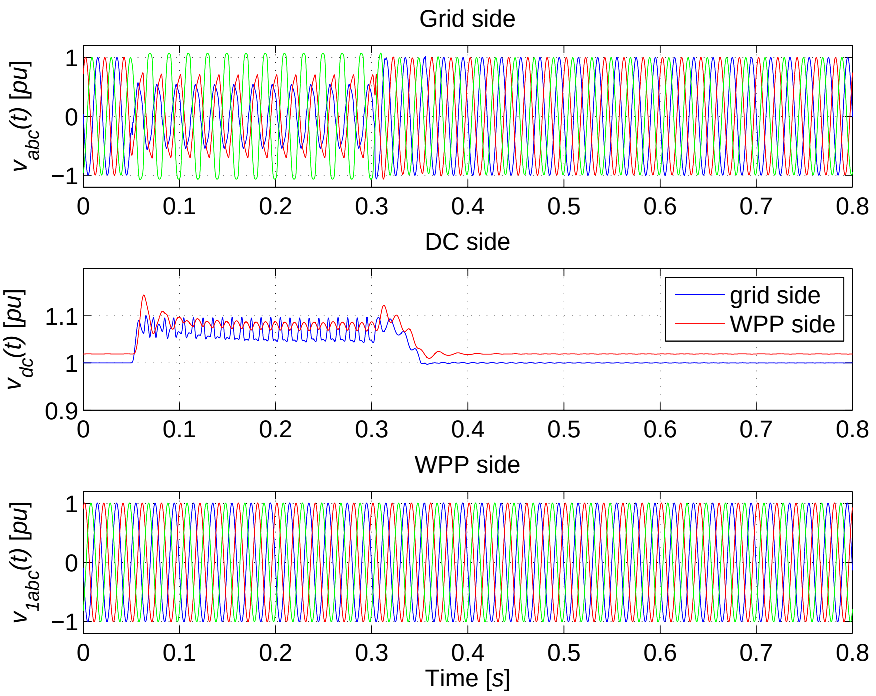

(a) Simulated voltage response

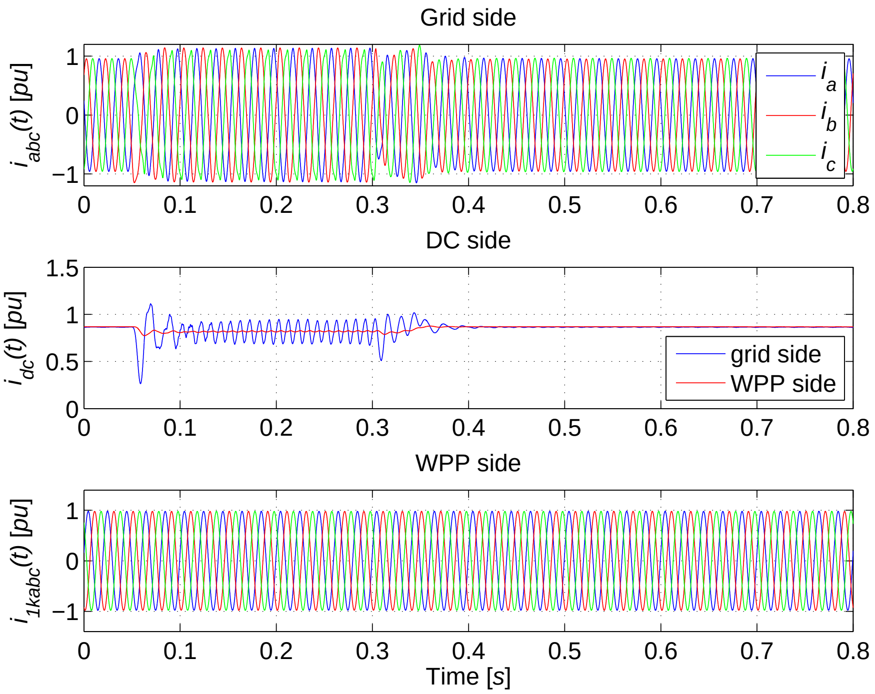

(b) Simulated current response

Figure 5.8: Simulated power and current response during three-phase fault using a DC chopper

verified from the simulation results that during a three phase fault at the grid end for $\Delta t_{fault} = 250$ [ms], the total energy dissipated into the chopper resistor is $E_{diss} \approx 45.0$ [MWs]. The physical size of the required resistor (including heat sink) and the efforts to remove the amount of the heat is enormous. The total power dissipated into the chopper resistor is given by,

$$P_{dis} = h_c \cdot A_{ch} \cdot (\Delta T) \tag{5.7}$$

Where h_c is the hear transfer coefficient, A_{ch} is the surface area of the chopper resistor, ΔT is the temperature difference between the chopper resistor surface and the ambient temperature. The required surface area of the resistor (A_{ch}) to remove a given amount of heat is determined by the type of fluid used to cool the surface area (for e.g., in case of air $h_c = 10 - 100$ [W/m^2K]) . The heat removing capacity of the chopper resistor is, therefore, determined by the surface area; higher the power to be dissipated - bigger the required surface area.

5.3.2 Data Communication

In case a DC chopper is not desired, an alternative solution to achieve LV-FRT is to lower the active power production from the WPP. As the host power system and the WPP are AC-AC decoupled, conditions at the grid end during disturbances need to be transported to the WPP end as data signals. One option to transport data signal is by using light guides pre-installed in most modern cables. The communication signal can be in the form of active power reference directly delivered to individual wind turbine control system. The new active power reference should over-right the local active power reference generated by the wind turbine controller. Alternatively, the voltage magnitude at the grid end can be communicated to the WPP side VSC end such that the voltage conditions at the grid end are directly mirrored at the collector network, in which case the wind turbines are required to have LV-FRT capability.

A HVDC power transmission from an off-shore WPP justifies its advantage only if the transmission distance is relatively long. However, the speed and reliability of data communication over such long distances is not very clear. The speed of data communication is determined by the total time required for the grid side controller to measure and calculate a reference signal plus the time for the signal to transmit over the entire HVDC cable length plus the time for the WPP end controller to execute the reference command. It is very essential to ensure that the total time delay involved in the process is less than the time for the DC voltage to rise above the maximum allowable limit at rated active power transmission. The total energy stored in the HVDC link during a fault event is determined by the amount of active power that is being transmitted, the size of equivalent DC capacitance and the duration of the fault.

$$\int (P_{WPP} - P_g)\, dt = \frac{1}{2} \cdot C \cdot \left(V_{dc,max}^2 - V_{dc,rated}^2\right) \tag{5.8}$$

Fig. 5.9 illustrates the time taken by the HVDC voltage to rise to 5 [%], 10 [%], 15 [%] and 20 [%] over-voltage for different equivalent DC capacitance (C_{eq}) per pole at rated WPP active power production of $P_{WPP} = 180$ $[MW]$, $P_g = 0$ and the DC voltage of 100 $[kV]$ per pole. If it is assumed that the system trip-off is set at 120 [%] of the DC nominal voltage and the average DC voltage during the fault to be maintained at 110 [%] of the DC nominal voltage, the maximum available system reaction time is ≈ 3 $[ms]$ for $C_{eq} = 250$ $[\mu F]$. By employing a larger DC capacitor, more energy can be stored in the HVDC side and the reaction time can be effectively increased. However, it can be seen in the plots in Fig. 5.9 that the increase in the available reaction time is very small even for a large increase in DC link capacitance, especially as the slope of the curves get steeper. While using data communication to ride-through grid side faults provides a simple solution, reliability of such a system over long distances should be realized first. Also it is often not practical to increase the size of DC capacitance for high power and voltage applications.

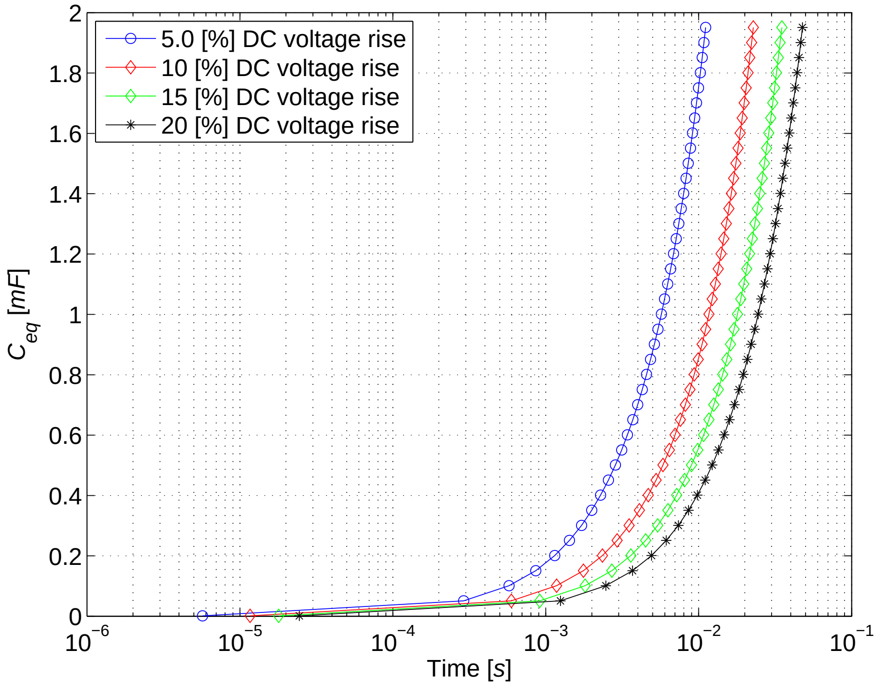

Figure 5.9: Calculated time for the HVDC voltage to reach maximum allowable limit for different equivalent DC link capacitance per pole

5.3.3 Wind Power Plant Side Frequency Control

Although the WPP side collector grid is AC-AC decoupled from the host power system, it should be noted that the state of HVDC voltage can provide a means for estimating the fault at the grid end to the WPP side VSC control. If the main grid undergoes a three phase to ground fault close to the grid side VSC, the AC voltage retain level is severely small. The grid end VSC is no longer able to control the DC voltage. If the increase in DC voltage is monitored from both end of the HVDC transmission system, a DC voltage control switch-over can be implemented between the two VSCs. The DC voltage control switch-over is discussed in further detail in the Chapter 6. As the DC voltage starts to rise and the grid end VSC relinquishes the DC voltage control, the role of the grid end VSC will be to limit the current. At the same time, the rise in DC voltage is monitored by the WPP end VSC control. If the voltage rise exceeds a pre-defined DC voltage threshold level, the WPP side VSC can be set to take-over the DC voltage control. The control objective of the WPP side VSC during normal condition is to provide a regulated AC voltage and frequency reference for the entire WPP as discussed earlier. However, during the FRT mode, the control of the WPP side VSC can be assigned to control the collector network frequency as a function of HVDC voltage, while still regulating a constant nominal AC voltage magnitude. In case of full-scale wind turbines, active power drop can be achieved according to the increase in AC side frequency.

On the other hand, the possibility to actively control the collector network frequency introduces an opportunity to directly utilize fixed-speed wind turbines in the WPP [67, 71, 75, 77]. Fixed-speed wind turbine has lesser number of components compared to a variable speed wind turbine. Therefore, a fixed-speed wind turbine is a less complex and a more robust system, which may be an advantage at off-shore conditions. In most of the previously presented work in relation to FRT response of a HVDC connected WPP based on fixed-speed wind turbines and frequency control, it is not very clear how the wind turbines, specifically the drive train of the wind turbine has been modeled. It is understood from earlier work in [53] that for various power system studies including power system stability, short-term voltage stability and LV-FRT, a single mass model does not properly represent the torsional oscillation of the shaft. Hereby, the generator rotor speed and the active power are also not properly represented.

The response of a fixed-speed wind turbine based WPP during collector network frequency control is analyzed in this section. The total installed capacity ($S_{WPP} = 180$ $[MVA]$) of the WPP, the number of turbines ($N = 50$) and the layout of the WPP are considered to be the same as in case of the WPP discussed earlier with full-scale wind turbines. The model of HVDC transmission system including the two VSCs, cables and other components remain the same; only the full-scale wind turbines in the WPP are replaced by fixed-speed wind turbines. The control structure of the WPP side VSC during the FRT mode is shown in Fig. 5.10.

In a fixed-speed wind turbine, an induction generator is directly connected to the AC grid without any power electronics interface. The response of induction generators to a change in AC grid frequency can be derived from the Thevenin equivalent of an induction generator circuit model [78].

$$T_e(s) = \frac{3}{s \cdot \omega} \cdot \frac{V_{s,th}^2 \cdot \left(R_r'\right)}{\left(R_{s,th} + R_r'/s\right)^2 + \left(X_{s,th} + X_r'\right)^2} \tag{5.9}$$

$$s = \frac{\omega - \omega_g}{\omega} \tag{5.10}$$

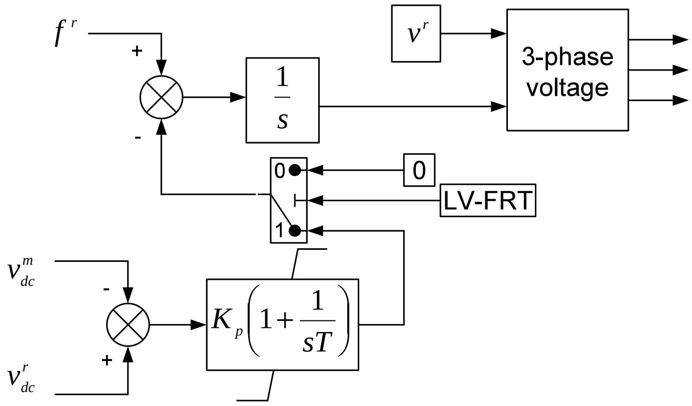

Figure 5.10: Frequency control during LV-FRT

where s is the slip ω, ω_g are the synchronous and generator shaft angular frequency, $R_{s,th}$, $R_r^{'}$ are the stator Thevenin equivalent and rotor resistance, $X_{s,th}$, $X_r^{'}$ are the stator Thevenin equivalent and rotor reactance and V_{th} is the Thevenin equivalent terminal voltage. As the electromagnetic torque of the induction generator decreases, the generator shaft speed will slowly increase, storing the excess of incoming wind power as inertia in the rotating mass.

5.3.3.1 Aggregated Model of WPP with Fixed-speed Wind Turbines

The WPP is represented as an aggregated model. If it is assumed that all the wind turbines and all the induction machines in the WPP are identical, a single machine aggregated model of the WPP is possible by summing up all the individual machines [53, 61].

$$S_{agg} = \sum_{i=1}^{N} S_i \tag{5.11}$$

Where S_{agg} is the rating of the aggregated generator, whereas S_i is the rating of the i^{th} generator in the WPP with N number of wind turbines. Similarly the other major components like transformers and capacitors of the WPP are also aggregated by summing up all the individual component ratings. The inter-connecting cables and the cables connecting the rows or the feeder to the off-shore platform are all modeled as single π equivalent representation. The characteristics of the fixed-speed wind turbine used in the simulation model is shown are Fig. 5.11.

The wind turbine aerodynamic model takes in the wind velocity and the speed of the generator shaft as inputs and the mechanical torque as output back to the induction generator model. The drive train of the wind turbine can either be modeled using a simplified single mass model or a detailed two mass model. In a simplified model, the stiffness of the shaft is not included and the inertia constant of the generator shaft

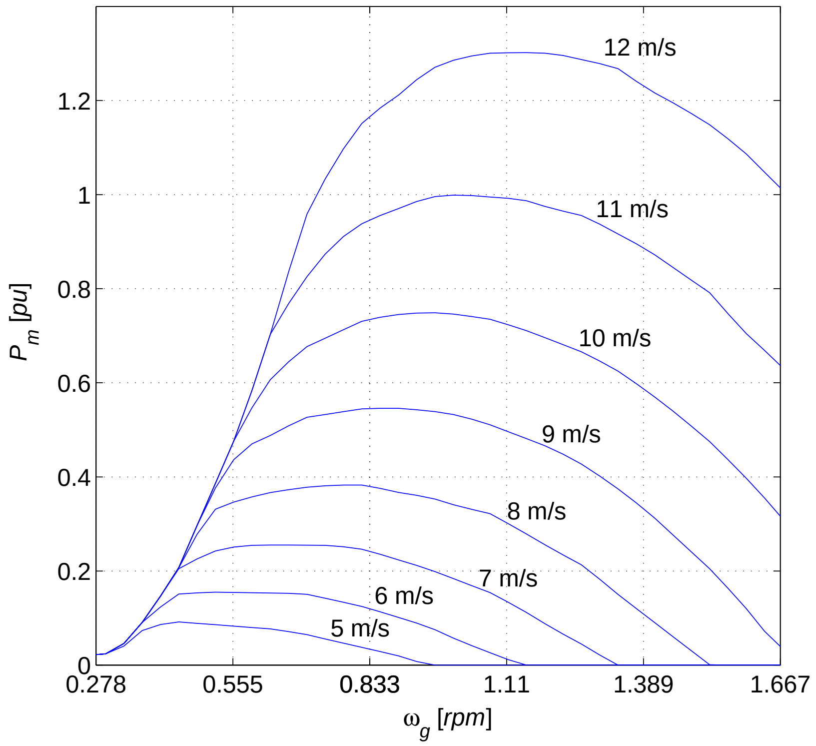

Figure 5.11: Characteristics of the wind turbine

and the rotor shaft are lumped together.

$$2 \cdot (H_r + H_g)\frac{d\omega_g}{dt} = \tau_m - \tau_e - F \cdot \omega_g \tag{5.12}$$

where H_r, H_g are the inertia constant of the rotor and the generator, ω_g is the generator shaft speed, τ_m, τ_e are the mechanical and electrical torque respectively and F is the friction factor.

Whereas, a two mass model (also discussed in Chapter 4) takes into account two separate inertia's of the generator shaft and the rotor shaft connected to each other with proper damping and stiffness.

$$2 \cdot H_r\frac{d\omega_r}{dt} = \tau_r - K_r\theta_s - D_r\omega_r \tag{5.13}$$

$$2 \cdot H_g\frac{d\omega_g}{dt} = -\tau_e + K_g\theta_s - D_g\omega_g \tag{5.14}$$

$$\frac{d\theta_s}{dt} = (\omega_r - \omega_g) \tag{5.15}$$

where K_r, K_g are the rotor and the generator shaft stiffness, D_r, D_g are the rotor and the generator shaft damping and θ_s is the torsional twist about the axis of rotation of the shaft (for details see [53]).

In a full-scale wind turbine model, it was stated that the generator flux dynamics can be eliminated due to the presence of DC link. However, in case of a fixed-speed wind turbine, the generator is directly connected to the AC side. This implies that the generator dynamics can no longer be neglected. In the simulation model, the induction generator is represented by a fourth order state-space model as presented in [79]. The electrical representation of the induction machine model in dq reference frame is shown in Fig. 5.12. The parameters of the induction generator used in the simulation are presented in Table. 5.1.

Table 5.1: Induction generator parameters

	Parameters		Parameters
S_{nom}	180 $[MVA]$	f_m	50 $[Hz]$
p	2	V_0	690 $[V]$
R_s	0.0196 $[pu]$	L_{ls}	0.0397 $[pu]$
R_r'	0.01909 $[pu]$	L_{lr}'	0.0397 $[pu]$
L_m	1.35 $[pu]$	H_{g+r}	8 $[s]$
F	0.055 $[pu]$		

The model equations of induction generators referred to the stator side are,

$$V_{qs} = R_s \cdot i_{qs} + \frac{d}{dt}\phi_{qs} + \omega \cdot \phi_{ds} \tag{5.16}$$

$$V_{dc} = R_s \cdot i_{ds} + \frac{d}{dt}\phi_{ds} - \omega \cdot \phi_{qs} \tag{5.17}$$

$$V_{qr}^{'} = R_r^{'} \cdot i_{qr}^{'} + \frac{d}{dt}\phi_{qr}^{'} + (\omega - \omega_e) \cdot \phi_{dr}^{'} \tag{5.18}$$

$$V_{dr}^{'} = R_r^{'} \cdot i_{dr}^{'} + \frac{d}{dt}\phi_{dr}^{'} - (\omega - \omega_e) \cdot \phi_{qr}^{'} \tag{5.19}$$

$$T_e = \frac{3}{2} \cdot p \cdot (\phi_{ds} \cdot i_{qs} - \phi_{qs} \cdot i_{ds}) \tag{5.20}$$

where V_{ds}, V_{qs} are the terminal voltages, $V_{dr}^{'}$, $V_{qr}^{'}$ are the rotor voltages, i_{ds}, i_{qs}, $i_{dr}^{'}$, $i_{qr}^{'}$ are the terminal and rotor currents, ϕ_{ds}, ϕ_{qs}, $\phi_{dr}^{'}$, $\phi_{qr}^{'}$ are stator and rotor fluxes, ω is the synchronous frequency, ω_e is the electrical angular frequency, p is the number of poles, R_s, $R_r^{'}$ are stator and rotor resistances.

5.3.3.2 Results

To test the LV-FRT capability of the system under study, a three phase voltage dip is introduced at the grid end for a period of $\Delta t_{fault} = 150$ $[ms]$. The grid strength is set at $SCR = 10$ with $|Z_g| = 80$ $[\Omega]$ and the applied wind velocity $v_{wind} = 10$ $[m/s]$.

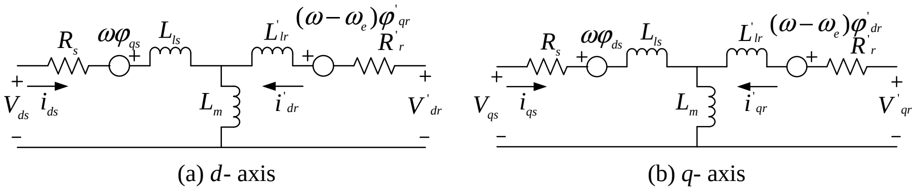

(a) *d*- axis (b) *q*- axis

Figure 5.12: Electrical representation of the induction machine in dq reference frame

Case I: In the first case, the drive train of the wind turbine is represented using a single mass model. The simulated voltage response of the system at different locations is shown in Fig. 5.13. It should be noted that the voltage magnitude at the WPP side is relatively constant during the fault event; while only the frequency is altered. The WPP side VSC has been taken into frequency control mode; hence the production of active power from the wind turbines has been reduced as shown in Fig. 5.14a. The DC voltage has been controlled and maintained within tolerable limits.

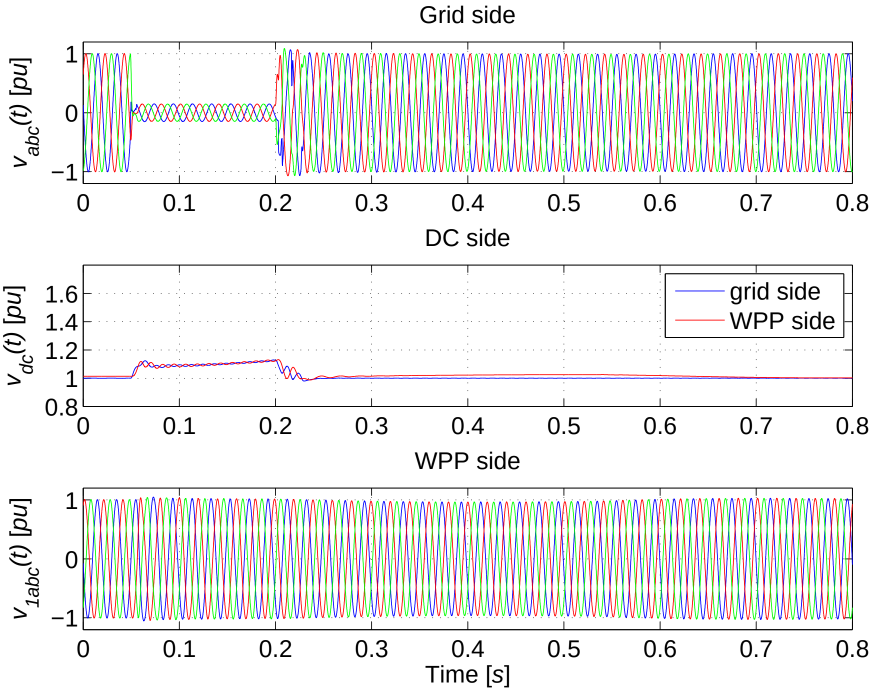

Figure 5.13: Simulated voltage response during three-phase fault of a fixed-speed wind turbines based WPP

The HVDC voltage control switch-over between the grid side VSC and the WPP side VSC takes place when the DC voltage exceeds a pre-defined threshold level. At this point the measured HVDC voltage is higher than the assigned reference value;

therefore, the change in collector network frequency at the beginning of the control mode is much faster as shown in Fig. 5.15a, while the production of active power by the wind turbines also follows the frequency response to reduce accordingly. When the implemented controller maintains the HVDC voltage level, a controlled change in frequency can be observed. As the fault is cleared, the grid side VSC starts to deliver the active power. The HVDC voltage drop is monitored from both ends and when the voltage level drops below a pre-defined lower threshold level, the control action is reverted to the normal situation. However, it has to be taken into account that a very fast jump in AC frequency at the collector network can provoke speed instability or lead to an unstable condition for the induction generators as a large change in slip value will be experienced. The value of collector network frequency is, therefore, ramped back to the normal operating point of 50 $[Hz]$ as shown in Fig. 5.15. During the fault, a large amount of input wind power is stored in the rotating mass. The ramp applied to the frequency also controls the rate of increase of active power during the immediate post fault recovery. However, if the slope of the ramp is too small, the induction generators will be able to follow the frequency change and any control over the active power increase rate is lost. In Fig. 5.14a, it can be observed that at $t \approx 0.6$ $[s]$, the frequency ramp is equal to 50 $[Hz]$ and the normal conditions of voltage magnitude and frequency are maintained hereafter.

Case II: It has also been mentioned earlier that the shaft torsional bending is not modeled by a single mass representation of the wind turbine drive train. This is mainly due to the fact that both the high speed and low speed shaft on either side of the gear-box are lumped into one mass, ignoring the stiffness of the shaft. As a result the speed of the generator shaft and rotor shaft are represented as one. In a two mass model an appropriate value of stiffness, K_s, and damping, D_s, are included, which implies that the ‘soft’ shaft oscillations are not neglected. Therefore, the predicted speed of the wind turbine generator shaft for the same system but represented by two different mass models are not identical as shown in 5.15. In other words, it can be said that the system dynamics predicted by a single mass model is very optimistic because only a small deviation of generator speed and power are estimated.

The simulated power response of the system at different locations with a two mass model representation of the drive train is shown in Fig. 5.16. As illustrated in the figure, a large amount of oscillating active power is released during the immediate post fault recovery, even under controlled frequency ramp down. In many sense, a fixed-speed wind turbine is more difficult to control. A large amount of active power oscillation during the post fault recovery means that the WPP side VSC and the grid side VSC need to be considerably over-sized in terms of current rating. Apart from the active power, it is also illustrated in the power plot that induction generators consume a large amount of reactive power during the post fault recovery. If no variable reactive power source for e.g., SVC or ASVC (advanced static VAR compensator) is installed, the WPP side VSC needs to deliver the required reactive power demand. The over-sizing factor of the WPP side VSC is even further increased due to the requirement of added reactive current.

It is not very clear how the variation in the wind velocity across the WPP area

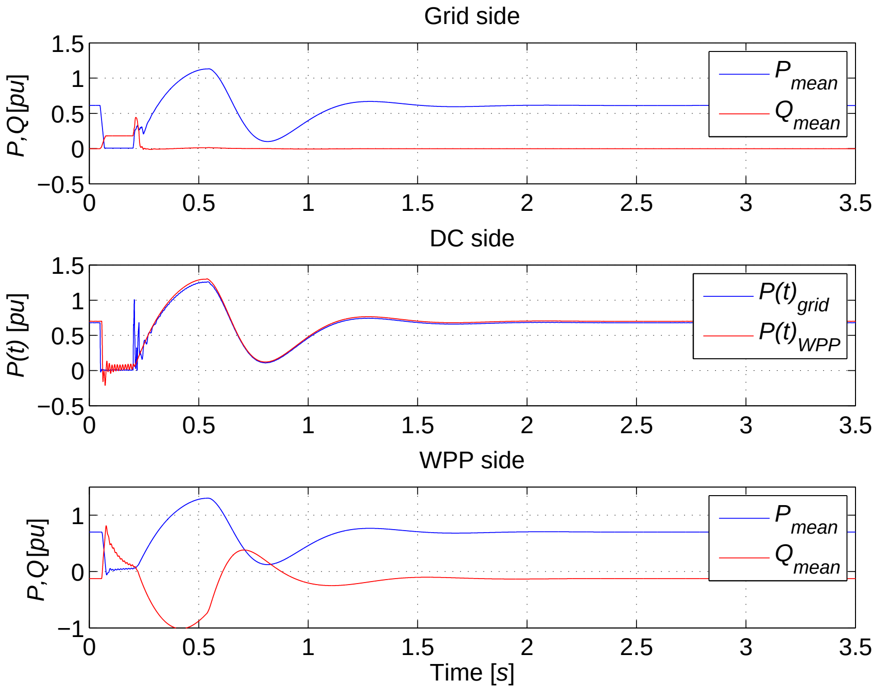

(a) Simulated power response

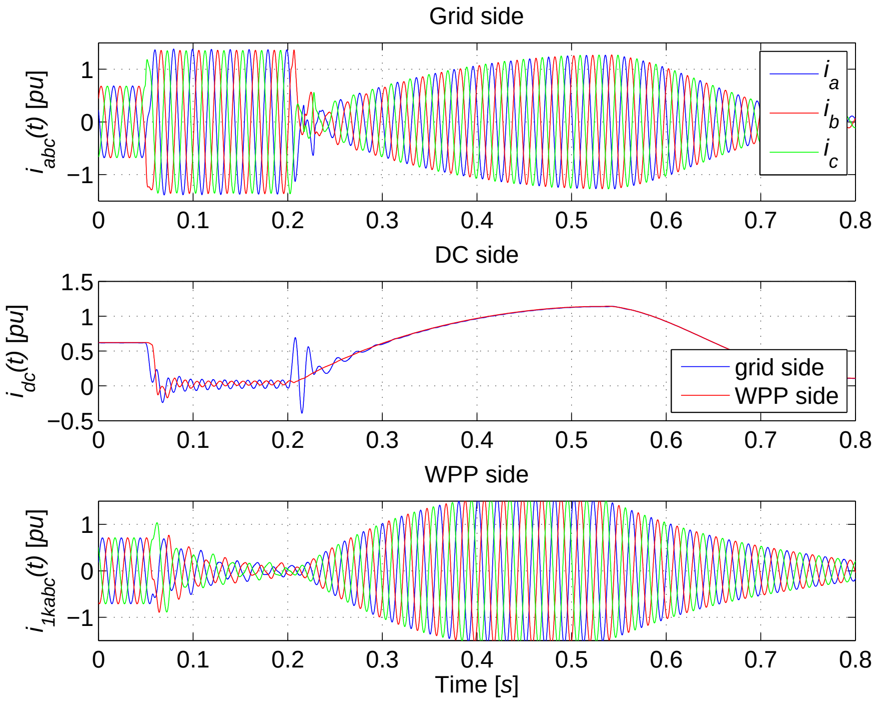

(b) Simulated current response

Figure 5.14: Simulated power and current response during three-phase fault of a fixed-speed wind turbines based WPP

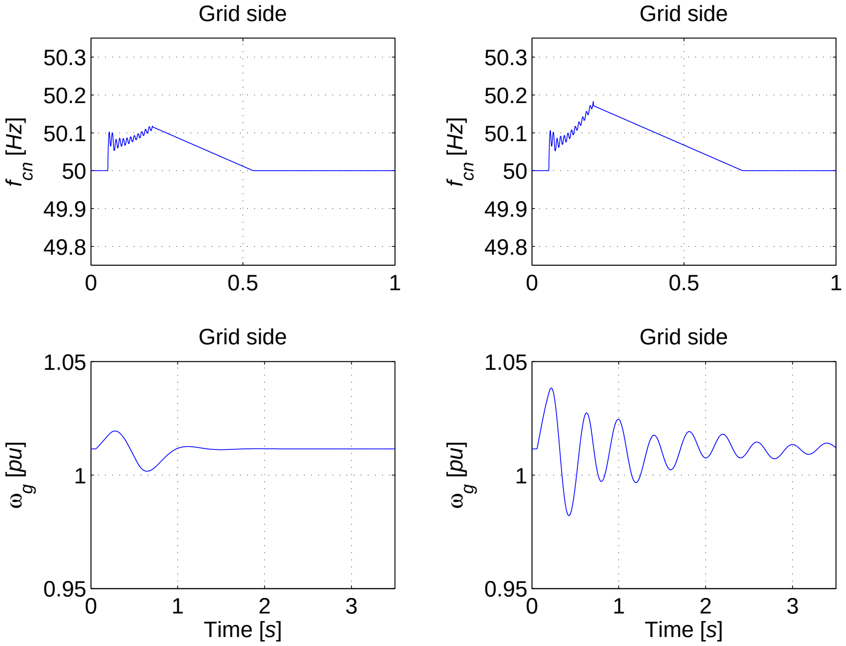

(a) Single mass model (b) Two mass model

Figure 5.15: Collector network frequency and the wind turbine generator speed

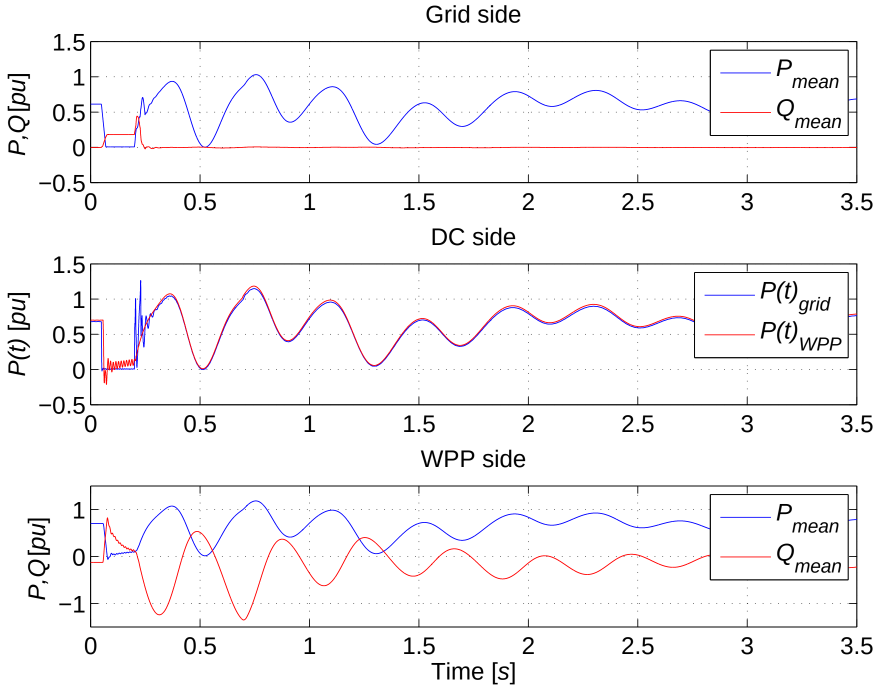

Figure 5.16: Simulated power response using two mass model

will affect the FRT event. In a large WPP area, the difference in wind velocity seen by different wind turbines can be significant. The difference in wind velocity can be due to wind turbulence, propagation time of wind across the WPP area, and also due to wake effects. Fixed-speed wind turbines definitely provide a relatively cheap solution, however, the centralized frequency control of all wind turbines in a WPP via the WPP side VSC needs to be carefully analyzed. The other major drawbacks of a fixed-speed wind turbine are: (i) lower annual energy production, (ii) higher mechanical stresses in the gear box, (iii) less control-ability.

5.3.4 Wind Power Plant Side AC Voltage Control

In the earlier section, a centralized frequency control of the WPP assigned to lower the active power production during grid side fault was discussed. Alternatively, it is proposed and investigated in this report that a centralized AC voltage control at the WPP collector network can provide a controlled response from the system, including the wind turbines and the VSCs in the HVDC transmission system. The investigated system is mainly based on full-scale wind turbines. Majority of modern state-of-the-art full-scale wind turbines are already facilitated with LV-FRT control. If the voltage conditions at the grid end can be imitated at the WPP collector grid during events concerning faults, the WPP can actively participate and lower the active power production; eliminating the need of a common DC chopper. The occurrence of the grid end fault is indirectly communicated by the physical state of the HVDC voltage; hence no data signal is required to be transmitted. The excess of active power in an individual wind turbine system is either stored in the mechanical system (as inertia in the rotating mass of the rotor blades) or dissipated into the wind turbine DC link chopper resistor. The choice is determined the type of FRT strategy implemented in the wind turbine. However, even though a DC chopper is utilized to dissipate the excess of energy during the ride-through sequence, the amount of energy to be removed and the corresponding efforts in a single wind turbine is significantly lower compared to the total energy in a common DC chopper at the HVDC link. Detailed analysis and results are further presented in Chapter 6.

5.4 Negative Sequence Current Control

The control of negative sequence current to eliminate the DC voltage and active power ripple was discussed earlier in Chapter 4. The need for negative sequence control arises when the three phase voltages at the PCC are unbalanced. It has been mentioned earlier that the available room for negative sequence currents during asymmetrical voltages at the PCC maybe very small or mostly null based on the unbalance factor. The voltage unbalance is commonly measured by an unbalance factor, and the definition used in this work is,

$$u_u[\%] = \frac{v_n}{v_{p1}} \times 100 \tag{5.21}$$

Where v_n is the negative sequence voltage, v_{p1} is the nominal positive sequence voltage. It was discussed earlier that the available room for negative sequence current may be restricted in a HVDC system when the amount of active power transport is at the rated value. The range of negative sequence control can, however, be further increased given the following conditions,

1. If the WPP is producing lower than the rated power due to lower available wind velocity. This can be generally possible as wind turbines are rated at or higher than 12 $[m/s]$ wind velocity, while the average wind velocity in off-shore conditions is around 10 $[m/s]$ - based on the example of Horns Rev wind-farm of similar size considered in this work [11].

2. If the current rating of the VSC is increased. For a very large WPP, this condition may not provide enough economic advantage, but is definitely open to further detailed optimization.

3. If the active power export is reduced to create room for negative sequence current.

Small unbalance in three phase voltages ($u_u < 5$ [%]) in a power system is generally caused by unbalanced loads, uneven impedance in the transmission line etc. A more detailed assessment of voltage unbalance in a power system is presented in [80, 81]. Whereas, large unbalance in three phase voltages in a power system is generally caused by an asymmetrical fault (for e.g., single phase to ground fault). From the prospective of the VSC, it maybe more practical to avoid high peak-to-peak DC voltage oscillations and preserve system control stability under an unbalanced voltage situation. However, it may also be on the interest of the host power system to receive support with negative sequence currents to compensate the unbalance in the three phase voltages. In many cases, it is possible that the HVDC link is terminated in a part of a power system connected to one or more industrial plants with induction machines. The ability of a VSC-HVDC system to participate in the compensation of voltage unbalance could provide technical and economical benefits to the WPP owner or the grid operator or both.

If the unbalance factor is small, the level of negative sequence demand is also small and hence the current capability of the VSC maybe sufficient to export the necessary negative sequence current. On the other hand, if the unbalance factor is large, it becomes necessary to reduce active current export in order to make room for negative sequence currents. In this section it will be assumed that the grid requirements allow for the reduction in active power export during fault events. Based on these assumptions, four different negative sequence current control strategy will be analyzed in terms of DC voltage oscillation and AC voltage unbalance compensation; Case I: Zero negative sequence current control, Case II: DC voltage oscillation control, Case III: Negative sequence voltage compensation control, and Case IV: Negative sequence reactive current control.

Among the four strategies mentioned above, Case I and Case II have already been discussed earlier. The analysis of negative sequence voltage compensation (Case III) can follow directly from the inner current control equations of the grid side VSC.

$$0 = R_k \cdot i_{kdn}(t) + L_k \cdot \frac{di_{kdn}(t)}{dt} + \omega \cdot L_k \cdot i_{kqn}(t) + v_{dn}(t) \tag{5.22}$$

$$0 = R_k \cdot i_{kqn}(t) + L_k \cdot \frac{di_{kqn}(t)}{dt} - \omega \cdot L_k \cdot i_{kdn}(t) + v_{qn}(t) \tag{5.23}$$

During AC voltage unbalances, the VSC can be set to eliminate the negative sequence voltages from its terminals by exchanging an appropriate amount of negative sequence currents. It is possible to solve these equations for i_{kdn} and i_{kqn}, and use them as reference values for the negative sequence current control loop (i^r_{kdn}, i^r_{kqn}). To ensure the stability of the system, the AC voltage compensation control needs to be relatively slower than the inner current control. For this reason all the fast variations in the negative sequence voltage needs to be deliberately ignored (implementing a low pass filter), which further simplifies the above equations by justifying the elimination of the current derivatives. In most cases, it can also be verified that the resistance R_k is relatively very small and hence neglected.

$$i^r_{kqn} = \frac{-R_k i_{kdn} - v_{dn}}{\omega \cdot L_k} \tag{5.24}$$

$$i^r_{kdn} = \frac{R_k i_{kqn} + v_{qn}}{\omega \cdot L_k} \tag{5.25}$$

Implementing an open-loop control with the above derived current references in (5.24 & 5.25) for the negative sequence current control loop provides a simple control design. However, this requires that, (i) the equivalent impedance value between the converter terminals and the PCC point are accurately known, and (ii) the PCC is close to the VSC terminals. The level of voltage compensation with such an open-loop control is also somewhat restricted as the converter negative sequence voltage is maintained constant at zero. Nevertheless, a combination of open-loop control together with feed-back control (implementing PI regulators) can be used to improve and broaden the performance of the unbalance compensator. If the PCC is further away from the VSC terminals, feedback control of the PCC side negative sequence voltage will provide better accuracy. For the purpose of system evaluation and comparison in this work , the control philosophy implemented separately for $d-$ and $q-$ axis is as follows,

$$i^r_{kn} = G_c(v^r_n - v_n(n)) \tag{5.26}$$

Where, G_c is a function of error $\tilde{e} = (v^r_n - v_n(n))$ representing a PI controller. Finally, the last strategy (Case IV) with negative sequence reactive current control is simply a proportional gain applied to the negative sequence voltage error $\tilde{e} = (v^r_n - v_n(n))$. In this case the reference negative sequence active current (i^r_{dn}) is set to be zero and the reference negative sequence reactive current $i^r_{qn} = 5 \cdot \tilde{e}$.

To analyze the four different negative sequence current control structures, a negative sequence voltage dip or an unbalance factor of $u_u = 5$ [%] is applied to the grid voltage at $t = 0.98$ [s]. The simulated response of the three phase currents and the corresponding negative sequence voltage at the PCC for each control philosophy is illustrated in Fig. 5.17. The strength of the host power system $SCR = 5$ and $|Z_g| = 160$ [Ω] is applied to all the cases. The steady state active power transmission prior to the applied negative sequence voltage is 0.76 [pu].

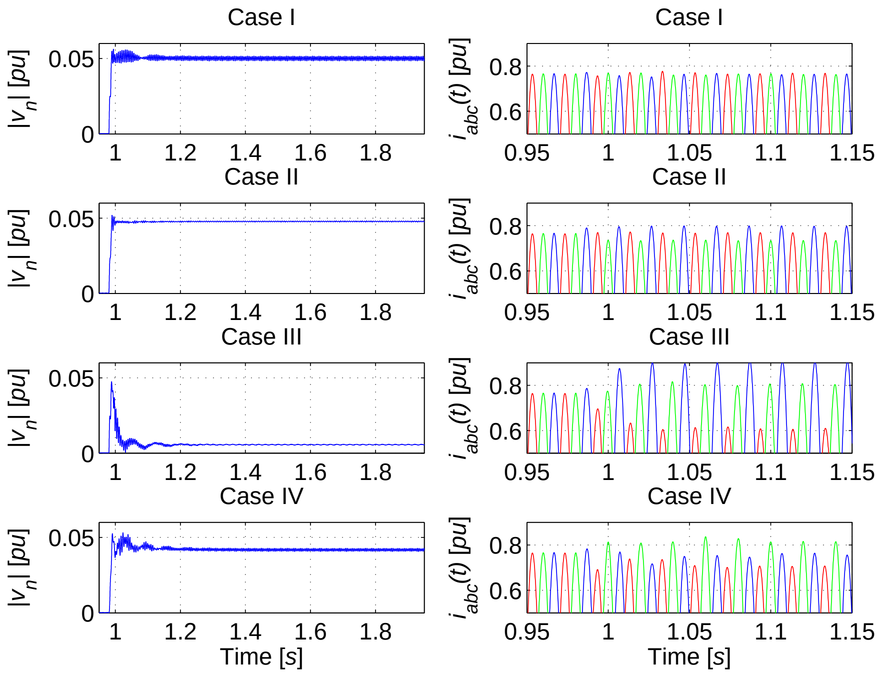

Figure 5.17: Comparison of different negative sequence current control strategies

In Table 5.2 numerical results of the comparison are presented, including peak-to-peak active power and peak-to-peak DC voltage ripples for each of the four control methods in percentage of the average value prior to the applied unbalance.

Table 5.2: Comparison results of different negative sequence current control strategies; $|v_n| = \sqrt{v_{dn}^2 + v_{qn}^2}$, $|i_n| = \sqrt{i_{dn}^2 + i_{qn}^2}$

	$\lvert v_n\rvert$ [pu]	$\lvert i_n\rvert$ [pu]	$\tilde{P}_g$ [%]	$\tilde{V}_{dc}$ [%]
Case I	0.05	≈ 0.0	± 5.04	± 0.345
Case II	0.0475	0.037	$\approx \pm 0.0$	$\approx \pm 0.0$
Case III	$5.65e-3$	0.175	± 23	± 1.56
Case IV	0.0417	0.064	± 11.6	± 0.83

Case I with zero negative sequence control - obviously does not provide any compensation to the the negative sequence voltage at the PCC. On the positive side, the three phase currents are balanced and the peak-to-peak ripple in both active power and DC voltage are relatively small compared to Case III and Case IV and also compared to a case with no negative sequence control. Therefore, it provides a perfect solution when there is no room for negative sequence current.

Case II with DC voltage oscillation control - is the best adapted control during network voltage unbalances. It provides no or a very small amount of negative sequence compensation of the voltage at the PCC. However, the DC voltage oscillation is removed and is best suited from the VSC point of view.

Case III with negative sequence voltage compensation control - provides a very good compensation to the negative sequence voltage at the PCC. However, this is achieved in the expense of higher negative sequence current and higher DC voltage and active power oscillation. It is evident that higher the strength of the host power system, higher will be the required negative sequence current (DC voltage ripple will increase accordingly) to compensate for the same amount of unbalance factor. On a positive note, it is illustrated that a HVDC transmission system is able to compensate for small voltage unbalances in a power system. In most of the European Union countries, the regulation to keep the unbalance factor below 2 [%] is imposed [82]. The maximum unbalance factor that can be compensated by a HVDC transmission system clearly depends upon the current limits of the VSC, maximum tolerable level of DC voltage peak-to-peak ripple and the strength of the host power system.

Case IV with negative sequence reactive current control - is suitable for large voltage unbalances or during asymmetrical faults. During an asymmetrical fault, the reactive current export from the VSC is usually based on the highest voltage among the three phases in order to avoid over-voltages. This means that the faulty phase is not compensated with any reactive current. Therefore, it might be an option to provide a negative sequence reactive current control during unbalanced faults. In this way, the problem of over-voltage is not just avoided but improved by drawing reactive current from the particular high voltage phase and at the same time considerable support is provided to the faulty phase(s). The applied negative sequence voltage gain can be fully based on the capacity of the VSC and the tolerable limit of the DC voltage oscillation.

Six

Wind Power Plant AC Voltage Control for Fault Handling

In this chapter a controlled voltage dip method applied at the WPP collector network to ride through grid side faults will be discussed. It is shown that the proposed control philosophy ensures a satisfactory response from the entire HVDC system including the WPP during various types of fault. Faults occurring at the WPP collector network are also discussed. Finally, hardware-in-the-loop test results of a full-scale wind turbine connected to a physical VSC representing a WPP side VSC of a HVDC system are presented.

LV-FRT is one of the most challenging requirements to fulfill, and more so in case of a long HVDC transmission system with one end connected to a WPP. A HVDC transmission system is composed of power electronic devices, whereas, the WPP collector grid is fully governed by power electronics (in the form of wind turbine VSCs and WPP side VSC). Unlike electrical machines, power electronic devices have very strict current and voltage limits. It is possible to extend the limits of the VSCs, but in the expense of added components and cost.

In this chapter the control of AC voltage (controlled voltage dip) at the WPP collector network in relation to LV-FRT will be presented. Many existing large WPPs are grid connected via HVAC transmission line. On demand from the grid requirements, most of the modern wind turbines have LV-FRT capabilities. The experience of riding-through low voltage faults is ever maturing within the wind turbine industry and the option to allow the same wind turbine type for different transmission options (HVAC or HVDC) would provide an enormous benefit.

6.1 WPP side AC voltage Control

Similar to frequency control, AC voltage control also requires a switch-over of HVDC voltage control between the two end VSCs after a fault is detected at the host power system. The main principle behind HVDC voltage control is to provide an energy balance between the sending end (WPP end) and the receiving end (grid end). When the active power export to the host power system is restricted, the task to provide energy balance in the HVDC transmission system is assigned to the WPP side VSC. The WPP side VSC executes a collector network AC voltage control philosophy (controlled voltage dip), hereby, reducing the total active power generation from the WPP. The control of AC voltage at the WPP directly follows a similar procedure that was discussed in Chapter 4 during the evaluation of HVDC voltage control method for the grid side VSC. A fundamental difference is in the fact that the grid side VSC is connected to a power system and is able to synchronize to the available three phase voltages at the PCC. The control of DC voltage is achieved directly by controlling the amount of active current exported to the connecting grid. However, in case of WPP side VSC, there are no synchronous generators or any synchronizing voltage sources available. It is the responsibility of the WPP side VSC to provide three phase synchronizing voltages to the entire WPP during normal operating conditions and also during the fault event if possible. Based on the fact that wind turbines are equipped with a full-scale back-to-back VSC system, they are capable of controlling active and reactive power as a function of available voltage at the collector network. As such, a WPP represent a current source and the response of the current source to the change in collector network voltage is very fast. A single line layout of the electrical system at the WPP is shown in Fig. 6.1.

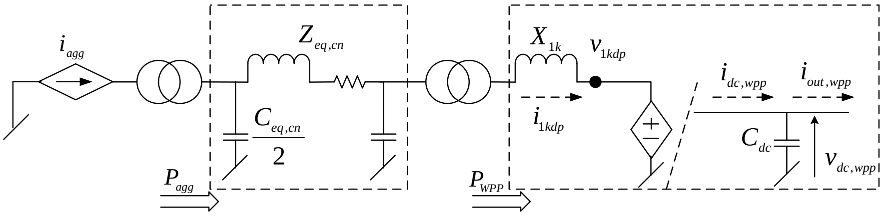

Figure 6.1: Single line representation of the WPP and the WPP side HVDC VSC

The main control objective is to provide a power balance between the collector network AC power and the HVDC side power during the fault event. If a sustained power balance is achieved during all conditions where the system needs to stay connected to the host power system , the magnitude of the HVDC voltage can be controlled within tolerable limits.

$$P_{wpp} = P_{dc,wpp} \tag{6.1}$$

The above expression neglects any losses in the WPP side VSC or the losses in the inductor, therefore the DC side current can be derived as,

$$i_{dc}(t) = \frac{3 \cdot \left(v^{r}_{1kdp}(t) \cdot i_{1kdp}(t) \right)}{2 \cdot v_{dc,wpp}(t)} \tag{6.2}$$

In eq. (6.2), current $i_{1kdp}(t)$ is given by the WPP. The collector network voltage is set by the WPP side VSC, so the AC voltage $v_{1kdp}(t)$ is also the reference value for the converter AC voltage controller. During the normal operating condition, the value of

$v_{1kdp}^{r}(t)$ is equal to its 1.0 $[pu]$ value or a value corresponding to optimized reactive power compensation of the WPP collector network. During a FRT, the WPP side VSC is assigned to control the collector network AC voltage and consequently the DC voltage at the HVDC transmission side. A properly implemented DC voltage control maintains the energy balance over the DC capacitor, and any imbalance will lead to an increase in the DC voltage level given by the expression below (refer Fig. 6.1).

$$i_{dc,wpp}(t) - i_{out,wpp}(t) = C_{dc} \cdot \frac{dv_{dc,wpp}(t)}{dt} \tag{6.3}$$

Integrating the above equation over the sampling period $n \cdot T_s$ to $(n+1) \cdot T_s$, the following expression can be derived,

$$i_{dc,wpp}(n) - i_{out,wpp}(n) = C_{dc} \cdot \frac{1}{T_s} \cdot \left(v_{dc,wpp}(n+1) - v_{dc,wpp}(n)\right) \tag{6.4}$$

$v_{dc}(n+1)$ is the DC voltage reference, $v_{dc}^{r}(n)$. Substituting eq. (6.2), the following expression can be derived.

$$\begin{aligned} v_{1kdp}^{r}(n) = {} & \frac{2}{3} \cdot \frac{v_{dc,wpp}(n)}{i_{1kdp}(n)} \cdot \frac{C_{dc}}{T_s} \cdot \left(v_{dc,wpp}^{r}(n) - v_{dc,wpp}(n)\right) \\ & + \frac{2}{3} \cdot \frac{v_{dc,wpp}(n)}{i_{1kdp}(n)} \cdot i_{out,wpp}(k) \end{aligned} \tag{6.5}$$

Therefore, the control of the WPP side VSC during a FRT event can be established based on the above expression. Compared to the response time of the HVDC voltage controller, the response time of the current control in wind turbines is relatively fast and, therefore, can be considered as ideal. The design of HVDC voltage control can follow standard procedure with plant transfer function given as $(C_{dc} \cdot T_s)/(z-1)$.

Apart from the main control philosophy, in order to allow the WPP side VSC to control the DC voltage, it is also necessary to ensure a smooth transition during the exchange of control between the two end VSCs. As no data communication between the WPP side and the grid side VSC is used due to the reasons involving delay and data reliability, the process of transition is fully based on DC voltage measurements at both ends of the transmission line. Following a grid side fault, the grid side VSC active power transfer can be restricted by the applied current limits. Beyond this point and until the fault is cleared, the grid side VSC will operate under current limit mode. This implies that the grid side VSC relinquishes the HVDC voltage control when operating under current limit mode. At the WPP end, wind turbines may continue to produce the same amount of active power as in the pre-fault. The difference in the active power will thus be stored in the HVDC capacitors (including VSC capacitors and cable capacitors) ultimately increasing the HVDC voltage level. The WPP side VSC control unit is assigned to monitor the HVDC voltage at all time. When the DC voltage level exceeds an upper threshold limit $v_{dc,uth} = 1.05$ [%] of the rated value, the WPP side VSC is set to take-over the control of HVDC voltage.

However, the levels of HVDC voltage at the two ends of a transmission line are not equal because of the long HVDC cable parameters as illustrated in Fig. 6.2. The grid end voltage can be predicted ($v_{dc,calc}$) at the WPP end from the known value of cable resistance and the measured WPP end DC current, $i_{dc,WPP}$. This is, however, only correct during steady state operating conditions, but following a disturbance, the predicted DC voltage is not equal to the actual value until a new steady state value is reached. This can be explained because the WPP side DC current cannot be used to predict the grid side DC voltage dynamics precisely. On the other hand, the grid side DC current values are unknown at the WPP end unless data communication is utilized. Therefore, one should pay careful attention that the grid side HVDC voltage does not exceed critical upper limit while the WPP side controller detects and reacts to the DC over-voltage. In this case it becomes necessary that the upper threshold limit, $v_{dc,uth}$, is carefully chosen. However, if the upper threshold level is too small, it may trigger a false FRT mode during other events or disturbances causing DC voltage change.

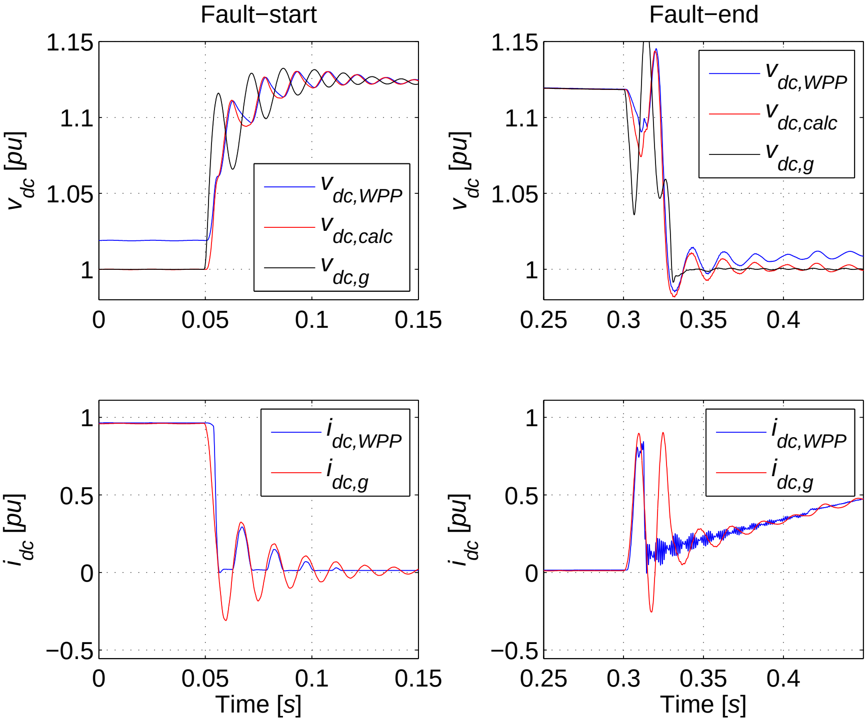

Figure 6.2: HVDC voltage and current level at different locations during grid side fault

As the grid fault is cleared, the grid side AC voltage starts to recover. The total reactive current export decreases, allowing more room for active current. During the fault, a large amount of energy is stored in the HVDC capacitors. The current limit mode of the grid side VSC is turned off only when the HVDC voltage jumps back to the rated value, $v_{dc.lth} = 1.0$ $[pu]$. Therefore, this allows for the energy stored in the capacitors to dissipate or the DC voltage to return back to the rated value as fast as possible by exporting momentary inrush active current out to the grid. The simulated response of the reference current and the actual current at the grid side VSC during a fault is shown in Fig. 6.3. Simultaneously, the decrease in HVDC voltage is also monitored from the WPP end, and the WPP end controller allows collector network AC voltage to increase back to its nominal value. This also causes a sudden momentary inrush of active power from the WPP to the HVDC link. Once the collector network AC voltage fully recovers, the wind turbine controller applies a ramp to the recovering active power, which is also followed by active power damping control in individual wind turbines. It is, therefore, verified that a smooth exchange of DC voltage control between the two end VSCs is possible based on the state of the DC voltage measured independently at each end.

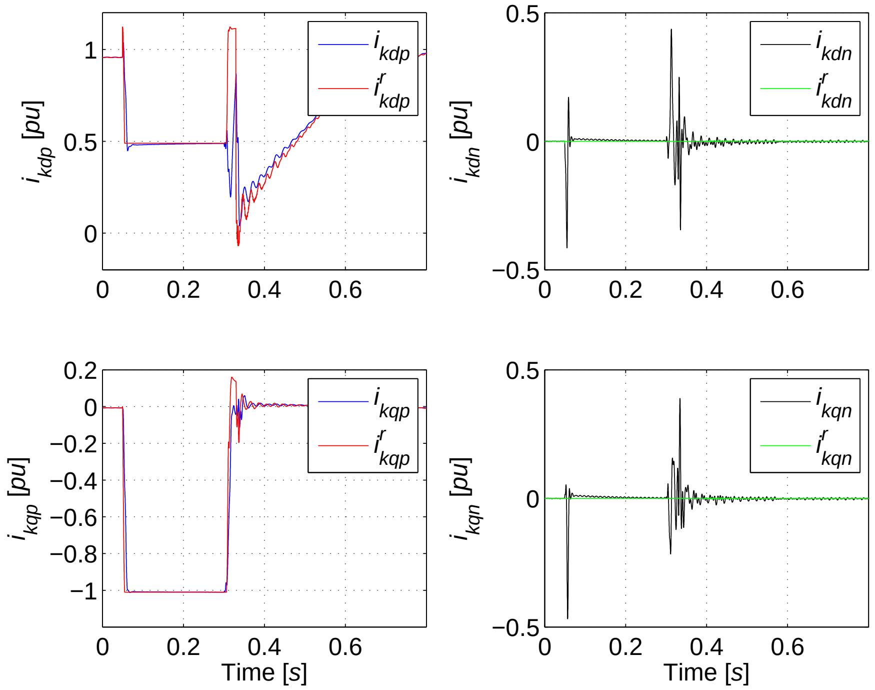

Figure 6.3: Grid side VSC current in dq rotating reference frame during fault

6.1.1 Balanced faults

In this section different balanced fault conditions at the main grid will be discussed.

Case I: Three Phase to Ground Fault

A three phase to ground fault close to the grid side VSC provides the most challenging requirements in terms of LV-FRT. In Case I, a complete three phase to ground at the HV side of the grid transformer is simulated. It is assumed that the fault is cleared after $\Delta t_{fault} = 250$ $[ms]$. The majority of the highlighted results are taken from the LV side of the grid transformer and the HV side of the WPP park transformer. A grid side transformer with a $X_{trans} = 12$ [%] impedance value is used in the simulation model. A SCR of 7 between the host power system and the WPP is used with $Z_g = 114.28$ $[\Omega]$ and $X/R = 7$. The wind velocity at the WPP is set to be $v_{wind} = 15$ $[m/s]$, which ensures that maximum power is delivered by the WPP. A situation with maximum power delivered by the WPP represents a worst case scenario for the FRT test. The simulated voltage response of the system is shown in Fig. 6.4.

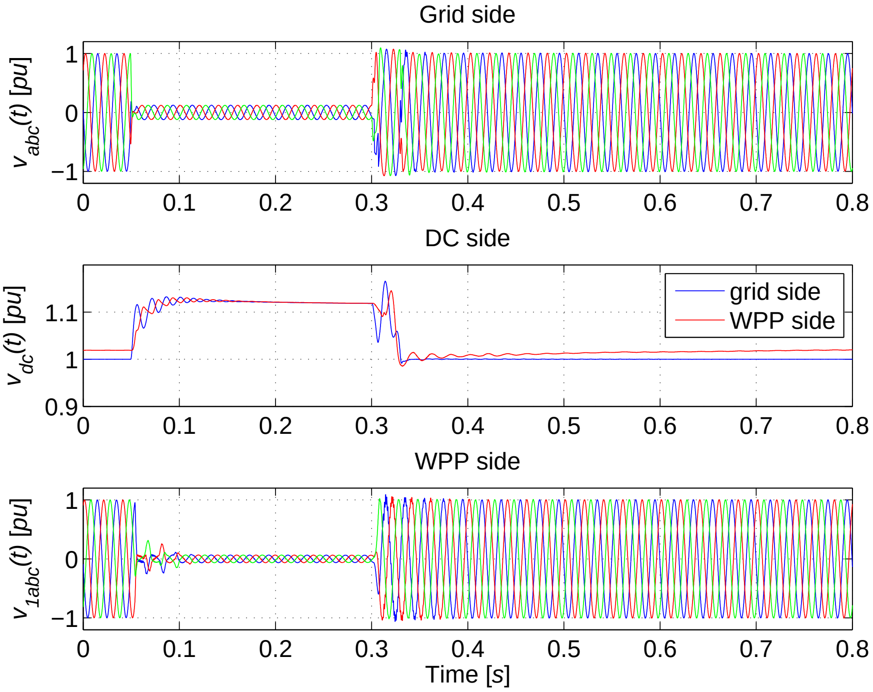

Figure 6.4: Simulated voltage response during a three-phase to ground fault

Following a grid side fault, the DC voltage control switch-over takes place to provide a controlled voltage dip at the collector network. The DC voltage reference during the fault is set to be $V^{r}_{dc,frt} = 1.05$ $[pu]$. However, it can be observed that the steady-state error between the measured and the reference DC voltage is not zero. When a complete short circuit occurs at the HV side of the grid transformer, the active power delivered to the grid is minimum, $P_g \approx 0.0$, as shown in Fig. 6.5a. The only available active power sink in the system is the system losses. Even though the active power produced by the WPP is zero, the HVDC voltage can not be fast adjusted to the reference value via the control system. When the fault is so severe, the WPP side VSC goes into the state of short-circuit or a very low AC voltage level (lower limit of the collector network AC voltage control). The total energy stored in the HVDC capacitors during the reaction time of the over-all controller (plus the time required to allow for the control switch-over) cannot be dissipated elsewhere except for the system losses, hence the DC voltage steady-state error is non-zero. However, as shown in the voltage HVDC plots, by carefully selecting a proper value of DC voltage upper threshold limit, $v_{dc,uth}$, it can be ensured that the HVDC voltage remains within a safe limit during a severe fault. It is assumed that the DC over-voltage trip-off limit of the the VSC-HVDC is $v_{dc,trip} = 1.2$ $[pu]$ or 20 [%] higher than the nominal value.

A slight difference in the DC side power plots, prior to the applied fault, between the grid side and the WPP side can be noticed in Fig. 6.5a. The difference is due to the losses in the transmission cables. During the FRT event when the active power transfer is reduced, there is no current flow in the DC side and hence the active power at both ends drop to a very small level. The excess of energy is stored in the rotating mass of the wind turbine. The model of full-scale wind turbine described in Chapter 4 is used in these simulations. As individual wind turbines actively participate in storing the excess of energy, there is no need for a centralized storage or power dissipation unit. The post fault active power recovery is also governed by the wind turbine controller.

The response of the wind turbine during the process of controlled voltage dip in the WPP collector network is illustrated in Fig. 6.7. The wind turbine RMS voltage, V_{wt}, is taken from LV side of the wind turbine transformer. As the wind turbine exports a large amount of reactive current during the controlled voltage dip created by the WPP side VSC, the level of wind turbine LV side voltage is relatively higher than the voltage dip introduced at the output of the WPP side VSC. The difference is determined by the total impedance in the collector network including the cable impedance and transformers impedances. The wind turbine transformer has a $X_{trans} = 6$ [%] impedance and the park transformer has a $X_{trans} = 12$ [%] impedance in the simulation model. The level of reactive current export is determined by the available voltage level at the wind turbine terminals. However, it is at all time ensured by the wind turbine VSC controller that the modulus of the total reference current is limited within 1.1 $[pu]$. Therefore, the WPP side VSC does not encounter any risk of over-current while its terminal voltage is lowered as illustrated in Fig. 6.6.

The wind turbine DC link voltage is not so much affected during the FRT sequence, as the excess of input power is stored in the mechanical system. After the dip is removed, the stored energy is slowly released which results in the wind turbine generator shaft oscillation. The oscillation in speed is also observed in the active power output plot. Nevertheless, it may also be an option to utilize the wind turbine DC link capacitor to store all or part of excess power. This may reduce the amount of mechanical stress on the wind turbine shaft and gear-box in particular during voltage dips, but on the other hand, the size of wind turbine DC link capacitor will increase. Alternatively, a DC chopper can also be used.

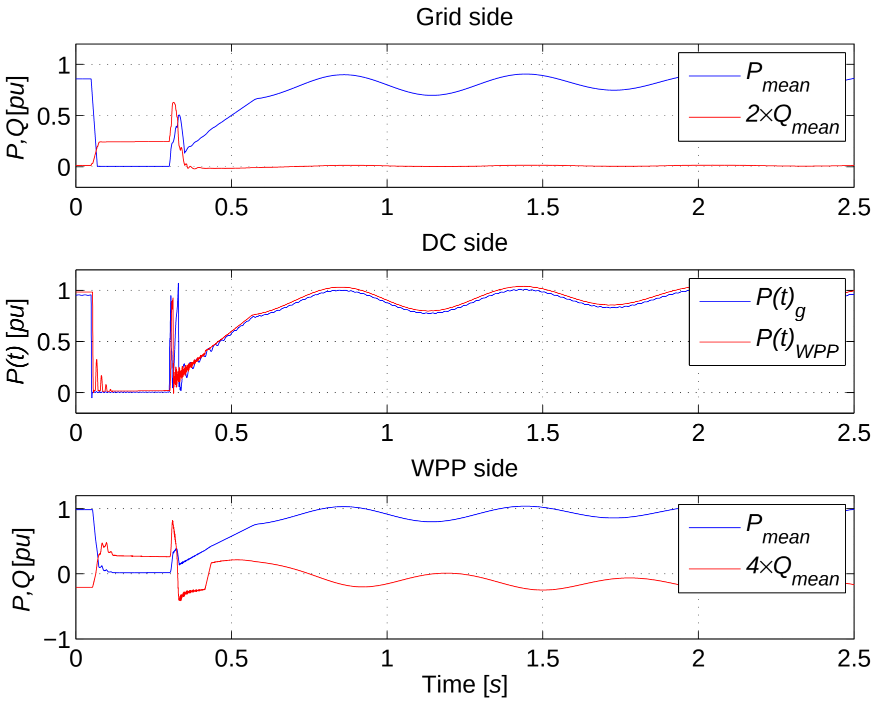

(a) Simulated power response

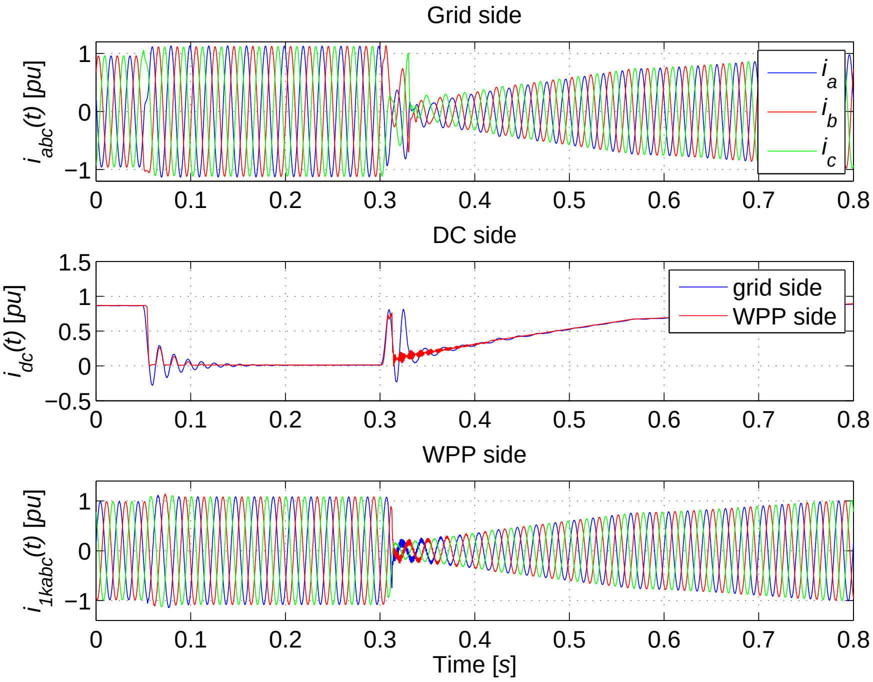

(b) Simulated current response

Figure 6.5: Simulated power and current response during a three-phase to ground fault

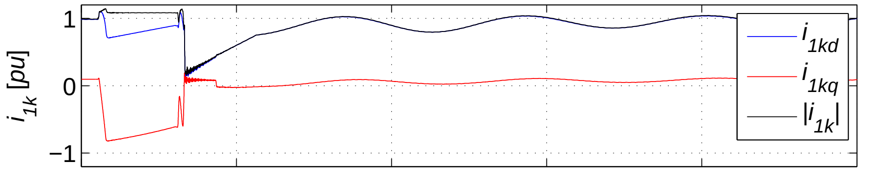

Figure 6.6: WPP side converter current in dq reference frame; $|i_{1k}| = \sqrt{i_{1kd}^2 + i_{1kq}^2}$

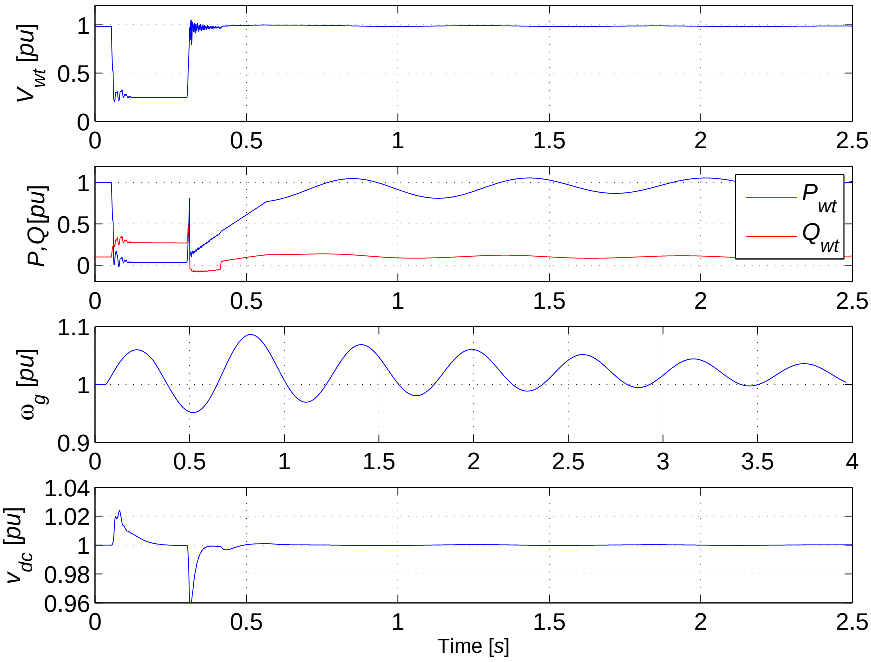

Figure 6.7: Simulated response from the wind turbine during a three-phase to ground fault

Case II: Multiple Voltage Dips

Multiple voltage dips or extended dips are also a common phenomenon in the power system and it is a requirement for the WPP to ride-through or stay connected temporarily. It is illustrated via simulation results that the presented control philosophy has the ability to control the HVDC voltage under such conditions.

In Fig. 6.8, a case with a complete three phase to ground ($v_{retain} \approx 0.0$ [pu]) followed by a voltage dip of ($v_{retain} = 0.6$ [pu]) at the HV side of the grid transformer is illustrated. After $\Delta t_{fault} = 200$ [ms], the three phase to ground fault is cleared but is followed by another voltage dip for $\Delta t_{fault} = 300$ [ms] immediately. Due to the follow-up dip, the grid side fault is not completely over. However, the retain voltage at the HV side is much higher after the three phase to ground fault is cleared. This creates some room for active power transfer towards the grid as the level of reactive current export to the grid is reduced. As a result, a sudden drop in DC voltage occurs at the grid side because the grid side VSC is still working under current limit mode (exporting maximum possible active current). The drop in DC voltage is also observed by the WPP side controller and as it is seen in the figure, the DC voltage is slowly pulled down to its reference value $V^r_{dc,frt}$ until the steady state error is zero. Unlike during a complete three phase to ground fault, it is now possible for the assigned controller to freely manipulate the DC voltage. The control of HVDC voltage is done by indirectly controlling the collector network AC voltage; the corresponding simulated response of the collector network AC voltage is as shown in Fig. 6.8a. It is also confirmed from the current response (not shown in the report), that the total current amplitude running through the WPP side VSC does not exceed beyond set limits of 1.1 [*pu*].

Case III: Response to Weak Grid Connection

The response of the collector network AC voltage controller applied to different grid strength ($SCR = 3,$ and 10) is illustrated in Fig. 6.9. It can be observed that the overall control of the HVDC voltage during the grid side fault is not so much affected by the strength of the host power system. However, some differences can be observed when the fault is cleared. A small difference can be noticed in the active and reactive power plots during the post fault recovery of the HVDC voltage. In case of a weak power system, the export of inrush active power to allow for the HVDC voltage to discharge quickly constrains the recovery of grid side AC voltage slightly. The only other major difference is seen on the dynamics of the AC voltage and reactive power after the fault is cleared. This is because - the weaker the host power system is, the more sensitive is the AC voltage at the PCC to the active power variation from the grid side VSC. For a very weak grid ($SCR < 3$) connection of a VSC-HVDC transmission system, all the grid side VSC controllers need to be less dependent on the stiffness of the voltage at the PCC and the control parameters tuned accordingly. Analysis of very weak grid connection is not included in this report. However, it is demonstrated that the implemented AC voltage control at the WPP collector network is capable of controlling the HVDC voltage and riding-through different levels of balanced faults in the grid irrespective to the strength (weak or strong) of the host power system.

6.1.2 Unbalanced faults

The most common type of faults in a power system is unbalanced in nature [83]. As with balanced faults, a VSC-HVDC connecting an off-shore WPP to a host power system needs to ride-through unbalanced faults. During an unbalanced fault, e.g., a line-to ground fault, the grid side VSC has to accommodate the imbalance in the PCC voltages and continue its operation at-least temporarily.

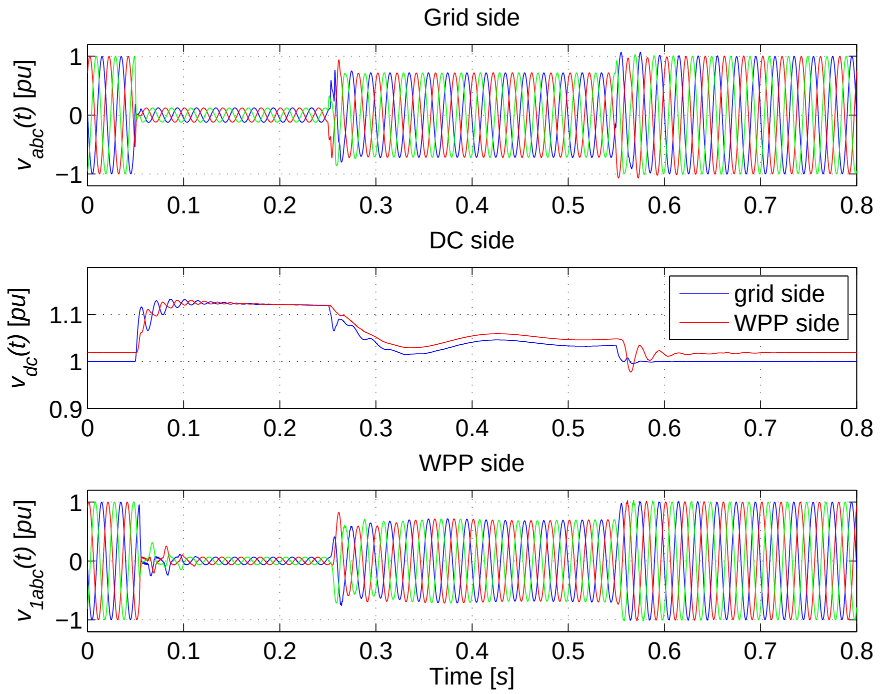

(a) Simulated voltage response

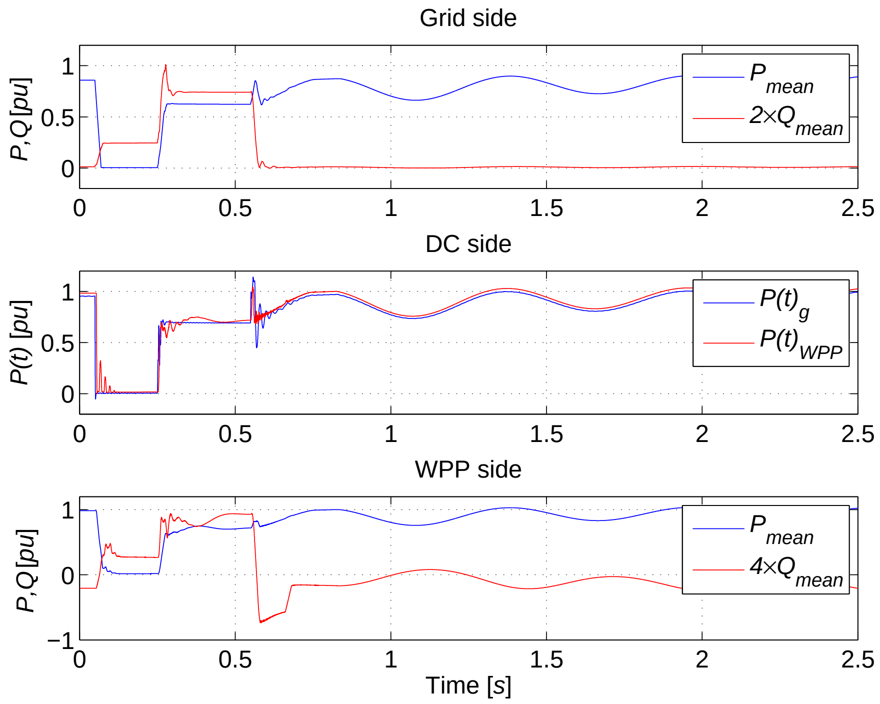

(b) Simulated power response

Figure 6.8: Simulated voltage and power response during a multiple voltage dip

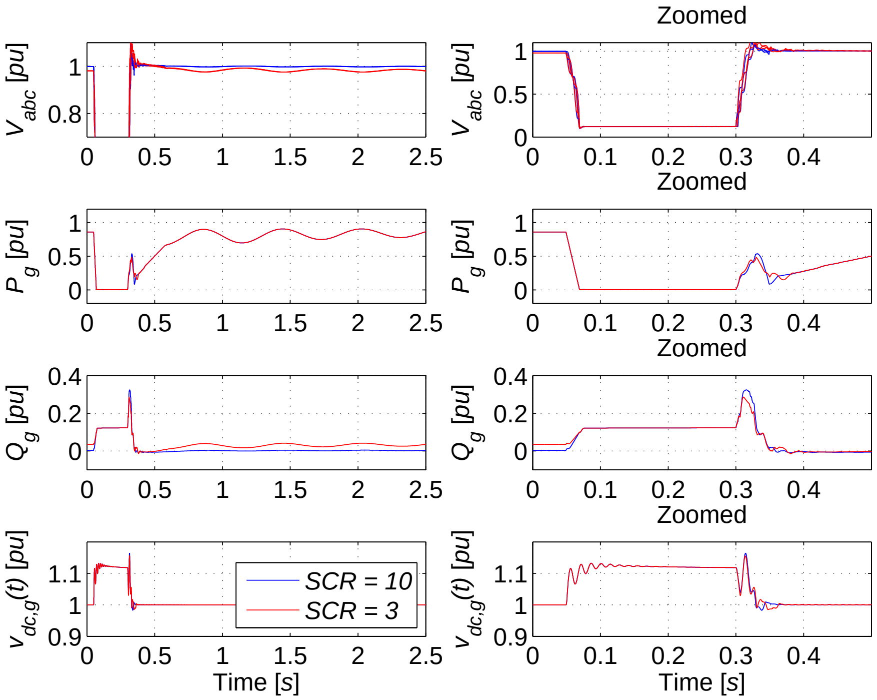

Figure 6.9: Simulated voltage and power response during a three-phase to ground fault for different grid strength

Provided that a sufficient room for the controlled negative sequence currents is available, the HVDC voltage can be set free from $2 \cdot f_m$ oscillation. In this situation, the control of HVDC voltage by the WPP side VSC provides no further added complications. Assuming that no room for controlled negative sequence current is available, the oscillation in the active power is directly reflected onto the HVDC voltage, because the AC side active power and DC power should equal each other except for the losses. Oscillating power in the DC side means that the voltage and the current also possess the $2 \cdot f_m$ ripple. Even though the HVDC transmission cables are long, some or part of these oscillations in the HVDC voltage and current are reflected at the WPP end. The control of DC voltage at the WPP end during a FRT mode requires both, DC voltage and current, as inputs. When such oscillating parameters are applied to the control equation (6.5), the resulting AC voltage peak reference (v_{1kd}^r) for the WPP side VSC is also oscillating. The transformation of this reference voltage into *abc* stationary reference frame will generate an unbalanced voltage in the collector grid. The full-scale wind turbine used in the simulation model is already equipped with negative sequence control or FRT capability during unbalanced faults. The WPP will, therefore, act accordingly by injecting balanced three phase currents, irrespective to the unbalance in the collector network AC voltage.

However, it has to be noted that a third order harmonic voltage will be super-imposed on the fundamental frequency voltage due to the transformation of oscillatory reference in *dq* rotating reference frame into *abc* stationary reference frame. Following the reference frame transformation, a 100 [*Hz*] signal with a DC offset gets resolved into 50 [*Hz*] fundamental plus a small fraction is resolved into 150 [*Hz*] harmonics. This is revealed by the Fourier transform of the resulting three phase voltage waveforms as shown in Fig. 6.10. The presence of such harmonics is only temporary or short lived during the period of FRT sequence time frame.

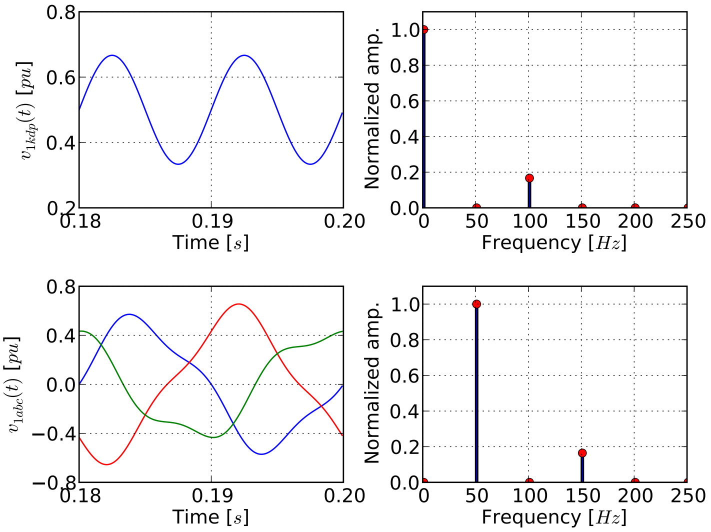

Figure 6.10: Harmonic presence in the WPP collector AC voltage during unbalance fault in the host power system

The simulated voltage response at different locations following a single line to ground fault at the HV side of the grid side transformer is illustrated in Fig. 6.11. A SCR of 7 between the host power system and the WPP is used, $Z_g = 114.28$ [Ω] and $X/R = 7$. The duration of fault is $\Delta t_{fault} = 250$ [ms]. The resulting AC voltage unbalance in the off-shore collector network is shown in the bottom plot of Fig. 6.11.

The simulated power and current response at different locations following the single line to ground fault at the HV side of the grid side transformer is shown in Fig. 6.12. As the collector network is unbalanced, the WPP side VSC draws an oscillating active power from the WPP. It shall be noticed that the unbalance factor of the three phase AC voltage at the collector network is relatively smaller than that at the grid end. This is because the peak-to-peak ripple on the DC voltage at the WPP end is reduced due to the long cable parameters. Therefore, the active power peak-to-peak ripple at the WPP end is relatively lower than at the grid end, however, the DC component of the active powers are equal except for the cable losses.

It is in practice possible to get rid of the third harmonics content at the WPP collector network by adding third harmonic compensation terms to the modulation

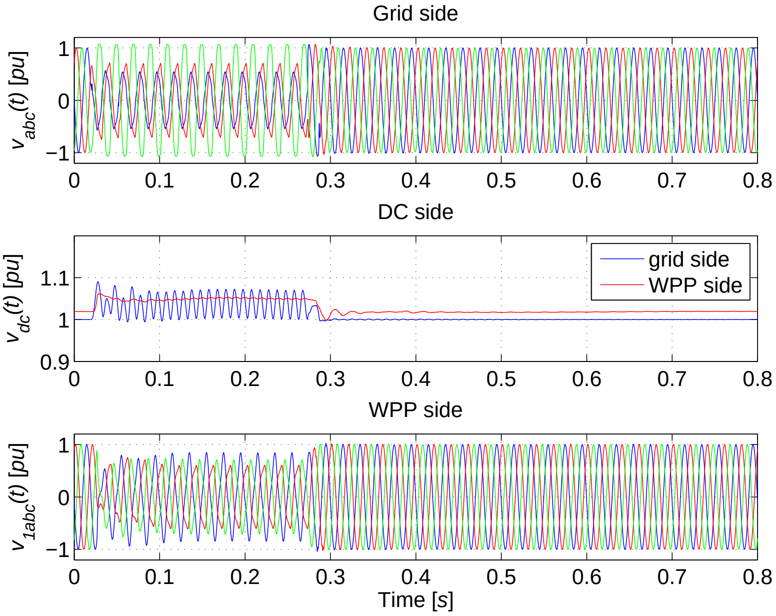

Figure 6.11: Simulated voltage response during a single line to ground fault

signals. Alternatively, a large gain drop at frequency $2 \cdot f_m$ (for e.g., a notch filter) can be directly applied to the collector network AC voltage control reference (v^r_{1kd}) or to the feed-forward terms $v_{dc,wpp}$ and $i_{out,wpp}$. If this condition is satisfied, the three phase voltages at the collector network can be considerably balanced. An ideal notch filter is practically not possible to achieve, therefore, a considerable drop in gain for a narrow band of frequency around $2 \cdot f_m$ will have to be accommodated. Therefore, one should also make sure that the important dynamics of the controller are not affected by the implemented filter response. The simulated voltage and power response of the system with notch filters applied to the feed-forward terms are shown in Fig. 6.13. As expected, the active power at the WPP end is considerably free from sinusoidal ripples, and at the same time, the WPP side AC voltage is also balanced. The HVDC voltage control is achieved because the DC component of the active power at the WPP end and the grid end are equal except for the losses. Although not shown in the report, the control of collector network AC voltage during other kind of unbalanced faults (double line to ground and line to line faults) were also confirmed from the simulation results.

6.1.3 WPP Side Faults

The most typical faults in an on-land transmission system are due to natural causes like falling of tree branches, conductor clashes due to wind or water, lightning strikes etc. These fault causes are almost irrelevant in the sub-marine cable systems but faults originating from other different technical causes can occur. On the other hand,

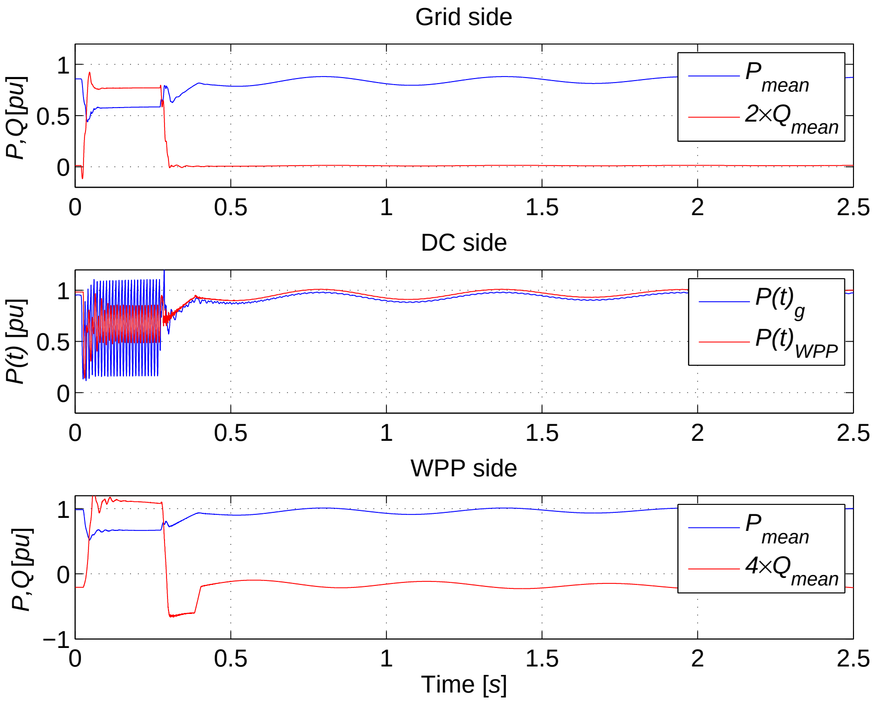

(a) Simulated power response

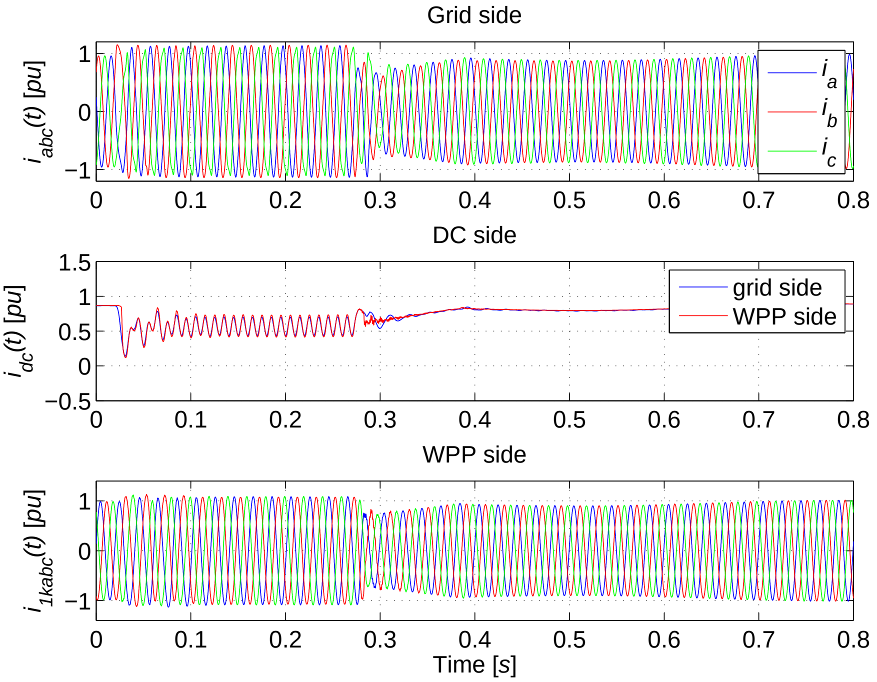

(b) Simulated current response

Figure 6.12: Simulated voltage and power response during a single line to ground fault

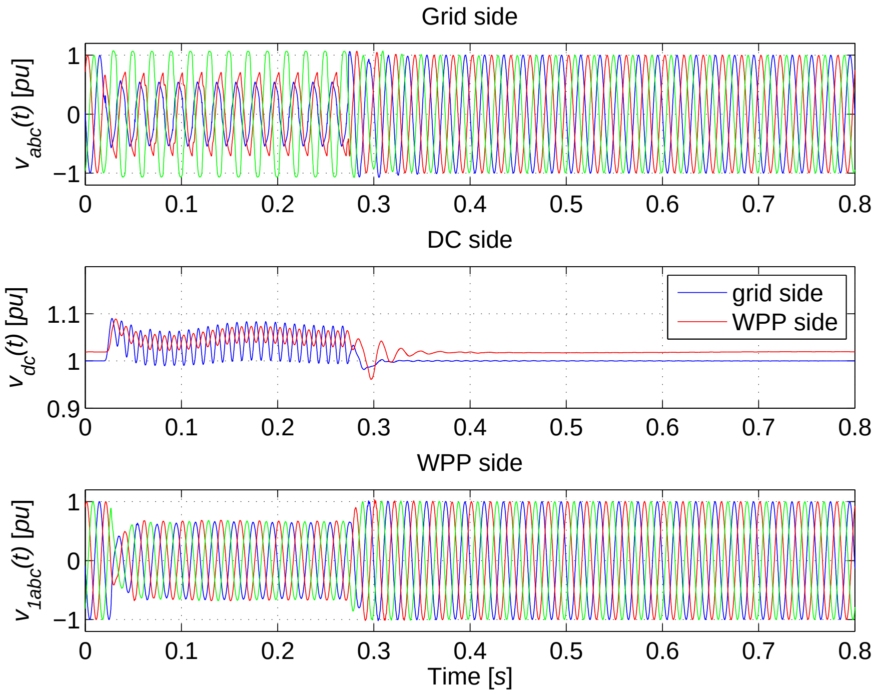

(a) Simulated voltage response

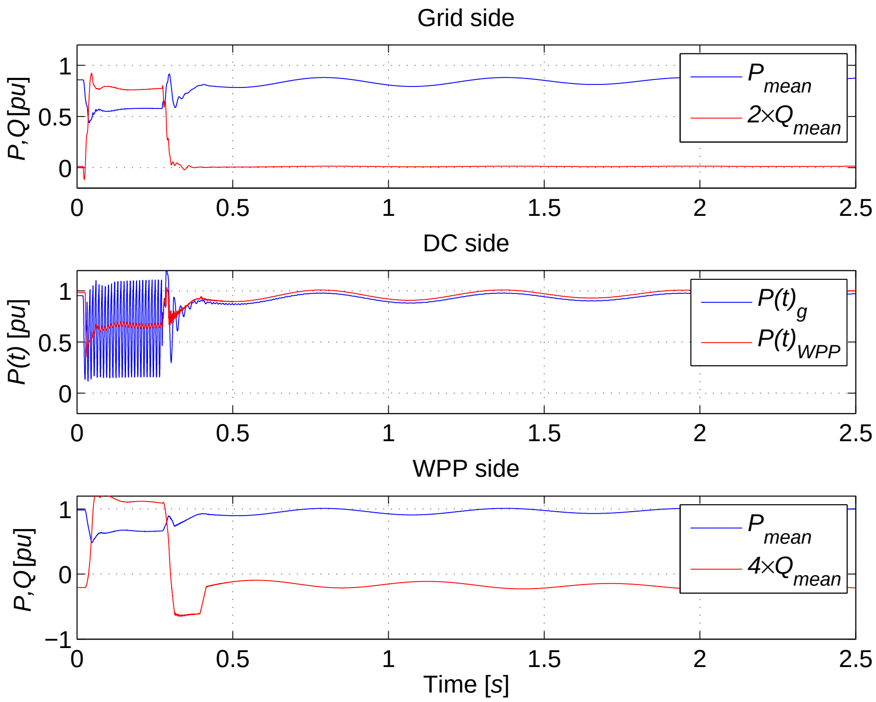

(b) Simulated power response

Figure 6.13: Simulated voltage and power response during a single line to ground fault at the grid end with notch filters applied

most of the faults in a stand-alone off-shore WPP will be difficult to clear. The system will have to eventually trip-off following a severe fault until the maintenance crew repairs the damage. However, some faults may be localized to an individual wind turbine or a single feeder (row in the collection grid) as shown in Fig. 6.14. In case of a very large WPP, there may be more than one park transformers, each allocated to a certain number of feeders. In such a situation, the particular feeder or the circuit consisting of the faulty transformer can be isolated from the WPP and the normal services may be resumed after a temporary disturbance.

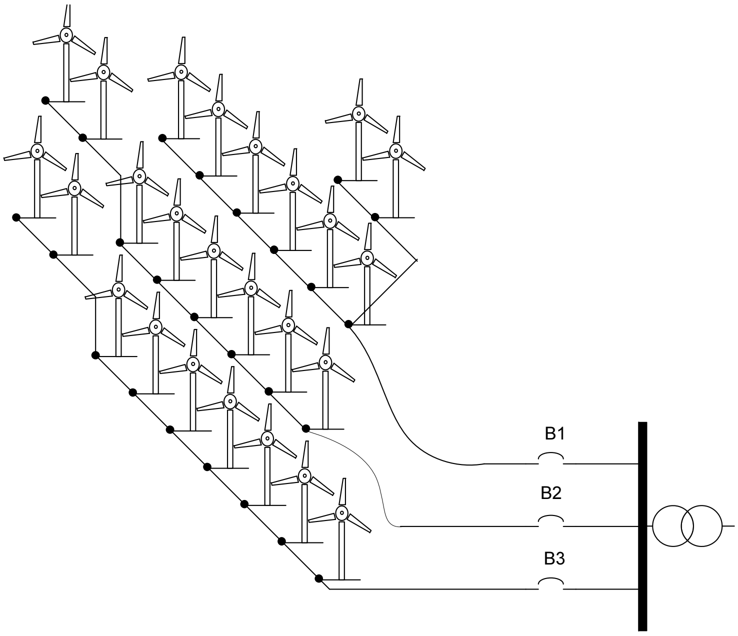

Figure 6.14: An example of off-shore WPP layout

When a fault occurs in the WPP area, the wind turbines respond to the collector network voltage dip by limiting the active current injection. This is one of the direct advantages of having an AC voltage control in the WPP collector network. But the WPP side VSC is not equipped with a direct current vector control. In such a situation, the WPP side VSC may be over-loaded with the fault current determined by, (i) the fault resistance, (ii) the equivalent system impedance between the WPP side VSC and location of the fault, and (iii) the WPP side VSC voltage level. To prevent the over-current, an indirect current control is implemented. The fault current can be limited by limiting the WPP VSC voltage - there always exists a minimum voltage level based on the equivalent system impedance which will ensure that the total current does not exceed safe limits. When the current through the WPP VSC exceeds the pre-defined upper threshold, the AC voltage limit mode is applied. The current feedback is derived from the three phase currents measured at the terminals of the WPP side VSC which can be transformed into dq reference frame. The VSC voltage is suddenly reduced to a level such that current from the WPP side VSC is restricted within its maximum limit (see Fig. 6.15). Provided that the fault is cleared by the timer set on the circuit breaker, the fault current will stop and the nominal voltage can be re-established.

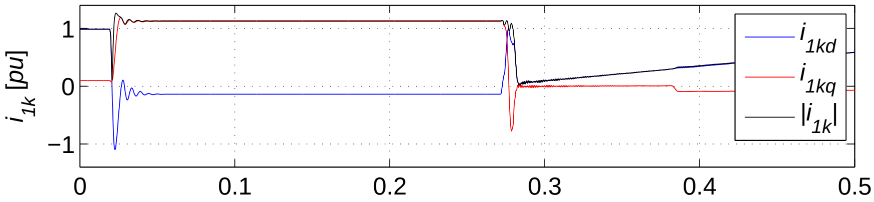

Figure 6.15: WPP side converter current in dq reference frame. A severe fault occurs at the LV side of the park transformer and the current is limited by the implemented voltage limit mode; $|i_{1k}| = \sqrt{i_{1kd}^2 + i_{1kq}^2}$

In Fig. 6.16 and Fig. 6.17 a case with a three phase fault at the WPP applied at the LV side of the park transformer is shown. The considered fault presents the most harsh fault situation in the WPP, which may or may not be possible to clear in the real world. However, to test the system response, it is assumed that the fault is cleared after $\Delta t_{fault} = 250$ [ms]. When the fault occurs, the WPP VSC starts to deliver the fault current. The voltage limit mode is set on so as to limit the current within safe limits by lowering the WPP VSC voltage level. During this sequence, the losses in the WPP VSC and the components within the location of the fault is delivered by the HVDC side, so the WPP side active power is slightly negative. As a result, a drop in the HVDC voltage can be observed. To maintain the HVDC voltage level, the grid end VSC is also required to send the active power in the opposite direction; compensating the losses in the converters and the HVDC cables. When the fault is cleared, the current through the WPP VSC decreases rapidly and as it drops below a pre-defined lower threshold, the nominal voltage is re-set.

It is, therefore, possible to indirectly imitate the voltage conditions at the PCC during fault events by the WPP side collector network such that the wind turbines can actively participate during the required FRT operations. This has been verified for all the fault cases that can occur in the main grid. Some major advantages of having such a control option during LV-FRT are summarized below.

1. The commercially available wind turbine topology (including the generator and the back-to-back VSC) and its control system do not require any modification or changes (including all the control systems) should they connect to an HVAC transmission system or a HVDC transmission system.

2. The system does not need to rely on data communication for cases like FRT control when very fast and reliable response is required. Rather, the communication of the fault is done via a physical signal (HVDC voltage level in this case).

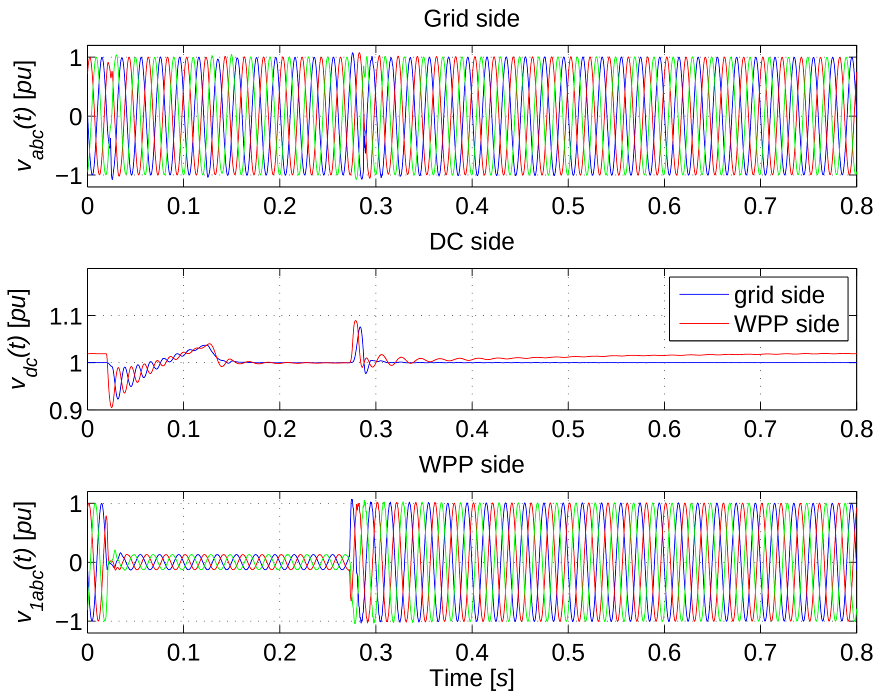

(a) Simulated voltage response

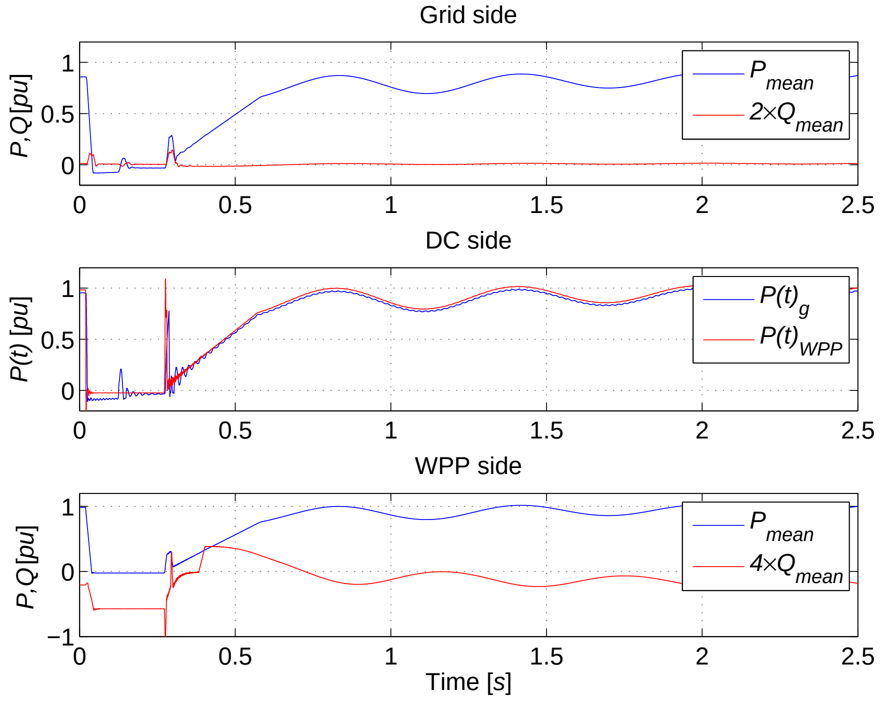

(b) Simulated power response

Figure 6.16: Simulated voltage and power response during a WPP collector network fault

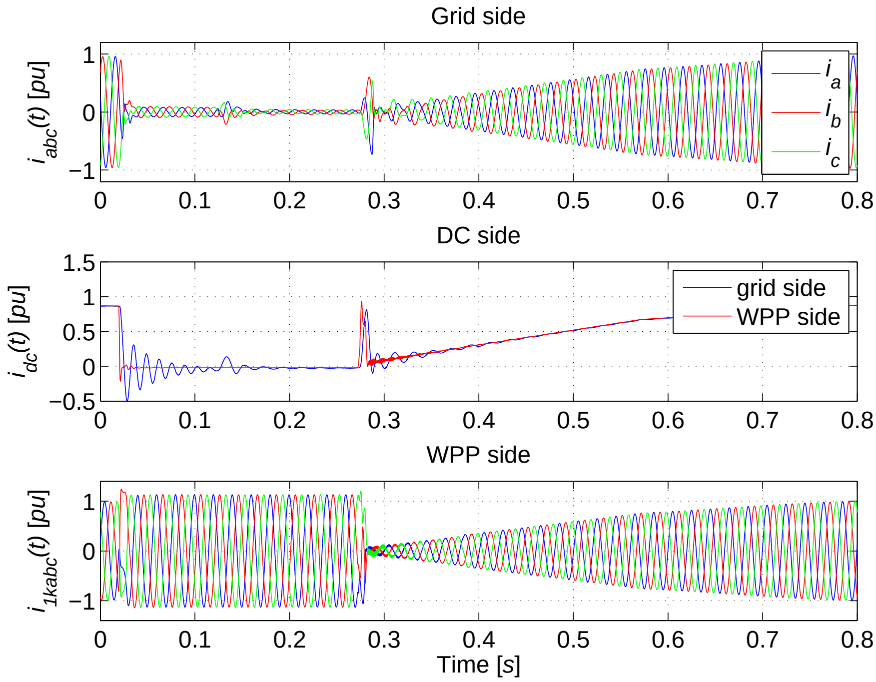

(a) Simulated voltage response

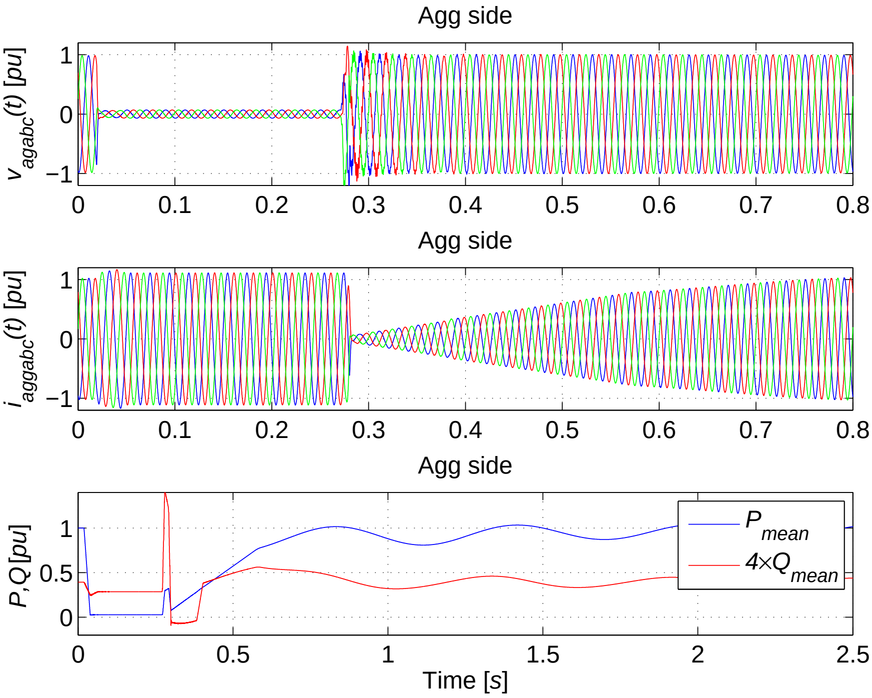

(b) Simulated voltage, current and power response at the Agg side

Figure 6.17: Simulated current response and the response from the aggregated WPP model during a WPP collector network fault

3. It is not necessary to implement two different detection and control techniques for the main grid fault and the WPP collector network fault. During both the cases, wind turbines in the WPP respond according to the change in voltage level in the AC collector grid.

Any faults occurring at the HVDC transmission cables are not included in this report. As with WPP side faults, the probability of fault occurrence in the HVDC transmission cables is very small and in most cases, it will not be possible to ride-through such faults and the HVDC system shut-down will be necessary.

6.2 Power-Hardware-in-The-Loop Test

HIL (hardware-in-the-loop) simulation is a technique used to understand the behavior of a new device, or to develop and test complex systems, or to predict an outcome under different system conditions. A HIL simulation often refers to a system in which part of a full simulation has been replaced with actual physical components [84, 85]. Based on the inter-connection method of actual physical components with the simulation part in HIL; HIL can generally be classified into two categories. CHIL (control-hardware-in-the-loop) simulation is a scenario where there is no power transfer to or from the hardware being tested, in contrast to the more challenging case in PHIL (power-hardware-in-the-loop) simulation, where the interface point involves conservation of energy so that real power is virtually exchanged between the simulation software and the actual hardware. Appropriate power amplification and conversion apparatuses must be included. The closed-loop PHIL of the device and the network model provides insight on both the performance of the control scheme as well as its effect on the power system. Hence, PHIL simulation is an effective method to test or verify the functionality of new control systems and different power components interactions [86, 87].

The WPP collector network, as discussed earlier, is fully governed by power electronic devices. Therefore, the interaction between WPP based on full-scale wind turbines and the WPP collector grid becomes increasingly important. For example, the WPP collector grid's dynamic response to transient events will be influenced by the VSC-HVDC link controls. Hence, the relevant influences on the VSC-HVDC and the WPP need to be carefully investigated. This section focuses at what can be considered a first step into the development of a PHIL system to test functions of control and operation of a VSC-HVDC transmission-link. In PHIL test setup the wind turbine and the AC collector grid is built in the RSCAD simulation program, modeling the full-scale wind turbines with correct aerodynamics, VSCs and control systems. A single wind turbine model is used to represent a WPP. The WPP side VSC-HVDC connection is represented by a down scaled two-level converter and the power termination is done through a DC chopper. The control algorithms of the VSC are coded and downloaded to a dedicated DSP/micro-controllers. This particular experiment contribute towards building an in-depth knowledge on the steady-state and dynamic behavior of WPPs connected through VSC-HVDC links, and in order to provide recommendation for future developments. A picture of the setup implemented during the project is shown in Fig. 6.18.

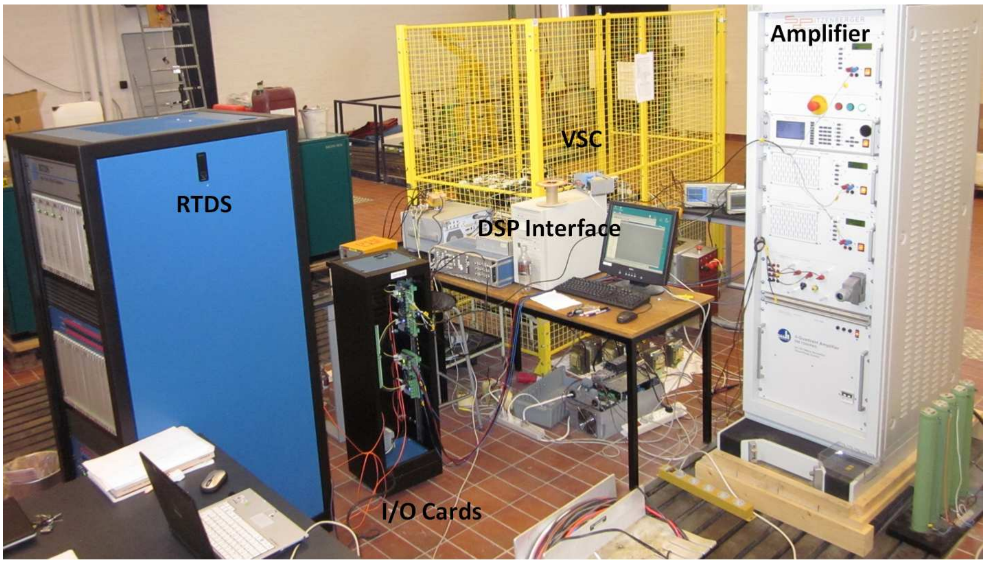

Figure 6.18: Picture showing the different components of the implemented PHIL test experiment

6.2.1 PHIL Implementation Setup

The block diagram of the experimental test setup that has been developed is shown in Fig. 6.19. The PHIL test platform is comprised of a RTDS (Real time digital simulator) [88], a Spitzenberger Spies three phase 7.5 $[kW]$ power amplifier [89] with frequency range from DC to 5 $[kHz]$ large signal bandwidth $(-3dB)$, a VSC and a DC chopper. The top half of the Fig. 6.19 presents the wind turbine model implemented in the RTDS platform and the bottom half represents the hardware setup. The communication between the RTDS and the external hardware components is done via input/output AD/DA cards. A slight time delay (around four time steps) in the system was observed between the input and the output signals, which has not been resolved during this work but has been taken into consideration for future improvement. A proper scaling factor is implemented in the simulation to accurately amplify the voltage magnitude to and from the external channels. The HV side of the wind turbine transformer is connected via an impedance to a controlled voltage source with rated voltage at 33 $[kV]$, a standard MV level at the WPP collector grid. The control signal for the voltage source is the input from the measurements done at the output bus (BH1) of the external VSC. The external VSC represents the WPP side VSC of a HVDC line.

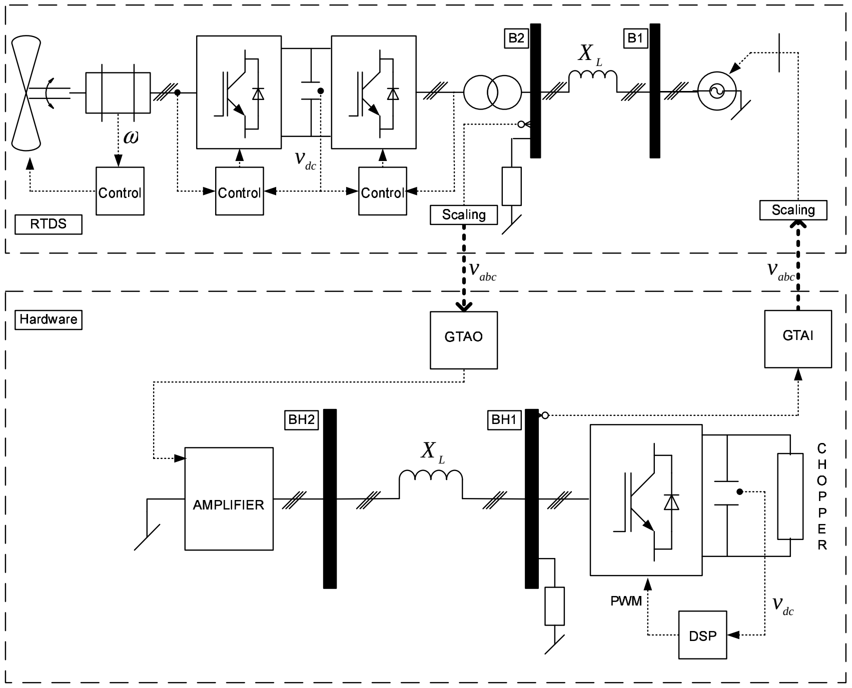

Figure 6.19: Block diagram of the PHIL test setup

The DC voltage of the external VSC is terminated through a DC chopper. The role of the DC chopper is to maintain a tolerably constant DC voltage. The DC chopper emulates the role of the grid end VSC (not to be confused for a HVDC chopper implemented for FRT) as it has not been possible at this time to implement a proper grid end VSC. For what is being evaluated, the use of the chopper to emulate the grid end VSC is fully justifiable because the DC chopper can maintain the DC voltage to a given value and the other responsibilities of the grid end VSC does not affect the DC side anyways. The DC voltage in the hardware is set at 500 $[V]$ and the AC voltage $V_0 = 300$ $[V]$. The rated power of the wind turbine model is $P_{wt,rated} = 2.5$ $[MW]$, therefore, by selecting an appropriate power rating for the external system $P_{hw,rated} = 2.0$ $[kVA]$ the per unit ratio between the impedance in the hardware and the model can be calculated. The value of the impedance in the model can be set to represent any given condition, for e.g. if the WPP is modeled as a single up-scaled wind turbine (aggregate WPP model), the impedance value can be calculated from the π equivalent model of the WPP collector grid.

6.2.2 Voltage Sourced Converter

The VSC in the setup representing the WPP end VSC is a two-level IGBT based converter with a switching frequency $f_s = 4.0$ $[kHz]$ and the switches are hard switched based on PWM signals. The AC terminals of the VSC is connected to a LC filter to eliminate the PWM generated harmonics ($L = 5.5$ $[mH]$, $C = 20$ $[\mu F]$ and $R = 1[\Omega]$ damping resistor in series with the capacitors). As explained earlier, the main function of the WPP end VSC of a HVDC transmission system is to maintain the AC voltage and frequency constant at the WPP. The constant frequency reference ($f = 50$ $[Hz]$) is generated via a virtual PLL in the controller. To maintain the AC voltage magnitude, a DC voltage feedback loop is implemented. The DC link of the VSC is initially energized directly from a three phase variable transformer and a diode bridge rectifier. For DC voltage below the rated value ($V_{dc} \leq V_{dc,rated} = 500$ $[V]$), the modulation index between the AC and the DC side of the VSC is maintained constant at $m = 0.98$. The modulation index is defined as the ratio between the mean value of the DC and peak value of the per phase AC voltage ($m = 2 \cdot \hat{v}_a / \overline{V}_{dc}$). When the WPP is connected, the flow of active power will cause some fluctuation on the DC voltage magnitude. Also the sending end voltage is slightly higher than the receiving end DC voltage due to the resistance along the transmission cable and the variation is determined by the amount of active power transmitted. In the implemented lab setup, a small variation in DC voltage is possible due to the hysteresis control action of the DC chopper. The DC voltage feedback loop thus compensates all these variations by constantly updating the required modulation index to achieve a fixed AC voltage magnitude.

$$v_a^r = m \cdot sin(\omega \cdot t) \tag{6.6}$$

$$v_b^r = m \cdot sin\left(\omega \cdot t + \frac{2 \cdot \pi}{3}\right) \tag{6.7}$$

$$v_c^r = m \cdot sin\left(\omega \cdot t + \frac{4 \cdot \pi}{3}\right) \tag{6.8}$$

This provides a simple and robust voltage regulation at the WPP AC collector grid. The response of the VSC during a DC voltage sweep from 1.0 *pu* to 1.1 *pu* is shown in Fig. 6.20. For a 10 % increase in the DC voltage, the AC RMS voltage is tolerably constant; ≈ 1.0 % change. The small change is observed because of the variation in the AC voltage harmonics (which is caused by the decrease in the modulation depth) as shown in the bottom two plot of Fig. 6.20. However, in reality DC voltage change of such high magnitude cannot be expected in a HVDC system under normal conditions. A slightly better response should be possible in case of a more precisely tuned filter.

6.2.3 Wind turbine model

The wind turbine model is prepared in a real time simulation platform, RTDS. The implemented wind turbine model includes the following; (i) the mechanical parts as rotor blades inertia and associated pitch control, (ii) a PMSG (Permanent magnet synchronous generator), (iii) a back-to-back VSC and the control system, (iv) a wind turbine transformer, (v) an AC side filter and (vi) a DC chopper at the DC link for LV-FRT. The system diagram of the wind turbine model is presented in Fig. 6.21.

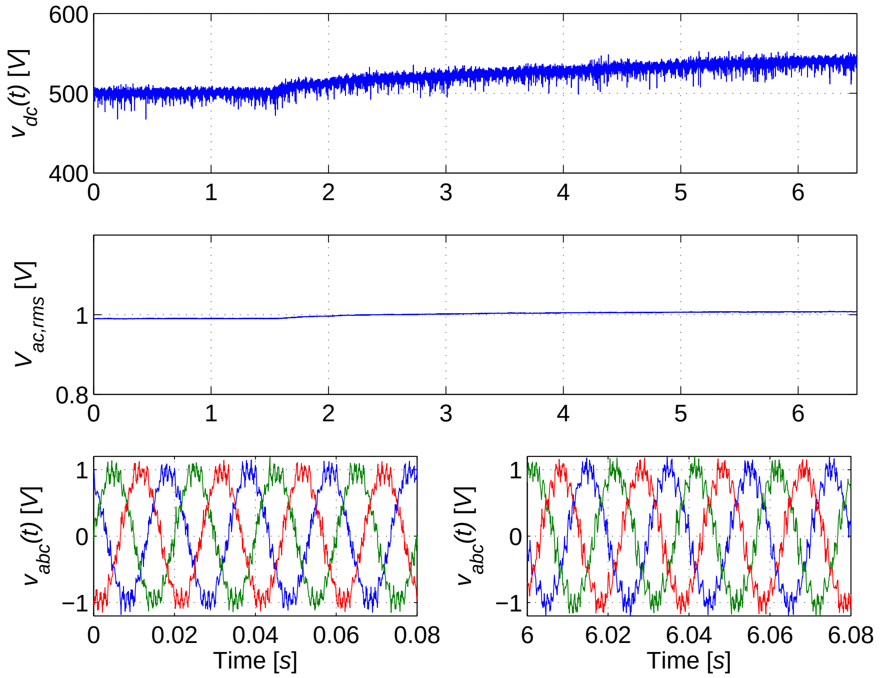

Figure 6.20: VSC response under DC Voltage sweep test

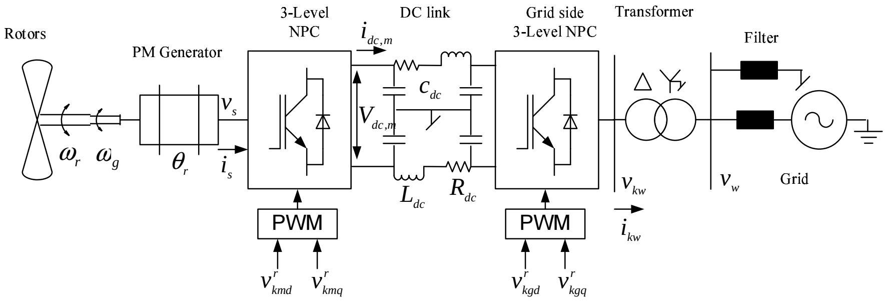

Figure 6.21: Wind turbine model diagram

The back-to-back VSC of a wind turbine and its control system can be divided into two parts, (i) the generator side VSC and its control, (ii) the grid side VSC and its control. A detailed discussion on variable speed direct drive PM wind turbine system can be found on [90–92]. The function of the generator side VSC is to optimize the generator speed to maintain the maximum power tracking. The control of rotor speed is achieved by controlling the stator currents in dq rotating reference frame. The signals that are controlled are the voltage references for the PWM modulation, v^r_{kmd} and v^r_{kmq}. A dynamic model of PM generator (without damper winding) in synchronously rotating rotor angle (θ_r) aligned reference frame is given by,

$$v_{sd} = -R_s \cdot i_{sd} - (L_s + L_{md}) \cdot \frac{di_{sd}}{dt} + (L_s + L_{mq}) \cdot \omega_e \cdot i_{sq} \tag{6.9}$$

$$v_{sq} = -R_s \cdot i_{sq} - (L_s + L_{mq}) \cdot \frac{di_{sq}}{dt} - (L_s + L_{md}) \cdot \omega_e \cdot i_{sd} + \omega_e \cdot \Psi \tag{6.10}$$

Where, R_s and L_s are the generator resistance and inductance, L_m is the mutual inductance, ω_r is the generator shaft speed, Ψ is the magnet flux. The control of stator current in q- axis is used to control the generator electromagnetic torque (τ_e), which ultimately controls the speed of the generator or rotor shaft. The control of $d-$ axis current is used to control the generator terminal voltage.

$$\tau_e = \frac{3}{2} \cdot p \cdot \Psi \cdot i_{sq} \tag{6.11}$$

Where, p is the number of poles. In order to achieve the speed control, an optimum rotor speed ($\omega_{r,opt}$) is derived based on the measured generator active power and maximum power point tracking characteristics of the wind turbine. A general block diagram of the generator side controller is shown in Fig. 6.22.

The function of the grid side VSC is to maintain the energy balance in the DC link by exchanging active power at the PCC and provide reactive power support. The general equations describing a grid side VSC in dq synchronously rotating reference frame aligned to the PCC voltage vector are,

$$v_{kwd} = v_{wd} + R_{trans} \cdot i_{kwd} - \omega_m \cdot L_{trans} \cdot i_{kwq} + L_{trans} \cdot \frac{di_{kwd}}{dt} \tag{6.12}$$

$$v_{kwq} = v_{wq} + R_{trans} \cdot i_{kwq} + \omega_m \cdot L_{trans} \cdot i_{kwd} + L_{trans} \cdot \frac{di_{kwq}}{dt} \tag{6.13}$$

Where, R_{trans} and L_{trans} are the transformer equivalent resistance and inductance respectively, ω_m is the AC voltage fundamental frequency. The active current control (i_d) is achieved by controlling the DC side voltage and the reactive current control (i_q) is achieved by controlling the AC voltage. As already discussed earlier, during the grid side VSC control of the HVDC transmission system, the VSC control reference frame is aligned to the voltage vector at the PCC by use of a PLL, which implies that $v_{wq} = 0$. The AC voltage at the collector grid is controlled by the WPP side HVDC VSC, so individual wind turbines do not apply direct AC voltage control mode to avoid any possible control interactions between the two control systems.

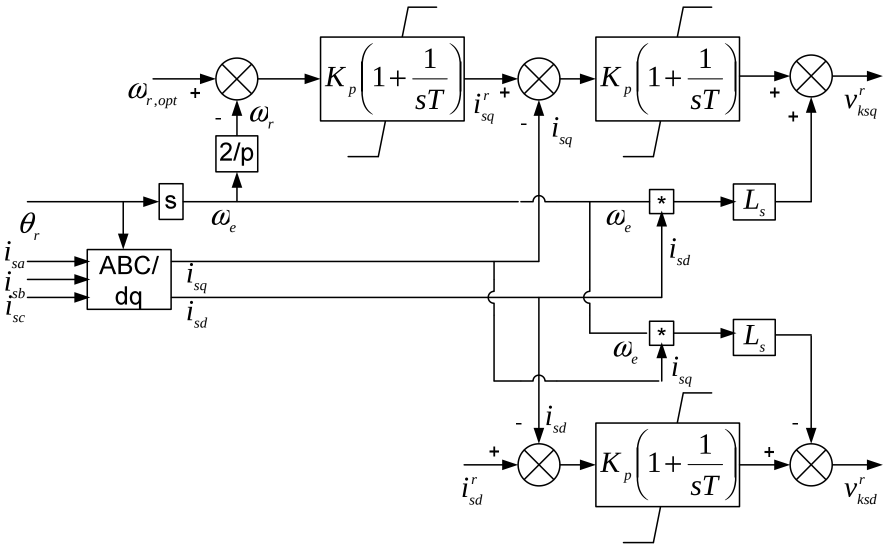

Figure 6.22: Generator side VSC control

Alternatively, a proportional AC voltage control is applied in the wind turbine grid side VSC. The grid side controller diagram in shown in Fig. 6.23.

$$e(t) = (v^r_{ac} - v_{wac}(t)) \tag{6.14}$$

$$i^r_{kwq} = k_v \cdot e(t) \tag{6.15}$$

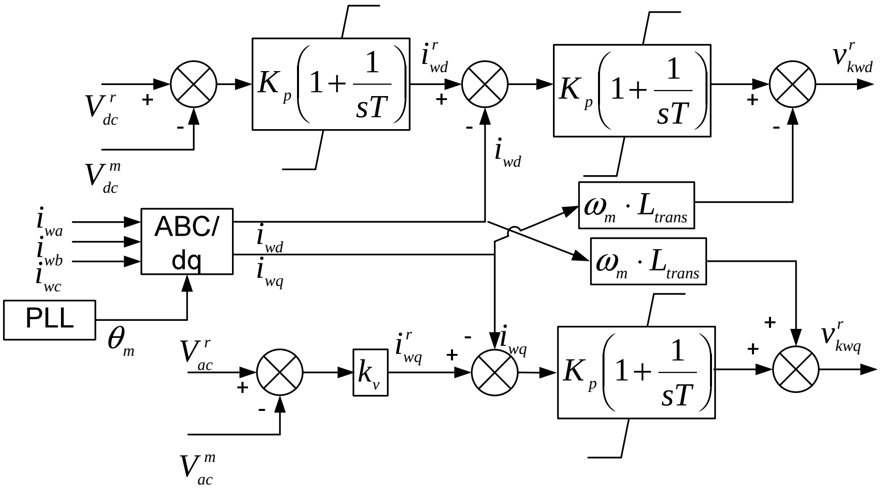

Figure 6.23: Grid side VSC control

To fulfill the criteria of wind turbine staying connected to the AC collector network during a fault event, a DC chopper is implemented. The excess of energy between the input power from the wind and the output electrical active power to the grid is slightly stored in the DC link capacitor and the rest is dissipated into the chopper resistor. Therefore, in this model the speed of the generator shaft remains relatively constant during the grid side voltage dip events as no power is stored in the rotating mass of the rotor blades. The current limit of the wind turbine VSC is applied in two parts; (i) 1.1 [pu] during voltage dips or faults, (ii) 1.2 [pu] during normal voltage conditions. Some major parameters of the wind turbine model are listed in Table 6.1.

Table 6.1: Wind turbine parameters

	Parameters		Parameters
S_{nom}	2.5 [MVA]	f_m	50 [Hz]
V_{dc}	6.8 [kV]	V_0	4 [kV]
f_g	3.82 [Hz]	X_{ls}	0.1 [pu]
R_s	0.01 [pu]	X_{md}	1 [pu]
X_{mq}	0.65 [pu]	H_g	4 [s]
Ψ	1.2 [pu]		

6.2.4 Results and Discussion

In this section some major test results are presented, specifically the co-ordination between the WPP end VSC of the HVDC system and the wind turbine. Before connecting the wind turbine model prepared in the real time simulator to the external hardware requires an orderly start-up procedure. The experimental setup start-up procedure is listed below.

1. The DC side of the VSC is energized to a nominal DC voltage level directly from a 400 [V] AC grid via a transformer and a three phase diode rectifier.

2. Once the DC side is energized, the DC chopper and the VSC gate pulses are unblocked. However, the upper threshold level of the DC chopper is set slightly higher than the nominal DC voltage level. Therefore, the DC chopper is not activated until the wind turbine amplifier starts to deliver active power to the VSC.

3. The AC side output breaker of the VSC is closed and the three phase AC voltages appear across the capacitors of the VSC LC filter at the terminals. The magnitude of the output AC voltage is determined by the implemented modulation index.

4. The three phase voltages across the filter capacitors are measured via a voltage measurement board, which applies an amplification gain such that the peak voltage measurement is less than 10 [V]. The maximum voltage that the I/O cards can handle is ± 10 [V].

5. The voltage measurements are fed to the wind turbine model in RTDS with appropriate scaling factor via GTAI (analogue input) card. These signals constantly update (every 50 [μs]) the controlled voltage source representing the WPP side VSC in the model. The nominal voltage level of the controlled voltage source is 33 [kV].

6. The voltage measurements at the output terminal of the wind turbine at bus B2 (Fig. 6.19) are fed to the the amplifier input channels after applying proper scaling factor via GTAO (analogue output) card.

7. The wind turbine model in RTDS is initiated.

Consequently, the controller of the grid side VSC of the wind turbine synchronizes to the available voltage at the PCC. The exchange of active and reactive power is determined by the applied wind velocity and the amplitude of the AC voltage at the PCC. In the main hardware loop, the power amplifier emulates the wind turbine response and delivers the scaled down active and reactive power to the VSC. In the simulation model the controlled voltage source emulates the HVDC WPP side VSC. Any reactions from the VSC are immediately communicated to the simulation model in real time.

The wind turbine model and the experimental setup is first run until a steady state condition is maintained (completing the wind turbine start-up process). Before the first run, it is necessary that the model is properly initialized. The DC capacitors are initialized to the nominal DC voltage level, the generator speed at 1 [pu] and the turbine blades running freely with no electromagnetic torque applied from the generator. As the wind turbine is connected to the AC network, the exchange of active power takes place. The speed of the generator slightly reduces because of the applied electromagnetic torque. The generator shaft speed, active power and reactive power slowly build up to a steady state value determined by the maximum power tracking characteristics of the wind turbine system and the voltage level at the PCC. A satisfactory operation of the system at the steady state is verified. The active and reactive power during the start-up is illustrated in Fig. 6.24.

In order to verify a well coordinated response during AC voltage dip situations, the control system of the WPP end VSC is triggered into FRT mode, such that the VSC responds by lowering its retain voltage level. Two different voltage retain levels were evaluated at $v_{retain} = 0.5$ [pu] and $v_{retain} = 0.2$ [pu] with $\Delta t_{fault} = 150$ ms. The voltage and current response of the system at the HV side of the wind turbine transformer are shown in Fig. 6.25a. After the fault is detected, the wind turbine control limits the exchange of active power while the reactive power is determined by the level of voltage dip. The limitation of the active current is given by the following expression, except that a peak surge current can be observed immediately after the fault is detected.

$$i_{kwd} = \sqrt{i_{lim,wt}^2 - i_{kwq}^2} \tag{6.16}$$

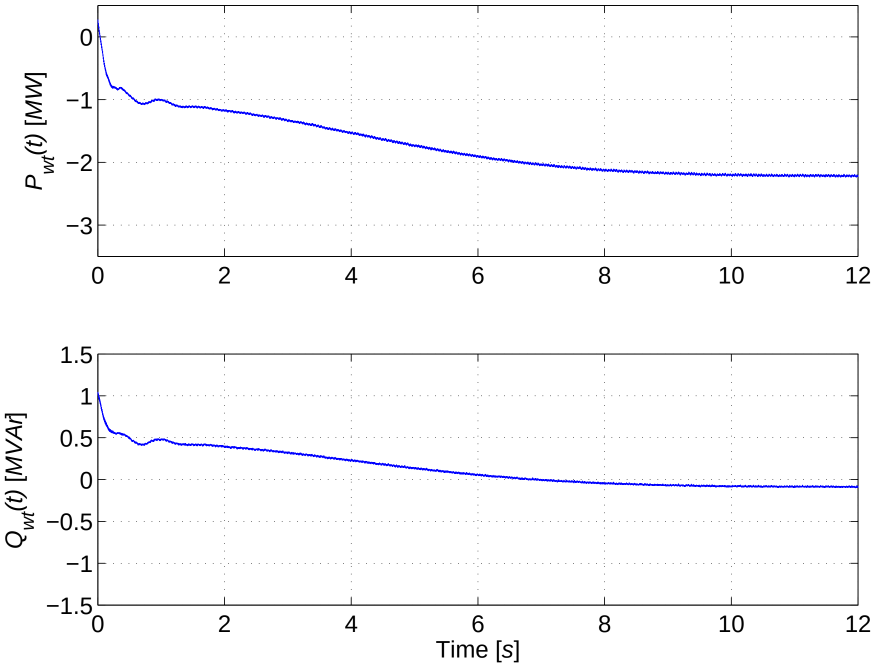

Figure 6.24: Start-up sequence of the wind turbine

After the fault is detected, the modulus of the reference current limit is applied at $|i_{lim,wt}| = \sqrt{i_{kwd}^2 + i_{kwq}^2} = 1.1$ $[pu]$. Apart from the reference current limitation and control philosophy, a low-level hardware protection is always implemented on a VSC to protect the switching devices from excessive over-current, which is often activated when the high level protection fails to control the current. However, the peak surge current (half sine-wave) carrying capacity for $t_{surge} < 10$ $[ms]$ of general IGBTs are much higher than the nominal current capacity. Therefore, the current spike seen in the plots will neither affect the wind turbine VSC nor the WPP side VSC nor will it trigger the low level hardware protection.

The active and reactive power outputs from the wind turbine are shown in Fig. 6.25b for the two different voltage dip levels. The convention used is such that the direction of active and reactive power from the wind turbine towards the collector grid is taken as negative. The difference in the active power between the generator side VSC and the grid end VSC is slightly stored in the DC link capacitor and mainly dissipated in the chopper resistor. When the voltage dip is cleared, the active power from the generator end VSC plus the energy stored in the DC capacitor is suddenly released in to the collector grid. What is implemented in this work is a very harsh power recovery condition for the wind turbine and collector network during the post fault period. In many cases, it is common to implement a soft power recovery by utilizing a power slope (dP/dt) or gradient. This implies that the total energy dissipated by the DC chopper will slightly increase, but the sudden jump in the active power output and the DC voltage can be eliminated, ensuring a very smooth AC voltage recovery after fault.

The total active power delivered by the power amplifier measured at the hardware side at steady state prior to the applied voltage dip is $P_{wt,hw} \approx 1.8$ $[kW]$. A comparison of currents measured in the simulation and in the external experiment during the applied voltage dip of $v_{retain} = 0.5$ $[pu]$ is presented in Fig. 6.26. It can be observed that the simulated currents show a good agreement with the measured currents during the steady state condition. However, the amplitude of the measured currents in the external setup is slightly higher during the transient and voltage dip situations. It was also briefly mentioned earlier that a delay of four sampling time is introduced between the voltage measurements at the output of the external VSC and the voltage references that is sent to the power amplifier. During the steady state operation, the effect of the delay will simply reduce the voltage angle between the power amplifier output and the external VSC terminal as compared to the voltage angle between the wind turbine terminal and the controlled voltage source in the real time simulation. The effect of this reduced voltage angle can be compensated or re-adjusted by manipulating the size of the external inductance between the two end voltages in the external setup. However, the voltage angle will be in a relatively dynamic state (adjusted by the implemented current control of the wind turbine VSC) during a voltage dip situation, the system delay cannot be compensated (or is very complicate to compensate) and the resulting currents in the external system is different from what is desired. The main purpose of the experiment is to study the co-ordination between the wind turbine VSC and the external VSC when physically connected to each other. This has been, nevertheless, achieved within a fairly reasonable accuracy despite some differences from the delay.

The response of the DC voltage during the introduced voltage dip is shown in Fig. 6.27. Once the AC voltage recovers, the DC voltage is controlled back to the nominal value and as such the wind turbine is able to provide a FRT response during the grid side voltage dips. As a DC chopper is implemented in this work, the mechanical side of the wind turbine remains relatively undisturbed during the disturbance and hence the mechanical oscillation and time constants are not observed in the power curve. This is also verified from the speed plot in Fig.6.27. Only a small insignificant change in the generator speed can be noticed which is due to the sudden slump in the DC voltage level as seen in the DC voltage plot, otherwise the mechanical side remains unaffected.

The results presented above provide a positive overall picture on this first step of development. These results confirm a good co-ordination between the wind turbine and the WPP side VSC. The response from the wind turbine is very identical to the situation when it is connected to a strong AC super grid, as the WPP side VSC is able to provide a stable voltage regulation at the collector network. The performance of the wind turbine and the external VSC was as expected. In an all, two different full-scale wind turbine systems were tested. The simulation results presented earlier was based on full-scale wind turbines with induction generator while the results presented from the experimental work is based on direct drive full-scale wind turbines with

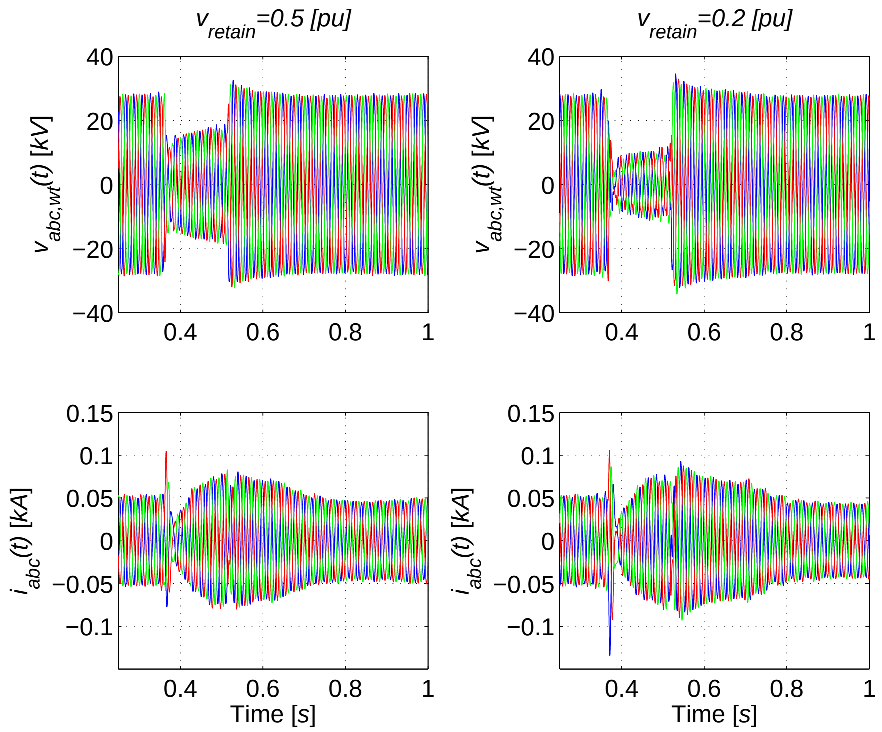

(a) Voltage and current at the HV side of the wind turbine transformer

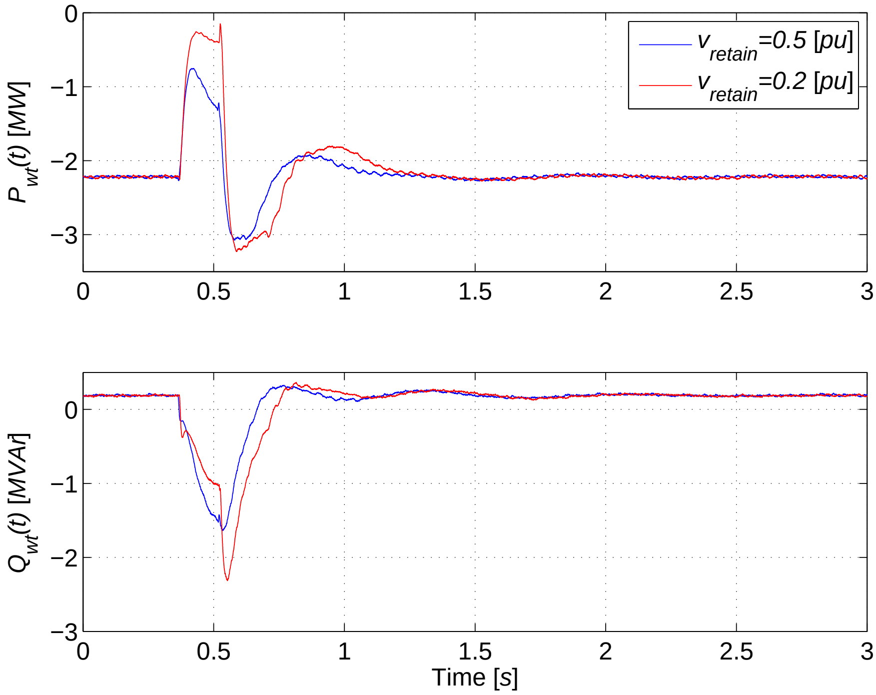

(b) Active and reactive power exchange from the wind turbine

Figure 6.25: Response from the wind turbine during applied voltage dips

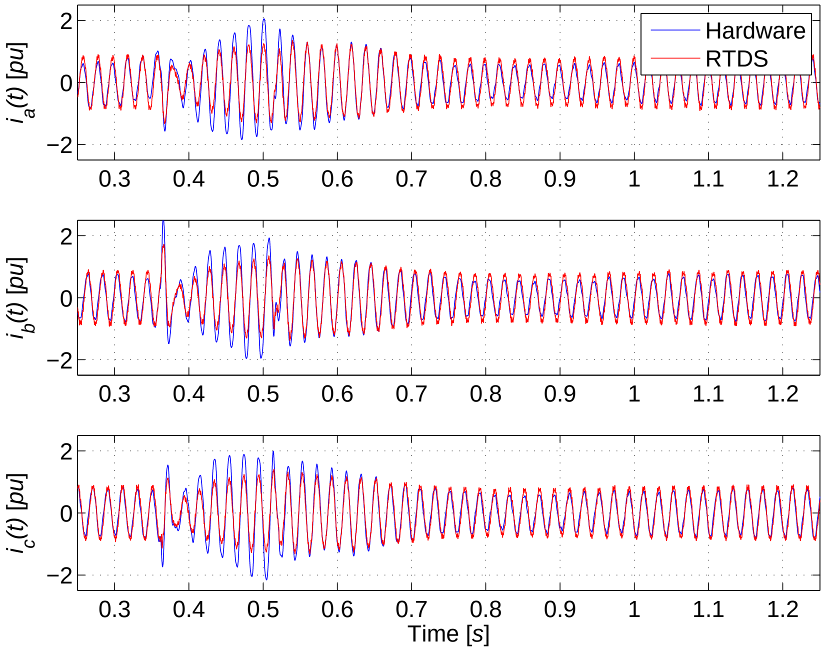

Figure 6.26: Comparison of currents measured at the HV side of the transformer in the simulation model and the output of the amplifier in the external hardware

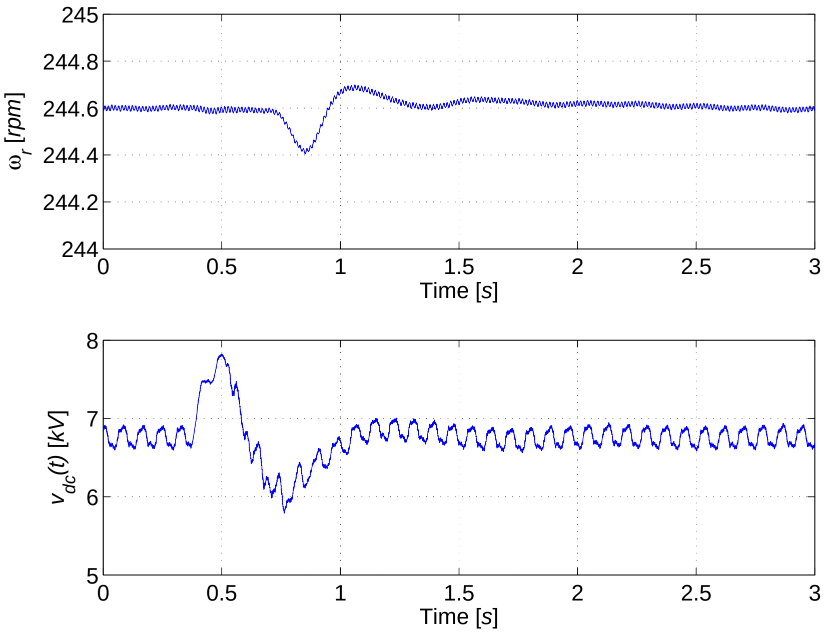

Figure 6.27: Wind turbine generator speed and DC link voltage, $v_{retain} = 0.2\ pu$

PM generator. There were also two different FRT schemes implemented in the two separate wind turbine models. One of them utilized a DC chopper and the other used mechanical inertia as power storage during voltage dips. Therefore, among all the presently available full-scale wind turbine systems, the concept of controlled voltage dip at the collector network to ride through grid side faults has been verified.

Seven

Conclusion

The work reported in this dissertation can be divided into three main parts. The first part was mainly focused on the comparison of different power transmission solutions for an off-shore WPP including HVAC transmission, HVDC transmission with MVAC collector network and HVDC transmission with MVDC collector network. The second part was focused on the development of a dynamic simulation model including a proper WPP model, VSC and its control, cables and all other components required for a HVDC transmission system. In the last part, different control solutions were discussed and results were presented to verify how the implemented control would allow for the HVDC system to meet different grid code requirements. A partial solution was also tested and verified in the laboratory.

7.1 Summary of the Work

The global wind power generation is experiencing a rapid growth. With the growing size of wind turbines and the total installed capacity of the WPPs, it is a trend now and for the future to locate them in the off-shore conditions. As the transmission distance increases, so does the efforts required to transport the bulk power to the near-by power system. Until recently, the power transmission is done via HVAC sub-marine sea cables. However, cables have higher capacitance per unit length. All cables have a limit current carrying capacity. The surplus of reactive power due to cable charging, therefore, reduces the total active power transmission capability of a HVAC cable system. On the other hand, the charging current also adds to the total losses in the system. It is verified in the report that the total system losses become more and more significant with the increase in transmission length as the losses in the cables completely dominate. For a medium sized WPP, the main limitation is imposed by the current capacity of the cables and not by the voltage angle or the transmission mid point voltage rise.

In comparison, a HVDC transmission system does not have any limitations over the transmission distance. There are two different types of HVDC transmission system discussed in the report. One of them is composed of MVAC collector network and the other with MVDC collector network. A detailed comparison of total system losses between the HVAC system and the two HVDC systems are presented. It is illustrated that for a medium sized WPP, HVAC solution obviously provides a more efficient system for short distances below 90 [km]. However, the efficiency of a HVAC system deteriorates much faster for distances longer than 100 [km], and the corresponding HVDC transmission system provides a better solution. Among the two HVDC systems studied in this work, there is very little difference in terms of losses comparison. The VSC used for a HVDC system is based on MMC topology whereas the DC-DC converter is based on a full-bridge topology. The main advantage of a DC collector network is the reduced size and weight of the transformer in the off-shore sub-station and the wind turbine. This is because a standard 50 [Hz] transformer can be replaced by a MF transformer of the DC-DC converter. On the other hand, the main component of a DC collector network, which is a DC-DC converter, is not fully tested for such high power applications. Most importantly, DC circuit breakers for such applications are not totally convincing. With due consideration to these issues, it is safe to assume that WPPs in the near future will adopt AC collector network and, therefore, a system as such is investigated in more detail.

In order to study various dynamic behavior of a HVDC transmission system connecting a WPP, a dynamic simulation model is developed. The model includes wind turbine, collector network, transformers, VSCs, cables and other major components of the system. The performance of the system under normal operating condition is first analyzed. At the WPP collector network the total reactive power requirement is optimally divided between the wind turbines and the WPP side VSC. The WPP side VSC is assigned to operate as an infinite bus. This way the control system of the WPP side VSC can be designed with minimum complexity. The current limit at the collector network is provided by the wind turbine (collector network side VSC) control system. The grid side VSC of the HVDC system is set to control the HVDC voltage and hereby provide energy balance to the system. The grid side VSC has the ability to control the AC voltage at the PCC independently. Unlike HVAC transmission, the reactive current need not be transported the entire transmission length. The requirements of frequency control of the main grid are fulfilled by use of a telecommunication signal. The frequency measurement at the PCC is communicated to the WPP side VSC. As the WPP is an isolated system the choice of frequency at the WPP is solely determined by the WPP side VSC. The high level park controller can be used to detect the change in frequency and adopt a frequency droop control. A new power reference is then communicated to individual wind turbines.

The most challenging requirements, however, is related to LV-FRT. Different FRT options are investigated in this report. The first option includes frequency control at the collector network. This option is considered very suitable to be used with fixed speed wind turbines. As a fault occur at the grid side, the HVDC voltage level increases. Based on the detected HVDC over-voltage at the WPP end, the WPP side VSC is set to take over the DC voltage control while the gird side VSC enters current limit mode. The difference between the measured DC voltage and an allocated reference value is used as an error signal to allow the control of the collector network frequency. The wind turbines based on induction generators respond by decreasing the output active power. A well co-ordinated performance during the fault event was observed. However, it was also observed that the immediate post fault response from the wind turbine is rather difficult to control and that leads to considerable over current requirement for the WPP side VSC.

A commonly discussed option for LV-FRT is to implement a DC chopper in order to dissipate the excess of power during a fault event. However, the required size of DC chopper and the efforts to remove the heat is enormous. Therefore, an indirect control method to imitate the grid side voltage dip at the WPP side collector network based on full-scale wind turbines is derived and investigated in this report. Based on the measured HVDC voltage rise at the WPP end, the collector network AC voltage is reduced in a controlled way. The full-scale wind turbines installed in the WPP are already equipped with low voltage FRT capability. Therefore, the excess of energy during grid end faults are stored in the rotating mass of the wind turbine blades and there is no need for power dissipation. Although not investigated in this report, the proposed control structure can also be applied to doubly fed induction generator based wind turbines. Any fault at the collector network is also dealt in the same way. The only difference is that an additional current limit mode is required for the WPP side VSC to protect itself against fault current. This is achieved by implementing a voltage magnitude control. Therefore, no separate detection and control option is required for faults occurring at the grid end or the WPP end. This provides a big advantage of being able to use a similar wind turbine regardless of HVAC or HVDC transmission system.

Finally an experimental setup is prepared to test and validate a proper co-ordination between the WPP side VSC and a full-scale wind turbine. In the experimental setup, the wind turbine model is prepared in RTDS and the simulated terminal voltages of the wind turbine are amplified by a power amplifier. Therefore, the power amplifier acts as a wind turbine and is connected to a VSC. The VSC is controlled to setup a required AC voltage magnitude and frequency at its terminal. It is verified that the response of the wind turbine and the WPP side VSC during controlled voltage dip is as predicted and no unexpected behaviors were recorded. The electrical structure and control of future off-shore WPPs are analyzed in this report.

7.1.1 List of Major Findings

1. Based on the present scenario, HVDC transmission system with MVAC collector network provides most efficient solution for long distance power transmission system from an off-shore WPP.

2. By directly immitating grid side frequency condition at the collector network, known components and control can be applied at the WPP level (for example park pilot control for different frequency control requirements).

3. Reactive power compensation of the MVAC collector network can be optimally distributed among the HVDC WPP side VSC and individual wind turbines.

4. Besides the regular control schemes, the grid side VSC of a HVDC link can be used to provide negative sequence control. However, any concrete answers in relation to negative sequence control does not exist yet as they would be more determined by the grid code requirements. Some suggestions are outlined,

   a) HVDC VSC can be used to provide full negative sequence voltage compensation for small unbalances ($v_n \leq 5\%$), depending upon different system parameters.

   b) For large unbalances or unbalanced faults, a constant negative sequence reactive current reference can be applied to provide reactive current support to the faulty phases. The range of negative sequence current reference may also depend upon different system parameters, especially the current limit of the VSC.

5. Controlled AC voltage immitation (without telecommunicaiton) at the collector network provides the best solution to ride-through grid side low voltage faults. This way the collector network side faults need not be treated any differently and the existing wind turbine control can be directly used regardless of HVAC or HVDC transmission system. The validity of the proposed control was also shown via experimental results.

7.2 Future Work Suggestions

The following topics, which are also very relevant for this work, is proposed for future work.

1. The experimental setup developed in order to study the co-ordination between the WPP side VSC and the full-scale wind turbines can provide a very good background to test and validate different control strategies in relation to the control and operation of a HVDC transmission system during normal operating conditions and disturbances. The setup can be further elaborated by adding a proper grid side VSC. This way the switch-over sequence of DC voltage control between two VSCs can be analyzed in further detail. The setup also provides a very good platform to pre-test the wind turbine side control system.

2. A single wind turbine model in RTDS was used to represent a WPP during the experiment. A RTDS based system provides a very fast solution to simulate a large WPP with many wind turbines. This will provide a very good opportunity to investigate detailed response from individual wind turbines when subjected to a voltage dip controlled by a VSC. As a future work, a detailed WPP model in RTDS can be prepared. This will also allowtesting the frequency response requirements of the WPP.

3. An economical comparison and other impacts of different FRT schemes can be investigated. As mentioned earlier a DC chopper provides a very simple

solution but the efforts required to dissipate the excess of energy is enormous. On the other hand, wind turbines are subjected to mechanical stresses during voltage dips. Cost and benefits of the two systems can be analyzed.

4. A detailed investigation on different simplifications that can be allowed on a wind turbine design when connected via HVDC system will be very interesting.
5. As the collector network is completely based on power electronic devices, harmonic stability analysis of the collector network can be done.
6. Grid requirements on negative sequence voltage control are slowly evolving. Further study and verification on the subject can be performed.
7. Though some work has already been done in relation to DC collector network as mentioned in some reference provided in the report, further investigation on this topic will be very interesting.

Bibliography

[1] (2011, July). [Online]. Available: http://www.thewindpower.net

[2] (2011, May). [Online]. Available: http://www.offshorecenter.dk

[3] “Delivering offshore wind power in europe,” European WInd Energy Association, Policy recommensations for large-scale development of offshore wind power in Europe by 2020, 2007.

[4] (2011, September) Thanet off-shore wind farm. [Online]. Available: http://www.vattenfall.co.uk/en/thanet-offshore-wind-farm.htm

[5] (2011, September) Horns rev ii. [Online]. Available: http://www.dongenergy.com/Hornsrev2/EN/Pages/index.aspx

[6] (2011, September) Borwin 1. [Online]. Available: http://www.abb.com/industries/ap/db0003db004333/a8e328849ac67b66c125774a00243367.aspx

[7] P. Kundur, *Power system stability and control.* McGraw-Hill, Inc., 1994.

[8] C. S. Schifreen and W. C. Marble, “Charging current limitations in operation or high-voltage cable lines,” *Power Apparatus and Systems, Part III. Transactions of the American Institute of Electrical Engineers*, vol. 75, no. 3, pp. 803 –817, jan. 1956.

[9] J. J. Dougherty and C. S. Schifreen, “Long cable lines-alternating current with reactor compensation or direct current,” *Power Apparatus and Systems, Part III. Transactions of the American Institute of Electrical Engineers*, vol. 81, no. 3, pp. 169 –178, april 1962.

[10] L. Colla, F. Gatta, A. Geri, S. Lauria, and M. Maccioni, “Steady-state operation of very long ehv ac cable lines,” in *PowerTech, 2009 IEEE Bucharest*, july 2009, pp. 1 –8.

[11] (2009, August) Horns rev off-shore wind farm. [Online]. Available: http://www.hornsrev.dk/index.en.html

[12] P. Noergaard, “A multi-turbine power curve approach,” in *Nordic wind power conference*, march 2004.

[13] (2009, August) The construction of Nysted wind farm. [Online]. Available: http://www.dongenergy.com/Nysted/EN/Pages/index.aspx

[14] H. Brakelmann, "Efficiency of hvac power transmission from offshore-windmills to the grid," in *Power Tech Conference Proceedings, 2003 IEEE Bologna*, vol. 2, june 2003, p. 6 pp. Vol.2.

[15] S. Y. King and N. A. Halfter, *Underground power cables*. Longman Inc., 1982.

[16] (2011, September). [Online]. Available: http://www.abb.com/industries/ap/db0003db004333/148bff3c00705c5ac125774900517d9d.aspx

[17] (2011, September). [Online]. Available: http://www.energy.siemens.com/us/en/power-transmission/hvdc/hvdc-plus/references.htm#content=2010%20Trans%20Bay%20Cable%20Project%2C%20USA

[18] S. Chaudhary, R. Teodorescu, and P. Rodriguez, "Wind farm grid integration using vsc based hvdc transmission - an overview," in *Energy 2030 Conference, 2008. ENERGY 2008. IEEE*, nov. 2008, pp. 1 –7.

[19] N. Flourentzou, V. Agelidis, and G. Demetriades, "Vsc-based hvdc power transmission systems: An overview," *Power Electronics, IEEE Transactions on*, vol. 24, no. 3, pp. 592 –602, march 2009.

[20] (2011, March) Siemens. [Online]. Available: http://www.energy.siemens.com/hq/en/power-transmission/hvdc/

[21] (2010, December) Abb. [Online]. Available: www.abb.com/hvdc

[22] T. Ackermann, Ed., *Wind Power in Power Systems*. John Wiley & Sons, Ltd, 2005.

[23] P. Bresesti, W. Kling, R. Hendriks, and R. Vailati, "Hvdc connection of offshore wind farms to the transmission system," *Energy Conversion, IEEE Transactions on*, vol. 22, no. 1, pp. 37 –43, march 2007.

[24] A. Lesnicar and R. Marquardt, "An innovative modular multilevel converter topology suitable for a wide power range," in *Power Tech Conference Proceedings, 2003 IEEE Bologna*, vol. 3, june 2003, p. 6 pp. Vol.3.

[25] M. Saeedifard and R. Iravani, "Dynamic performance of a modular multilevel back-to-back hvdc system," *Power Delivery, IEEE Transactions on*, vol. 25, no. 4, pp. 2903 –2912, oct. 2010.

[26] B. Chuco and E. Watanabe, "A comparative study of dynamic performance of hvdc system based on conventional vsc and mmc-vsc," in *Bulk Power System Dynamics and Control (iREP) - VIII (iREP), 2010 iREP Symposium*, aug. 2010, pp. 1 –6.

[27] U. Gnanarathna, A. Gole, and R. Jayasinghe, “Efficient modeling of modular multilevel hvdc converters (mmc) on electromagnetic transient simulation programs,” *Power Delivery, IEEE Transactions on*, vol. 26, no. 1, pp. 316 –324, jan. 2011.

[28] S. Allebrod, R. Hamerski, and R. Marquardt, “New transformerless, scalable modular multilevel converters for hvdc-transmission,” in *Power Electronics Specialists Conference, 2008. PESC 2008. IEEE*, june 2008, pp. 174 –179.

[29] B. Jacobson, P. Karlsson, G. Asplund, L. Harnefors, and T. Jonsson, “Vsc-hvdc transmission with cascaded two-level converters converter topology and main circuit,” in *Cigre 2010*, 2010.

[30] R. Marquardt and A. Lesnicar, “A new modular voltage source inverter topology,” in *EPE’03, Toulous*, 2003.

[31] M. Bierhoff and F. Fuchs, “Semiconductor losses in voltage source and current source igbt converters based on analytical derivation,” in *Power Electronics Specialists Conference, 2004. PESC 04. 2004 IEEE 35th Annual*, vol. 4, 2004, pp. 2836 – 2842 Vol.4.

[32] “Extruded cables for hvdc power transmission,” Prysmain Cables & Systems, Tech. Rep.

[33] L. Max, “Design and control of a dc collection grid for a wind farm,” Ph.D. dissertation, Chalmers University of Technology, Goteborg, Sweden, 2009.

[34] M. Carmeli, F. Castelli-Dezza, G. Marchegiani, M. Mauri, and D. Rosati, “Design and analysis of a medium voltage dc wind farm with a transformer-less wind turbine generator,” in *Electrical Machines (ICEM), 2010 XIX International Conference on*, 2010, pp. 1 –6.

[35] J. Sabate, V. Vlatkovic, R. Ridley, F. Lee, and B. Cho, “Design considerations for high-voltage high-power full-bridge zero-voltage-switched pwm converter,” in *Applied Power Electronics Conference and Exposition, 1990. APEC ’90, Conference Proceedings 1990., Fifth Annual*, Mar. 1990, pp. 275 –284.

[36] R. W. Erickson and D. Maksimovic, *Fundamental of Power Electronics*, 2nd ed. Kluwer Academic Publishers, 2004.

[37] N. Mohan, T. M. Undeland, and W. P. Robbins, *Power Electronics: Converters, Applications, and Design*. John Wiley & Sons, Ltd, 2003.

[38] (2010, December) Metglas® amorphous alloy 2605sa1 - technical bulletin. [Online]. Available: www.metglas.com

[39] S. Meier, T. Kjellqvist, S. Norrga, and H.-P. Nee, “Design considerations for medium-frequency power transformers in offshore wind farms,” in *Power Electronics and Applications, 2009. EPE ’09. 13th European Conference on*, 2009, pp. 1 –12.

[40] B. Van Eeckhout, D. Van Hertem, M. Reza, K. Srivastava, and R. Belmans, “Economic comparison of vsc hvdc and hvac as transmission system for a 300 mw offshore wind farm,” *European Transactions on Electrical Power*, vol. 20, pp. 661–671, July 2010.

[41] L. Kocewiak, J. Hjerrild, and C. L. Bak, “Wind farm structures impact on harmonic emission and grid interaction,” in *European Wind Energy conference and Exhibition, Warsaw*, 2010.

[42] G. Saccomando and J. Svensson, “Transient operation of grid-connected voltage source converter under unbalanced voltage conditions,” in *Industry Applications Conference, 2001. Thirty-Sixth IAS Annual Meeting. Conference Record of the 2001 IEEE*, vol. 4, sep-4 oct 2001, pp. 2419 –2424 vol.4.

[43] C. Du, “Vsc-hvdc for industrial power systems,” Ph.D. dissertation, Chalmers University of Technology, Goteborg, Sweden, 2007.

[44] R. Pena, J. Clare, and G. Asher, “Doubly fed induction generator using back-to-back pwm converters and its application to variable-speed wind-energy generation,” *Electric Power Applications, IEE Proceedings -*, vol. 143, no. 3, pp. 231 –241, may 1996.

[45] *Grid Code - High and extra high voltage*, E.ON Netz GmbH, Bayreuth Std., 2006.

[46] H.-S. Song and K. Nam, “Dual current control scheme for pwm converter under unbalanced input voltage conditions,” *Industrial Electronics, IEEE Transactions on*, vol. 46, no. 5, pp. 953 –959, Oct. 1999.

[47] L. Xu, B. Andersen, and P. Cartwright, “Vsc transmission operating under unbalanced ac conditions - analysis and control design,” *Power Delivery, IEEE Transactions on*, vol. 20, no. 1, pp. 427 – 434, jan 2005.

[48] Y. Suh and T. Lipo, “Modeling and analysis of instantaneous active and reactive power for pwm ac/dc converter under generalized unbalanced network,” *Power Delivery, IEEE Transactions on*, vol. 21, no. 3, pp. 1530 –1540, july 2006.

[49] I. Etxeberria-Otadui, U. Viscarret, M. Caballero, A. Rufer, and S. Bacha, “New optimized pwm vsc control structures and strategies under unbalanced voltage transients,” *Industrial Electronics, IEEE Transactions on*, vol. 54, no. 5, pp. 2902 –2914, oct. 2007.

[50] F. Wang, J. Duarte, and M. Hendrix, “Design and analysis of active power control strategies for distributed generation inverters under unbalanced grid faults,” *Generation, Transmission Distribution, IET*, vol. 4, no. 8, pp. 905 –916, august 2010.

[51] A. Leon, J. Mauricio, J. Solsona, and A. Go andmez Expo andsito, “Adaptive control strategy for vsc-based systems under unbalanced network conditions,” *Smart Grid, IEEE Transactions on*, vol. 1, no. 3, pp. 311 –319, dec. 2010.

[52] S. Meier, “Noble voltage source converter based hvdc transmission system for offshore wind farms,” Technical Licenciate, Royal Institute of Technology, 2005.

[53] V. Alkhmatov, “Analysis of dynamic behaviour of electric power system with large amount of wind power,” Ph.D. dissertation, Technical University of Denmark, Kgs. Lyngby, Denmark, 2003.

[54] R. Sharma and T. Rasmussen, “Laboratory investigation of variable speed control of synchronous generator with a boost converter for wind turbine applications,” in *Scientific Proceedings - European Wind Energy Conference & Exhibition*, 2008, pp. 85–88.

[55] J. K. Pedersen, “Power transmission from large offshore wind farms,” in *Universities Power Engineering Conference (UPEC)*, 1999.

[56] M. Haque, M. Negnevitsky, and K. Muttaqi, “A novel control strategy for a variable-speed wind turbine with a permanent-magnet synchronous generator,” *Industry Applications, IEEE Transactions on*, vol. 46, no. 1, pp. 331 –339, 2010.

[57] A. D. Hansen and G. Michalke, “Modelling and control of variable speed multi pole permanent magnet synchronous generator wind turbine,” *Wind Energy*, vol. 11, September 2008.

[58] J. N. Nielsen, V. Akhmatov, J. Thisted, E. Gr?ndahl, P. Egedal, M. N. Frydensbjerg, and K. H. Jensen, “Modelling and fault-ride-trough tests of siemens wind power 3.6 mw variable-speed wind turbines,” *Wind Engineering*, vol. 31, pp. 441–452, 2007.

[59] G. Ramtharan, N. Jenkins, and O. Anaya-Lara, “Modelling and control of synchronous generators for wide-range variable-speed wind turbines,” *Wind Energy*, vol. 10, pp. 231–246, 2007.

[60] V. Akhmatov, A. H. Nielsen, J. K. Pedersen, and O. Nymann, “Variable-speed wind turbines with multi-pole synchronous permanent magnet generators. part i: Modelling in dynamic simulation tools,” *Wind Engineering*, vol. 27, no. 6, pp. 531–548, December 2003.

[61] A. Perdana, “Dynamic models of wind turbines,” Ph.D. dissertation, Chalmers University of Technology, Goteborg, Sweden, 2008.

[62] (2010) The european offshore wind industry - key trends and statistics: 1st half 2010. EWEA. [Online]. Available: http://www.ewea.org/

[63] A. Ellis, Y. Kazachkov, E. Muljadi, P. Pourbeik, and J. Sanchez-Gasca, “Description and technical specifications for generic wtg models; a status report,” in *Power Systems Conference and Exposition (PSCE), 2011 IEEE/PES*, march 2011, pp. 1 –8.

[64] J. Conroy and R. Watson, “Aggregate modelling of wind farms containing full-converter wind turbine generators with permanent magnet synchronous machines: transient stability studies,” *Renewable Power Generation, IET*, vol. 3, no. 1, pp. 39 –52, march 2009.

[65] V. Akhmatov, “An aggregated model of a large wind farm with variable-speed wind turbines equipped with doubly-fed induction generators,” *Wind Engineering*, vol. 28, no. 4, pp. 479–486, June 2004.

[66] G. B. N. J. A. Shafiu, O. Anaya-Lara, “Aggregated wind turbine models for power system dynamic studies,” *Wind Engineering*, vol. 30, no. 3, pp. 171–185, May 2006.

[67] Y. Xue and V. Akhmatov, “Grid-connection of large offshore windfarms utilizing vsc-hvdc: Modeling and grid impact,” *Wind Engineering*, vol. 33, pp. 417–432, January 2009.

[68] C. Feltes, H. Wrede, F. Koch, and I. Erlich, “Enhanced fault ride-through method for wind farms connected to the grid through vsc-based hvdc transmission,” *Power Systems, IEEE Transactions on*, vol. 24, no. 3, pp. 1537 –1546, aug. 2009.

[69] G. Ramtharan, A. Arulampalam, J. Ekanayake, F. Hughes, and N. Jenkins, “Fault ride through of fully rated converter wind turbines with ac and dc transmission,” *Renewable Power Generation, IET*, vol. 3, no. 4, pp. 426 –438, december 2009.

[70] Y. Jiang-Häfner and R. Ottersten, “Hvdc with voltage source converters-a desirable solution for connecting renewable energies,” in *Large-scale integration of wind power into power system*, Oct 14-15 2009.

[71] A. Arulampalam, G. Ramtharan, N. Caliao, J. Ekanayake, and N. Jenkins, “Simulated onshore-fault ride through of offshore wind farms connected through vsc hvdc,” *Wind Engineering*, vol. 32, pp. 103–113, March 2008.

[72] T. Vrionis, X. Koutiva, N. Vovos, and G. Giannakopoulos, “Control of an hvdc link connecting a wind farm to the grid for fault ride-through enhancement,” *Power Systems, IEEE Transactions on*, vol. 22, no. 4, pp. 2039 –2047, nov. 2007.

[73] L. Xu, L. Yao, and C. Sasse, “Grid integration of large dfig-based wind farms using vsc transmission,” *Power Systems, IEEE Transactions on*, vol. 22, no. 3, pp. 976 –984, aug. 2007.

[74] X. Lie, Y. Liangzhong, and C. Sasse, “Power electronics options for large wind farm integration: Vsc-based hvdc transmission,” in *Power Systems Conference and Exposition, 2006. PSCE ’06. 2006 IEEE PES*, 29 2006-nov. 1 2006, pp. 760 –767.

[75] L. Xu and B. R. Andersen, “Grid connection of large offshore wind farms using hvdc,” *Wind Energy*, vol. 9, pp. 371–382, December 2005.

[76] M. Haque, K. Muttaqi, and M. Negnevitsky, “Control of a stand alone variable speed wind turbine with a permanent magnet synchronous generator,” in *Power and Energy Society General Meeting - Conversion and Delivery of Electrical Energy in the 21st Century, 2008 IEEE*, july 2008, pp. 1 –9.

[77] K. Tanomura, J. Arai, Y. Noro, K. Takagi, and M. Kato, “New control for hvdc system connected to large windfarm,” *Electrical Engineering in Japan*, vol. 166, no. 4, pp. 31–39, 2009.

[78] I. J. Nagrath and D. P. Kothari, *Electric Machines*. Tata McGraw-Hill Publishing Company Limited, 2000.

[79] *Matlab/Product help/Simulink/Simpowersystems/Asynchronous macnines*, The MathWorks, Inc., 2008.

[80] A. von Jouanne and B. Banerjee, “Assessment of voltage unbalance,” *Power Delivery, IEEE Transactions on*, vol. 16, no. 4, pp. 782 –790, oct 2001.

[81] Y. Wang, L. Xu, and B. Williams, “Compensation of network voltage unbalance using doubly fed induction generator-based wind farms,” *Renewable Power Generation, IET*, vol. 3, no. 1, pp. 12 –22, march 2009.

[82] G. Burchi, C. Lazaroiu, N. Golovanov, and M. Roscia, “Estimation of voltage unbalance in power systems supplying high speed railway,” *Electrical Power Quality and Utilisation*, vol. 11, no. 2, pp. 113–119, 2005.

[83] J. J. Grainger and W. D. Stevenson, *Power System Analysis*. McGraw-Hill, Inc., 1994.

[84] X. Wu, S. Lentijo, and A. Monti, “A novel interface for power-hardware-in-the-loop simulation,” in *Computers in Power Electronics, 2004. Proceedings. 2004 IEEE Workshop on*, aug. 2004, pp. 178 – 182.

[85] S. T. Cha, I. K. Park, and Q. Wu, “Real-time hardware-in-the-loop (hil) testing for power electronics controllers,” in *Accepted for presentation at Asia-Pacific Power and Energy Conference, APPEEC 2012*, 2012.

[86] M. Steurer, F. Bogdan, W. Ren, M. Sloderbeck, and S. Woodruff, “Controller and power hardware-in-loop methods for accelerating renewable energy integration,” in *Power Engineering Society General Meeting, 2007. IEEE*, june 2007, pp. 1 –4.

[87] W. Ren, M. Sloderbeck, M. Steurer, V. Dinavahi, T. Noda, S. Filizadeh, A. Chevrefils, M. Matar, R. Iravani, C. Dufour, J. Belanger, M. Faruque, K. Strunz, and J. Martinez, “Interfacing issues in real-time digital simulators,” *Power Delivery, IEEE Transactions on*, vol. 26, no. 2, pp. 1221 –1230, april 2011.

[88] (2011, September) Rtds technologies. [Online]. Available: http://www.rtds.com/index/index.html

[89] (2011, September) Spitzenberger & spies gmbh & co. kg. [Online]. Available: http://www.spitzenberger.de/

[90] M. Chinchilla, S. Arnaltes, and J. Burgos, “Control of permanent-magnet generators applied to variable-speed wind-energy systems connected to the grid,” *Energy Conversion, IEEE Transactions on*, vol. 21, no. 1, pp. 130 – 135, march 2006.

[91] N. Strachan and D. Jovcic, “Stability of a variable-speed permanent magnet wind generator with weak ac grids,” *Power Delivery, IEEE Transactions on*, vol. 25, no. 4, pp. 2779 –2788, oct. 2010.

[92] A. Yazdani and R. Iravani, “A neutral-point clamped converter system for direct-drive variable-speed wind power unit,” *Energy Conversion, IEEE Transactions on*, vol. 21, no. 2, pp. 596 – 607, june 2006.

A

Publications

This Work has also been reported in following publications:

1. **R. Sharma**, T. W. Rasmussen, K. H. Jensen, and V. Akhmatov, “Hvdc solution for offshore wind park comprising turbines equipped with full-range converters,” in EWEC Conference and Exhibition, Warsaw, Poland April 2010.
2. **R. Sharma**, T. W. Rasmussen, K. H. Jensen, and V. Akhmatov, “Modular vsc converter based hvdc power transmission from offshore wind power plant: compared to the conventional hvac system,” in IEEE EPEC 2010, Halifax, Canada, 25-27 August 2010. (IEEE EPEC 2010 paper award)
3. **R. Sharma**, T. W. Rasmussen, K. H. Jensen, and V. Akhmatov, “Comparative study of electrical structures for future offshore wind power plants,” in EPE Joint Wind Energy and T&D Chapters Seminar 2011, Trondheim, Norway, 9-11 May 2011.
4. **R. Sharma**, S. T. Cha, Q. Wu, T. W. Rasmussen, K. H. Jensen, J. Østergaard, “Power-hardware-in-the-loop test of VSC-HVDC connection for offshore wind power plants”, in Large-Scale Integration of Wind Power into Power Systems, Aarhus, Denmark 25-26 October 2011.
5. **R. Sharma**, T. W. Rasmussen, B. B. Jensen. “Application of a synchronous generator with a boost converter in wind turbines: an experimental overview”, submitted for publication in IET Renewable Power Generation, Manuscript ID: RPG-2011-0210.
6. **R. Sharma**, K. H. Jensen, T. W. Rasmussen, V. Akamatov, “Electrical structure of off-shore wind power plants with HVDC power transmission based on full-converter wind turbines: simulation model and fault-ride-through analysis”, prepared for submission at IEEE Trans. on Power Delivery.
7. **R. Sharma**, K. H. Jensen, “AC voltage control at the wind power plant collector network during low voltage fault-ride-through for a HVDC transmission system”, European Patent filed, 2011P04420EP.
8. **R. Sharma**, K. H. Jensen, “Control of HVDC connected offshore wind power plant during unbalanced grid faults”, European Patent filed, 2011P18719EP.

The list of other publications during the project period:

1. I. A. Aristi, R. Garcia-Valle, **R. Sharma**, G. Rodakis, K. H. Jensen, “Electromagnetic validation of fault-ride through capabilities of wind turbines”, in International Workshop on Large-Scale Integration of Wind Power into Power Systems. Quebec, Canada, 2010.
2. J. Liu, R. Garcia-Valle, I. A. Aristi, **R. Sharma**, K. H. Jensen, T. Sørensen, “EMT Validation of Fault-Ride-Through Capabilities of Wind Turbines Induction Generators with Full-rating Converter”, in International Workshop on Large-Scale Integration of Wind Power into Power Systems. Quebec, Canada, 2010.
3. T. W. Rasmussen, **R. Sharma**, “Speed control of a synchronous generator equipped with a passive rectifier and a boost converter”, in UPEC, Cardiff, Wales, 31 Aug. - 3 Sept. 2010. (Best paper award in power electronics UPEC 2010)

B

Transformer Design

The size (volume and weight) of an off-shore transformer is an important parameter, while the losses in the core and the windings are also equally significant. During the design of the transformer in this work, the main focus is, therefore, put on those parameters. The major input parameters for a transformer design are the power, voltage and current specifications, turns ratio, and core material specifications. Cores of standard size are not available for the given power level, therefore, core dimensions should be calculated as a part of transformer design. As for the geometry of the core, C-cores are selected. Similarly, the primary and the secondary winding conductor size needs to be calculated for lower losses and lower total volume.

The transformer primary winding in this work is referred to the low voltage side with fewer number of turns compared to the secondary winding which is also the high voltage side. For the primary side of the transformer winding solid foil conductors are selected, while for the secondary winding, strand type conductors (litz wires), are chosen. An approximate layout illustration of the transformer core and winding is shown in Fig. B.1.

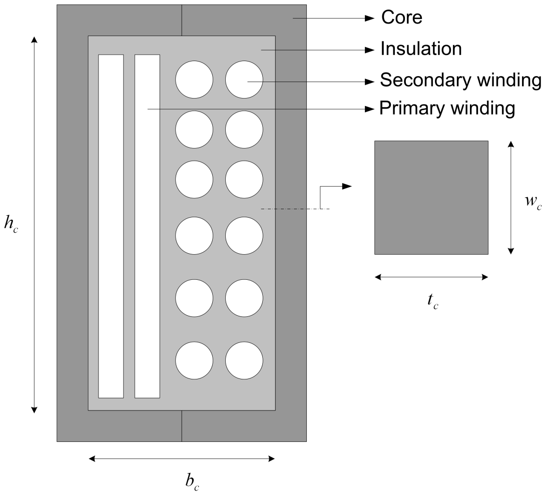

Figure B.1: Transformer core and winding representation.

The thickness of the foil conductor in the primary winding can be determined from the skin depth.

$$\delta = \sqrt{\frac{2.\rho}{2.\pi.F_s.\mu_0.\mu_c}} \tag{B.1}$$

where δ is the skin depth, ρ is the resistivity of the copper, F_s is the switching frequency, μ_0 is the permeability of the free space, μ_c is the relative permeability of the copper. $t_{cu,p}$ is the primary winding conductor thickness.

$$t_{cu,p} = \delta \tag{B.2}$$

The cross-section area ($a_{cu,p}$), and the height ($h_{cu,p}$) of the conductor can be calculated from the known value of allowable current density ($J_{cu,p} = 4$ $[A/mm^2]$) and the primary side input current ($I_{in,p}$).

$$a_{cu,p} = \frac{I_{in,p}}{J_{cu,p}} \tag{B.3}$$

$$h_{cu,p} = \frac{a_{cu,p}}{t_{cu,p}.n_{lay,p}} \tag{B.4}$$

where $n_{lay,p}$ is the number of layers per turn of the primary winding. To calculate the total height and the total breadth of the winding, the thickness of the insulation layer needs to be determined. In, it has been mentioned that the epoxy cast resin as an insulation material has a dielectric strength of 18 $[kV/mm]$. With practical design constraints and maximum transient over-voltage in consideration, $t_{in} = 12$ $[kV/mm]$ is chosen.

$$h_{cu,tot,p} = h_{cu,p} + 2.t_{in,p} \tag{B.5}$$

$$t_{cu,tot,p} = N_p.n_{lay,p}.(t_{in,p} + t_{cu,p}) + t_{in,p} \tag{B.6}$$

For the secondary winding, the height of the winding is determined by the number of winding turns and the number of winding layers. The concept of winding layers for the secondary winding is different from that of the primary winding. In the primary winding, layers represent the same winding turn split into layers. In the secondary winding, layers represent the number of turns put on top of each other.

$$h_{cu,tot,s} = \frac{N_p}{n_{lay,s}}.(t_{cu,s} + t_{in,s}) + t_{in,s} \tag{B.7}$$

$$t_{cu,tot,s} = n_{lay,s}.(t_{cu,s} + t_{in,s}) + t_{in,s} \tag{B.8}$$

The cross section area of the secondary winding conductor can be again found from the known allowable current density ($J_{cu,s}$), secondary output current ($I_{0,s}$) and the conductor fill factor (k_{cu}). According to, the copper fill factor for a Litz wire with special winding arrangements can be achieved as high as 0.75. With due consideration to practical constraints, a winding fill factor of 0.7 is selected. The diameter of the wire ($t_{cu,s}$) can be calculated by assuming the wire as one single circular conductor.

$$t_{cu,s} = \sqrt{\frac{4.a_{cu,s}}{\pi}} \tag{B.9}$$

From the above derived parameters, the inner dimensions of a C-core can be calculated.

$$h_c = max(h_{cu,tot,p}, h_{cu,tot,s}) \tag{B.10}$$

$$b_c = (b_{cu,tot,p} + b_{cu,tot,s}) \tag{B.11}$$

To calculate the cross section area of the core (a_c), the volt-second applied during the positive portion of the voltage waveform (λ_1) is required.

$$\lambda_1 = \int_t^{t+t_{pos}} v_1(t)dt \tag{B.12}$$

$$a_c = \frac{\lambda_1}{2.N_p.B_{pk}} \tag{B.13}$$

Where B_{pk} is the peak flux density in the core.

If a square core is assumed the thickness of the core (t_c) and the width of the core (w_c) are equal. The Length of the core (l_c) is calculated from these parameters.

$$l_c = 2.h_c + 2.b_c + 2.w_c \tag{B.14}$$

Similarly the volume of the core (v_c) can be calculated.

$$v_c = a_c.l_c \tag{B.15}$$

However, the volume of the core can be further optimized. For example, the inner dimensions of the core are optimized by assigning different layers of winding in primary and secondary and the set of results that gives the lowest volume of the core can be finally selected.

C

Snap Shots

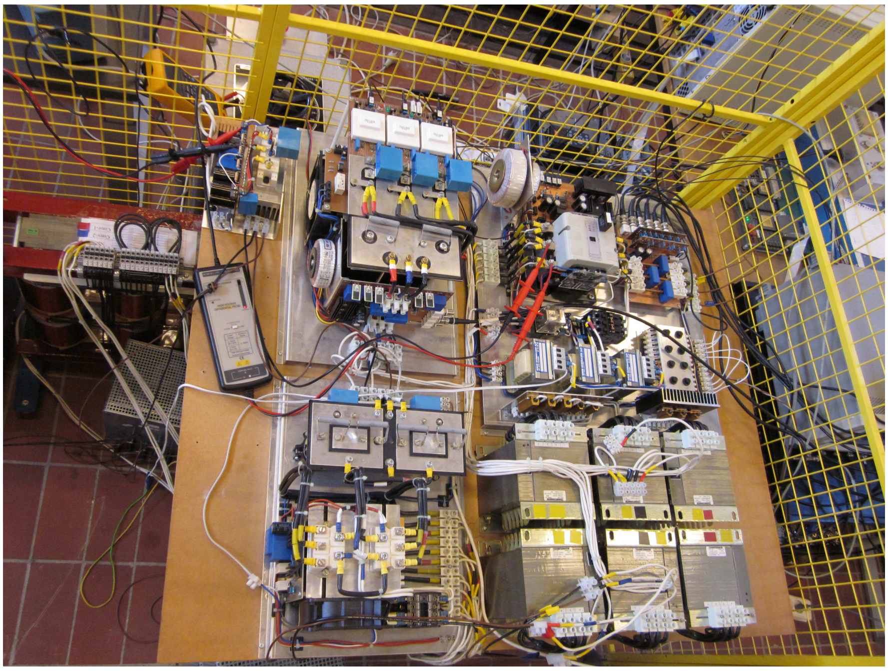

Figure C.1: Experimental set-up View 1 - Voltage sourced converter

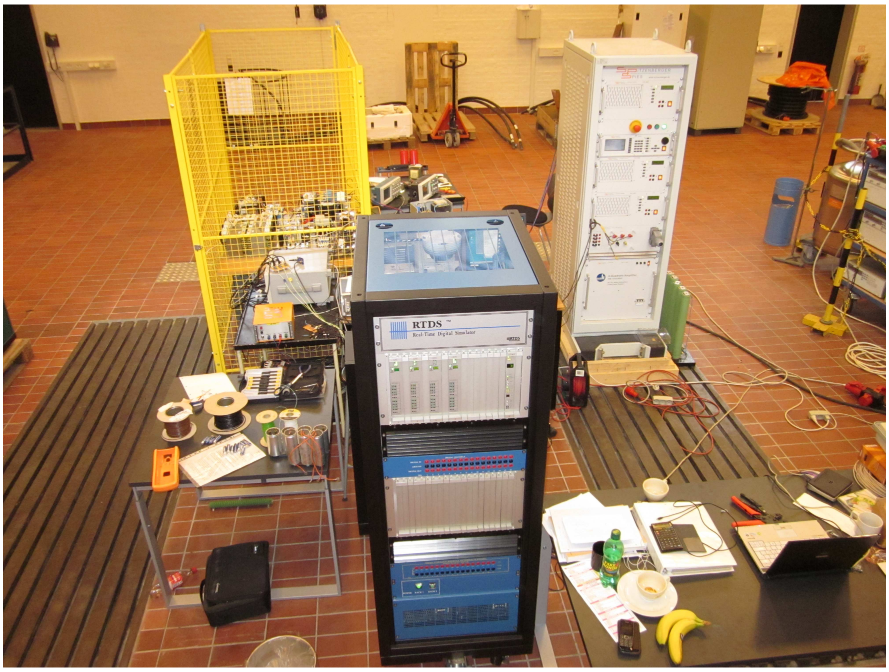

Figure C.2: Experimental set-up View 2

Figure C.3: Experimental set-up View 3

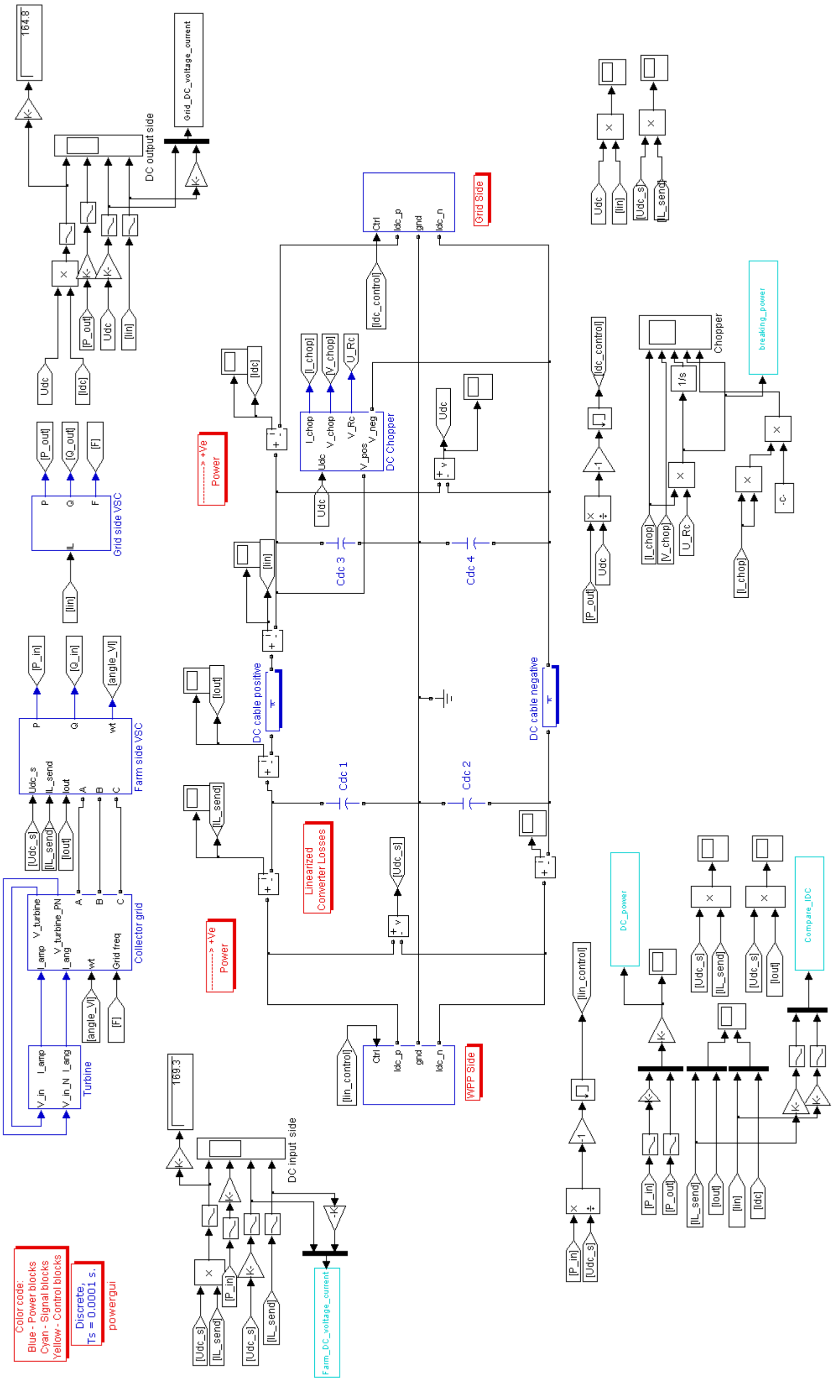

Figure C.4: Selected snap-shot of the simulation model - top level

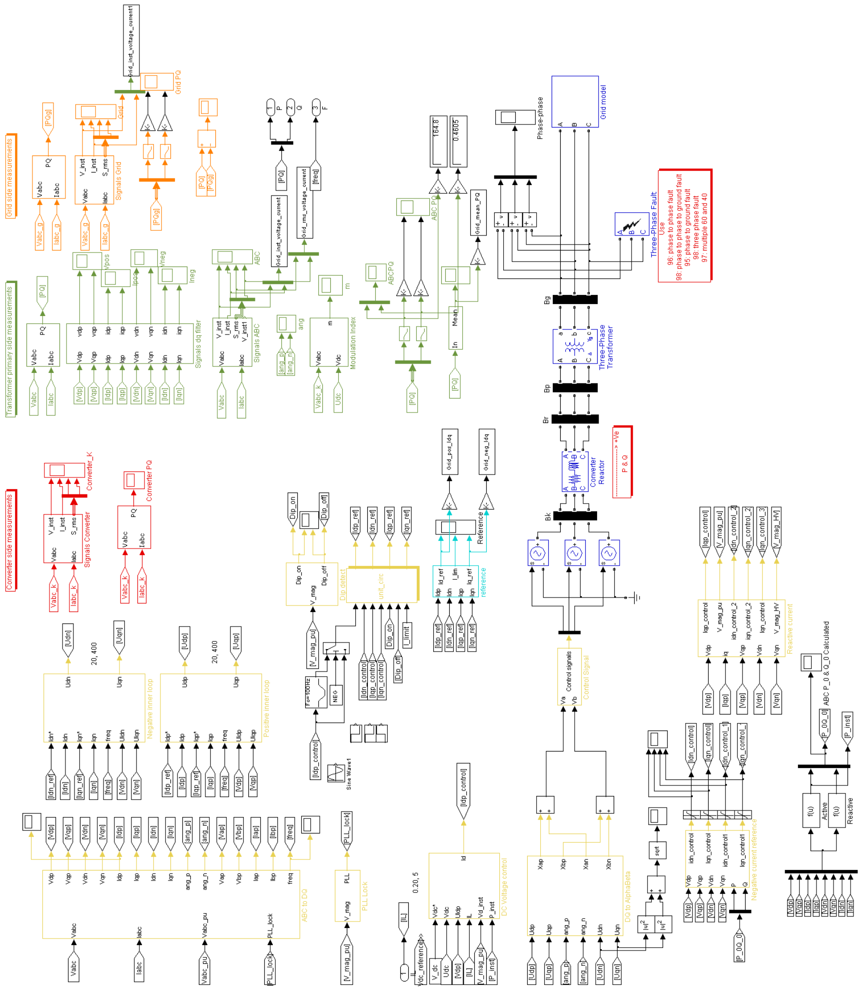

Figure C.5: Selected snap-shot of the simulation model - Grid side

www.elektro.dtu.dk

Department of Electrical Engineering
Centre for Electric Technology (CET)
Technical University of Denmark
Elektrovej
Building 325
DK-2800 Kgs. Lyngby
Denmark
Tel: (+45) 45 25 38 00
Fax: (+45) 45 93 16 34
Email: info@elektro.dtu.dk